Title

A quantitative phosphoproteomics screen to identify critical targets of the LKB1 tumor suppressor reveals GAP proteins for Ras superfamily GTPases as novel substrates of AMPK family kinases

Permalink

https://escholarship.org/uc/item/4d32m3d9

Author

Kamireddy, Anwesh

Publication Date

2020

Peer reviewed|Thesis/dissertation

UNIVERSITY OF CALIFORNIA SAN DIEGO

A quantitative phosphoproteomics screen to identify critical targets of the LKB1 tumor suppressor reveals GAP proteins for Ras superfamily GTPases as novel substrates of AMPK family kinases

A dissertation submitted in partial satisfaction of the
requirements for the degree Doctor of Philosophy

in

Biology

by

Anwesh Kamireddy

Committee in charge:

Professor Reuben J. Shaw, Chair
Professor Gen-Sheng Feng, Co-Chair
Professor Randy Hampton
Professor Tony Hunter
Professor Jing Yang

2020

The Dissertation of Anwesh Kamireddy is approved, and is acceptable in quality and form for publication on microfilm and electronically:

Co-Chair

Chair

University of California San Diego

2020

DEDICATION

I dedicate this thesis to my grandparents, who have always supported me at every step of my life. The values they instilled in me have taken me to many successes. Words cannot do justice to the impact they have had on my life.

TABLE OF CONTENTS

LIST OF FIGURES

LIST OF TABLES

ACKNOWLEDGMENTS

The first and foremost person I would like to thank is my advisor, Dr. Reuben Shaw. I was fortunate to get the opportunity to rotate in his lab and eventually turn that rotation project into a stepping stone for my final dissertation. Reuben’s passion for science and his ‘never-give-up’ attitude has given momentum to the project when it was feeling stuck. Reuben has been an extremely supportive mentor and ensured that I developed as a scientist, and for that I cannot thank him enough.

Many thanks to my committee members, Dr. Tony Hunter, Dr. Gen-Sheng Feng, Dr. Randy Hampton and Dr. Jing Yang for their guidance on the project, unwavering support and mentorship. I would like to thank them all for taking time out of their busy schedules to meet with me individually and give me advice on the project. Their advice has helped the project become fruitful.

I would like to thank the Salk Institute mass spectrometry core team - James Moresco, Jolene Diedrich and Antonio Michel Pinto. Their help in setting up and executing this large-scale screen was invaluable. The screen could not have been possible without the several rounds of optimizations and pilots that we performed to get to the final assay. The extended meetings, technical insights and several pilot studies have enabled the project to be successful and have help lay the foundation for several such follow-up studies in the future.

I would like to thank Anna Zagorska and Jon Goodwin for their vital help in establishing the detachment assay and performed the initial pioneering work that formed the basis for this thesis.

I am extremely grateful to the members of the Shaw lab, past and present, especially Sébastien Herzig, Nate Young, Portia Lombardo, Robert Svensson, Pablo Hollstein, Sonja Brun, Stephanie Curtis, Daniel Garcia, Amanda Hutchins, Liliana Vera, Kristina Hellberg, Matthew Chun, Erin Toyama, Lillian Eichner, Hector Galvez, Stephanie Mount, Amun Patel, Joshua Baumgart and Chien-Min Hung for all their mentorship, valuable suggestions, and friendship. Every member of the Shaw lab has been extremely supportive and they have made my time in the lab unforgettable. I thank them all for all the wonderful memories they have provided throughout my graduate studies

Lastly, my sincere and deepest gratitude to my family, especially my mother and my sister. I cannot thank them enough for their continuous and unparalleled love, help and support. I am forever grateful to my mother and grandparents who stressed the importance of education and I know that this respect for education has, in some unconscious way, shaped my values and made me the person that I am today. I especially thank my wife, Manasa for her patience and unwavering support through my Ph.D. studies, without whom I would never have been able to achieve his milestone.

Chapter Two in part is currently being prepared for submission for publication of the material. The study was designed by Anwesh Kamireddy and Reuben J. Shaw, who analyzed the data and wrote the thesis with feedback from all authors. Reuben Shaw directed and supervised the writing and oversaw the project which formed the basis for this chapter. The other authors include James Moresco, Jolene Diedrich, Antonio Michel Pinto, Sébastien Herzig, Stephanie Curtis, Joshua Baumgart and Jingting Yu.

Chapter Three, in full, is a reprint of the material as it appears in: Young NP, Kamireddy A, Van Nostrand JL, Eichner LJ, Shokhirev MN, Dayn Y, Shaw RJ. (2016). AMPK governs lineage specification through Tfeb-dependent regulation of lysosomes. Genes Dev. 2016 Mar 1;30(5):535-52. doi: 10.1101/gad.274142.115. On this publication, I was the second author. Nathan P. Young was the primary author. Reuben Shaw directed and supervised the writing and oversaw the project which formed the basis for this chapter.

VITA

2014-2020	University of California San Diego, La Jolla, CA Doctor of Philosophy in Biology
2009-2014	Genomics Institute of Novartis Research Foundation, San Diego, CA Scientific Associate II
2008-2009	Prodo laboratories, Irvine, CA Research Associate II
2006-2008	University of California Irvine, Irvine, CA Master of Science in Biotechnology
2002-2006	Visveswaraiah Technological University, Karnataka, India Bachelor of Engineering in Biotechnology

PUBLICATIONS

1. Islet isolation from human pancreas with extended cold ischemia time. Kühtreiber WM, Ho LT, **Kamireddy A**, Yacoub JA, Scharp DW. Transplant Proc. 2010 Jul-Aug;42(6):2027-31. doi: 10.1016/j.transproceed.2010.05.099. PMID: 20692399

2. Small-molecule inducer of β cell proliferation identified by high-throughput screening. Shen W, Tremblay MS, Deshmukh VA, Wang W, Filippi CM, Harb G, Zhang YQ, **Kamireddy A**, Baaten JE, Jin Q, Wu T, Swoboda JG, Cho CY, Li J, Laffitte BA, McNamara P, Glynne R, Wu X, Herman AE, Schultz PG. J Am Chem Soc. 2013 Feb 6;135(5):1669-72. doi: 10.1021/ja309304m. Epub 2013 Jan 25. Erratum in: J Am Chem Soc. 2013 Mar 20;135(11):4573. PMID: 23330637

3. Inhibition of DYRK1A and GSK3B induces human β-cell proliferation. Shen W, Taylor B, Jin Q, Nguyen-Tran V, Meeusen S, Zhang YQ, **Kamireddy A**, Swafford A, Powers AF, Walker J, Lamb J, Bursalaya B, DiDonato M, Harb G, Qiu M, Filippi CM, Deaton L, Turk CN, Suarez-Pinzon WL, Liu Y, Hao X, Mo T, Yan S, Li J, Herman AE, Hering BJ, Wu T, Martin Seidel H, McNamara P, Glynne R, Laffitte B. Nat Commun. 2015 Oct 26;6:8372. doi: 10.1038/ncomms9372. PMID: 26496802

4. AMPK governs lineage specification through Tfeb-dependent regulation of lysosomes. Young NP, **Kamireddy A**, Van Nostrand JL, Eichner LJ, Shokhirev MN, Dayn Y, Shaw RJ. Genes Dev. 2016 Mar 1;30(5):535-52. doi: 10.1101/gad.274142.115. PMID: 26944679

5. The AMPK-related kinases SIK1 and SIK3 mediate key tumor suppressive effects of LKB1 in NSCLC. Hollstein PE, Eichner LJ, Brun SN, **Kamireddy A**, Svensson RU,

Vera LI, Ross DS, Rymoff TJ, Hutchins A, Galvez HM, Williams AE, Shokhirev MN, Screaton RA, Berdeaux R, Shaw RJ. Cancer Discov. 2019 Nov;9(11):1606-1627. doi: 10.1158/2159-8290.CD-18-1261. Epub 2019 Jul 26. PMID: 31350328

6. Selective DYRK1A inhibitor for the treatment of Type 1 Diabetes: Discovery of 6-azaindole derivative GNF2133. Liu, Yahu; Jin, Qihui ; Zou, Yefen; Ding, Qiang ; Yan, Shanshan; Wang, Zhicehng; Hao, Xueshi; Nguyen, Bao; Zhang, Xiaoyue; Pan, Jianfeng ; Mo, Tingting; Jacobsen, Kate; Lam, Thanh; Wu, Tom; Petrassi, H. Michael ; Bursulaya, Badry; DiDonato, Michael ; Gordon, W; Liu, Bo; Baaten, Janine; Hill, Robert ; Nguyen-Tran, Van; Qiu, Minhua ; Zhang, You-Qing ; **Kamireddy, Anwesh** ; Espinola, Sheryll ; Deaton, Lisa; Ha, Sukwon; Harb, George ; Jia, Yong; Li, Jing; Shen, Weijun; Schumacher, Andrew ; Colman, Karyn ; Glynne, Richard; Pan, Shifeng; McNamara, Peter; Laffitte, Bryan; Meeusen, Shelly ; Molteni, Valentina; Loren, Jon. Journal of Medicinal Chemistry. Submitted on December 20th 2019. Publication under review.

ABSTRACT OF THE DISSERTATION

A quantitative phosphoproteomics screen to identify critical targets of the LKB1 tumor suppressor reveals GAP proteins for Ras superfamily GTPases as novel substrates of AMPK family kinases

by

Anwesh Kamireddy
Doctor of Philosophy in Biology
University of California San Diego, 2020
Professor Reuben Shaw, Chair
Professor Gen-Sheng Feng, Co-Chair

Liver kinase B1 (LKB1), encoded by the gene *STK11*, is a serine/threonine kinase that directly phosphorylates and activates a family of 14 downstream kinases known as the AMP-activated protein kinase (AMPK)-related protein kinases (AMPKRs). LKB1 is a

tumor suppressor gene inactivated in the cancer predisposition disorder Peutz-Jeghers syndrome as well as in 20% of all human lung cancers. LKB1 plays critical roles in a number of developmental, physiological, and pathogenic processes through regulation of metabolism, cell growth, cell polarity and autophagy. LKB1 accomplishes these functions through its activation of the AMPKRs and thus delineation of which AMPKRs are critical for particular processes is an area of active interest and study.

After decades of connections to cancer and metabolic diseases, our initial studies into LKB1 and the AMPKRs uncovered an unexpected role for AMPK, a metabolic regulator in cells, in lineage specification during embryogenesis. Embryonic stem cells lacking AMPK are incapable of forming normal chimeric embryoid bodies (EBs) upon differentiation. These AMPK-null EBs expressed lower levels of the transcription factor Tfeb, a master transcriptional regulator of lysosomes, resulting in diminished endolysosomal function and a defective endoderm. These results collectively uncovered a mechanism by which LKB1 through AMPK acts as a novel regulator of cell fate determination during differentiation.

In parallel efforts to explore LKB1-dependent functions of AMPK and its related AMPKRs, we discovered that detachment of cells from their substratum is a universal promoter of LKB1-driven AMPKR activation and downstream substrate phosphorylation. Using an enrichment technique based on antibodies that capture a phosphorylated substrate motif targeted by AMPKRs for phosphorylation, we performed quantitative phosphoproteomic screens on a panel of detached mammalian cells that expressed LKB1, but were null for pairs of AMPKRs. We identified several known substrates of AMPKRs

which underwent detachment-induced, LKB1-dependent increases in phosphorylation, thus validating our approach. We additionally identified several novel candidate proteins containing an optimal AMPKR motif which underwent an LKB1-dependent increase in phosphorylation. We validated six of these candidate proteins, including RASAL2, RalGAPα, SIPA1-Like proteins, MISP, BAIAP2L1 and MTSS2 as novel AMPKR substrates. Collectively, these results reveal unexpected effectors of LKB1 function and shed light on specific roles these AMPKRs play in cells.

CHAPTER ONE:

Introduction to Liver Kinase B1 (LKB1) and the AMPKR family of kinases

Cell signaling, protein phosphorylation and cancer

Cell signaling is the process by which cells constantly receive and respond to a diverse set of intracellular and extracellular stimuli to regulate basic cell functions, such as growth and survival. Cells have evolved over time to utilize proteins as highly effective molecules to transmit these signals to generate an apt response. Cells are able to respond to innumerable signals with a limited set of proteins by regulating their location, activity and concentration[1]. Cells can control the amount of protein in the cell by altering gene expression, protein synthesis and degradation. A more rapid method by which cells are able to transmit signals is by the post-translational modification (PTM) of proteins themselves. PTMs of proteins can regulate their activity, localization, stability and interaction with other proteins[2–4]. There are over 400 types of protein PTMs. However, one of the most common and well-studied type is phosphorylation[1,5].

Protein phosphorylation is a reversible form of PTM, wherein a kinase can add a phosphate group to a specific amino acid residue, and a phosphatase can remove a phosphate group from a residue. Currently, 536 human kinases[6,7] have been discovered, which can be grouped into ten families, based on sequence similarity. Similarly, the 241 active human phosphatases identified[8] can be classified into ten folds/trees, based on multiple sequence alignment of phosphatase domains, which determines substrate specificity[1,2]. Together these proteins control the phosphorylation status of over 100,000 human phosphosites[9–11]. Kinases catalyze the transfer of the phosphate group from high energy molecules, such as adenosine triphosphate (ATP), to a specific amino acid side chain on a protein substrate, yielding a phospho-protein target and a lower energy by product, such as adenosine diphosphate

(ADP)[2]. ATP is the most common energy donor used in the phosphorylation reaction, followed by guanosine triphosphate (GTP). The most common frequently observed type of protein phosphorylation involves the transfer of a phosphate group to amino acids with a free hydroxyl group, such as serine (~85%), threonine (~12%) or tyrosine (~1%)[1,2]. However, recently several instances of phosphorylation of histidine, aspartate, glutamate, cysteine, lysine and arginine have also been discovered[12]. These latter phosphorylations are difficult to isolate in-vitro and hence their endogenous rolls are challenging to study[12]. Features of protein phosphorylation, such as its specificity, reversibility and fast kinetics make it an ideal PTM for signal transduction.

Protein phosphorylation is a key regulator of several cellular functions including cell growth, proliferation, migration, differentiation, survival, metabolism control, subcellular trafficking, etc[2,13]. There are several mechanisms by which protein phosphorylation can regulate these processes. One mechanism is by controlling the protein's activity, which can be completely inhibited, activated or modulated to suit cellular demands[14]. Alternatively, phosphorylation within conserved domains critical for protein-protein contact can modify (disrupt or promote) these interactions and thus affect pathway activity[15]. The third mechanism by which protein phosphorylation can regulate cell signaling is by altering the subcellular location of the protein[16] and thus modulate access to binding partners, substrates or regulatory proteins. Lastly, protein phosphorylation on a given site of a protein might be a prerequisite for subsequent ubiquitination and targeting for proteasomal degradation, thereby regulating protein amount in the cell[17,18]. Signal transduction by protein phosphorylation is highly complex, but a comprehensive understanding of the role of kinases and phosphatases in regulating cellular function is vital to develop effective therapies for numerous pathologies, including cancer[2,19].

Cancer refers to a large group of diseases caused by uncontrolled growth of abnormal cells anywhere in the body. Cancer is caused by irregular changes (mutations) to genes that regulate normal cell growth and homeostasis[20,21] in the cell, and is the second leading cause of death in the world, after cardiovascular diseases[22]. Deregulation of phosphorylation, which controls several critical cell functions, has been linked to the initiation and progression of cancer[19–21,23,24]. This deregulation of phosphorylation can occur by several mechanisms. Mutation resulting in gain or loss of a key phosphorylatable amino acid on a protein prevents regulation by upstream kinases and results in altered protein function (which can promote cancer growth). Alternatively, mutations to kinases or phosphatases themselves can alter their activity and modulate phosphorylation of downstream substrates. Lastly, a mutation in the proteins that are involved in regulating a kinase or phosphatase's stability, translocation, expression, activation or inhibition can also result in deregulation of the phosphorylation-dependent signaling cascade[19,23,24]. Despite several advances in the development of therapies against several kinases[25,26] and phosphatases[27–29] implicated in cancer progression, an understanding of the entire oncogenic phosphoproteome is far from complete.

LKB1 is a tumor suppressor

One set of genes that are critical to preventing the progression of cancer are tumor suppressors. These are genes that encode proteins responsible for restricting cell cycle progression and cell growth, promoting DNA repair and apoptosis[21]. When these genes acquire loss of function mutations, cells can undergo uncontrolled division, causing cancer. Liver Kinase B1 (LKB1), also known as serine/threonine kinase 11 (STK11), is a ubiquitously expressed tumor suppressor gene inactivated in numerous human cancers[30]. It was originally discovered as the gene on human chromosome 19p13 commonly mutated in a familial cancer disorder called Peutz-Jeghers syndrome, a rare autosomal dominantly inherited disorder[31] characterized by multiple hamartomatous polyps in the gastrointestinal tract as well as pigmentation of the mucous membranes. These patients also present an increased risk for early onset tumors not limited to the gastrointestinal tract[32]. LKB1 is evolutionarily conserved back to *Caenorhabditis elegans* (as PARtitioning of cytoplasm family member-4; par-4) and has two potential homologues in *Saccharomyces cerevisiae* that perform similar functions[33]. LKB1 has been shown to be mutated or lost in over 30% of lung adenocarcinomas[30,34–37], over 20% of pancreatic ductal adenocarcinomas[38,39], and 20% of cervical cancer[40], establishing its role as a *bona fide* tumor suppressor. LKB1 has been determined to play a critical role not only in lung cancer metastasis[30,36,37], but also in other types of cancers such as breast[41–43], cervix[40], skin[44,45], brain[46], head and neck[47,48], ovary[49] and pancreas[38,39]. Whether the molecular mechanisms disrupted in LKB1's loss of function in lung tissues are similar to other tissues is still an area under investigation.

LKB1 structure and activation

In cells, LKB1 typically exists in the cytoplasm as a heterotrimeric complex with its two regulatory subunits - the pseudokinase STE20-related kinase adapter protein (STRAD) and the scaffolding protein Mouse Protein 25 (MO25, also known as Calcium-binding protein 39)[50–52]. Protein kinases are typically activated by phosphorylation of key residues in their activation loop, resulting in a conformational change that enables better binding of its substrates. Zeqiraj et. al., solved the crystal structure of LKB1 and help shed light on its phosphorylation-independent activation by its complex members[53]. They demonstrated that the binding of LKB1's complex members promote its activation loop being positioned similar to that of active kinases, resulting in a 100-fold increase in its activity without needing to be phosphorylated[53]. STRAD and MO25 both exist in cells as an α and β-isoform and either of the two isoforms of MO25 and STRAD are capable of binding to LKB1 and promoting its translocation from the nucleus to the cytoplasm[54,43]. However, the exact roles of the different isoforms of these proteins is not well understood.

Human LKB1 is 433 amino acids long and contains regulatory domains in both the N- and C-terminus, and a kinase domain in the middle[55]. The N-terminal domain contains a nuclear localization signal, while the C-terminus has several post-translationally modifiable sites that can regulate the activity, localization and degradation of LKB1[56,57]. LKB1 has been shown to undergo phosphorylation on several sites, some of which are autophosphorylation sites (Ser31, Thr185, Thr189, Thr336 and Thr402) while others residues are phosphorylated by different kinases (Ser307, Ser325, Ser334, Thr366, Ser399 and Ser428)[33,58–61]. Among these numerous modifications on LKB1, there are a few key phosphorylation events known to result in a change of LKB1 activity. LKB1 is phosphorylated by Protein Kinase C (PKC) ζ on Ser307, Ser399 and Ser428 which promotes its nuclear to cytoplasmic translocation and activation[60–62]. LKB1 can also be phosphorylated on Ser428 by protein kinase A (PKA) and ribosomal protein S6 kinase 90 kDa (p90-RSK) resulting in cell type specific increase of its activity[58,62]. ERK and Cyclin D1-Cdk4/6 can phosphorylate LKB1 on Ser325, which inhibits

LKB1's interaction with its substrates[63,64]. Phosphorylation of LKB1 by AKT on Ser334 results in its interaction with 14-3-3 and inhibition caused by nuclear retention[59]. Ataxia telangiectasia mutated (ATM) can phosphorylate Thr366 and activate LKB1[58,65].

Apart from phosphorylation-mediated activity modulation of LKB1, there are a number of other PTMs that regulate LKB1 activity *in vitro*. LKB1 undergoes polyubiquitination by S-phase kinase-associated protein 2 (SKP2) on five lysine residues (K41, K44, K48, K62, and K63), promoting increased interaction with MO25 and hence LKB1 activation[66]. LKB1 is also SUMOylated in response to energy and hypoxic stress on K178, which promotes LKB1 activation and nuclear export[67,68]. Farnesylation of Cys430 in LKB1 results in its translocation to the plasma membrane[55]. Neddylation promotes LKB1 stability while S-Nitrosylation on Cys430 promotes enhanced degradation[69,70]. Under oxidative stress conditions, 4-Hydroxy-trans-2-nonenal (HNE) modifies K97 on LKB1, inhibiting it[71]. Over ten lysine residues on LKB1 have been found to be acetylated. The protein deacetylase SIRT1 deacetylates LKB1 to promote its binding to STRADα and subsequent cytoplasmic localization and activation[72].

LKB1 is a master kinase that activates the AMPKR family of kinases

LKB1 can directly phosphorylate and activate a family of 14 kinases known as AMP-activated protein kinase (AMPK)-related protein kinases (AMPKRs)[50,51,54,73]. LKB1 and its substrates belong to the Ca2+/calmodulin-dependent protein kinase like (CAMKL) subclass of protein kinases[74]. These include two AMP-activated protein kinases (AMPKα1 and AMPKα2), three salt-inducible kinases (SIK1, SIK2 and SIK3), four microtubule affinity-regulating kinases (MARK1, MARK2, MARK3 and MARK4), two brain-specific kinases (BRSK1 and BRSK2, also known as SAD-B and SAD-A), Nua (novel)/SNF1-like kinases (NUAK1 and NUAK2) and sucrose non-fermenting 1–related kinase (SNRK). In turn, these 14 kinases phosphorylate numerous downstream substrates, some of which are common to several members of the AMPKR family[73]. Similar to LKB1, the AMPKαs and the MARKs are conserved back to yeast, where they have crucial roles of maintaining metabolism[75] and cell polarity[76,77] respectively. LKB1's kinase activity is also responsible for the maintenance of other key cellular functions including cell cycle[78–80], cell growth[32,73,81], genomic stability[82–84], embryo development[85–87], cell adhesion[88–91] and anoikis[92]. Deregulation of any of these key cellular functions can contribute to the tumorigenic and metastatic potential of a cell, which is evident by the kinase domain of LKB1 being the site of a majority of mutations in tumors[32].

AMPK exists in cells as a heterotrimeric complex consisting of a catalytic α subunit and two regulatory subunits (β- and γ-subunits)[93]. The mechanism by which LKB1 phosphorylates AMPKα is well understood. Cellular energy stresses that result in a decrease in the ratio of intracellular ATP:AMP cause the binding of AMP to the γ subunit of AMPK, inducing the exposure of AMPKα's Thr172 in the activation loop, which can be phosphorylated by LKB1 and leads to AMPK's activation[51,54,93–95]. Through downstream phosphorylation of its numerous substrates, AMPK activation turns off ATP-consuming processes within the cell, such as protein synthesis[96–98], lipogenesis[99], and gluconeogenesis[100], and turns on ATP-producing processes, such as glycolysis[101,102], autophagy[103–105], mitophagy[103,106,107] and fatty acid oxidation[108,109] to establish cellular energy homeostasis and promote cell survival[94,110–112] under energy stress[73,93,113–117]. Other AMPKRs exist in cells as monomers and have analogous threonine residues on their activation loops that can be phosphorylated by LKB1. However, the context of their regulation is unclear. There are very few instances where researchers have observed LKB1 is required for the activation of other AMPKRs, such as MARK1-4[89,118], NUAK1[91] and SIK1[118,119], and the underlying reported stimuli has been cell detachment and cell suspension. One of the most understudied aspects in the field is LKB1's role in detached and suspended cells, and key questions remain outstanding. Is LKB1, directly or indirectly sensing detachment and inducing cell death[118,119] or promoting cell survival[97,110,111]? Alternatively, is LKB1 rewiring metabolism[97] or polarity complexes upon suspension, or a combination of these effects? The current evidence suggests a concurrence between the cell undergoing detachment from its extracellular matrix (ECM) and the activation and signaling of LKB1-dependent kinases[89,91,110–112,118,119]. One possible way in which LKB1 could exhibit its tumor suppressive and metastasis inhibitory role is by inhibiting cell survival upon cell detachment from the extracellular matrix[120–124]. This form of programmed cell death is known as anoikis[124]. Cell detachment-induced LKB1 activation of one or more of these AMPKR substrates could trigger the initiation of anoikis. Gaining insight into whether cell detachment is a universal activator of AMPKRs by LKB1 will be helpful in further understanding LKB1's function as a tumor suppressor and metastasis inhibitor.

Identifying substrates of the AMPKR kinase family

Given AMPK's key role in regulating cellular metabolism, a number of groups have performed screens to identify its substrates. Screening approaches have included conditions that activate AMPK using either physiological activators, such as exercise[125,126], or pharmacological activators such as 2-Deoxy-D-glucose (2DG)[127,128], 5-Aminoimidazole-4-carboxamide ribonucleotide (AICAR)[107], A769662[107,128] and Metformin[129]. However, these AMPK activation studies have been performed in specific tissues such as mouse liver[129] or human skeletal muscles[125,126], or in cell lines such as HEK293T[127], U2OS[128] or mouse hepatocytes[107,130], and not in tissues or cells where the LKB1-dependent signaling has a critical role in tumor suppression, such as the lung or colon[30,34,36,131,132]. Apart from screens to identify AMPK substrates, to date only one screen has been performed aimed at discovering non-AMPK AMPKR substrates. Our lab has used an *in-silico* peptide library screening approach to identify substrates of the MARK kinases[89], similar to a previous approach to identify novel AMPK substrates[96]. However, no comprehensive approach to specifically decode substrates of all the AMPKR family members has been undertaken. Due to the current lack of knowledge of all the AMPKR substrates and their diverse functions, we remain unable to assign specific roles to each of the fourteen AMPKRs downstream of LKB1 regulation. Only recently has it been proven by independent groups that it is in fact the SIK kinases[118,133,134] that are partially responsible for LKB1's tumor suppressive role in mouse models of lung cancer and not AMPK[135]. Using cell detachment as a global activator of AMPKRs, we aimed to undertake a phosphoproteomic screening approach to identify substrates of AMPKRs and shed light on their specific roles in cells.

A recently published retrospective cancer study, on 240 advanced lung adenocarcinoma patients treated with immune checkpoint inhibitors, concluded that patients who had LKB1 mutations in their tumors had lower clinical benefit[136]. On similar lines, a preclinical trial of immune checkpoint inhibitors treating 174 lung adenocarcinoma patients identified loss of LKB1 function as the key driver of resistance to a successful clinical outcome[137,138]. A comprehensive understanding of how the deregulation of specific AMPKRs result in a lack of response to immune checkpoint inhibitor-mediated therapies is an area of active research. Identifying critical substrates of these specific AMPKRs and their function could shed light on designing future therapies to effectively treat lung adenocarcinoma and other cancers.

To identify new substrates of the AMPKRs, we first developed an assay where we would achieve the maximum activation of the LKB1 pathway. The goal of this approach was to utilize a platform to measure the rapid and robust downstream phosphorylation of the AMPKRs and in turn of their substrates. As discussed later in detail, we discovered that cell detachment results in a robust LKB1-dependent increase in AMPKR activation and downstream substrate phosphorylation. Using Lentiviral expression and CRISPR/Cas9-mediated genetic deletion approaches, we generated a panel of lung adenocarcinoma cell lines that express LKB1 and are null for pairs of AMPKRs. On these cells, we performed thorough quantitative phosphoproteomic analysis under attached and detached conditions as a way to identify novel AMPKR substrates. Using this approach, we were able to identify over hundred novel candidate substrates and further validated six novel substrates of the AMPKRs, which help provide a better understanding of the wide range of essential cellular functions regulated by this kinase family.

CHAPTER TWO:

A quantitative phosphoproteomics screen to identify critical targets of the LKB1 tumor suppressor reveals GAP proteins for Ras superfamily GTPases as novel substrates of AMPK family kinases

ABSTRACT

Liver kinase B1 (LKB1), also known as serine/threonine kinase 11 (STK11), is a master kinase that directly phosphorylates and activates a family of 14 downstream kinases, known as the AMP-activated protein kinase (AMPK)-related protein kinases (AMPKRs). The functions of a few AMPKRs, such as the AMPKαs and MARKs, in regulating metabolism and cell polarity respectively have been well established. However, the roles that the other 8 AMPKRs play in mediating LKB1's diverse cellular functions remain largely unknown. We discovered that cell detachment induces LKB1-dependent activation of several AMPKR kinases and phosphorylation of their downstream substrates. Using cell detachment as a stimulus, we combined CRISPR/Cas9-mediated genetic deletion of the AMPKRs with quantitative phosphoproteomics to discover novel substrates of the AMPKRs. We identified over 250 proteins containing an optimal AMPKR substrate motif that were undergoing LKB1-dependent increases in phosphorylation, several of which were known substrates. Consequently, we have identified numerous novel candidate AMPKR substrates and successfully validated six proteins as direct AMPKR substrates. Among them, we establish members of the Rap-GAP domain-containing proteins, including RalGAPα's and the SIPA1-Like proteins as novel AMPK substrates. RASAL2, a RasGAP domain containing protein, was discovered to be a novel substrate of multiple AMPKRs, including AMPK. Two I-Bar domain containing proteins, BAIAP2L1 and MTSS2 were identified as AMPKR substrates. BAIAP2L1 was found to be phosphorylated by both the AMPKαs and the MARKs, while MTSS2 was found to be a non-AMPK AMPKR substrate. We also determined MISP, a mitotic spindle position regulating protein, to be a novel AMPK

substrate. Ongoing and future work involves narrowing down the specific upstream AMPKRs responsible for phosphorylating each candidate protein and determining the effect the phosphorylation has on their function. We hope that by accurately assigning substrates to specific AMPKRs, we will gain a better understanding of the roles of AMPKR role in cells.

INTRODUCTION

LKB1 is an evolutionarily conserved and ubiquitously expressed tumor suppressor inactivated in numerous human cancers[30,34,36]. It was initially discovered as the gene mutated in a familial cancer disorder known as Peutz-Jeghers syndrome, a rare autosomal dominantly inherited disorder[4] characterized by multiple hamartomatous polyps in the gastrointestinal tract as well as pigmentation of the mucous membranes. LKB1 has been well established as a tumor suppressor and inhibitor of metastasis in numerous cancer types, most frequently in non-small cell lung cancer (NSCLC)[30,34,36,38,39,41–43].

LKB1 directly phosphorylates and activates a family of 14 kinases known as AMP-activated protein kinase (AMPK)-related protein kinases (AMPKRs)[51,54,73,114]. These include two AMP-activated protein kinases (AMPKα1 and AMPKα2), three salt-inducible kinases (SIK1, SIK2 and SIK3), four microtubule affinity-regulating kinases (MARK1, MARK2, MARK3 and MARK4), two brain-specific kinases (BRSK1 and BRSK2 also known as SAD-B/SAD-A), two Nua (novel)/SNF1-like kinases (NUAK1 and NUAK2) and the sucrose non-fermenting 1–related kinase (SNRK). Similar to LKB1, the AMPKαs and the MARKs are conserved between yeast and humans, where they have crucial roles in maintaining metabolism[75] and cell polarity[76,77] respectively. The AMPKRs phosphorylate numerous downstream substrates and are responsible for the maintenance of other key cellular functions including cell cycle[78–80], cell growth[32,73,81], genomic stability[82–84], embryo development[85–87], cell adhesion[88–91] and anoikis[92]. Each AMPKR has a threonine residue in its activation loop that can be phosphorylated by LKB1 resulting in its activation. LKB1 has been found to phosphorylate and activate AMPKα when the ratio of AMP:ATP in the cell increases. Once AMPKα is activated, it inhibits ATP-consuming processes and promotes ATP-producing processes to restore cellular energy levels[93]. However, the sensing of AMP by AMPK has been shown to be due to direct binding of 5'AMP molecules to conserved nucleotide binding domains in a regulatory protein, AMPKγ, that forms a complex with AMPKα[93]. Thus, there is no evidence that energy sensing by LKB1 per se. Based on a plethora of data on AMPK regulation, LKB1 is believed to simply be constitutively active and specific stress cues may direct it towards one or another of its 14 downstream kinases[53]. Apart from AMPKα, the exact mechanism and situations by which LKB1 activates the other AMPKRs is unclear and remains understudied. When cells undergo detachment or are forced into suspension, LKB1 has been found to directly activate specific AMPKR's such as MARK1-4[89,118], NUAK1[33], SIK1[118,119] and AMPK[91,110–112]. However, whether LKB1 is inducing anoikis[118,119] or promoting cell survival[110–112]in detached and suspended cells has not been established.

Numerous screens have attempted to identify novel AMPK substrates, using pharmacological[107,127–130] and physiological activators[125,126], as well as an *in-silico* peptide library-based[96,126] approach, mostly in hepatocytes or fibroblasts aimed at decoding the targets of AMPK involved in restoration of metabolic homeostasis. Similarly, an *in-silico* peptide library screen to discover substrates of the MARK kinases was reported[89], which identified a substrate involved in lung cancer cell metastasis. However, apart from screens to identify substrates of AMPK and MARK kinases, no screens to find substrates of the other eight AMPKRs have been reported, hence it has remained difficult to understand the specific roles of each of these eight AMPKRs. Recently, a few groups including ours have utilized genetically engineered mouse models of NSCLC to discover that the three kinases in the SIK subfamily of AMPKRs regulate key aspects of LKB1's tumor suppressive role[118,133,134]. However, the handful of known SIK substrates remain very incomplete compared to the thirty to forty known substrates of AMPK. Surprisingly, given the prominent role of LKB1 in lung cancer, none of the previous functional biochemical screens for AMPK or MARK substrates from any laboratory were performed in lung cancer cell lines.

Therefore, the aim of this study was to discover novel substrates of the AMPKRs, that may play a role in LKB1-dependent lung cancer suppression, and we utilized our finding that cell detachment results in a robust LKB1-dependent increase in overall AMPKR activation and downstream substrate phosphorylation. To identify candidate AMPKR substrates, proteins that contain phosphorylated serines within the optimal AMPKR substrate motif were immunoprecipitated using the PTMScan Phospho-AMPK substrate motif kit and analyzed with quantitative phosphoproteomic approaches. To further refine our analysis and selectively assign candidate substrate phosphorylation to a given subfamily of AMPKRs, we used CRISPR/Cas9 gene editing technology to delete pairs of AMPKRs in LKB1-expressing cells, and subjected these cells to detachment and downstream analysis. Using this approach, we were able to identify several candidate substrates and further validated six novel substrates of the AMPKRs. Our findings altogether shed new light on the wide range of essential cellular functions which the AMPKRs regulate.

RESULTS

Cell detachment induces LKB1-dependent activation of the AMPKR kinase family.

It has been well established that energy stresses that cause an increase in cellular AMP and ADP levels result in LKB1-dependent phosphorylation and activation of AMPKα[51,94,95]. Activated AMPKα then promotes the restoration of cellular energy homeostasis by acutely inhibiting anabolism and activating catabolism[93]. However, despite intensive study, it is still unknown which specific stimuli triggers LKB1-dependent activation of the other twelve AMPKRs. Discreet research articles have shown that LKB1 can activate AMPKRs, such as AMPKα[91,110–112,118], MARK1-4[89,118], NUAK1[91] and SIK1-3[118,119] upon cell detachment and cell suspension. Based on these clues, a key question we were looking to answer was whether cell detachment could be a trigger for global LKB1-dependent activation of AMPKRs.

To investigate the role LKB1 plays during cell detachment, we first generated pairs of lung carcinoma cell lines that had either a gain or loss of expression of LKB1, depending on the inherent LKB1 status in the cells. LKB1 null cells, such as A549 and H460, were stably transduced with retroviral pBABE vector expressing wild-type LKB1 and empty vector control. Conversely, LKB1-competent lung carcinoma cells, such as H2009 and H1975 were infected with viruses expressing an sgRNA against LKB1 or a control non-targeting one (NR1) in order to generate LKB1-null cell lines. These pairs of cells were subjected to detachment *in-vitro* by exposing them to an enzyme-free cell dissociation buffer containing EDTA, a method that has been shown to result in the LKB1-dependent activation of AMPKα[91,110] and NUAK1[91]. Corresponding attached cells were used as a control to truly study detachment-induced effects. Detached cells can be biochemically assayed by a strong reduction in the amount of phosphorylated Focal Adhesion Kinase (FAK) (pTyr397) upon detachment[139,140]. When we subjected A549 cells to the detachment assay, we found a consistent LKB1-dependent detachment-induced increase in phosphorylation of AMPKα and MARK family kinases (Figure 2.1). In lung tumor cells that had wild-type LKB1 added back, we also observed NUAK1 undergoing a strong electrophoretic mobility shift (also known as band-shift) in response to detachment, probably due to increased phosphorylation.

A549 cells have been well recognized as a suitable cell line to study LKB1 and AMPKR-dependent AMPKR regulation of key cellular functions. A549 cells have been widely used to study the function of MARK kinases, including MARK2's role in cell invasion[141], MARK3's role in regulating cell polarity[88] and MARK4's role in controlling cell migration[121]. Apart from their use in the study of MARK kinase family, A549 cells have been widely used to explore AMPK's regulation of metabolism[112], mitophagy[142], and inhibition of apoptosis[143,144]. Lastly, A549 cells are a useful model system to study the effect of LKB1's role in lung tumorigenesis by understanding its activation of NUAK1 to promote p53-dependent cell growth arrest[145] and activation of the SIK kinases and their role in the regulation of soft agar colony formation[43], oncogenesis[134], metastasis and anoikis[119]. Previous work done by our lab has shown that A549 cells had detectable levels of mRNA and protein of all the AMPKRs, except MARK1[43]. All these features made A549 cells with addback of wild-type LKB1 a powerful and tractable cell line to further study detachment-induced LKB1 activation of AMPKRs and identify novel substrates.

To our surprise we observed several AMPKRs, including AMPKα, MARK family kinases, and the SIK family kinases, undergoing a strong LKB1-dependent detachment-induced increase in phosphorylation of their activation loop threonine (Figure 2.2). NUAKs and BRSK1 were observed to undergo a band-shift in LKB1 expressing cells, which was further enhanced upon detachment. The band-shift is the consequence of LKB1-dependent phosphorylation of the AMPKRs (Figure 2.3). Similarly, in H1355 cells where we generated a stable addback of wild-type LKB1, we observed a strong LKB1-dependent activation of several AMPKR's upon cell detachment (Figure 2.4). Along with activation of several AMPKR's, several downstream known substrates of AMPKα, NUAK1, MARK, SIK were observed to undergo an increase in phosphorylation or band-shift in a LKB1-dependent detachment induced manner in A549 (Figure 2.5) and H1533 cells (Figure 2.6).

To further understand the extent of AMPKR activation upon detachment versus the attached state, we blotted entire cell lysates with the AMPK phospho-substrate motif antibody, and observed the strongest intensity in LKB1-expressing detached cells in both A549s (Figure 2.7) and H1355s (Figure 2.8). Collectively these results indicate that cell detachment causes robust LKB1-dependent activation of several AMPKR family members, which consequently phosphorylate several of their downstream substrates.

Quantitative phosphoproteomic screen identifies several known and predicted substrates of the AMPKRs.

To identify specific substrates of the AMPKRs we set up a cellular system in which we could query the function of AMPKR subfamilies, since closely-related paralogs are expected to target a common set of substrates. To do so, we knocked out pairs of AMPKR family members that share high sequence identity and been shown to have overlapping or redundant roles in cells, using CRISPR/Cas9. Using lentiCRISPR-v2[146] based stable expression of validated single sgRNA's, we were able to generate isogenic knockout lines of A549 cells expressing wild-type LKB1 deficient in AMPKα1+AMPKα2, MARK1+MARK4, MARK2+MARK3, NUAK1+NUAK2, SIK1+SIK3, SIK1+SIK2+SIK3, SADA+SADB (BRSK2+BRSK1) and SNRK alone. Control non-targeting guides were used in the A549 cells expressing empty vector and wild-type LKB1. In order to co-delete pairs of AMPKRs, we used lentiviral vectors that had distinct antibiotic resistant markers. We then immunoblotted for the AMPKRs and their known downstream substrates to validate functional loss of the given AMPKR in that cell line (Figure 2.9).

Previously, our lab determined the optimal consensus motif that AMPKα[96] and MARK[89] kinases preferentially phosphorylate using peptide library screening technology. Both these AMPKR subfamilies target the protein sequence [LMIVS]-[RK]-[RKH]-X-X-p[S] as one of their optimal substrate phosphorylation motifs. Based on this motif, Cell Signaling Technologies (CST) designed the PTMScan® phospho-AMPK substrate motif kit, which consists of a mix of rabbit monoclonal antibodies (raised against the above phospho-peptide sequence) conjugated to beads. CST had validated the specificity of this antibody kit using H1650 cells and determined that the motif that the antibodies most preferentially recognize is [LMS]-X-R-X-X-p[ST]. Thus, this antibody kit likely recognizes proteins phosphorylated by AMPK and MARK kinases, and potentially also recognizes phosphorylated targets of other AMPKRs. Previously, this antibody kit has been used as a phospho-target capturing tool to identify novel AMPK substrates using a combination of two pharmacological AMPK activators in mouse hepatocytes[55]. However, these authors only focused their approach on identifying proteins regulated by AMPK activation. Here, we decided to apply this approach on a broader scale to identify proteins phosphorylated as a consequence of LKB1 expression and activation in the presence or absence of distinct AMPKR subfamilies in both attached and detached cells, in order to more comprehensively identify novel substrates of the AMPKR kinase family.

We subjected the panel of ten A549 cell lines to the detachment assay (Figure 2.10). The cells were collected for screening in both the 'attached' and 'detached' state, and were quickly lysed using SDS lysis buffer in order to preserve their phosphorylation status (Figure 2.11). The rationale for running the screen on attached cell lysates was to control for differences in cellular protein content that might occur upon the expression of LKB1 and/or downstream knockout of AMPKRs which would also be present in detached cells. An additional goal of the attached cell data was to obtain information on a given protein's basal phosphorylation status in attached cells, which might vary in the different AMPKR knock out cell lines, so as to determine the true extent of the detachment-induced phosphorylation effects on the protein. Lastly, the attached cell data itself might show interesting regulation of a protein's phosphorylation status that is detachment-independent.

About 10% of the cell lysates were individually trypsin-digested, TMT-labeled using the TMT10plex™ Isobaric Labels and combined into a single tube. The TMT10plex™ Isobaric Labels enabled us to directly compare a given protein across all cell lines, making it easier to study the effect of LKB1 and the AMPKRs. These TMT labeled peptides were then fractionated into 8 fractions using a High pH Reversed-Phase Fractionation Kit and run on an LC/MS to get 'Input' data on the lysates[147]. Compared to traditional Mass Spec techniques, fractionating the samples at the peptide-level has been shown to be a very successful approach to both increase the overall coverage of proteins detected and improve the signal-to-noise ratio[148]. Also, Reversed-Phase chromatography separates peptides very efficiently based on their hydrophobicity, which has been useful to study proteins that undergo several post-translational modifications[126–128]. The Input data enabled us to determine endogenous levels of proteins in the panel of cell lines. The remaining 90% of the lysate was diluted ten-fold to reduce the concentration of SDS using the 1X IAP Buffer provided. This diluted lysate was then subjected to immunoprecipitation overnight using the PTMScan® Phospho-AMPK Substrate Motif Immunoaffinity Beads, which preferentially bind to the phosphorylated AMPKR substrate motif on proteins. The bead-bound immunoprecipitate from each condition was individually trypsin-digested, TMT-labeled using the TMT10plex™ Isobaric Labels and combined into a single tube. Half of this combined sample was then fractionated into 8 fractions using a High pH Reversed-Phase Fractionation Kit and run on an LC/MS to get 'Enriched' data. The other half of the combined sample was further subjected to a secondary enrichment for phosphopeptides using the High-Select™ Fe-NTA Phosphopeptide Enrichment Kit and then run on the LC/MS to get 'Phosphoenriched' data. The reasoning behind the phosphopeptide re-enrichment was to potentially identify very low abundance proteins that might be substrates of the AMPKR kinase family members, for which the single 'Enriched data' set might not be robust enough. To ensure consistency and reproducibility of the data, biological triplicates were performed, where the detachment assay and following steps were performed on three separate occasions. Protein and peptide identification from the screen were done with Integrated Proteomics Pipeline – IP2 (Integrated Proteomics Applications). The tandem mass spectra were extracted and searched with ProLuCID[149] against the Uniprot human database. The identified proteins were then filtered using [150] and setting the false discovery rate to 1% at the protein level[147].

In the Attached-Input and Detached-Input mass spec runs, 4495 and 4594 individual proteins were identified to be common in all the three triplicate runs respectively (Figure 2.12), representing about 75% of all the proteins identified, indicating high reproducibility between the processing of the three runs. Furthermore, there was a greater than 90% overlap between the proteins identified in the Attached-Input and Detached-Input triplicate mass spec runs. To assess the reproducibility of the individual triplicate runs, we calculated the LKB1/pBabe intensity for each protein in each individual run and plotted the average of the three runs and standard deviation between the three runs (Figure 2.13). For the Attached-Input runs, 75.5% of the proteins had a standard deviation of under 0.1 for their LKB1/pBabe intensity. This indicated a very high technical robustness and reproducibility between the triplicate data sets. Also, we found about 5% of the 4495 proteins having a greater than 1.5-fold increase in protein expression upon the expression of LKB1 (Table 2.1). Conversely, only 3.5% of the proteins were found to be 1.5-fold down-regulated in their expression by LKB1 expression in A549 cells (Table 2.2). AFAP1L2, a protein which according to the Mass Spec data has a LKB1/pBabe ratio of around 2, did show higher protein expression in LKB1 cells as validated by western blot (Figure 2.14). A deeper exploration into the two protein lists across the eight AMPKR knockout lines could shed light on which AMPKR's are responsible for the transcriptional regulation of those proteins or protein stability, an area of the field currently understudied.

To further validate the robustness of the screen in identifying proteins that were modulated by LKB1 in response to detachment, we compared the Attached and Detached-Enriched and Phosphoenriched runs. In the Attached and Detached-Enriched runs we identified 1972 and 2534 individual proteins to be common in the triplicate runs respectively (Figure 2.15), which represent about 63% and 63.7% overlap between the triplicate runs. Similarly, for the Attached and Detached-Phosphoenriched runs we identified 230 and 271 individual proteins to be common in the triplicate runs respectively, which represents about 49.5 and 48.6% overlap between the triplicate runs. We then compared the proteins common to the triplicate Input, Enriched and Phosphoenriched data sets in the Attached and Detached state to check for overlap between the various data sets. We observed a significant overlap between the Input and the Enriched data sets in both cell states, representing about 83.3% and 92.5% in the Attached and Detached state respectively (Figure 2.16). This high overlap is critical in ensuring that we were able to study phosphorylation-dependent changes in enrichment instead of protein abundance increases. We also observed significant overlap between the Enriched and Phosphoenriched data sets in both cell states, which can help us understand the extent of the detachment-induced effects we observed on specific proteins. When we compared the Input and the Phosphoenriched data sets in the Attached and Detached state, we saw the overlap drop to about 50% and 70.1% respectively (Figure 2.17). Although this indicated that for some of the possible AMPKR substrates we might not have any Input data to normalize the signal against, the double enrichment of phosphopeptides could potentially identify low abundance substrates that previous mass spec techniques might have missed.

One key question we had was how effective the AMPKR phospho-substrate motif immunoprecipitation was at pulling down proteins that contained the optimal consensus sequence. To address this question, all protein sequences were checked for the presence of an optimal AMPKR phosphorylation motif [LMIVS]-X-R-X-X-[S] using R in the RStudio[151,152] programming environment. In the Input runs we observed about 41% of the proteins identified had the optimal AMPKR substrate motif in their sequence (Figure 2.18). Upon enrichment with the AMPKR phospho-substrate motif antibody, the percentage of proteins with the optimal motif marginally increased to 50.4 and 47.8% in the Attached and

Detached runs respectively. One reason for these results may be that although the AMPKR phospho-substrate motif antibody enriches the peptide sequence [LMS]-X-R-X-X-[pS], it also preferentially enriches all R-X-X-[pS], thus resulting in the dilution of the proteins with the AMPKR target motif. Moreover, our search was limited to asking whether the sequence exists on the proteins, not considering whether the Ser is actually phosphorylated, resulting only in a mild increase in the percent of proteins with the optimal AMPKR motif. However, the percent of phosphorylated substrates containing an optimal AMPKR substrate motif significantly changed when we checked the Phosphoenriched data sets, where we observe the Attached set has about 87.4% and the Detached set has about 79% proteins with the optimal motif. This is almost a doubling in the percentage of proteins with the optimal motif over the Input, indicating significant enrichment.

To further validate the effectiveness of the screen to identify novel substrates of the AMPKRs, we chose several candidate proteins to validate biochemically. We filtered the data to look at proteins that had a greater than 1.5-fold increase in their LKB1/pBabe ratio and also had the optimal AMPKR substrate motif. In the Detached-Enriched and Detached-Phosphoenriched triplicate runs, 76% and 92% of the proteins, respectively undergo a 1.5-fold increase in LKB1/pBabe intensity and also had the optimal AMPKR motif. The A549 cells expressing wild-type LKB1 that were null for SIK1+SIK2+SIK3, SADA+SADB and SNRK grew significantly slower than the other seven cell lines and were excluded from the rest of the analysis for concerns of indirect effects on many kinases due to altered cellular proliferation (data not shown). We performed unbiased clustering of 252 and 66 proteins from the Detached-Enriched (Figure 2.20 and 2.21) and Detached-Phosphoenriched (Figure

2.22) triplicate runs, respectively and generated heatmaps of clustered proteins. Several known (blue arrows) and previously predicted substrates (purple arrows) of the AMPKRs were observed in both the Enriched and Phosphoenriched sets, thus validating our approach in discovering novel substrates. Six candidate proteins (orange arrows) were then chosen to undergo further validation to determine whether they are bona fide AMPKR substrates.

RalGAPα and SIPA1L3, members of the RapGAP domain containing family of proteins, are novel AMPK substrates.

Energy stresses that cause a drop in the ratio of cellular ATP-to-AMP result in AMPK activation, which then promotes ATP-generating processes and inhibits ATP-depleting processes to restore cellular energy homoestasis[93,97,103,105,113–115,117]. One way by which AMPK achieves this effect is by directly phosphorylating Tuberin (TSC2) on Thr1271 and Ser1387, thus activating it[98]. Activated TSC2 inhibits mTOR by promoting the conversion of Rheb-GTP to Rheb-GDP, thereby inhibiting protein synthesis and cell growth, and indirectly promoting autophagy to eventually restore cellular ATP and prevent apoptosis[96,98,153]. TSC2 is one of the eleven members of the RapGAP domain containing proteins in humans (Figure 2.23)[154]. Surprisingly, two other members of the RapGAP family, RalGAPα1 (GARNL1/AS250L) and SIPA1L3 were identified as potential AMPKR substrates in the Detached-Enriched and Phosphoenriched runs. Importantly, this is the first time in which these proteins have been identified as possible substrates of the AMPKR kinases (Figure 2.24).

RalGAPα1 was a top candidate for LKB1-dependent phosphorylation in both the Attached and Detached-Enriched data sets, having a greater than 3-fold increase in its LKB1/pBabe intensity (Figure 2.25). In the Detached-Enriched data, this 3-fold increase in LKB1/pBabe intensity was reduced significantly in the AMPK, MARK and SIK1+SIK3 null cells, suggested that several of these AMPKRs may be upstream kinases for RalGAPα1. In contrast, none of the AMPKR knockout cell lines blunted the LKB1-dependent increase we observed in the attached state in any of our three Attached-Enriched data sets. Together, these results imply that RalGAPα1 undergoes a strong increase in detachment-induced phosphorylation that is dependent on activation of the LKB1 pathway, which happens during cell detachment. Hence, in the attached state, where LKB1 pathway activation is minimal compared to the detachment-induced state, the regulation of phosphorylation of some substrates by any given AMPKR may be too subtle to ascertain.

Scanning RalGAPα1 for possible AMPKR phosphorylation motifs using Scansite (https://scansite4.mit.edu), we identified Ser797 and Ser860 as ideal sites that the AMPKR phospho-substrate motif antibody would bind to. ClustalW alignment of the two RalGAPα1 sites showed that the Ser797 and Ser860 sites and their surrounding residues are well conserved across vertebrates, conform to the optimal AMPKR motif and to their equivalent sites on RalGAPα2, Ser766 and Ser820 (Figure 2.26). Fortunately, Ser797 and Ser860 were found in the Detached-Phosphoenriched data sets to undergo an LKB1-dependent increase in phosphorylation, which was significantly blunted in the A549 cells expressing wild-type LKB1 which were null for AMPKα (Figure 2.27). This indicated that LKB1 could be regulating RalGAPα1's phosphorylation through AMPKα. These two phosphoserines were also identified in the Attached-Phosphoenriched data sets (Figure 2.28) to be phosphorylated in an LKB1-dependent manner, although as was the case with the overall phosphorylation status of RalGAPα1 as described above, we couldn't robustly detect a specific reduction in phosphorylation of these sites in AMPK-deleted cells in the attached state (Figure 2.25).

Nonetheless, as shown earlier, we have established that cell detachment causes robust and rapid activation of AMPK and promotes downstream phosphorylation of its substrates (Figure 2.4), and the AMPK-dependent increase in phosphorylation on RalGAPα1 sites prompted us to determine if these were due to direct post-translational modifications. We attempted to normalize the changes in phosphorylation intensities observed on RalGAPα1 to the protein content of individual cell lines in order to ascertain the true extent of phosphorylation increase. However, no counts for RalGAPα1 were recovered in the Input data, precluding our ability to perform this analysis. We also attempted to verify overall protein expression of endogenous RalGAPα1 in these cells by Western blot, though we were unsuccessful due to the lack of specific antibodies that recognize endogenous protein. However, mRNA expression analysis showed that at least at the transcript level, there were no significant changes in RalGAPα1 expression regardless of LKB1 or AMPKR status (data not shown).

We next set out to test the involvement of AMPK on RalGAPα phosphorylation at targeted sites in a more direct manner. We did not readily have tools to study RalGAPα1 directly, but previously, Ducommun *et. al.* (2015)[107] had identified RalGAPα1's paralog, RalGAPα2 (AS250), as a possible AMPK substrate. Their group also used the AMPK phospho-substrate motif antibody coupled with immunoprecipitation to identify AMPKα substrates in murine hepatocytes. This finding was very satisfying since it underscored the validity of our screening approach to identifying AMPK substrates. RalGAPα1 and RalGAPα2 are highly similar (54.6% sequence similarity) to each other and ubiquitously expressed in the body. A collaboration with Gustav E. Lienhard (Dartmouth College, NH) enabled us to obtain human RalGAPα2 cDNAs with point mutants to several serines, including Ser766 and Ser820, which are equivalent to the candidate sites on RalGAPα1 (Figure 2.26). In a 2006 publication from the Lienhard lab, Gridley *et. al.*[155] showed that Ser766 and Ser820 do not undergo an insulin-induced increase in phosphorylation, indicating that these two sites are AKT-independent sites. To test whether AMPK directs the phosphorylation of these sites, we collaborated with Cell Signaling Technology (Danvers, MA) to develop phosphospecific antibodies against RalGAPα2 Ser766 and Ser820. Using these phosphospecific antibodies, we observed AMPK-dependent phosphorylation on both Ser760 and Ser820 when RalGAPα2 was overexpressed in HEK293T cells, which was further enhanced upon AMPK activation by a specific small molecule AMPK activator, 991 (Figure 2.29). These results strongly suggest that AMPK can direct the phosphorylation of exogenously expressed RalGAPα2 on Ser766 and Ser820.

Signal-induced proliferation-associated 1-like protein 3 (SIPA1L3) was another top candidate in both the Attached and Detached-Enriched data sets as having a greater than 3.1 and 2.3-fold increase in its LKB1/pBabe intensity, respectively (Figure 2.30). These results reveal that even under basal attached conditions there is a strong LKB1-dependent increase in SIPA1L3's phosphorylation, although there was no clear indication as to which AMPKRs might be regulating this effect in the attached state. However, in the detached state, the MARK1+MARK4 knockout cells, followed by the AMPK knockout cells among all AMPKR knockout lines had the strongest decrease in phosphorylation intensity. This suggested that the MARKs and/or AMPK could be upstream kinases to SIPA1L3. Scanning SIPA1L3 for possible AMPKR phosphorylation motifs using Scansite (https://scansite4.mit.edu), we identified Ser1544 as an ideal site recognized by the AMPKR phospho-substrate motif antibody. ClustalW alignment of SIPA1L3 from different species showed that Ser1544 and their surrounding residues are well-conserved across vertebrates, and also conform to the optimal AMPKR motif and to their equivalent sites on SIPA1L1's Ser1585 and SIPA1L2's Ser1488 (Figure 2.31). In the Attached-Phosphoenriched triplicate runs, phosphorylation of SIPA1L1's Ser1585 was observed only once and had a two-fold increase in LKB1-dependent increase in phosphorylation.

As an individual site, SIPA1L3's Ser1544 was found in the triplicate Detached-Phosphoenriched set to be undergoing a mild (1.17-fold) LKB1-dependent increase in phosphorylation, which was not completely lost in any of the AMPKR null cells (Figure 2.32). The discrepancy between the weaker induction of an individual site versus the stronger overall phosphorylation on SIPA1L3 between the attached and detached state suggests that one or more as-of-yet uncharacterized additional sites may account for the relatively stronger induction in overall phosphorylation.

Phosphorylation of SIPA1L3's Ser1544 site was also observed, albeit in only one of the Attached-Phosphoenriched runs, with a two-fold increase in LKB1-dependent increase in phosphorylation. However, the phosphoenriched comparisons did not show an obvious indication as to which upstream AMPKR was specifically involved in regulating this individual site's phosphorylation, a result that underscores the challenge to assign individual AMPKRs role in targeting individual substrate sites from proteomic data alone.

In order to more directly investigate the role of AMPK-related kinases in targeting the SIPA1L family, we first looked to see if AMPK could play a role in phosphorylating the cognate site in SIPA1L1, using available cDNAs of SIPA1L1 bearing point mutations targeting SIPA1L1's serines. Using these cDNA constructs and the pAMPK substrate motif antibody, we observed AMPK-dependent phosphorylation of wild-type SIPA1L1 expressed in HEK293T cells, which was lost in the Ser1585A mutant (Figure 2.33). These results strongly suggest that AMPK can direct the phosphorylation of exogenously expressed SIPA1L1 on Ser1585A.

RASAL2 is a novel substrate of the AMPKRs.

RAS protein activator like 2 (RASAL2), is a member of the RAS GTPase-activating protein (RasGAP) family (Figure 2.34) and likely plays a contextual role in cancer, as it has been reported to have a tumor suppressive role[156–159] in several cancer types and an oncogenic[160–163] role in others[164]. RASAL2 was a top candidate hit in both the Attached and Detached-Enriched data sets, having more than 2-fold increase in its LKB1/pBabe intensity in both runs (Figure 2.35). These results indicated that RASAL2's phosphorylation is dependent on LKB1, which in these datasets could be observed independent of detachment. A few observations could be drawn from analyzing the enriched data sets. In the attached state, the proteomic data alone could not conclusively reveal which AMPKR is regulating RASAL2's phosphorylation. However, in the detached state the MARK2+MARK3 and SIK1+SIK3 knockout cells had a strong decrease in phosphorylation intensity. This suggested that the MARKs and SIKs could be upstream kinases for RASAL2. Scanning RASAL2 for possible AMPKR phosphorylation motifs using Scansite (https://scansite4.mit.edu), we identified five candidate sites on the protein including Ser56, Ser89, Ser736, Ser864 and Ser899. ClustalW alignment of RASAL2 from different species illustrated that the five candidate sites and their surrounding residues are well conserved across vertebrates and conform to the optimal AMPKR motif (Figure 2.36).

We then analyzed the datasets from the phosphoenriched conditions. In these datasets, the Attached-Phosphoenriched runs contained Ser89, Ser736 and Ser864-specific data, and these sites were found to be undergoing a LKB1-dependent increase in phosphorylation which was inhibited by the MARK2+MARK3 knockout cells (Figure 2.37), further suggesting that these kinases could be responsible for phosphorylating those sites under basal attached conditions. Unfortunately, no phosphorylation of these specific candidate sites on RASAL2 phosphorylation was found in the Detached-Phosphoenriched runs, which could simply indicate that this dataset was underpowered to provide enough coverage across these candidate sites. Nonetheless these results overall prompted us to test the role of LKB1 and AMPKRs on RASAL2 more directly.

To validate whether LKB1 can promote the phosphorylation of RASAL2 through one of the AMPKRs, we decided to immunoprecipitate endogenous RASAL2 from A549 cells under attached and detached conditions and blot back with the AMPK phospho-substrate motif antibody (Figure 2.38). We also included 991-treated conditions to see if activation of AMPK itself would have an effect on RASAL2 phosphorylation. In both whole lysates and immunoprecipitated protein, we readily observed that RASAL2 undergoes a strong detachment-induced band-shift irrespective of LKB1 status in the cell, reflecting that RASAL2 phosphorylation likely involves additional kinases beyond LKB1. However, in the immunoprecipitated protein we did observe a strong LKB1-dependent, detachment-induced increase in AMPK phospho-substrate motif antibody binding, which was partially diminished in the AMPK null cells. Also, we saw an AMPK-specific slight increase in pAMPK motif binding upon 991 treatment. Taken together, these results suggest that AMPK and other additional AMPKRs likely phosphorylate endogenous RASAL2.

To identify the specific sites on RASAL2 that underwent LKB1 and AMPKR-dependent increase in phosphorylation, we submitted samples of endogenous RASAL2 immunoprecipitated from A549 cells under attached, detached and 991-treated conditions for phosphoenriched proteomic analysis. Unfortunately, only the Ser864 among the five candidate AMPKR sites was detected. The Ser864 site appeared to undergo a LKB1-dependent increase in phosphorylation, which intriguingly was AMPK-independent (Figure 2.39), consistent with the hypothesis that other AMPKRs such as MARK or SIK kinases could potentially phosphorylate this site.

In the triplicate Detached-Enriched state (Figure 2.35), we observed that the LKB1-dependent increase in enrichment intensity of RASAL2 was completely inhibited by knocking out SIK1+SIK3. To investigate whether LKB1 can promote phosphorylation of RASAL2 through the SIKs upon detachment, we decided to immunoprecipitate endogenous RASAL2 from SIK1+SIK3-null A549 cells expressing wild-type LKB1 under attached and detached conditions and blot back with the AMPK phospho-substrate motif antibody (Figure 2.40). We observed a strong LKB1-dependent, detachment-induced increase in AMPK phospho-substrate motif antibody binding to the immunoprecipitated RASAL2, which was completely diminished in the SIK1+SIK3 null cells and partially diminished in AMPK and SIK1+SIK2 null cells, indicating that several AMPKRs might be responsible for this increase in RASAL2 phosphorylation. In order to decipher which of the three SIK kinases are most responsible for the strong LKB1-dependent, detachment-induced increase in phosphorylation of RASAL2, we knocked down the SIK kinases individually or in combination in A549 cells expressing wild-type LKB1 using siRNA treatment. We then immunoprecipitated endogenous RASAL2 from this panel of SIK knockdown cells under attached and detached conditions and blotted back with the AMPK phospho-substrate motif antibody (Figure 2.41). We observed that although knockdown of all three SIKs individually can cause a mild decrease in AMPK phospho-substrate motif antibody binding to the immunoprecipitated RASAL2 upon detachment compared to LKB1 expression alone, only SIK1+SIK3 knockdown completely reduced the antibody binding. Taken together, these results suggest that SIK1, SIK3 and AMPK likely phosphorylate endogenous RASAL2 upon detachment. Identifying which of the five AMPKR specific candidate sites are phosphorylated upon detachment in a LKB1-dependent manner and delineating the effect of these phosphorylations on RASAL2's function are areas currently under investigation.

I-Bar domain containing proteins, MTSS2 and BAIAP2L1, are novel AMPKR substrates

Inverse Bin-Amphiphysin-Rvs (I-BAR) domain-containing proteins are an evolutionarily conserved family of proteins involved in inducing a negative curvature on plasma membranes, resulting in membrane protusion[165]. The I-BAR protein family can be divided into two subfamilies, the Brain-specific angiogenesis inhibitor 1-associated protein 2 (BAIAP2) and BAIAP2-like proteins (BAIAP2L1/BAIAP2L2) subfamily and the Metastasis suppressor proteins (MTSS1 and MTSS2) subfamily (Figure 2.42). Our screen identified BAIAP2L1 and MTSS2 as possible substrates of the AMPKRs. Interestingly, several family members have been previously identified or predicted to be substrates of the AMPKRs. The best-studied one is BAIAP2 (also known as IRSp53), which has been established as an AMPK[117,127–129] and MARK2[141] substrate. Phosphorylation of BAIAP2 by the AMPKRs results in 14-3-3 binding to those sites, thereby inhibiting the protein[166–168]. Another subfamily member, BAIAP2L1 (also known as IRTKS) was also identified as a possible AMPK substrate in previous screens[127,130] and as a direct AMPKα2 interactor[169]. MTSS1 (also known as MIM) has also been identified as a possible AMPK substrate[107,130].

BAIAP2L1 was identified as a hit candidate that might be regulated by multiple AMPKRs, similar to BAIAP2. In the triplicate Attached-Enriched datasets, BAIAP2L1 had a 1.5-fold increase in its LKB1/pBabe intensity (Figure 2.43). This LKB1-dependent increase was completely inhibited by knocking out AMPKα1+α2 or MARK1+MARK4, indicating that in the basal attached state there is an LKB1-dependent phosphorylation of BAIAP2L1 that is promoted through AMPKα and MARK1/4 kinases. We scanned

BAIAP2L1 for possible AMPKR phosphorylation motifs using Scansite (https://scansite4.mit.edu), and identified Ser147, Ser331 and Ser422 as optimal AMPKR substrate motif sites. ClustalW alignment of the three BAIAP2L1 sites showed that the Ser147, Ser331 and Ser422 sites and their surrounding residues are well-conserved across vertebrates, conform to the optimal AMPKR motif and to their equivalent sites on their subfamily members BAIAP2 and BAIAP2L2 (Figure 2.44). Unfortunately, no phospho-serine specific data was detected for BAIAP2L1 in this screen.

To determine whether AMPK can directly phosphorylate BAIAP2L1, we stably expressed wild-type and triple alanine point-mutant (3SA) msBAIAP2L1 in wild-type and AMPK-null U2OS cells and subjected them to AMPK activation using 991. The strongest BAIAP2L1 band-shift was observed only upon AMPK activation on wild-type protein, indicating that exogenous BAIAP2L1 can be phosphorylated by AMPK (Figure 2.45). However, an unexpected observation was that even in AMPK-null U2OS cells, wild-type BAIAP2L1 underwent a mild band-shift in response to 991 treatment. To investigate whether this band-shift was a cell type specific phenomenon, A549 cells were stably transfected with FLAG-tagged msBAIAP2L1 and subjected to detachment assays or 991 treatment. Upon AMPK activation with 991, msBAIAP2L1 underwent a strong band-shift, which was absent in AMPK-null cells, indicating that AMPK is an upstream kinase for BAIAP2L1 (Figure 2.46). Furthermore, during cell detachment, BAIAP2L1 underwent a strong band-shift in wild-type LKB1 expressing cells, which was blunted, though not completely ablated in AMPK-KO cells, confirming that another AMPKR apart from AMPK may phosphorylate BAIAP2L1 upon cell detachment. Based on the observations from our

Attached-Enriched data, in which AMPK and MARK1/4 kinases appeared to mediate BAIAP2L1 phosphorylation (Figure 2.43), we decided to directly investigate whether MARK kinases could also be responsible for phosphorylating BAIAP2L1 upon cell detachment. We performed knockdown of MARK2, MARK3 and MARK4 in wild-type LKB1 expressing A549 cells and subjected them to detachment (Figure 2.47). In the attached state, knockdown of MARK2 and MARK3 reduced BAIAP2L1's band-shift, and this effect was more strongly pronounced in the MARK2+MARK3 double knockdown. Interestingly, this result was in contrast to BAIAP2L1's regulation in the Attached-Enriched data set (Figure 2.43), where MARK2+MARK3 knockouts did not have any reduction in intensity. However, in the detached state we observed that knockdown of MARK2, MARK3, and MARK4 prevented BAIAP2L1's band-shift, suggesting that BAIAP2L1 may be targeted by MARK kinases in addition to AMPK.

Intriguingly, when we subjected A549 cells expressing either WT or S3A msBAIAP2L1 to the detachment assay, we observed that a significantly higher number of cells remained attached to the cell culture plate at the end of one hour in the S3A msBAIAP2L1 (Figure 2.48). This suggested that Ser147, Ser331 and Ser422 of BAIAP2L1 may be involved in regulating cell mobility and actin remodeling roles[165,170,171]. Taken together, these experiments demonstrate that AMPKα and MARK2, 3 and 4, are capable of phosphorylating BAIAP2L1 and indicate an area of future study to ascertain how regulation by AMPKRs on BAIAP2L1 affect cellular function.

MTSS2 (also known as MTSS1L) was another top candidate hit in both the Detached and Attached-Enriched data sets, and showed a greater than 3.5 and 2-fold increase in its LKB1/pBabe intensity, respectively (Figure 2.49). Unlike our observations on proteomic data with BAIAP2L1 there was no clear indication as to which upstream AMPKRs are involved in the LKB1-dependent increase in phosphorylation. Scanning MTSS2 for possible AMPKR phosphorylation motifs using Scansite (https://scansite4.mit.edu) we identified five sites, Ser274, Ser456, Ser569, Ser579 and Ser612, that the AMPK phospho-substrate motif antibody could bind to. ClustalW alignment of the MTSS2's from different species showed that Ser456, Ser569, Ser579 and Ser612 are well conserved across all vertebrates and conform to the optimal AMPKR motif (Figure 2.50). Ser274 is conserved only in higher vertebrates, and along with Ser569 are the only two sites that have an equivalent site on MTSS1. When we analyzed our phosphospecific data for these sites, we found that Ser456 underwent a detachment-induced LKB1-dependent increase in phosphorylation, which was inhibited in the MARK2+MARK3 knockout and SIK1+SIK3 knockout cells, indicating that these kinases could be responsible for this phosphorylation (Figure 2.51). In the detached state, Ser579 and Ser612 also undergo an LKB1-dependent increase in phosphorylation. However, the AMPKRs responsible for the phosphorylation on these sites was unclear.

To validate that phosphorylation of MTSS2 is downstream of LKB1 signaling, A549 cells were stably transfected with FLAG-tagged msMTSS2 and subjected to detachment assays or 991 treatment. Only during cell detachment did MTSS2 undergo a strong band-shifting in wild-type LKB1 expressing cells, which was AMPK-independent (Figure 2.52). To identify the sites on MTSS2 that might be regulated by the non-AMPK AMPKRs, we submitted FLAG-tagged msMTSS2 immunoprecipitated from A549 cells under attached and detached conditions (Figure 2.53) for phosphoproteomic analysis. Mouse MTSS2's Ser271, Ser419, Ser542, Ser575, which are equivalent to Ser274, Ser456, Ser579 and Ser612 in human MTSS2, underwent an LKB1-dependent, detachment-induced increase in phosphorylation which furthermore was not AMPK-dependent. Human/mouse MTSS2 Ser569/532 was not detected in any of the Mass Spec approaches, probably because trypsin digestion of the protein results in this serine's inclusion into a small 4 amino acid fragment, which is not ideal for proteomic detection. Since the human Ser532 is highly conserved across species and is also conserved in MTSS1, we decided to generate point mutants of this site along with other candidate sites of regulation by LKB1, including Ser274, Ser456, Ser579 and Ser612. We generated two mouse MTSS2 constructs with different point mutations, the S3A-MTSS2 construct has Ser271, Ser419 and Ser575 mutated to alanines and the S5A-MTSS2 construct is effectively the S3A-MTSS2 plus the Ser532 and Ser542 mutated to alanines.

To validate which of these sites are responsible for the band-shift observed, we stably expressed wild-type, S3A and S5A FLAG-tagged msMTSS2 constructs in A549 cells and subjected them to the detachment assay (Figure 2.54). When we immunoprecipitated MTSS2 from these cells and blotted back with the AMPK phospho-substrate motif antibody, we observed a LKB1-dependent, detachment-induced increase in the AMPK phospho-substrate motif antibody binding to MTSS2 which was completely lost only in the S5A-MTSS2 expressing cells. The lack of any increase in the AMPK phospho-substrate motif antibody binding to S3A-MTSS2 in detached cells compared to attached cells indicated that

Ser532 and Ser542 might not undergo an increase in LKB1-dependent phosphorylation upon cell detachment. Furthermore, in both whole lysates and immunoprecipitated protein, we readily observed that MTSS2 undergoes a strong LKB1-dependent, detachment-induced band-shift which was AMPK-independent. Interestingly, this band-shift was inhibited in both the S3A-MTSS2 and the S5A-MTSS2 expressing A549 cells that also expressed wild-type LKB1. This indicated that phosphorylation status of Ser271, Ser419 and Ser575 primarily regulated the band-shift observed. Taken together this indicates that cell detachment results in a LKB1-dependent phosphorylation on Ser271, Ser419 and Ser575 of msMTSS2, which is independent of AMPK. Future work involves studying the effect of these phosphorylations on MTSS2's function in the attached versus detached cell state.

Mitotic interactor and substrate of PLK1 (MISP) is a novel AMPK substrate

MISP (also known as C19orf21) is an actin/focal adhesion-associated protein involved in mitotic spindle positioning (Figure 2.52)[172,173]. In the triplicate Attached-Enriched data set, MISP had a 3-fold increase in its LKB1/pBabe intensity and did not seem to be regulated by any specific AMPKR (Figure 2.53). However, in the Detached-Enriched data, the 1.5-fold increase in its LKB1/pBabe intensity was robustly brought down to control empty-vector levels in the MARK1+MARK4 knockout cells. This suggested that MARK1 and/or MARK4 could be upstream kinases to MISP. Scanning MISP for possible AMPKR phosphorylation motifs using Scansite (https://scansite4.mit.edu) we identified Ser394 as an ideal site that the AMPK phospho-substrate motif antibody could bind to. ClustalW alignment of the MISP's from different species showed that the Ser394 and its surrounding residues are well conserved across mammals and conform to the optimal AMPKR motif

(Figure 2.54). When we searched the Phosphoenriched data sets for this site, we found that in the attached state, this site did undergo an LKB1-dependent increase in phosphorylation (Figure 2.55). Interestingly, in the detached state, we confirmed that the MARK1+MARK4 knockout cells were able to bring the LKB1-dependent increase in phosphorylation on Ser394 back to empty vector levels, indicating that MARK1 and MARK4 could be upstream kinases to MISP.

To validate that MISP is a substrate of the AMPKRs, A549 cells were stably transfected with wild-type and S364-365A (S2A) FLAG-tagged mouse MISP and subjected to detachment assays or 991 treatment (Figure 2.56). When we immunoprecipitated MISP and blotted it back with the AMPK phospho-substrate motif antibody, we saw a strong LKB1-dependent, detachment-induced increase in phosphorylation on Ser364, as read out by the AMPK phosphor-substrate motif antibody blot. A surprising finding was that AMPK activation by 991 was also able to phosphorylate mouse MISP on Ser364. To further verify whether AMPK is an upstream kinase of MISP, we transiently overexpressed the FLAG-tagged msMISP constructs in wild-type and AMPK-null 293T's and immunoprecipitated MISP (Figure 2.57). When we blotted the immunoprecipitate with the AMPK phosphor-substrate motif antibody, we saw an AMPK-dependent phosphorylation on MISP, which further increased upon AMPK activation. Taken together, these results revealed that AMPK can promote the phosphorylation of exogenously expressed mouse MISP on Ser364. Whether the MARKs can also phosphorylate MISP is something to be explored in the future.

DISCUSSION

Deciphering signal transduction in any given cellular pathway is a challenging process, but it is critical in order to understand the pathway's role in key cellular functions. Although several technologies have been developed to address this issue from a technical stand point, identifying a single agent or stimulus that can activate an entire pathway has been rate-limiting. Our approach combined the use of single pathway activators along with CRISPR/Cas9 mediated genetic editing of kinases, plus specific enrichment of possible substrates followed by a quantitative phosphoproteomic analysis of the data. In this study, we established cell detachment as a stimulus that promotes LKB1-dependent activation of several AMPKRs in multiple cell lines. Furthermore, these activated AMPKRs act as signaling cascade transducers that subsequently phosphorylate several of their downstream substrates. Utilizing CRISPR/Cas9 technology, we generated several AMPKR null cell lines in A549 cells expressing wild-type LKB1 and subjected them to cell detachment. Phosphoproteins containing phosphopeptides that matched the AMPKR consensus motif were enriched from the cell lysates and quantified across the various cell lines using phosphoproteomics. Thus, here we have performed and analyzed triplicate screens that included Attached and Detached conditions encompassing Input, Enriched and Phosphoenriched datasets in order to identify novel substrates of the AMPKRs.

Across these datasets, we observed LKB1-dependent changes that were likely due to differences in protein expression rather than changes in phosphorylation status. From the Attached-Input data across triplicate sets, we were able to ascertain that about 8% of the ~ 4.5K proteins underwent LKB1-dependent changes in protein expression. Further studies into the specific upstream AMPKRs responsible for changes in protein expression could shed light on transcriptional and post-translational mechanisms that are controlled by specific AMPKRs beyond direct substrate phosphorylation (Table 2.1-2.2). We have also identified over 250 proteins which have an optimal AMPKR substrate motif sequence and undergo an LKB1-dependent, detachment-induced increase in phosphorylation (Figure 2.20-2.22). Some of these were previously validated or predicted substrates of the AMPKRs, and furthermore our screens have revealed a number of novel AMPKR substrate candidates. Future studies will be aimed at refining our understanding of how distinct AMPKRs regulate the function of their direct phosphorylation substrates.

The RalGAP complex, consisting of a catalytically active α subunit and a regulatory β subunit, has been well established as an inhibitor of the Rals, which are Ras-like small GTPases[174]. Our discovery that the RalGAPα1/a2 are direct substrates of AMPK indicates that AMPK might have an indirect role in regulating Ral activity in cells. Ral proteins have been implicated in the regulation of several key cellular functions, including glucose homeostasis, exocytosis and promotion of tumors and metastasis[174–178]. Decoding the role of AMPK-dependent phosphorylation on RalGAPα1 and RalGAPα2 will be critical to understanding the effect AMPK activation has on the cellular functions of Ral proteins. The SIPA1L's are a family of well conserved RapGAP and PDZ-domain containing proteins that can inactivate Rap. From the limited research that has been done on these proteins, it appears that a function of SIPA1L1 and 3 includes the regulation of cytoskeletal organization and cell polarity through Rap in the brain and eye[154,179–181]. The discovery that AMPK can directly phosphorylate SIPA1L1/3 proteins on an evolutionarily conserved serine, suggests that it might have a role in regulating their function. Future work involves establishing which endogenous AMPKRs phosphorylates this conserved serine, and the role that this PTM has on protein function and its downstream cellular effect. A very interesting AMPK and SIK substrate we identified in this screen was RASAL2, a RAS GTPase that has been shown to have a tumor suppressive role in lung adenocarcinoma[158,164]. Our findings reveal that RASAL2 is phosphorylated by several AMPKRs, including AMPK. Understanding the true effect of RASAL2 phosphorylation on the several sites targeted by LKB1-dependent kinases will be critical to know whether or not some aspects of LKB1's tumor suppressive function is promoted by RASAL2.

The I-Bar domain-containing proteins MTSS2 and BAIAP2L1 were also identified as candidate AMPKR-regulated substrates in this screen. From the limited research that has been done on MTSS2, its role in the formation of membrane protrusions has been established[165,182], similar to other members of its protein family. Whether or not AMPKRs beside AMPK can regulate this aspect of MTSS2's biology is an area to be explored. Similarly, BAIAP2L1 has been shown to have a role in regulating cell polarity, promoting cell proliferation and inhibiting apoptosis[165,170,183]. Our work indicates that AMPK and the MARK kinases can regulate BAIAP2L1's role in cell detachment. However, the exact mechanism by which they control this process needs further exploration. In a broad context, it appears that several I-Bar domain-containing proteins are substrates of AMPKRs. Another surprising candidate protein that we validated to be an AMPKR substrate is MISP. MISP has an actin-binding domain and controls mitotic progression by regulating mitotic spindle positioning and orientation[172,173,184,185]. In our proteomic data, endogenous MISP appeared to be a possible substrate of MARK1 and MARK4 kinases, which is plausible since the MARK4 does play functional roles in cell cycle progression[186]. Surprisingly, exogenously expressed MISP is an AMPK substrate, implying that in AMPK null A549 cells expressing wild-type LKB1, some other AMPKR is compensating for the lack of phosphorylation on endogenous MISP. Follow-up work involves verifying the endogenous upstream AMPKR of MISP.

In summary, we undertook a phosphoproteomic approach to identify novel substrates of the AMPKRs. Through this approach, we identified several known substrates and a number of novel candidate proteins whose phosphorylation status is regulated by AMPKRs. We successfully validated six of these candidate hits, encompassing distinct families of proteins, as novel AMPKR substrates. Future work involves validating additional candidate hits from our screen, discerning the effect of phosphorylation on each protein's function and to gain an understanding of how LKB1 and the AMPKRs modulate cellular function through these substrates. Ultimately, decoding the entire list of conserved substrates of the AMPKRs in different tissues will shed light on how these kinases control such diverse and critical cell functions.

MATERIALS AND METHODS

Cell culture and cell lines

A549, H1355, H460, H1299, H1975 293T, U2OS cells were purchased from ATCC. All cell lines were maintained in Dulbecco's modified Eagle's medium (Mediatech) supplemented with 10% fetal bovine serum (Gibco™, Thermo Fisher Scientific) and cultured at 37°C in 10% CO_2. All cell lines were mycoplasma tested once a month. H460, H1355 and A549 lines were stably transduced by infection with retroviral pBABE vector expressing wild-type LKB1 and kinase dead LKB1 and selected using Hygromycin (500ug/ml) (Thermo Fisher Scientific - 10687010). AMPK $\alpha1^{-/-}$ and $\alpha2^{-/-}$ double knockout U2OS and 293T cells were generated as described previously[1].

LKB1 and AMPKR knockout cell lines

Knockout cells were generated using the Cas9/CRISPR-mediated gene editing technology. Small Guide RNAs (sgRNAs) targeting all fourteen human AMPKRs and LKB1 were selected using the optimized CRISPR design tool (http://crispr.mit.edu). Guides with high on-target scores and low off-target scores were chosen. Three independent guides that preferably targeted the earliest few exons common to all transcripts were chosen based from sequence alignment in Ensembl database. Oligonucleotides for sgRNAs were synthesized by IDT, annealed, phosphorylated and ligated into either the BsmbI-digested lentiCRISPRv2 Puro (Addgene - 98290), lentiCRISPRv2 Blast (Addgene - 98293), or lentiCRISPRv2 Blast (Addgene - 98292). All vectors were sequence verified by Eton Biosciences to ensure no additional mutations. Validation of guide specificity was assessed by Western blot or qPCR of A549, H1299 and H1975 cells transfected with gene-specific guide and control non-targeting guides, sgTom (sgNR1) or sgLacZ (sgNR2) by stable integration of lentiCRISPRv2 by lentiviral transduction with viral supernatant supplemented with polybrene (Millipore - TR-1003-G) followed by selection after 24 hours with Puromycin (Sigma-Aldrich - P9620-10ML) (2ug/ml), Blasticidin (Thermo Fisher Scientific

- R21001) (10ug/ml) or Neomycin (Thermo Fisher Scientific - 10131027) (600ug/ml). All oligonucleotide sequences are listed in Supplemental Table S1. The following are sample guides used for the genes listed:

LKB1 – CCTCGGTGGAGTCGATGCGG, AMPKα1 – CTGGTGTGGATTATTGTCACAGG,
AMPKα2 – ACGTTATTTAAGAAGATCCGAGG, MARK1 – AGTGGCTCCTTGCCTTTCGATGG,
MARK2 - GTTGCGGCCCCGAATCATGTTGG, MARK3 – TCTAGAGTGCCGCGTTTAATTGG,
MARK4 – TTGAGGTTGTGCCCGTCGAAGGG, NUAK1 – TGCTATAAAATCCATTCGTAAGG,
NUAK2 – AAGATCTGATGCACATACGGAGG, SIK1 – GACAGTACTCCACGGCCGACAGG,
SIK2 – AATAATCGATAAGTCTCAGCTGG, SIK3 – AGTTCAGGTGCAGCATAGGGAGG,
SAD-A – ATCTCAATGGCCCGCCGCGCAGG, SAD-B - GGGTGAGCTATTCGACTACCTGG
SNRK – CACTCTTTAGACACATGGGATGG.

Lentiviral production

Lentiviruses made from lentiCRISPRv2 were produced by co-transfection of the lentiviral backbone constructs and packaging plasmids onto growing, low-passage HEK293T cells. Lipofectamine 2000 (Thermo Fisher Scientific - 11668019) was used as a transfection reagent at a ratio of 3:1 lipofectamine/plasmid following the manufacturer's protocol. Viral supernatant was collected 60-72 hrs post-transfection, 0.45um-filtered and added to cells with polybrene or flash frozen for storage at -80°C.

Phosphatase treatment

Equilibrated cell lysates were incubated with Lambda Protein Phosphatase (New England Biolabs - P0753S) according to the manufacturers protocol for 30 minutes at 30°C. Reaction was quenched by boiling the samples 95°C for 5 minutes in 1X sample buffer.

Western blots and immunoprecipitation

Cells were lysed in cold cell lysis buffer (20mM Tris (pH 7.5), 150 mM NaCl, 1 mM EDTA, 1 mM EGTA, 1% Triton X-100, 2.5 mM pyrophosphate, 50 mM NaF, 5 mM β-glycero-phosphate, 50 nM calyculin A, 1 mM Na3VO4) supplemented with cOmplete EDTA-free Protease Inhibitor Cocktail (Sigma-Aldrich - 11873580001). Lysates were rotated on ice for 15 minutes after lysis, then centrifuged at 13,200 rpm at 4°C for 15 minutes. The supernatants were then normalized using a BCA Protein Assay kit (Thermo Fisher Scientific - PI23225).

For immunoprecipitation of FLAG-tagged proteins, equilibrated lysates were incubated with FLAG-M2-affinity gel (Sigma-Aldrich - A2220) for 4 hours with constant rocking at 4°C. For immunoprecipitation of endogenous protein, equilibrated lysates were incubated with the antibody for 3 hours with constant rocking at 4°C, followed by another of rocking at 4°C with Protein A - Sepharose 4B (Thermo Fisher Scientific - 101041) beads. Immunoprecipitates were washed four times with cold cell lysis buffer. All cell lysates and immunoprecipitates were boiled 95°C for 5 minutes in 1X sample buffer and resolved on SDS-PAGE gels.

Cell detachment assay

This protocol has been adapted from the Zagórska *et. al*[91]. 70-80% confluent cells were treated with fresh warm complete media for one hour. For the detached state, cells were washed once with warm Ca^{2+}-Mg^{2+}–free Phosphate-buffered Saline (PBS) and incubated at

37°C in the incubator for the specified time (60-90min) in Cell Dissociation Buffer (Thermo Fisher Scientific - 13151014). At the given time point, the detached cells were collected by quenching the Cell Dissociation Buffer in warm complete media and centrifuging the cells gently (3 min, 100g at room temperature). The pelleted cells were immediately lysed using cold cell lysis buffer (for western blotting) or 1% SDS lysis buffer (for pAMPK motif immunoprecipitation). For the control attached state, cells were washed once with cold Ca2+-Mg2+–free PBS and lysed directly on the plate using the appropriate lysis buffer and the cells collected by scraping.

RNAi transfection and oligos

RNAi mediated gene depletion of proteins was carried out by reverse transfection of siRNA oligos using Lipofectamine™ RNAiMAX Transfection Reagent (Thermo Fisher Scientific - 13778150) according to manufacturer's protocol. siRNA duplexes were used at 20nM. Negative control used was the Stealth RNAi™ siRNA Negative Control, Med GC (Thermo Fisher Scientific - 12935300). ON-TARGETplus SMARTpool siRNA targeting human MARK2 (L-004260-00-0005), MARK3 (L-003517-00-0005), MARK4 (L-005345-00-0005), SIK1 (L-003959-00-0005), SIK2 (L-004778-00-0005) and SIK3 (L-004779-00-0005) were obtained from Horizon Discovery. Cells were subjected to respective assays 72 hours post siRNA transfection.

mRNA preparation and qPCR

mRNA from cells was prepared using the RNeasy Plus mini kit (Qiagen - 74134). cDNA was synthesized from 2 µg of RNA using SuperScript III (Thermo Fisher Scientific

- 18080-051), and qPCR was carried out with diluted cDNA, appropriate primers, and SYBR Green PCR master mix (Thermo Fisher Scientific - 43-091-55) using a C1000 Thermal Cycler (BioRad). Relative mRNA levels were calculated using the 2−Ct method, using beta-actin as an internal control.

Plasmid Constructs

The following cDNA's were obtained from Origene; mouse BAIAP2L1-FLAG (MR208255), mouse MISP-FLAG (MR209752), mouse MTSS1L-FLAG (MR210224), human RalGAPα2-FLAG (RC213138). Human RASAL2 cDNA was obtained from Addgene (70519). Human SIPA1L3 cDNA was obtained from Transomic (TCH1003). Mouse SIPA1L1 cDNA was obtained from the Ultimate ORF collection. Synthetic Human RalGAPα2-FLAG cDNA was a gift from Gustav E. Lienhard. All the cDNAs were PCR amplified and subcloned into pDONR221 with BP Clonase from Invitrogen (11789020). Site-directed mutagenesis was performed using Q5 DNA polymerase New England Biolabs (M0491L) according to the manufacturer's instructions. All the pDONR clones were sequence verified by Eton Biosciences to ensure no additional mutations in the cDNA. To create mammalian expression vectors, pDONR clones were recombined into DEST vectors using LR Clonase from Invitrogen (11791019). DEST vectors used in this study include the following vectors from Addgene: pLenti-PGK-NEO vector (19067), pLenti CMV V5-LUC Blast (21474), pBABE-Hygro (1765) and pBABE-Puro (1764).

Reagents and antibodies

The following antibodies were from Cell Signaling Technologies (CST): LKB1 (3047), Phospho-AMPK Thr172 (2535), Total AMPKα (2532), MARK2 (9118), MARK3 (9311), MARK4 (4834), Phospho-MARK Family (Activation Loop) (4836), SIK2 (6919), NUAK1 (4458), FAK (71433) phospho-AMPK substrate motif (5759), Phospho-ACC Ser79 (3661), ACC (3662), Phospho-Raptor Ser792 (2083), Raptor (2280), Phospho-ULK1 Ser555 (5869), ULK1 (6439), BRSK1 (5935), BRSK2 (5460), MO25α/CAB39 (2716), Phospho-MFF Ser146 (49281), MFF (84580), Phospho-cdc25C Ser216 (4901), Phospho-HDAC4 (Ser246)/HDAC5 (Ser259)/HDAC7 (Ser155) (3443), Phospho-HDAC4 (Ser632)/HDAC5 (Ser661)/HDAC7 (3424), Phospho-GEF-H1 Ser886 (14143). Phospho-Tau (Ser262) (44-750G) and STRADα (PA5-28594) are from Thermo Fisher Scientific. The MARK1/2/3/4 Antibody (Phospho-Thr215) (OAAF07619) is from Aviva Systems Biology. NUAK2 (NBP1-81880) and SIK3 (NBP2-47278) antibodies are from Novus Biologicals. Phospho-FAK (Tyr397) (ab81298), SNRK (ab96762), CRTC3 (ab91654), Anti-SIK1 (phospho T182) + SIK2 (phospho T175) + SIK3 (phospho T163) antibody (ab199474) are from Abcam. The STRADβ (10688-1-AP) and MO25β (CAB39L) (16137-1-AP) antibodies are from Proteintech. Phospho-MYPT1 Ser 445 (588261) was obtained from MRC-PPU Reagents. PARD3B (sc-398761) and CRTC2 (sc-271912) were from Santa Cruz Biotech. Phospho-DIXDC1 Ser592, phospho-RalGAPa1 Ser766 and phospho-RalGAPa1 Ser820 were developed in collaboration with Gary Kasof at CST. The HRP-conjugated secondary antibodies against mouse (AP124P) and rabbit (AP132P) were obtained from Millipore. β-Actin (A5441) and Flag (F7425) antibodies were from Sigma-Aldrich. AMPK activator 991 was obtained from Glixx. FLAG-M2-affinity gel (A2220) used for FLAG-tagged protein immunoprecipitation is from Sigma-Aldrich.

pAMPK motif immunoprecipitation and Mass spectrometry

Attached and detached cells were lysed in SDS lysis buffer (20 mM Tris (pH 7.5), 150 mM NaCl, 1% SDS) and boiled at 95°C for 5 minutes. The lysates were diluted ten-fold to reduce the concentration of SDS using 1X PTMScan IAP Buffer (CST 9993). The lysates were pre-cleared with Protein A - Sepharose 4B (Thermo Fisher Scientific - 101041) beads for 1-hour constant rocking at 4°C. The beads were collected by centrifugation and the supernatants were then normalized using a BCA Protein Assay kit (Thermo Fisher Scientific - PI23225). 10% of the equilibrated lysates were flash frozen for storage at -80°C as 'Input' samples. The remaining 90% of the equilibrated lysates were incubated with PBS washed PTMScan (LXRXXS*/T*) Motif Antibody Beads (CST – 5564) for 4 hours with constant rocking at 4°C. Immunoprecipitates were washed six times with cold PTMScan IAP buffer and boiled in Mass Spec sample elution buffer (50 mM Tris pH 7.5, 50 mM DTT, 5% SDS) for 10 minutes. The boiled samples are passed through Micro Bio-Spin Columns (Bio-Rad 7326204) to remove the beads and flash frozen for storage at -80°C as 'Enriched' samples.

All the Input and Enriched samples were precipitated using methanol-chloroform. Dried pellets were dissolved in 8 M urea/100 mM TEAB, pH 8.5, reduced with 5mM tris (2-carboxyethyl) phosphine hydrochloride (TCEP), and alkylated with 50mM chloroacetamide. Samples were diluted to 2 M urea/100 mM TEAB and proteins were then trypsin digested overnight at 37 °C. The digested peptides were labeled with TMT (Thermo Fisher Scientific - 90309, lot UC276347). The 10-plex samples were pooled and half was fractionated using the Pierce High pH Reversed-Phase Peptide Fractionation Kit into 8 fractions (Thermo

Fisher Scientific - 84868). The other half was phosphoenriched by High Select Fe-NTA Phosphopeptide enrichment Kit (Thermo Fisher Scientific - A32992). The TMT labeled samples were analyzed on an Orbitrap Fusion Lumos mass spectrometer (Thermo Fisher Scientific). Samples were injected directly onto a 25 cm, 100 μm ID column packed with BEH 1.7 μm C18 resin (Waters). Samples were separated at a flow rate of 300 nL/min on a nLC 1200 (Thermo Fisher Scientific). Solutions A and B were 0.1% formic acid in water and 90% acetonitrile/0.1% formic acid, respectively. A gradient of 1–25% B over 180 min, an increase to 40% B over 30 min, an increase to 100% B over another 20 min and held at 90% B for a 10 min was used for a 240 min total run time for the bRP fractions. The phosphoenriched samples were injected twice with 120 min gradients of 1–25% B over 75 min, an increase to 40% B over 30 min, an increase to 100% B over another 10 min and held at 90% B for a 5 min. Column was re-equilibrated with solution A prior to the injection of sample. Peptides were eluted directly from the tip of the column and nanosprayed directly into the mass spectrometer by application of 2.8 kV voltage at the back of the column. The Lumos was operated in a data dependent mode. Full MS1 scans were collected in the Orbitrap at 120k resolution. The cycle time was set to 3 s, and within this 3 s the most abundant ions per scan were selected for CID MS/MS in the ion trap. MS3 analysis with multinotch isolation (SPS3) was utilized for detection of TMT reporter ions at 30k resolution[187]. Monoisotopic precursor selection was enabled and dynamic exclusion was used with exclusion duration of 10 s.

Protein and peptide identification were done with Integrated Proteomics Pipeline – IP2 (Integrated Proteomics Applications). Tandem mass spectra were extracted from raw files using RawConverter[188] and searched with ProLuCID[149] against Uniprot human database. The search space included all fully-tryptic and half-tryptic peptide candidates. Carbamidomethylation on cysteine and TMT labels on N terminus and lysine were considered as static modifications. Phosphorylation was considered as a variable modification on STY with a maximum of three modifications per peptide. Data was searched with 50 ppm precursor ion tolerance and 600 ppm fragment ion tolerance. Identified proteins were filtered to 10 ppm precursor ion tolerance using DTASelect[150] utilizing a target-decoy database search strategy to control the false discovery rate to 1% at the protein level[147]. Quantitative analysis was done with Census[189] filtering reporter ions with 20 ppm mass tolerance and 0.6 isobaric purity filter.

Mass Spec data analysis, normalization and clustering of data to generate heat maps of top hits

For a given protein, the IP2-normalized intensity for each of its peptides detected in a given channel is added to get a total for that channel. This is repeated for each of the other 9 channels as well, to get the total intensity for the protein in each cell line. Each protein's LKB1/pBabe intensity ratio is calculated in each of the triplicate runs and the average is determined. Only the proteins found in all the triplicate runs and having an average of LKB1/pBabe intensity ratio greater than 1.5 are then scanned across their sequence to identify any optimal AMPKR motifs on the protein. This was done using R in the RStudio programming environment[151,152]. Each protein that has an optimal AMPKR motif and a LKB1/pBabe intensity ratio of greater than 1.5 is then selected for gene expression clustering using GeneCluster 3.0[190] (http://bonsai.hgc.jp/~mdehoon/software/cluster/). The genes are centered by their means and Hierarchical gene clustering is done using the average linkage clustering method to generate unbiased clustering of the hits identified. The clustered data is used to generate a heat map using Java TreeView (Version 1.1.6r4)[191] (http://jtreeview.sourceforge.net/) and images of gene cluster are extracted.

Identifying potential AMPKR motifs in proteins

Protein sequences were analyzed for the presence of an optimal AMPKR phosphorylation motif of [LMIVS]-X-R-X-X-[S]. Analysis was performed using R in the RStudio programming environment[151,152]. Data was then processed using Dplyr from the Comprehensive R Archive Network[192]. Protein sequences were acquired from Ensembl (Database version 98) using BiomaRt 2.43.0 and AnnotationDbi 1.48.0 packages from Bioconductor 3.10[193–197]. Protein sequences were scanned for the specified amino acid residue sequence variations conforming to the optimal AMPKR motif to identify proteins containing sites of potential phosphorylation. Conforming sites were extracted for manual review.

Generating Venn diagrams and GO terms enrichment analysis

To compare the differential expressed (DE) proteins, we generated the area-proportional Venn diagrams for different conditional comparisons. For each list of DE proteins, we firstly converted the protein IDs into gene names via UniProt retrieve/ID mapping tool[198], and then showed the common sets of those unique gene sets in Venn diagrams. All the graphs were done by R packages *Vennerable*[198] and *VennDiagram*[199] for two-set and three-set comparisons, respectively.

To further explore the biological functions of those DE proteins, we identified the GO terms that their corresponding gene sets enriched at using function *findGo.pl* in HOMER[200]. The top 50 enriched terms with adjusted P values (Bonferroni corrected) < 0.05 were plotted in three categories, including biological process, cellular component and molecular function. Plots were generated with in-house R codes.

Statistical analyses

Statistical analyses are all performed using Graph Pad Prism 7.

ACKNOWLEDGEMENTS

We would like to thank Gary Kasof from Cell Signaling Technology for developing the phospho-RalGAPα1-Ser766 and phospho-RalGAPα1-Ser820 antibodies. We also thank Dr. Gustav E. Lienhard for providing us with the Synthetic Human RalGAPα2-FLAG cDNA. Dana Gwinn made several point mutations to the SIPA1L1 and RalGAPα2 constructs. We would like to thank Jingting Yu and Maxim Shokhirev from the Integrative Genomics and Bioinformatics Core for bioinformatics help. Stephanie Curtis helped with the analysis for identifying optimal AMPKR motifs. Sébastien Herzig was critical in developing and optimizing the various assays used in the thesis.

This work was supported by grants to R.J. Shaw from the NIH (R35CA220538, P01CA120964), the Samuel Waxman Cancer Research Foundation and the Leona M. and

Harry B. Helmsley Charitable Trust grant #2012-PG-MED002. This work was supported by the Mass Spectrometry Core of the Salk Institute with funding from NIH-NCI CCSG: P30 014195 and the Helmsley Center for Genomic Medicine. We thank James Moresco, Jolene Diedrich and Antonio Michel Pinto for their expertise and support.

Chapter Two in part is currently being prepared for submission for publication of the material. The study was designed by Anwesh Kamireddy and Reuben J. Shaw, who analyzed the data and wrote the thesis with feedback from all authors. Reuben Shaw directed and supervised the writing and oversaw the project which formed the basis for this chapter. The other authors include James Moresco, Jolene Diedrich, Antonio Michel Pinto, Sébastien Herzig, Stephanie Curtis, Joshua Baumgart and Jingting Yu.

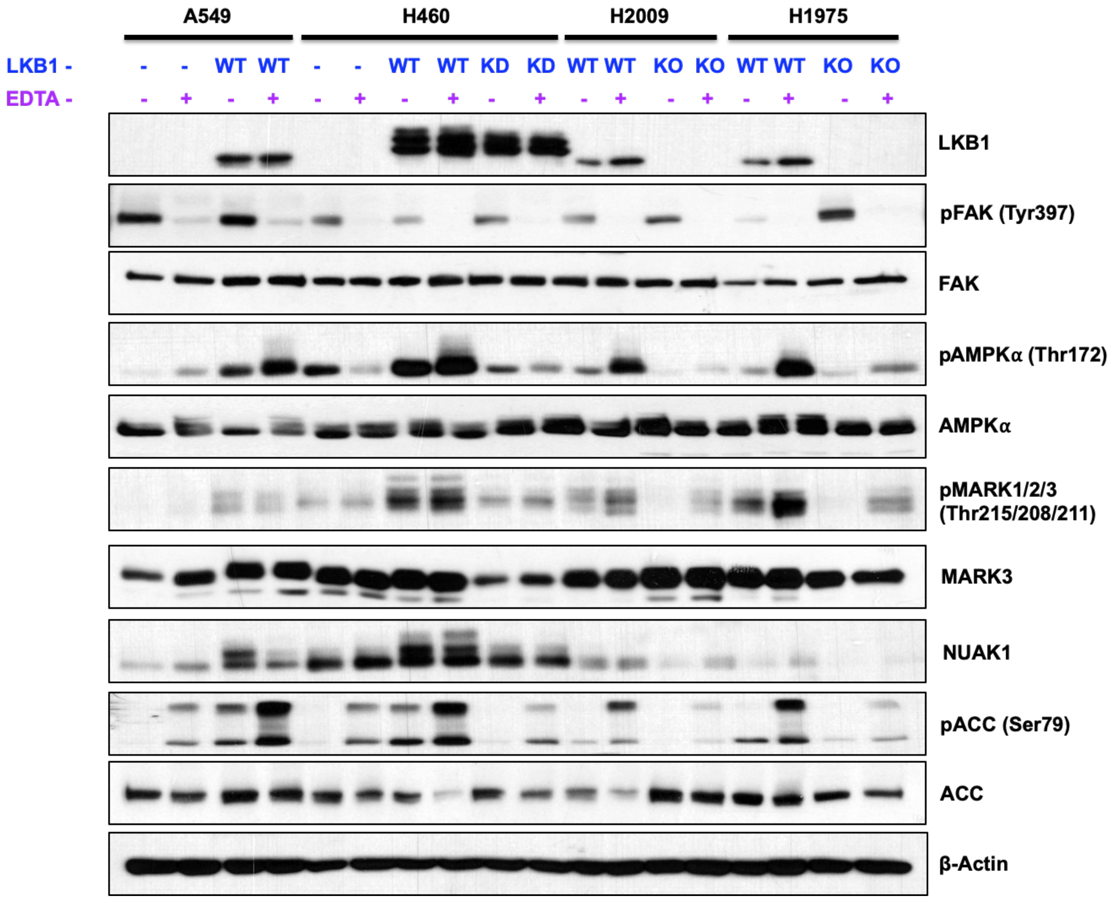

Figure 2.1. Several lung carcinoma cell lines exhibit detachment induced LKB1-dependent activation of AMPKα and MARK kinases.

Human lung carcinoma cell lines which are either LKB1 null or proficient for LKB1 were used to study the effect of detachment on AMPKR activation. In LKB1 null cells, such as A549 and H460, we generated cell lines that stably express wild-type (WT) or kinase dead (K78I) (KD) LKB1. Similarly, in LKB1 proficient cells, such as H2009 and H1975, we generated LKB1-null (KO) cells using CRISPR-Cas9. These cells were subjected to the detachment assay using enzyme-free cell dissociation buffer containing EDTA (denoted by EDTA +). Lysates were analyzed by western blotting with the indicated antibodies. Immunoblots depict phosphorylation status of MARK1, MARK2, MARK3 and AMPKα, and a direct AMPKα substrate ACC.

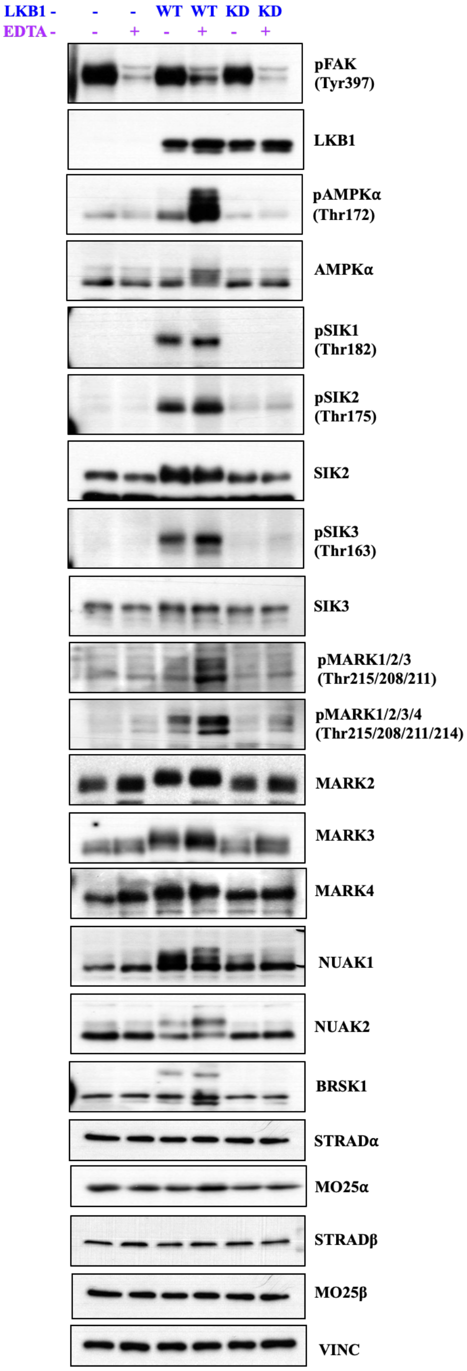

Figure 2.2. Cell detachment induces LKB1-dependent activation of several AMPKR family members in A549 cells.

Lysates from LKB1 null (-), wild-type (WT) and kinase dead (KD) LKB1 expressing A549 cells, under attached (EDTA -) and detached (EDTA +) conditions were analyzed by western blotting with the indicated antibodies. Immunoblots depict phosphorylation status of AMPKα, SIK1, SIK2, SIK3, MARK1, MARK2, MARK3 and MARK4. Immunoblots also depict LKB1 complex members STRADα and β and MO25α and β.

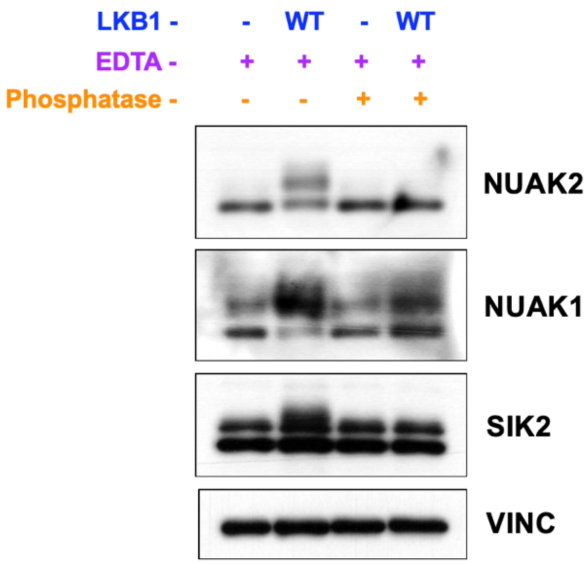

Figure 2.3. Bandshifting of AMPKRs is due to detachment induced LKB1-dependent phosphorylation.

Lysates from LKB1 null and wild-type (WT) LKB1 expressing A549 cells, under detached (EDTA +) conditions were subjected to lambda protein phosphatase treatment and analyzed by western blotting with the indicated antibodies.

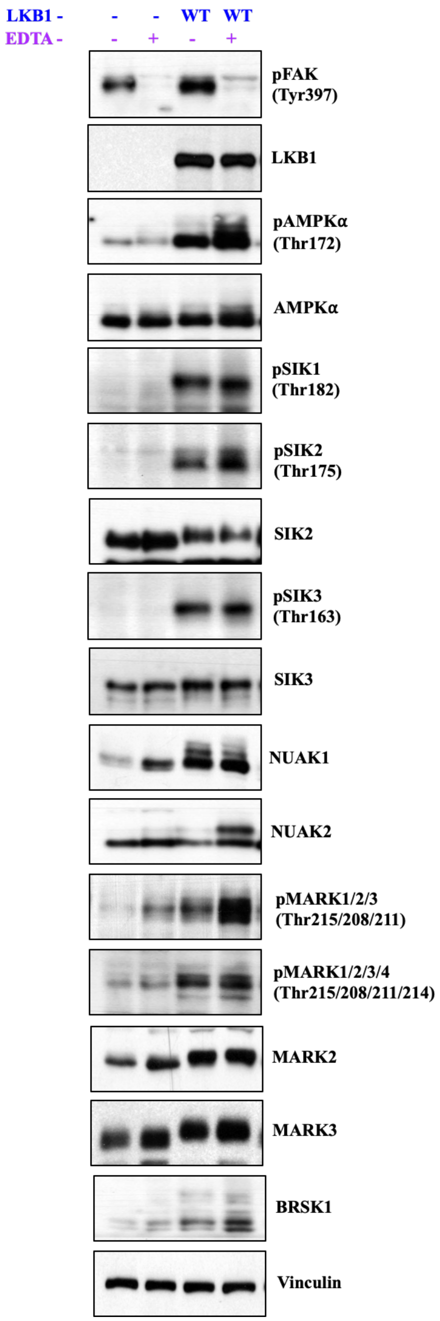

Figure 2.4. Cell detachment induces LKB1-dependent activation of several AMPKR family members in H1355 cells.

H1355, a human non-small cell lung adenocarcinoma cell line, which is inherently LKB1 null was made to that stably express wild-type (WT) LKB1. Lysates from these cells, under attached (EDTA -) and detached (EDTA +) conditions were analyzed by western blotting with the indicated antibodies. Immunoblots depict phosphorylation status of AMPKα, SIK1, SIK2, SIK3, MARK1, MARK2, MARK3 and MARK4.

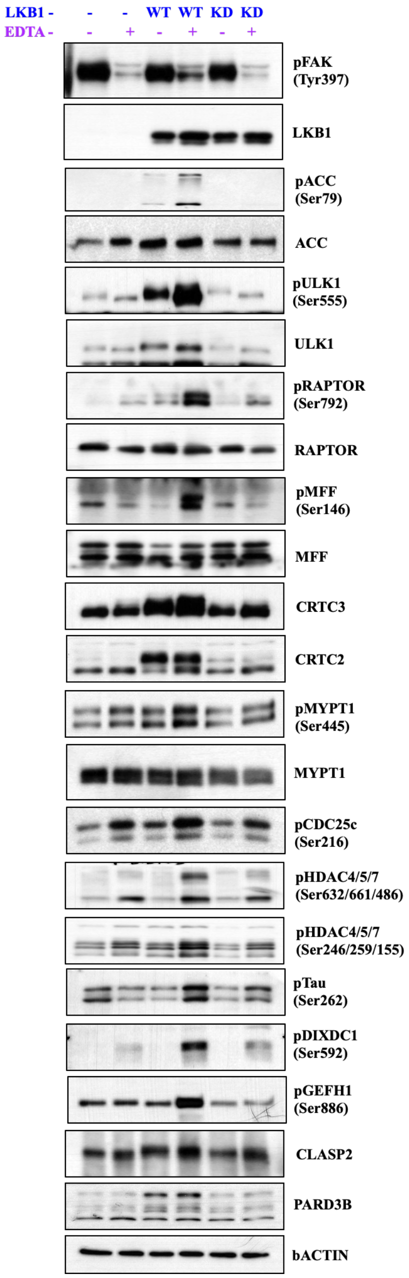

Figure 2.5. Several direct substrates of AMPKRs undergo an increase in detachment induced LKB1-dependent phosphorylation in A549 cells.

Lysates from LKB1 null, wild-type (WT) and kinase dead (KD) LKB1 expressing A549 cells, under attached (EDTA -) and detached (EDTA +) conditions were analyzed by western blotting with the indicated antibodies. Immunoblots depict phosphorylation status of direct AMPKα substrates (ACC, ULK1, RAPTOR, MFF, CDC25C), NUAK1 substrate (MYPT1), SIK kinase substrates (HDACs) and MARK kinase substrates (GEFH1, DIXDC1 and TAU).

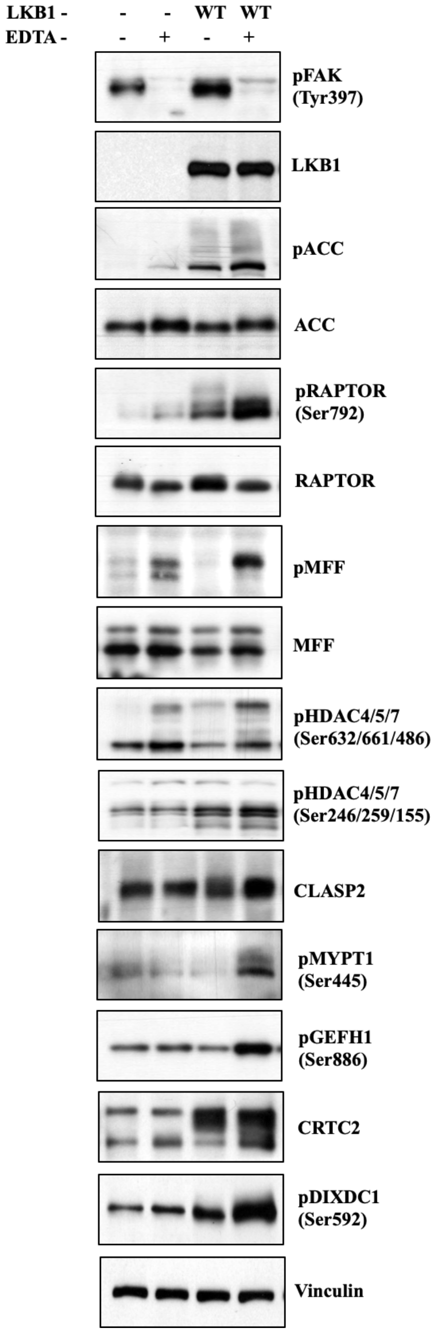

Figure 2.6. Several direct substrates of AMPKRs undergo an increase in detachment induced LKB1-dependent phosphorylation in H1355 cells.

Lysates from LKB1 null and wild-type (WT) LKB1 expressing A549 cells, under attached (EDTA -) and detached (EDTA +) conditions were analyzed by western blotting with the indicated antibodies. Immunoblots depict phosphorylation status of direct AMPKα substrates (ACC, RAPTOR, MFF), NUAK1 substrate (MYPT1), SIK kinase substrates (HDACs) and MARK kinase substrates (GEFH1 and DIXDC1).

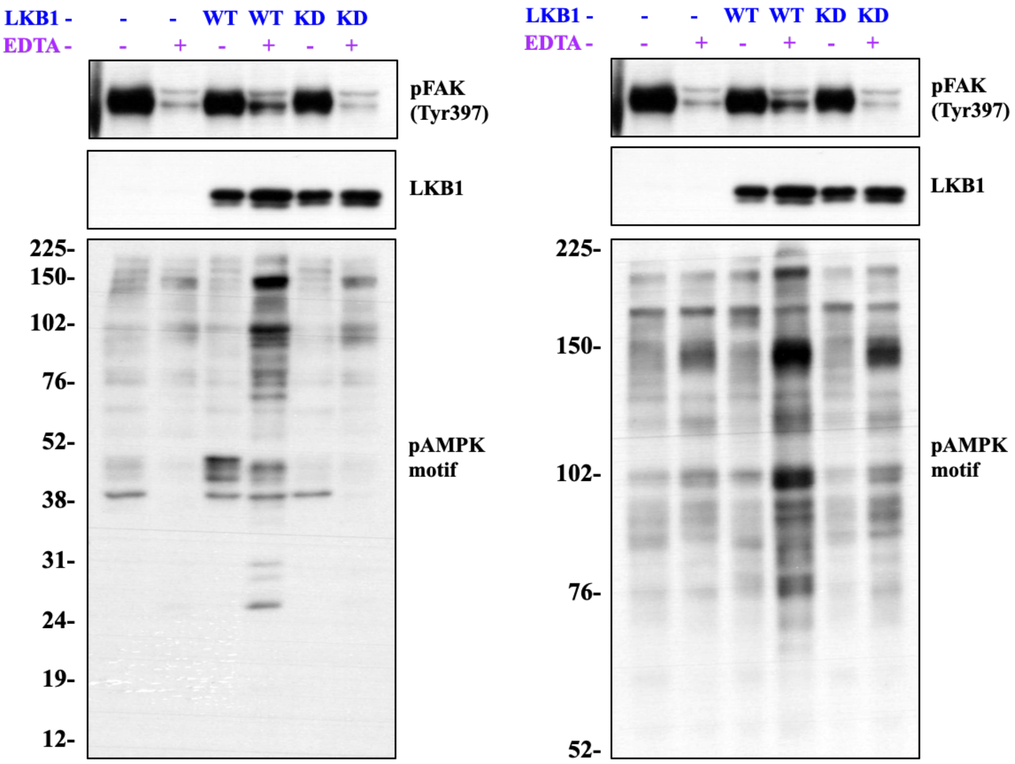

Figure 2.7. Cell detachment induces LKB1-dependent robust phosphorylation of AMPKR's downstream substrates in A549 cells.

Lysates from LKB1 null (-), wild-type (WT) and kinase dead (KD) LKB1 expressing A549 cells, under attached (EDTA -) and detached (EDTA +) conditions were analyzed by western blotting with the indicated antibodies.

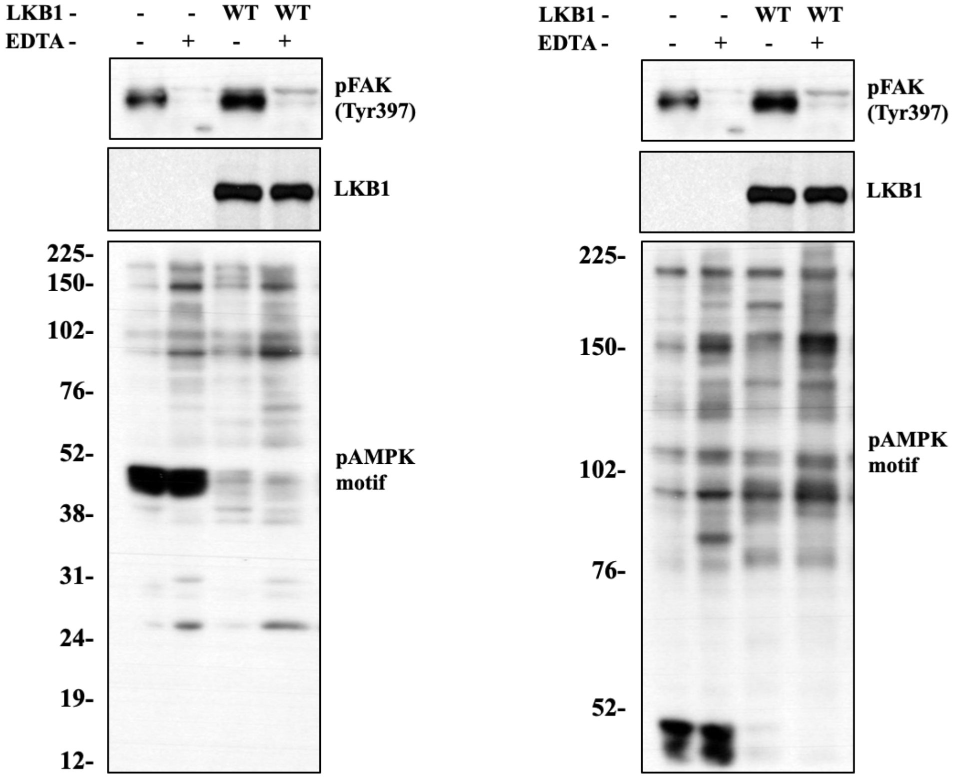

Figure 2.8. Cell detachment induces LKB1-dependent robust phosphorylation of AMPKR's downstream substrates in H1355 cells.

Lysates from LKB1 null (-) and wild-type (WT) LKB1 expressing H1355 cells, under attached (EDTA -) and detached (EDTA +) conditions were analyzed by western blotting with the indicated antibodies.

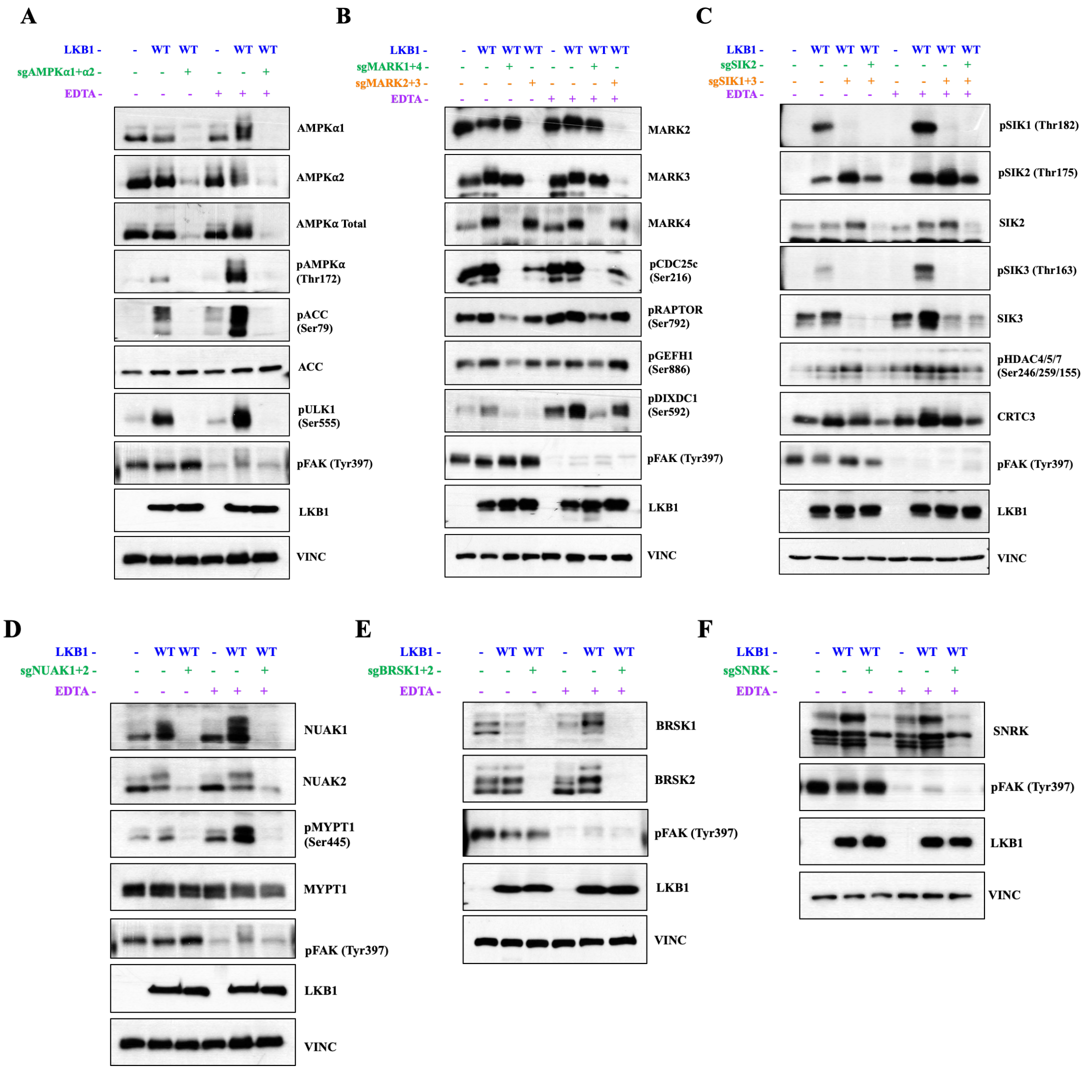

Figure 2.9. CRISPR/Cas9 mediated genetic deletion of AMPKR family members in A549 cells expressing wild-type LKB1.

Lysates from A549-LKB1 cells targeted to delete specific pairs of AMPKR were analyzed by western blotting with the indicated antibodies. Individual panels were blotted for the AMPKR family members and their substrates.

(A) Lysates from A549-LKB1 cells targeted to co-delete AMPKα1+AMPKα2.
(B) Lysates from A549-LKB1 cells targeted to co-delete MARK1+MARK4 and MARK2+MARK3.
(C) Lysates from A549-LKB1 cells targeted to co-delete SIK1+SIK3 and SIK1+SIK2+SIK3.
(D) Lysates from A549-LKB1 cells targeted to co-delete NUAK1+NUAK2.
(E) Lysates from A549-LKB1 cells targeted to co-delete BRSK1+BRSK2.
(F) Lysates from A549-LKB1 cells targeted to delete SNRK

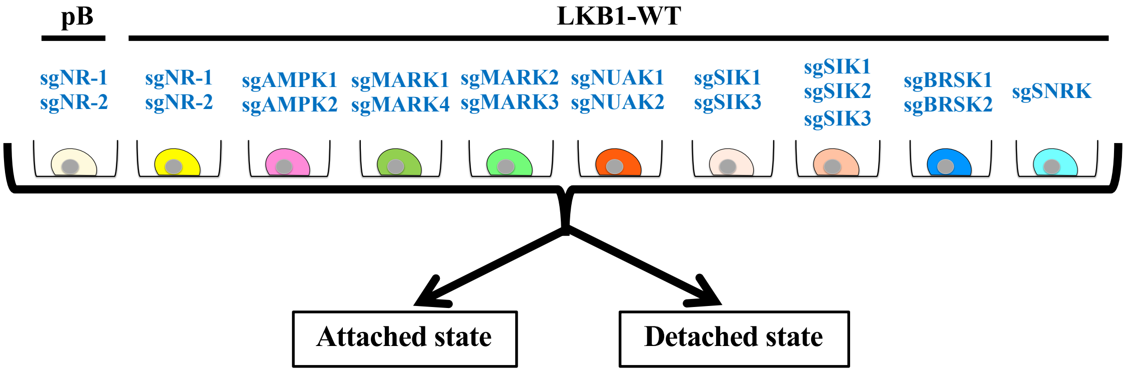

Figure 2.10. Schematic showing the panel of 10 different cell lines used in the screen.

Each of the 10 different cell lines are subjected to the detachment assay and their counterpart attached cells were used as a control.

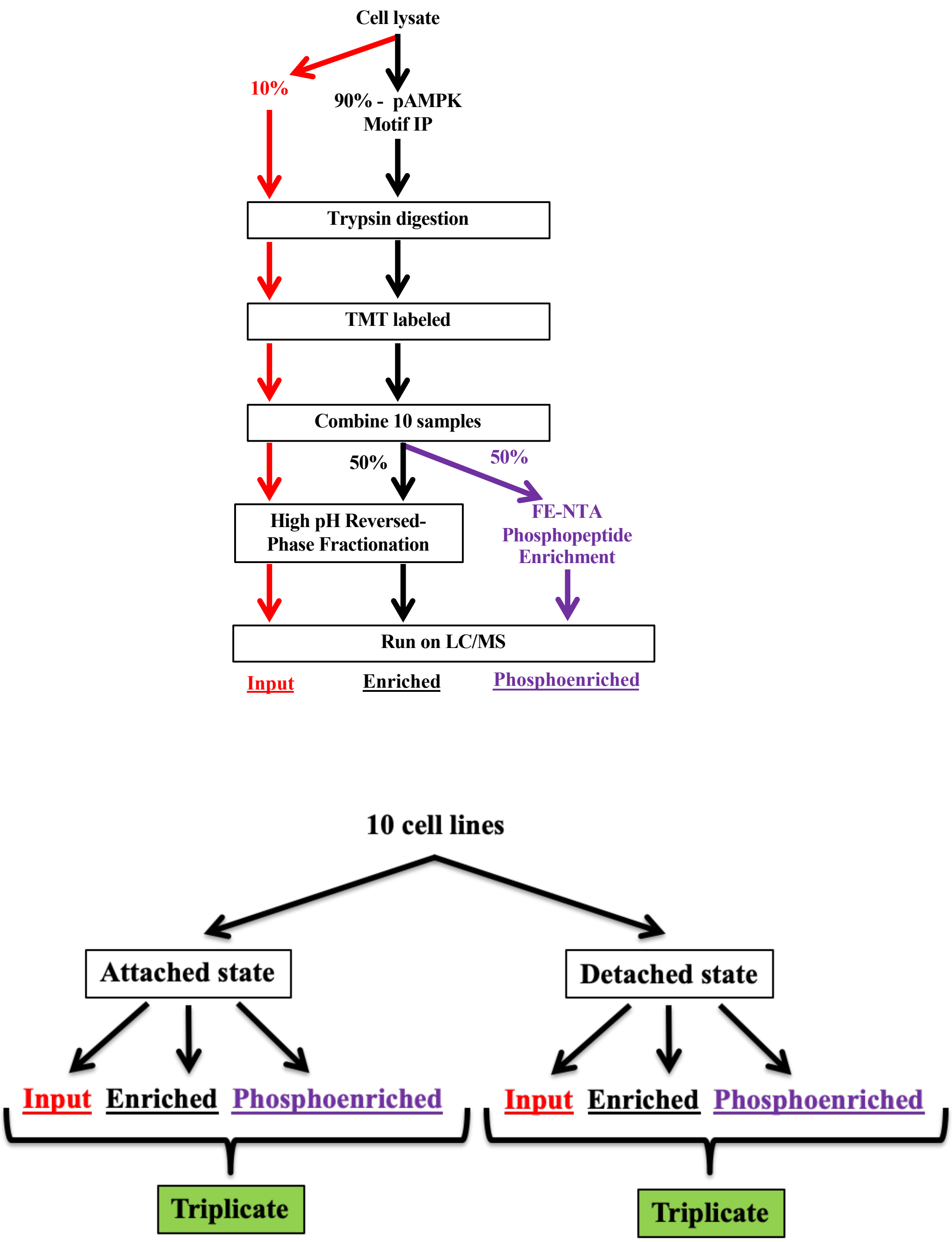

Figure 2.11. Experimental design and workflow of the samples used in the phosphoproteomic screen.

(Top) Cell lysates were processed to generate 10-plex Input, Enriched and Phosphoenriched data sets in both the attached and detached condition. Three biological replicates for each condition were tested.
(Bottom) Summary of the entire samples sent used in the screen.

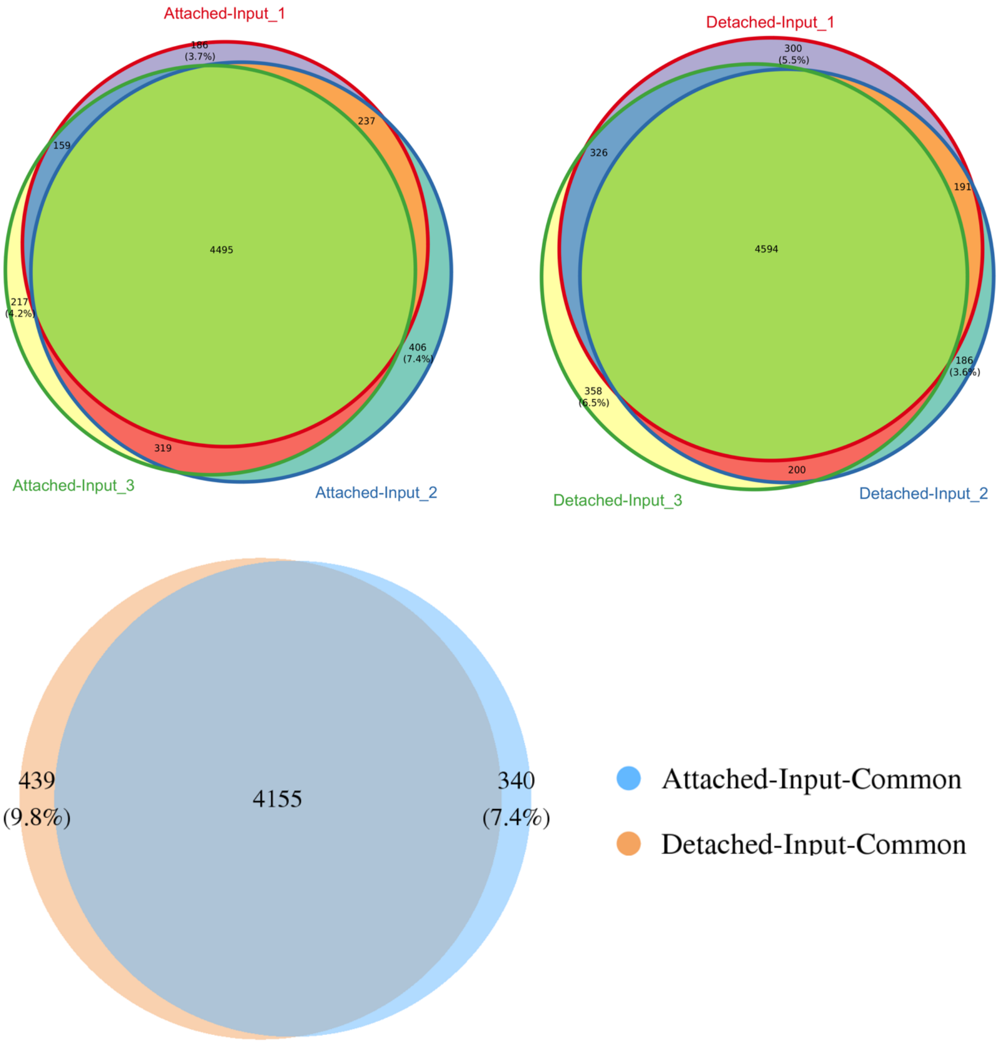

Figure 2.12. High overlap of proteins identified in the Input samples.

Venn diagrams showing the overlap of proteins identified in the Input triplicate data sets. Venn diagram were generated using Vennerable and VennDiagram.
(Top Left) Attached-Input data set
(Top Right) Detached-Input data set
(Bottom) Overlap of Attached-Input triplicate data (in blue) and Detached-Input triplicate data (in orange)

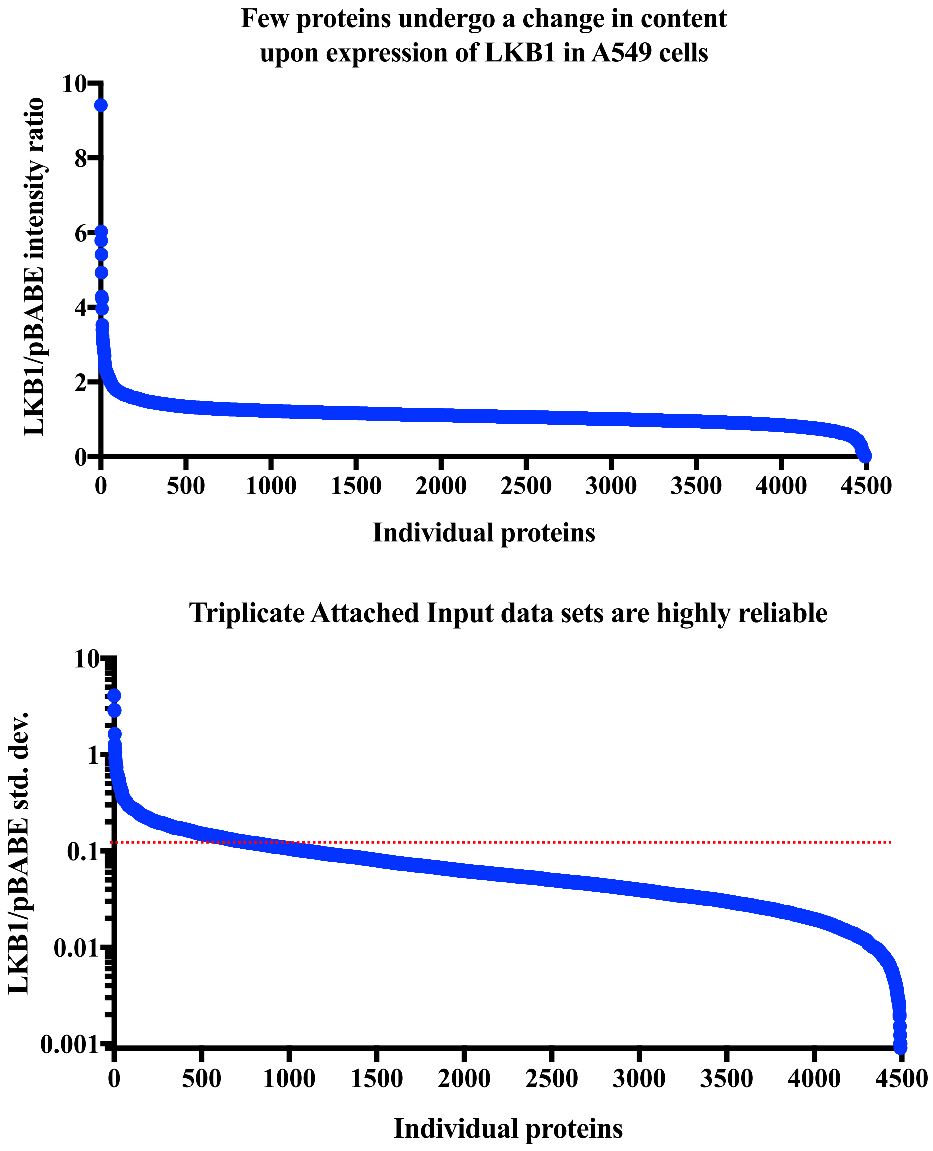

Few proteins undergo a change in content upon expression of LKB1 in A549 cells

Triplicate Attached Input data sets are highly reliable

Figure 2.13. The triplicate Attached-Input data set is very consistent across the three runs.

The normalized LKB1/pBabe intensity ratios of 4495 common proteins identified in the triplicate Attached-Input data set were calculated.
(Top) Individual protein's average is plotted
(Bottom) Individual protein's standard deviation is plotted

Table 2.1. Several proteins (~5% of the 4495 proteins) undergo a LKB1-dependent increase in expression in A549 cells.

Table showing the list of the proteins and their corresponding LKB1/pBabe ratio in the triplicate Attached-Input data set that undergo a >1.5-fold increase in protein content upon LKB1 expression.

GENE	LKB1/pBabe	GENE	LKB1/pBabe	GENE	LKB1/pBabe	GENE	LKB1/pBabe	GENE	LKB1/pBabe
KRT73	9.411	CPPED1	1.991	RBM38	1.740	PYGL	1.642	RNF121	1.574
PPL	6.031	SLC9A3R1	1.981	FDXR	1.740	S100A3	1.638	MCM5	1.573
DCDC2	5.790	GNG5	1.978	CRYZ	1.739	S100A6	1.637	PYCARD	1.570
PKP2	5.416	CAV2	1.976	ANXA4	1.732	AHNAK	1.637	H1F0	1.568
KRT3	4.927	DSG2	1.966	WDHD1	1.730	CEP55	1.636	MET	1.566
PODXL	4.290	RBPMS	1.952	SORD	1.729	CTNND2	1.633	UCK2	1.564
ESAM	4.224	RHPN2	1.935	TJP1	1.724	MCM2	1.630	UBE2T	1.559
ITGB4	3.963	KRT8	1.929	AURKA	1.717	MCM4	1.629	ITSN2	1.558
CALM2	3.532	MYO3B	1.928	KRT80	1.716	F8A1	1.629	TCEA1	1.558
HMGCS1	3.398	EPHA2	1.924	PLK1	1.713	SBNO1	1.628	KCNAB2	1.558
ACSS1	3.135	EML1	1.912	TRIO	1.713	GCLC	1.627	GINS3	1.557
SULT1A4	3.071	KRT18	1.891	CA8	1.711	RCC2	1.623	TDRKH	1.556
OCLN	3.030	TJP2	1.880	HKDC1	1.710	MCM7	1.623	CBS	1.554
CAVIN2	3.025	RIF1	1.877	PROCR	1.709	COL4A3BP	1.623	KIF11	1.554
SERPINE1	2.903	SIRPB1	1.870	ABCC4	1.707	KPNA2	1.621	PTK2	1.553
GLDC	2.896	CAV3	1.870	TRIM47	1.707	UBE2E1	1.613	WDR43	1.553
HPGD	2.860	CDC20	1.865	BAX	1.701	CAVIN1	1.607	KRT79	1.552
HNF1B	2.826	PSAT1	1.851	PPP1R14A	1.694	UBE2E3	1.604	RB1	1.550
ITGA6	2.797	RHPN2P1	1.846	ANXA3	1.689	UBE2S	1.603	SYNJ2	1.550
NDRG1	2.755	S100A10	1.838	HDAC6	1.686	HAVCR1	1.603	ATP1B1	1.549
GPRC5B	2.718	HMGA2	1.832	PLCB4	1.681	TMEM123	1.602	ASNS	1.544
PNMA2	2.684	EPHB1	1.829	DOCK10	1.680	HELLS	1.602	ADSS	1.542
TNFAIP2	2.526	SNX8	1.826	RHOF	1.678	TES	1.600	PDCD2L	1.540
ADA	2.478	CLU	1.818	PM20D2	1.673	AKR1B10	1.595	AKR1B15	1.537
CYP2S1	2.402	PFKFB2	1.811	SRC	1.673	F11R	1.594	SPR	1.537
MYO1B	2.331	CD9	1.807	MGLL	1.672	EFHD1	1.593	ARHGEF28	1.537
DSP	2.323	SQSTM1	1.804	DNM3	1.670	BAIAP2L1	1.590	UTP4	1.535
AHNAK2	2.304	MTHFD2	1.796	ADAM10	1.670	NDUFAB1	1.589	RBM19	1.527
NR0B1	2.304	LRRC20	1.794	KIF22	1.668	GINS2	1.589	RDH10	1.526
SYNE1	2.298	PVR	1.788	CAPG	1.665	ANO6	1.588	TNFAIP8	1.526
EPB41L1	2.294	NUSAP1	1.788	TIMELESS	1.664	PUS1	1.588	RIOX2	1.524
DPYSL5	2.245	TPX2	1.785	STEAP3	1.664	SYNGR2	1.587	YES1	1.523
RBPMS2	2.244	KRT2	1.781	HSPE1	1.662	MTHFD1L	1.586	EPS8L2	1.523
TSPAN15	2.236	SPATS2L	1.781	ABCB8	1.658	OGFOD1	1.585	ARHGAP5	1.523
KRT75	2.217	EPHB4	1.780	TYMS	1.656	PRXL2A	1.584	PRIM2	1.521
FHL1	2.203	EPB41L2	1.780	FBXO3	1.655	DUSP11	1.583	CYTH2	1.521
SPDL1	2.142	BIRC5	1.780	PYGM	1.654	METTL5	1.582	NPC2	1.516
PFKFB3	2.142	UBE2C	1.772	NOB1	1.652	MPHOSPH6	1.582	IGFBP3	1.515
MYO1A	2.139	GCA	1.766	FBXO22	1.652	RGS10	1.581	CAMK2D	1.513
TK1	2.121	KRT4	1.764	TACC3	1.650	AGFG2	1.579	TXNDC9	1.513
DPYSL3	2.117	DNM1	1.763	RAB11FIP1	1.650	MCM6	1.579	DNM2	1.512
CKB	2.107	EHD1	1.763	PPT1	1.650	ZWINT	1.578	USP3	1.511
AFAP1L2	2.065	GINS4	1.757	GSN	1.650	ARHGEF10	1.578	NASP	1.511
CCNB1	2.056	LIG1	1.756	HMOX1	1.648	ISYNA1	1.577	KIAA1671	1.510
UPP1	2.039	EPHB2	1.754	ECT2	1.648	RAB11FIP2	1.576	POLR3C	1.505
MERTK	2.037	PYGB	1.751	RPIA	1.646	RNF175	1.575	POLR1E	1.504
AXL	2.026	PSPH	1.744	MCM3	1.643	NF2	1.575	GINS1	1.502
MARCKS	1.996	METTL7B	1.741	UBE2E2	1.642	HS1BP3	1.574	BCCIP	1.501

Table 2.2. Small fraction (~3.5% of the 4595 proteins) undergo a LKB1-dependent decrease in expression in A549 cells.

Table showing the list of the proteins and their corresponding LKB1/pBabe ratio in the triplicate Attached-Input data set that undergo a >1.5-fold increase in protein content upon LKB1 expression.

GENE	LKB1/PBABE	GENE	LKB1/PBABE	GENE	LKB1/PBABE	GENE	LKB1/PBABE
KRT82	0.038	COL5A1	0.435	ALDH3A1	0.562	GBA	0.622
KRT86	0.042	PC	0.443	CADM1	0.563	KIFC3	0.625
KRT81	0.042	GSDME	0.448	CIRBP	0.564	SLC7A7	0.625
KRT87P	0.048	RAB23	0.448	SCARB2	0.570	LMBRD1	0.627
KRT85	0.049	SCD	0.448	CD63	0.570	MRTFB	0.627
UGT1A1	0.099	SLC7A5	0.450	FN1	0.576	CKAP4	0.627
TGM2	0.104	HMGB3	0.457	P3H4	0.577	PSMB8	0.629
HTRA1	0.110	SUSD2	0.457	HMGN2	0.577	SEC24D	0.630
ANXA10	0.111	RAB27B	0.461	ACSF2	0.578	ABCC3	0.630
TYMP	0.126	LXN	0.467	CLIC4	0.579	ATP2B1	0.630
NAMPT	0.133	IFIT3	0.472	SEC22B	0.580	MYL6B	0.631
ANXA8	0.137	MGST1	0.474	DECR1	0.580	GHDC	0.632
UGT1A9	0.148	SERPINH1	0.475	HMGN3	0.582	TTYH3	0.632
PTGES	0.157	B4GALT1	0.479	SERPINB9	0.582	HLA-B	0.635
AGR3	0.159	SDSL	0.483	STAMBPL1	0.584	FKBP10	0.635
AGR2	0.165	CUL4B	0.485	ACOX1	0.585	PSME2	0.636
ANXA8L1	0.166	ACO1	0.486	CD55	0.586	P3H3	0.636
NPC1	0.252	SOD2	0.490	CHMP1B	0.589	HLA-A	0.636
AKR1B1	0.261	LGALS1	0.494	SCARB1	0.591	NRP1	0.637
KYNU	0.293	GPX4	0.503	PSMB10	0.595	HLA-A	0.639
CD99L2	0.300	SLC3A2	0.504	TLN1	0.599	HLA-A	0.642
AKR1A1	0.309	BSG	0.516	PDLIM7	0.601	MAP1LC3B	0.642
CSRP1	0.311	HSPB8	0.518	AKAP2	0.603	HK2	0.642
NRCAM	0.320	BASP1	0.522	HK1	0.604	EPHX1	0.643
PLOD2	0.330	CNN2	0.522	P4HA2	0.606	NT5E	0.644
SLC27A2	0.339	CALD1	0.523	FTH1	0.607	GBE1	0.644
LIMCH1	0.341	MFGE8	0.525	STIM1	0.608	ALDH3B1	0.645
CPLX2	0.349	HMGCL	0.526	FLNA	0.608	HLA-A	0.648
MT1E	0.350	SERPINB8	0.528	EMC4	0.610	MSI2	0.649
MT1G	0.352	GLRX	0.535	CPT2	0.612	HLA-B	0.650
ANTXR1	0.356	TGFB1I1	0.536	TMEM106B	0.613	PTPN1	0.651
MT1H	0.364	GSTM3	0.538	LDHAL6B	0.613	GOPC	0.651
CES1P1	0.366	MEF2D	0.541	MICAL2	0.614	LBH	0.652
GPX1	0.371	PSME1	0.543	UBAP1	0.616	HLA-B	0.652
TAGLN	0.380	PGM2L1	0.546	MYL6	0.618	SLC44A1	0.655
CES1	0.385	NQO1	0.548	TEAD1	0.619	HLA-A	0.660
ISG15	0.426	NDUFB1	0.548	ZYX	0.619	ALDH3B2	0.662
CAT	0.427	WFS1	0.551	LDHA	0.619	HLA-A	0.664
LPCAT2	0.433	NOL3	0.556	RASA1	0.620	MPI	0.664
PALLD	0.434	UBE2L6	0.556	TM9SF1	0.621	APOL2	0.664

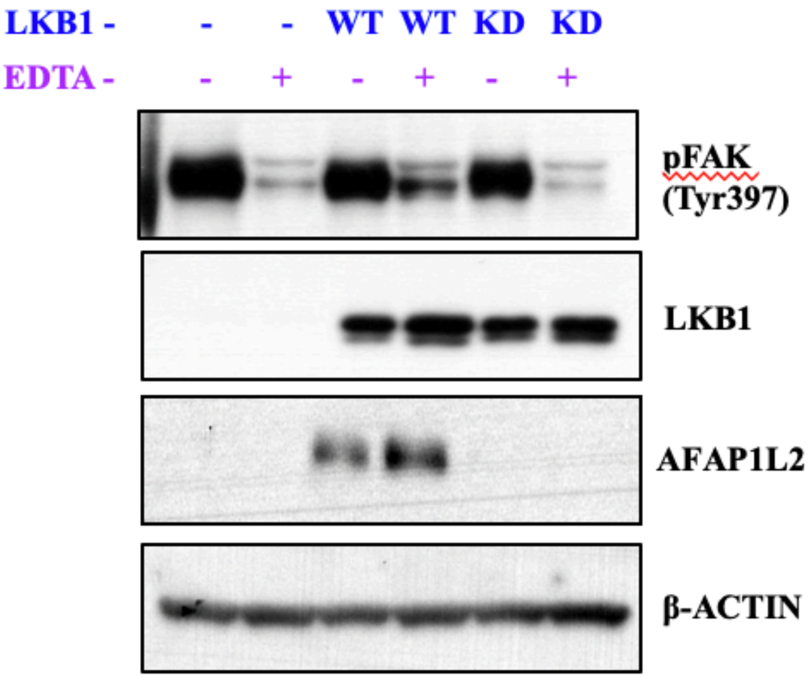

Figure 2.14. AFAP1L2 protein expression is dependent on LKB1 expression on A549 cells.

Lysates from LKB1 null (-), wild-type (WT) and kinase dead (KD) LKB1 expressing A549 cells, under attached (EDTA -) and detached (EDTA +) conditions were analyzed by western blotting with the indicated antibodies.

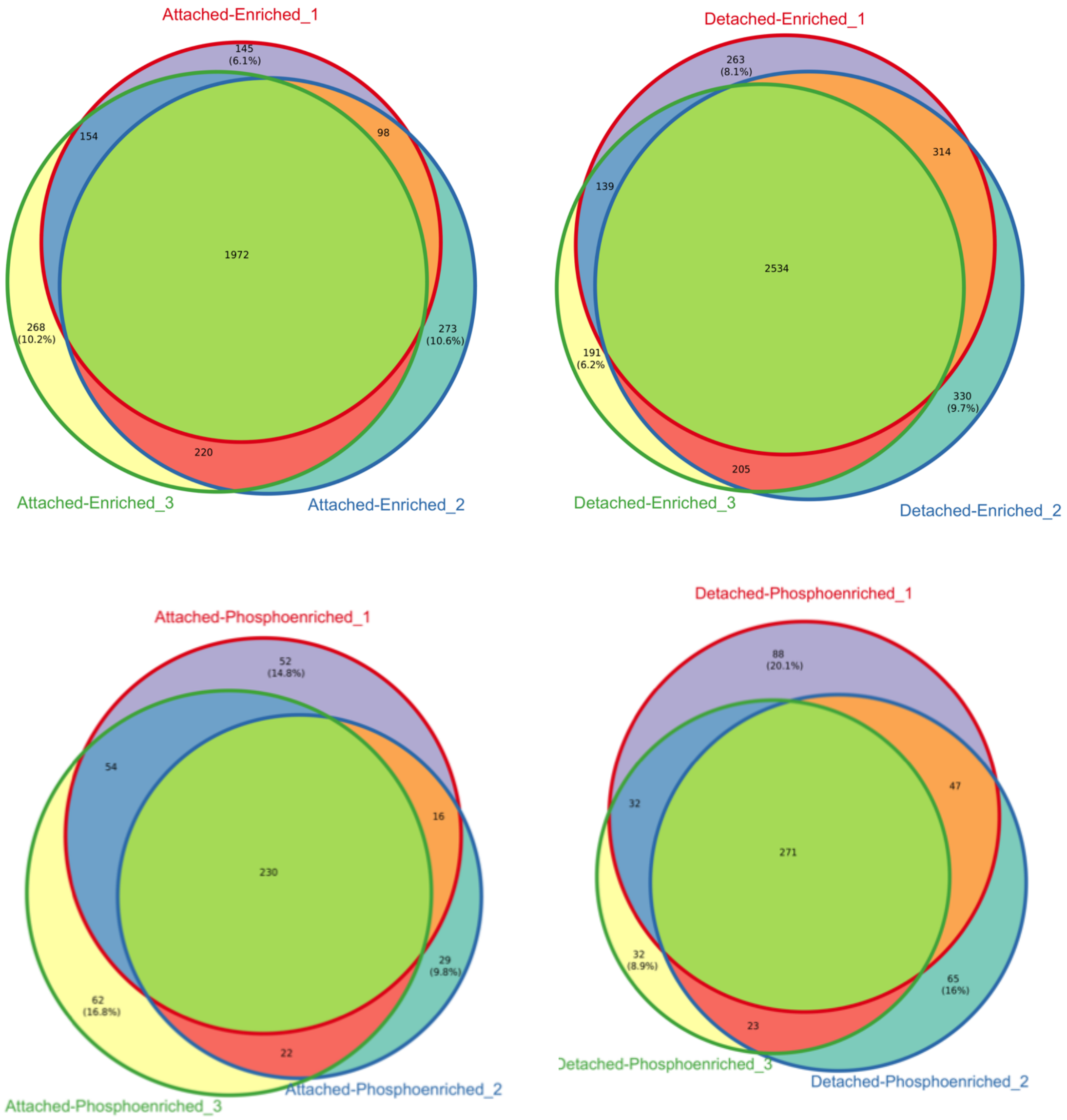

Figure 2.15. pAMPK motif Enriched and Phosphoenriched triplicate data sets have a high degree of overlap.

Venn diagram showing the overlap of proteins identified in the triplicate Enriched and Phosphoenriched data sets. Venn diagram were generated using Vennerable and VennDiagram.

(Top left) Triplicate Attached-Enriched data set.
(Top right) Triplicate Detached-Enriched data set.
(Bottom left) Triplicate Attached-Phosphoenriched data set.
(Bottom right) Triplicate Detached-Phosphoenriched data set.

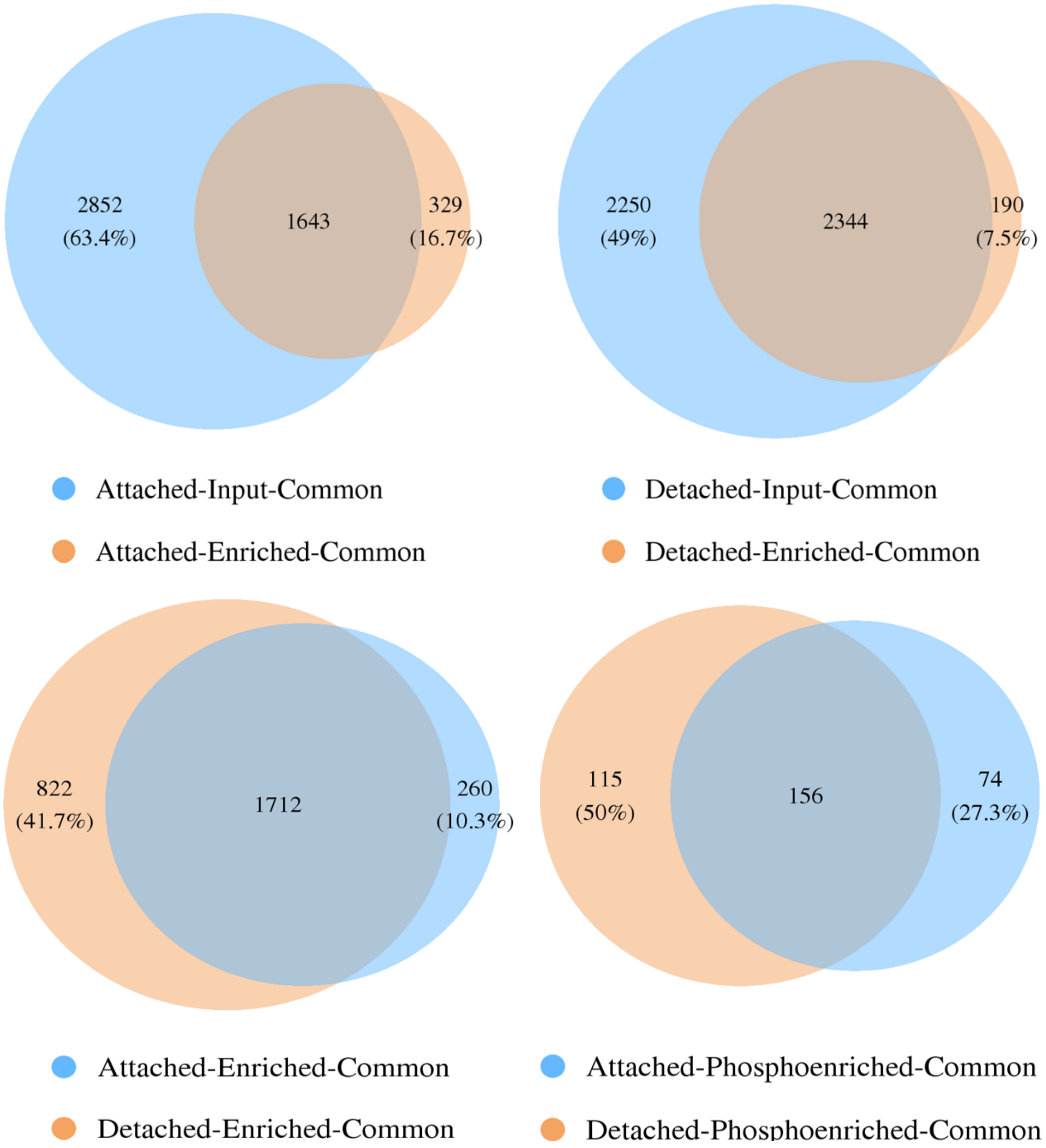

Figure 2.16. The Input, Enriched and Phosphoenriched triplicate data sets have a high degree of overlap.

Venn diagram showing the overlap of proteins identified in the triplicate Input, Enriched and Phosphoenriched data sets. Venn diagram were generated using Vennerable and VennDiagram.

(Top left) Attached-Input data set (in blue) and Attached-Enriched data set (in orange)
(Top right) Detached-Input data set (in blue) and Detached-Enriched data set (in orange)
(Bottom left) Attached-Enriched data set (in blue) and Detached-Enriched data set (in orange)
(Bottom right) Attached-Phosphoenriched data set (in blue) and Detached-Phosphoenriched data set (in orange)

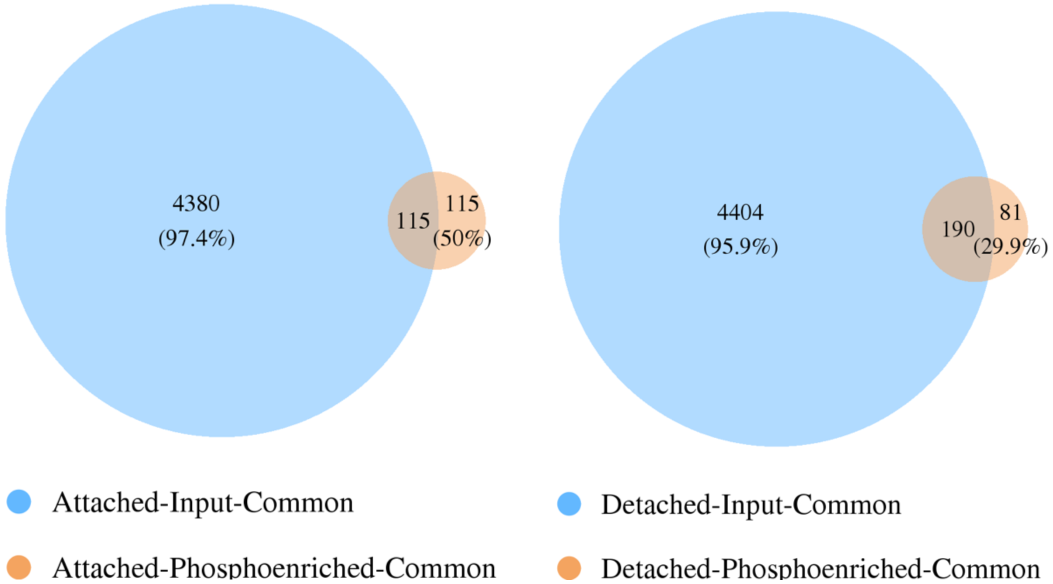

Figure 2.17. The Input and Phosphoenriched triplicate data sets have a lower degree of overlap.

Venn diagram showing the overlap of proteins identified in the triplicate Input, Enriched and Phosphoenriched data sets. Venn diagram were generated using Vennerable and VennDiagram.

(Left) Attached-Input data set (in blue) and Attached-Phosphoenriched data set (in orange)
(Right) Detached-Input data set (in blue) and Detached-Phosphoenriched data set (in orange)

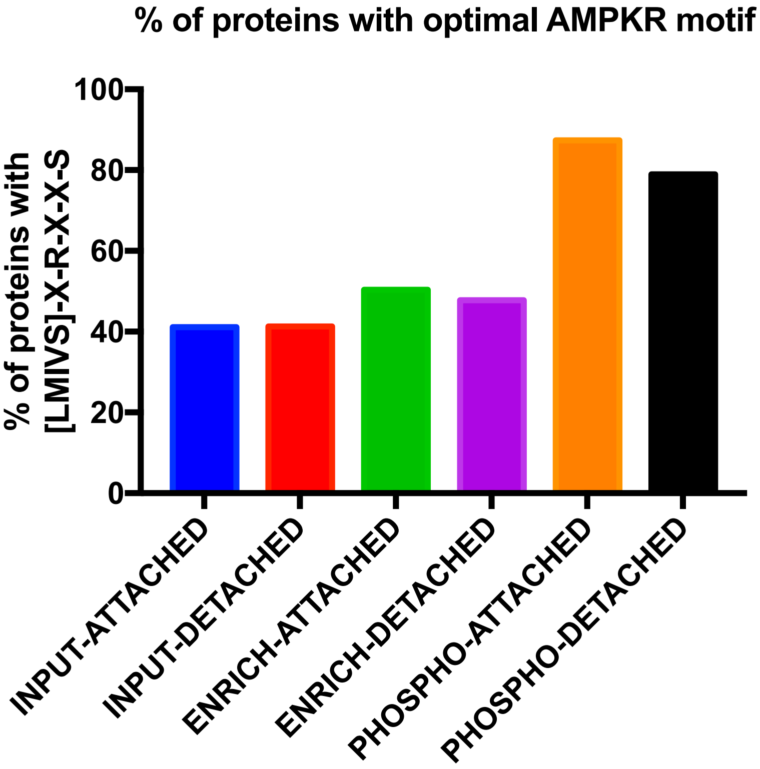

Figure 2.18. Screen has preferentially enriched for proteins with the pAMPKR motif.

Bar graph showing the % of proteins in the Attached and Detached state from the Input, Enriched, Phosphoenriched runs that have the optimal pAMPKR motif

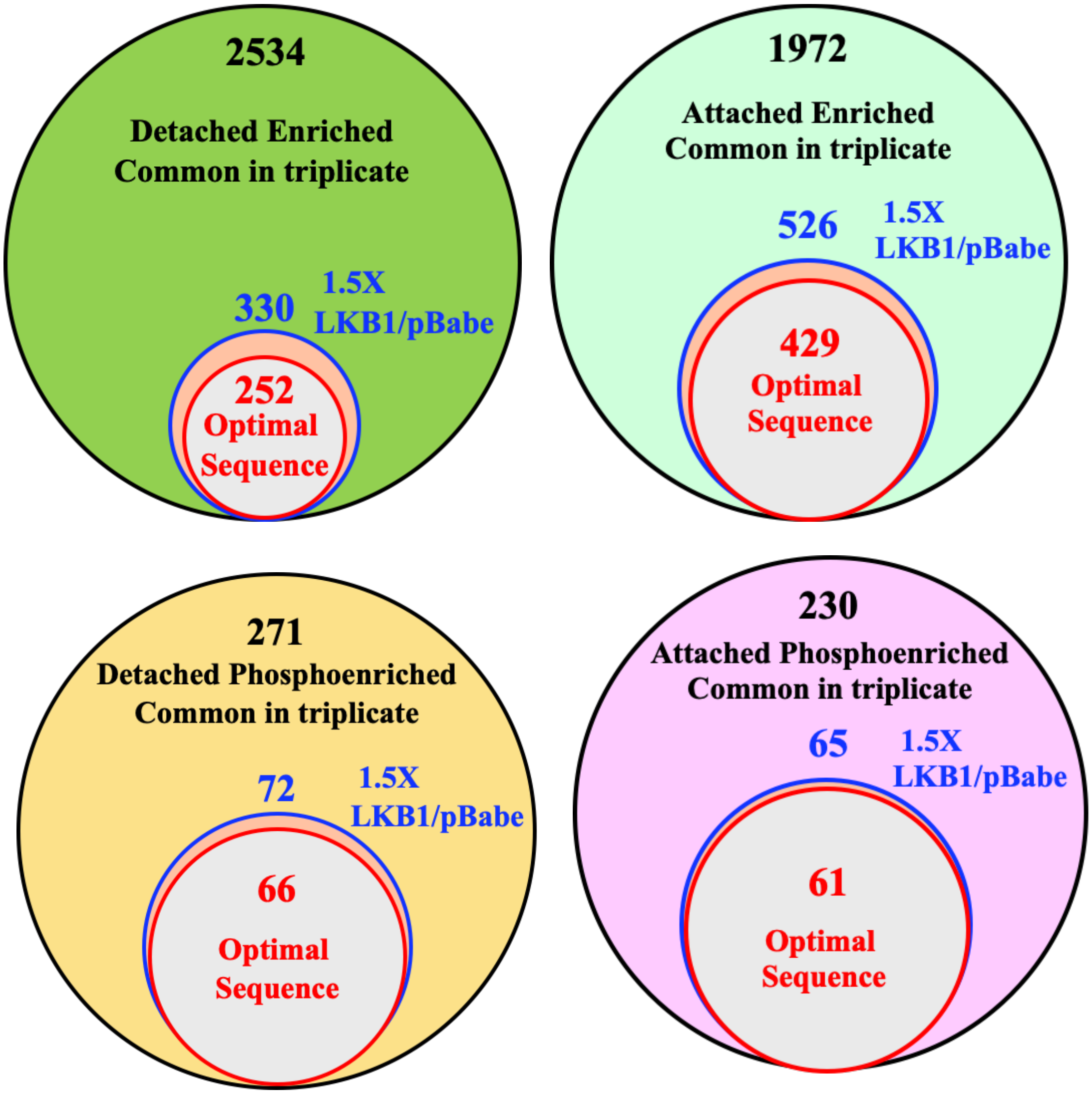

Figure 2.19. Majority of the proteins undergoing an LKB1-dependent increase in phosphorylation have the optimal AMPKR motif in their sequence.

Venn diagram showing the overlap between the proteins identified in the triplicate runs, the subset of the proteins that have a >1.5-fold increase in LKB1/pBabe intensity and the number in that subset that them have the optimal AMPKR motif in their peptide sequence.

(Top left) Detached-Enriched runs
(Top right) Attached-Enriched runs
(Bottom left) Detached-Phosphoenriched runs
(Bottom right) Attached-Phosphoenriched runs

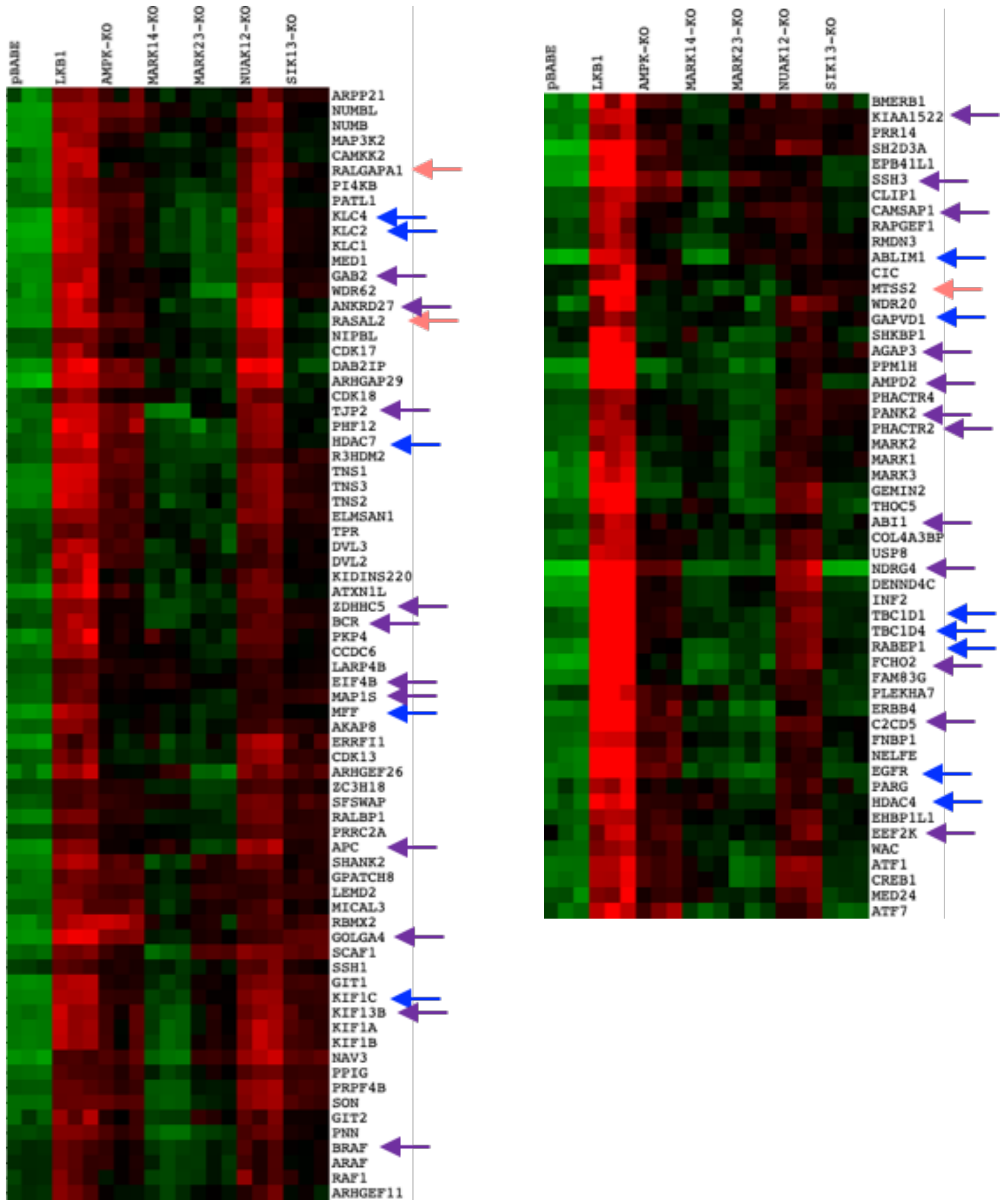

Figure 2.20. Detachment-Enriched data set identifies several known and predicted AMPKR substrates – 2 of the 7 clusters.

Triplicate Detached-Enriched data set proteins that have a >1.5-fold increase in LKB1/pBabe intensity and optimal AMPKR motif were subjected to unbiased clustering using GeneCluster 3.0. The heatmap generated was used to generate a visual map using Java TreeView.

2 of the 7 clusters are shown here. Blue arrows indicate previously validated AMPKR substrates. Purple arrows indicate other hits identified in other screens but never individually validated. Orange arrows indicate the hits we are following up on here.

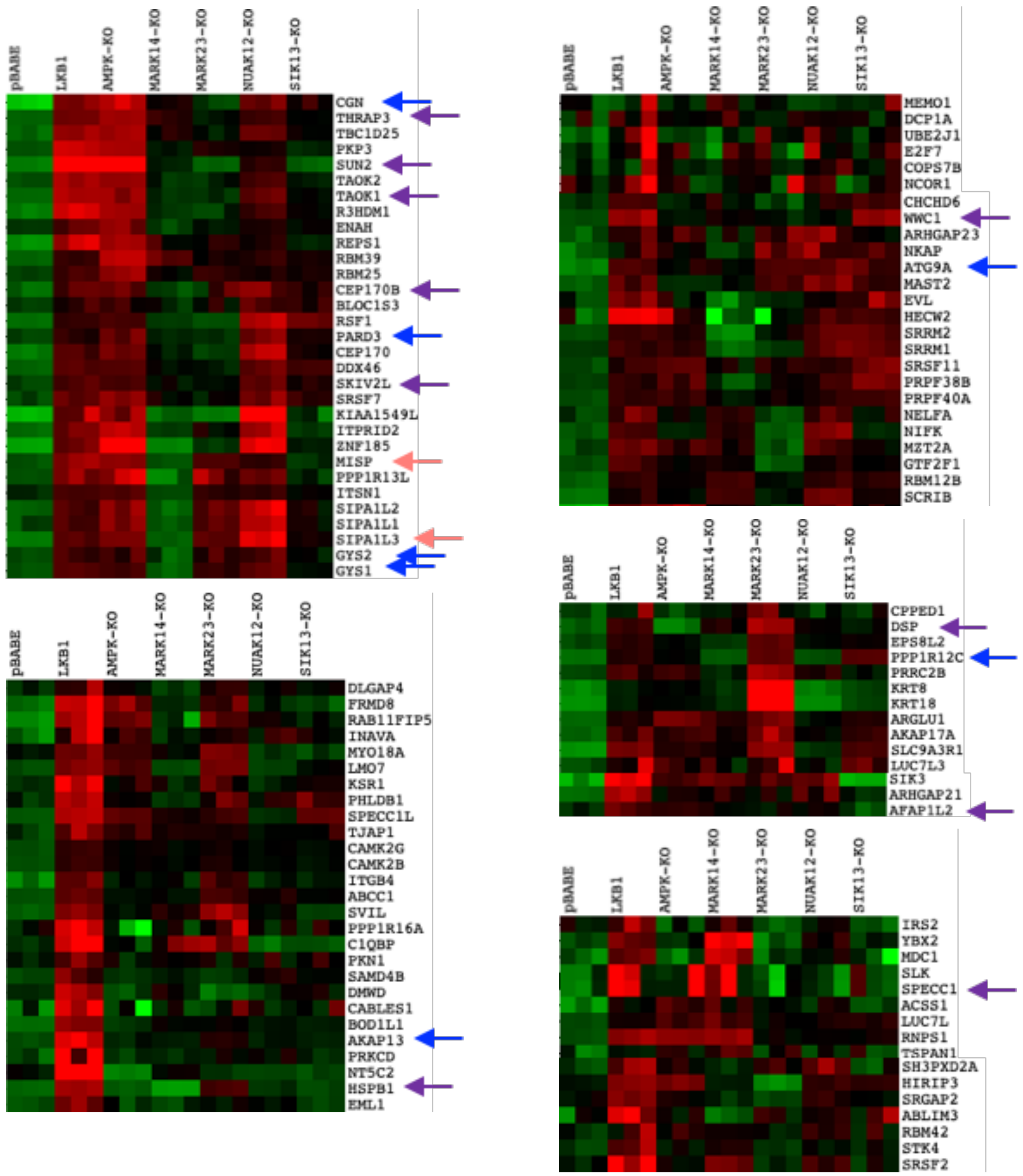

Figure 2.21. Detachment-Enriched data set identifies several known and predicted AMPKR substrates – 5 of the 7 clusters.

Triplicate Detached-Enriched data set proteins that have a >1.5-fold increase in LKB1/pBabe intensity and optimal AMPKR motif were subjected to unbiased clustering using GeneCluster 3.0. The heatmap generated was used to generate a visual map using Java TreeView.

5 of the 7 clusters are shown here. Blue arrows indicate previously validated AMPKR substrates. Purple arrows indicate other hits identified in other screens but never individually validated. Orange arrows indicate the hits we are following up on here.

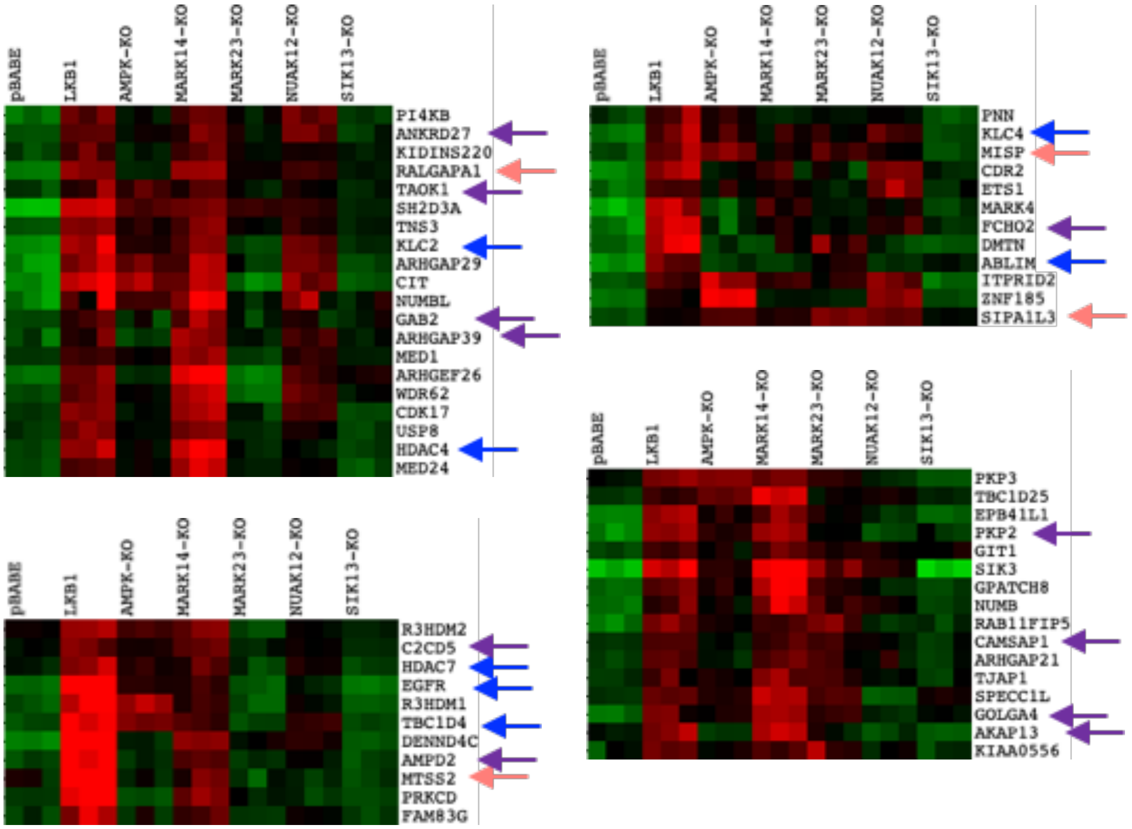

Figure 2.22. Detachment-Phosphoenriched data set also identifies several known and predicted AMPKR substrates – all the 4 clusters.

Triplicate Detached-Phosphoenriched data set proteins that have a >1.5-fold increase in LKB1/pBabe intensity and optimal AMPKR motif were subjected to unbiased clustering using GeneCluster 3.0. The heatmap generated was used to generate a visual map using Java TreeView.

All clusters are shown here. Blue arrows indicate previously validated AMPKR substrates. Purple arrows indicate other hits identified in other screens but never individually validated. Orange arrows indicate the hits we are following up on here.

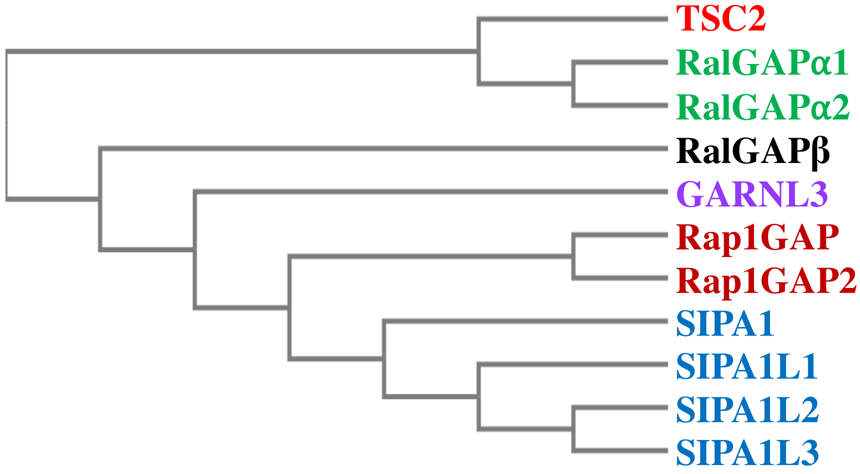

Figure 2.23. Simplified representation of the phylogenetic tree of RapGAP domain containing proteins.

Human sequences of the proteins were downloaded from Uniprot. The sequences were aligned and the phylogenetic tree was generated using ClustalW.

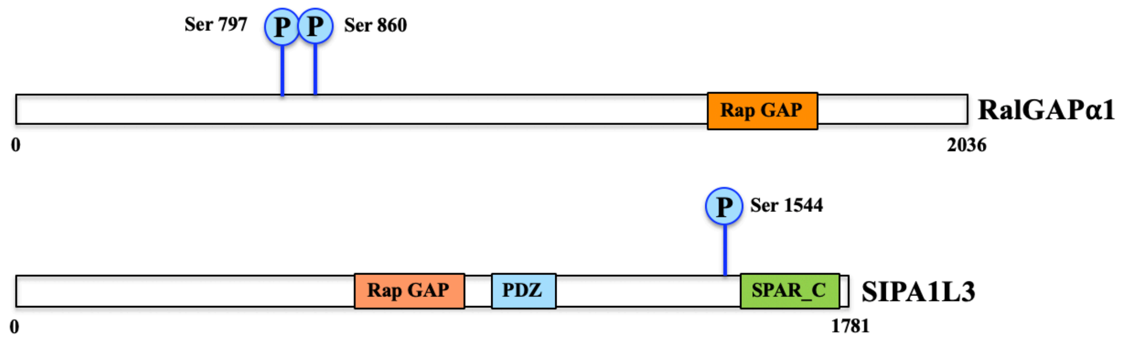

Figure 2.24. Schematic of domain architecture of human RalGAPα1 & SIPA1L3 highlighting location of the phosphorylation sites. Adapted from Phosphosite.org.

(Top) RalGAPα1 contains only the RapGAP domain
(Bottom) Apart from the RapGAP domain, SIPA1L3 contains a PDZ and a SPAR_C (C-terminal domain of SPAR protein) domain

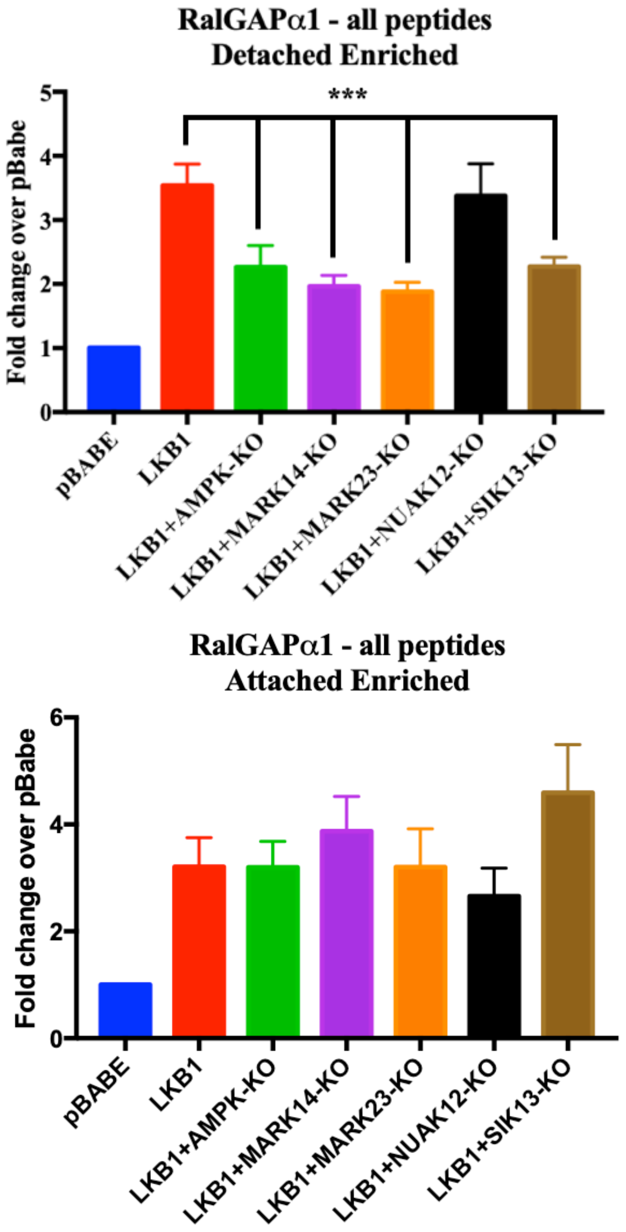

Figure 2.25. RalGAPα1 undergoes a significant LKB1-dependent increase in binding to the pAMPK motif antibody.

Average RalGAPα1 plotted for each cell line. ***, p< .0005 compared to LKB1. Bar graphs plot mean ±SD. Statistical significance was determined by Two-way ANOVA.

(Top) Triplicate Detached-Enriched data sets
(Bottom) Triplicate Attached-Enriched data

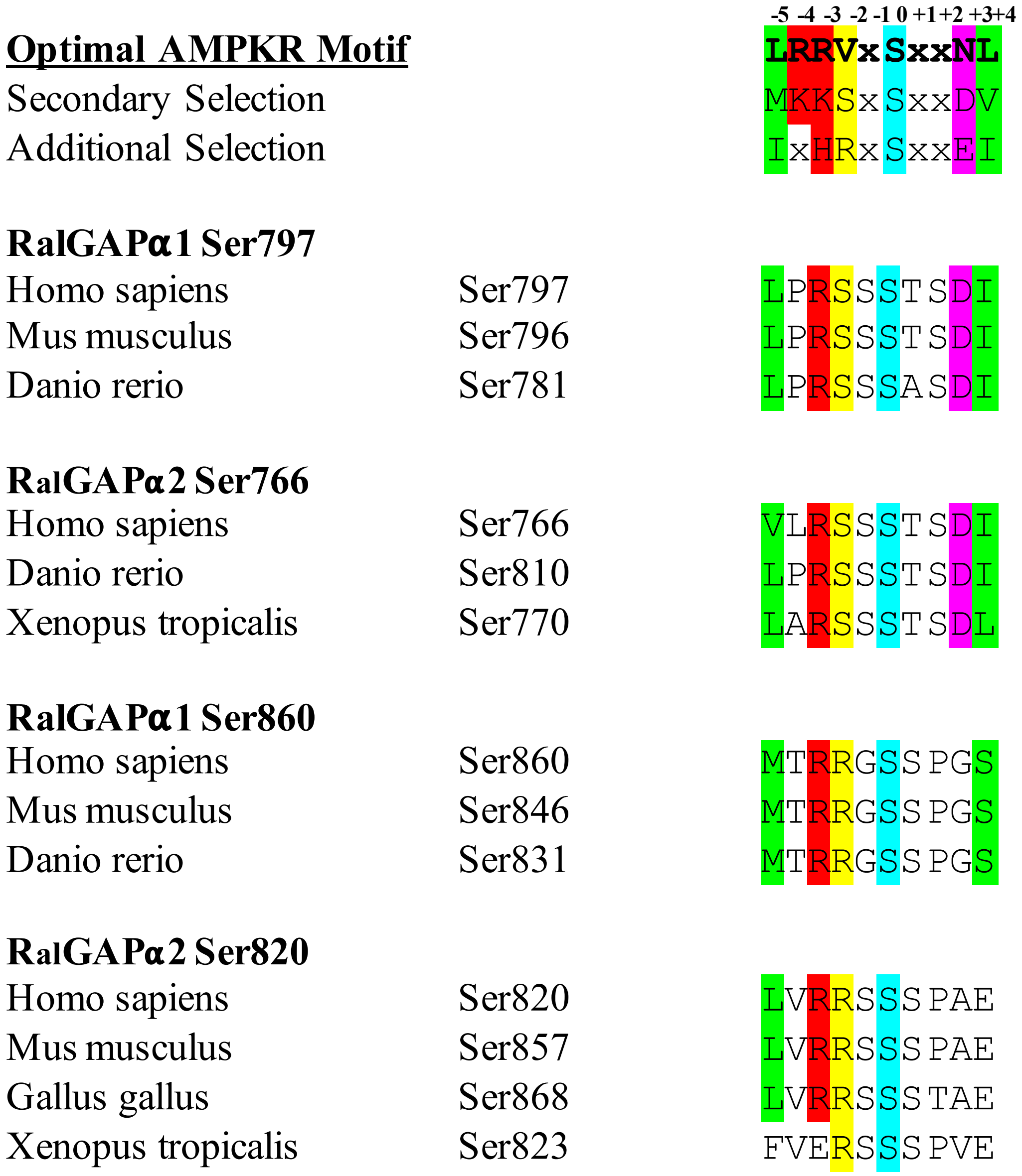

		-5 -4 -3 -2 -1 0 +1+2 +3+4
Optimal AMPKR Motif		**LRRVxSxxNL**
Secondary Selection		MKKSxSxxDV
Additional Selection		IxHRxSxxEI
RalGAPα1 Ser797		
Homo sapiens	Ser797	LPRSSSTSDI
Mus musculus	Ser796	LPRSSSTSDI
Danio rerio	Ser781	LPRSSSASDI
RalGAPα2 Ser766		
Homo sapiens	Ser766	VLRSSSTSDI
Danio rerio	Ser810	LPRSSSTSDI
Xenopus tropicalis	Ser770	LARSSSTSDL
RalGAPα1 Ser860		
Homo sapiens	Ser860	MTRRGSSPGS
Mus musculus	Ser846	MTRRGSSPGS
Danio rerio	Ser831	MTRRGSSPGS
RalGAPα2 Ser820		
Homo sapiens	Ser820	LVRRSSSPAE
Mus musculus	Ser857	LVRRSSSPAE
Gallus gallus	Ser868	LVRRSSSTAE
Xenopus tropicalis	Ser823	FVERSSSPVE

Figure 2.26. RalGAPα1's Ser797 and Ser860 and RalGAPα2's Ser766 and Ser820 are well conserved across vertebrates.

ClustalW alignment of RalGAPα1(2)'s Ser797(766) and Ser860(820) across species showing conservation of the AMPKR consensus phosphorylation motif across vertebrates.

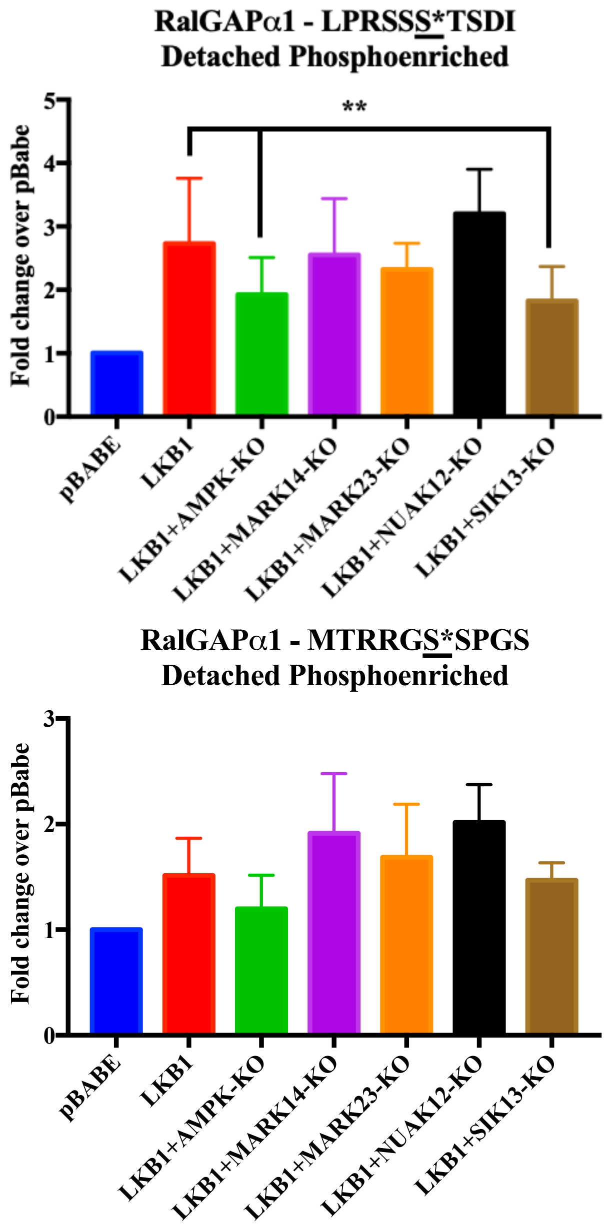

RalGAPα1 - LPRSSS*TSDI
Detached Phosphoenriched

RalGAPα1 - MTRRGS*SPGS
Detached Phosphoenriched

Figure 2.27. RalGAPα1's Ser797 and Ser860 undergo a strong LKB1-dependent increase in phosphorylation upon cell detachment, which can be inhibited by AMPK loss.

Bar graphs plot mean ±SD. **, p< .005 compared to LKB1. Statistical significance was determined by Two-way ANOVA.

(Top) Average phospho-Ser797 data from the triplicate Detached-Phosphoenriched data set plotted for each cell line
(Bottom) Average phosphor-Ser860 data from the triplicate Detached-Phosphoenriched data set plotted for each cell line

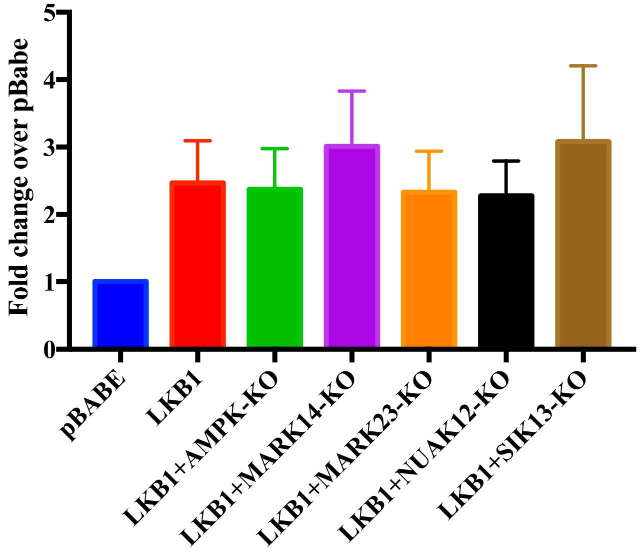

RalGAPα1 - LPRSSS*TSDI
Attached Phosphoenriched

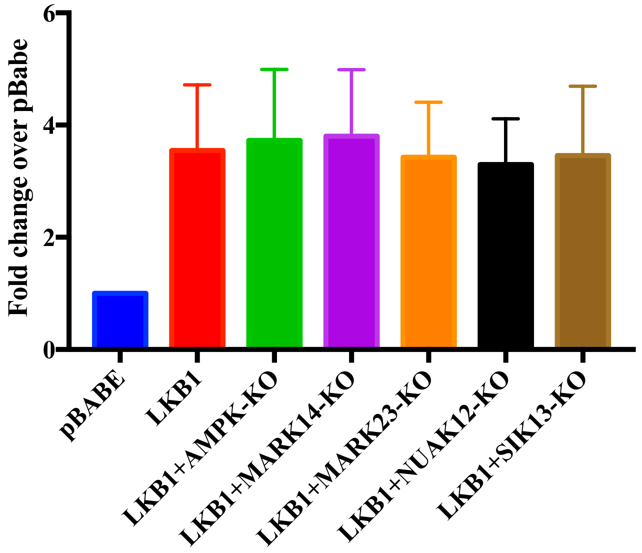

RalGAPα1 - MTRRGS*SPGS
Attached Phosphoenriched

Figure 2.28. RalGAPα1's Ser797 and Ser860 undergo a LKB1-dependent increase in phosphorylation in the attached condition.

Average RalGAPα1's phosphospecific data from the triplicate Attached-Phosphoenriched data set plotted for each cell line. Bar graphs plot mean ±SD.

(Top) RalGAPα1's phospho-Ser797 data
(Bottom) RalGAPα1's phosphor-Ser860 data

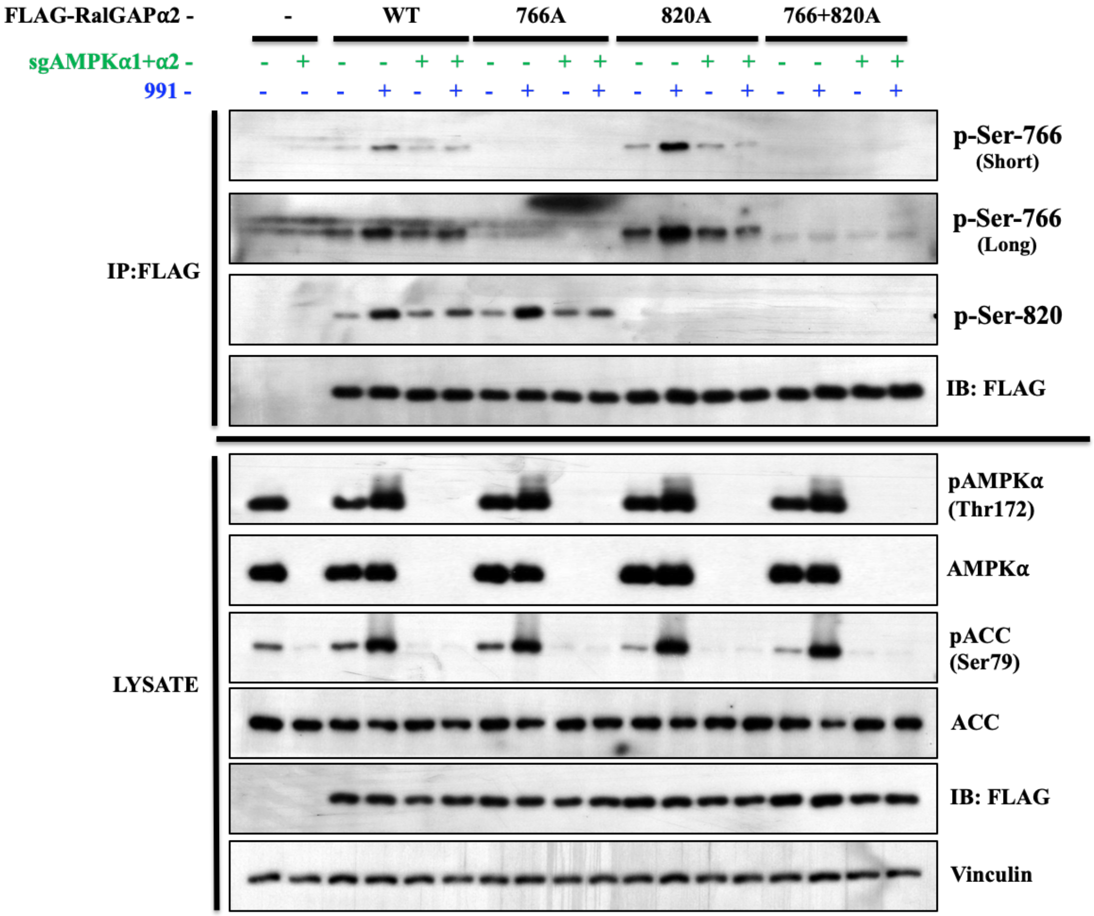

Figure 2.29. AMPK can phosphorylate RalGAPα2's Ser766 and Ser820.

Wild-Type and AMPK-null HEK293T cells transiently transfected with empty vector, FLAG tagged RalGAPα2 WT, S766A, S820A and S766A+S820A were treated with 991 or DMSO for 1 hour. Cells were lysed and lysates were subjected to FLAG immunoprecipitation (IP). The IP and lysates were immunoblotted with the indicated antibodies.

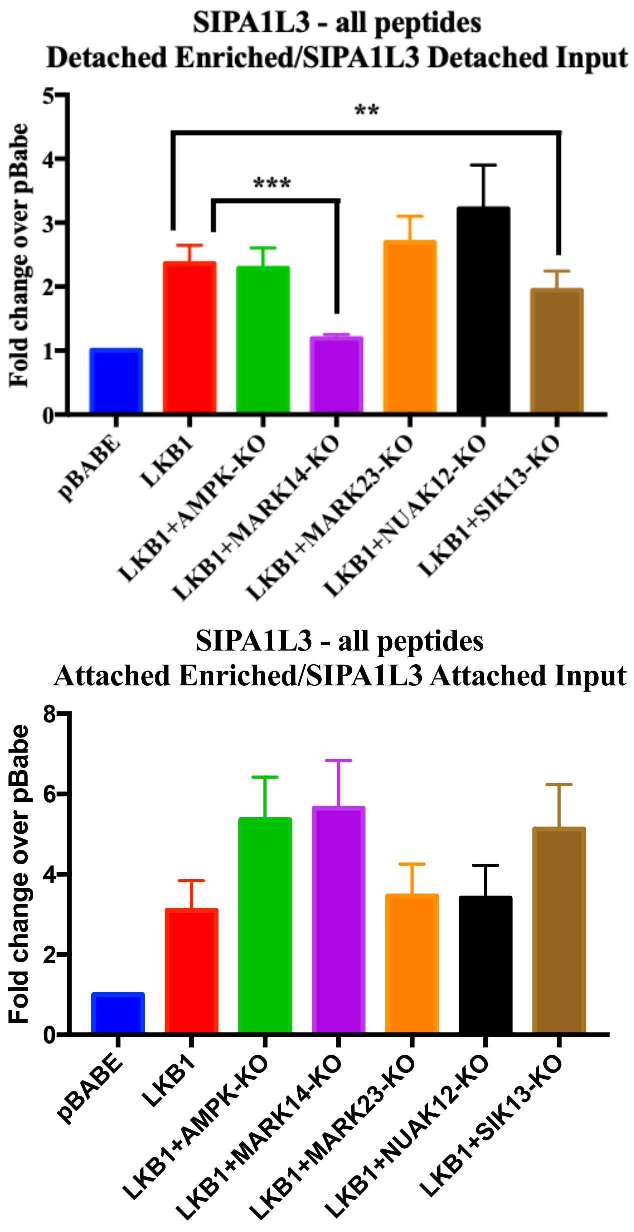

Figure 2.30. SIPA1L3 undergoes a strong LKB1-dependent enrichment when immunoprecipitated with the pAMPK motif antibody.

Average SIPA1L3 data from the triplicate Enriched data sets plotted for each cell line, normalized to total SIPA1L3 content in the corresponding Input runs. **, $p < .005$; ***, $p < .0005$ compared to LKB1. Bar graphs plot mean ±SD. Statistical significance was determined by Two-way ANOVA.

(Top) Triplicate Detached-Enriched data sets
(Bottom) Triplicate Attached-Enriched data

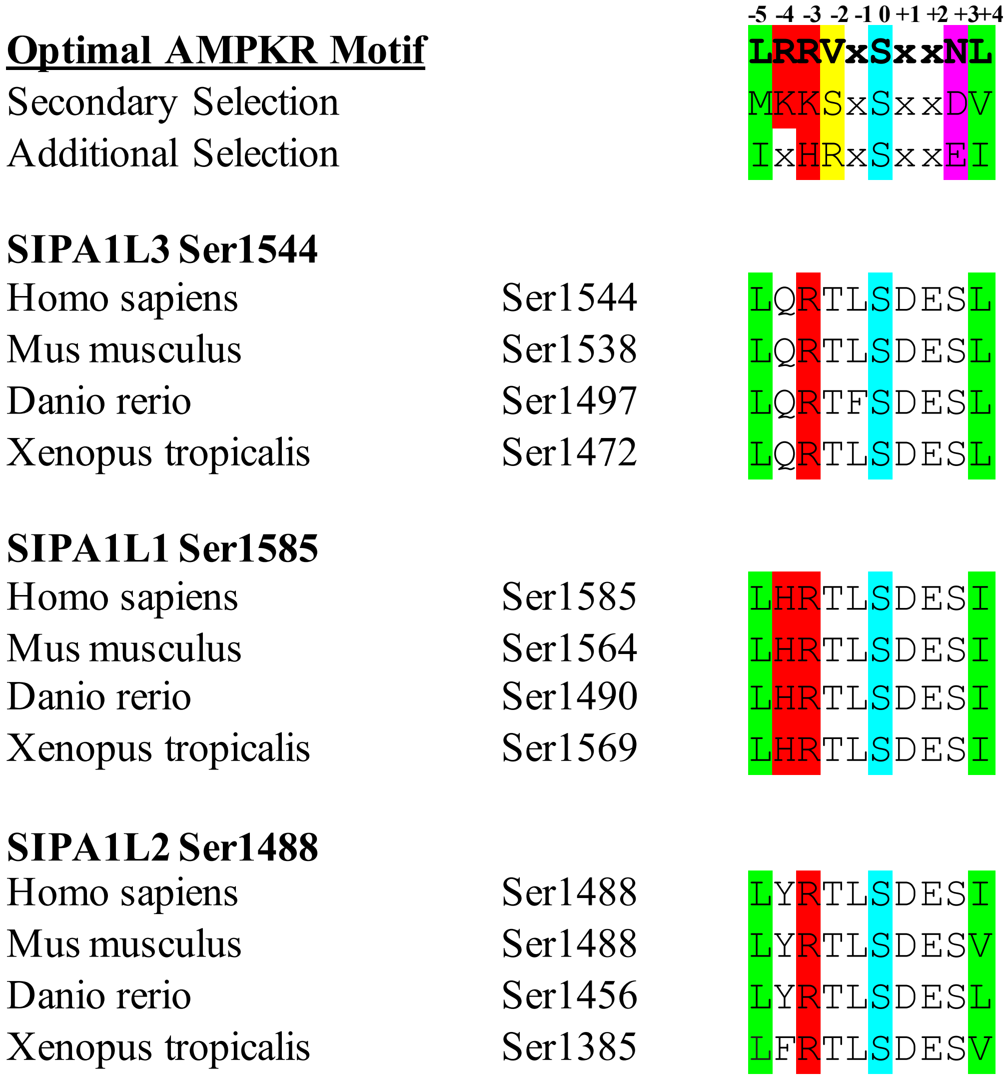

		-5 -4 -3 -2 -1 0 +1 +2 +3+4
Optimal AMPKR Motif		**LRRVxSxxNL**
Secondary Selection		MKKSxSxxDV
Additional Selection		IxHRxSxxEI
SIPA1L3 Ser1544		
Homo sapiens	Ser1544	LQRTLSDESL
Mus musculus	Ser1538	LQRTLSDESL
Danio rerio	Ser1497	LQRTFSDESL
Xenopus tropicalis	Ser1472	LQRTLSDESL
SIPA1L1 Ser1585		
Homo sapiens	Ser1585	LHRTLSDESI
Mus musculus	Ser1564	LHRTLSDESI
Danio rerio	Ser1490	LHRTLSDESI
Xenopus tropicalis	Ser1569	LHRTLSDESI
SIPA1L2 Ser1488		
Homo sapiens	Ser1488	LYRTLSDESI
Mus musculus	Ser1488	LYRTLSDESV
Danio rerio	Ser1456	LYRTLSDESL
Xenopus tropicalis	Ser1385	LFRTLSDESV

Figure 2.31. SIPA1L3's Ser1544, SIPA1L1's Ser1585 and SIPA1L2's Ser1488 are well conserved across vertebrates.

ClustalW alignment of SIPA1L3's Ser1544 showing its adherence to the optimal AMPKR consensus phosphorylation motif, conservation across species and to its family members, SIPA1L1 and SIPA1l2.

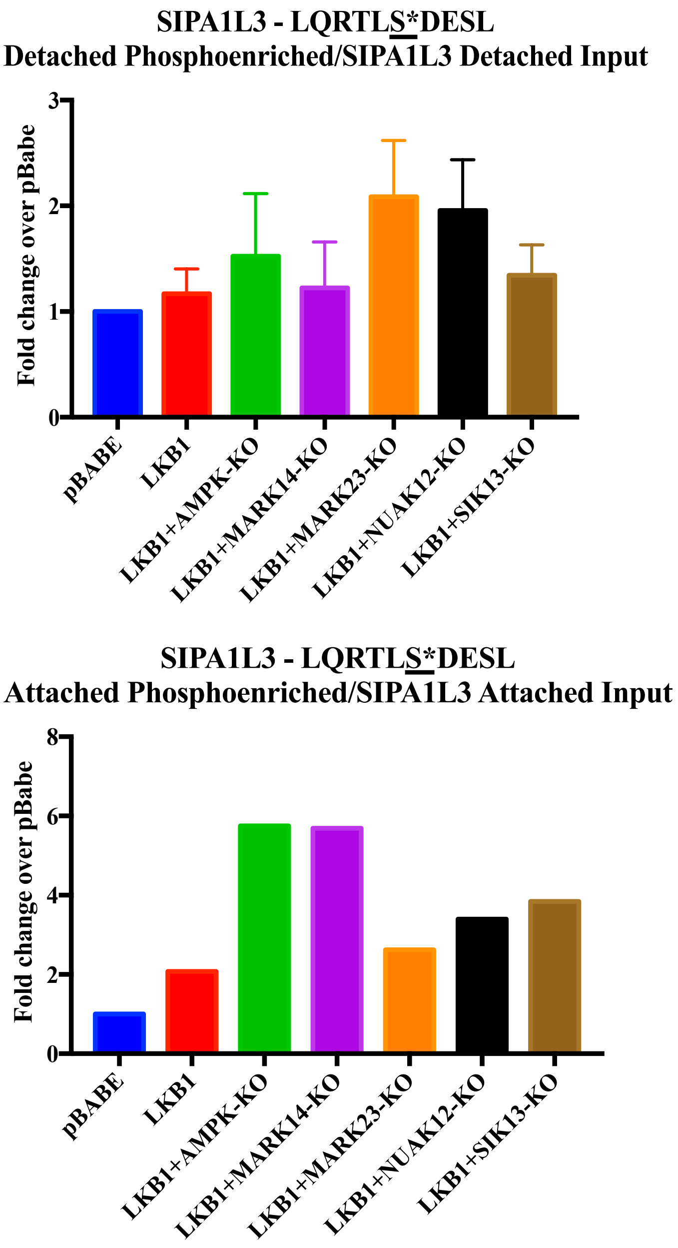

Figure 2.32. SIPA1L3's Ser1544 undergoes a mild LKB1-dependent detachment induced increase in phosphorylation.

(Top) Average phospho-Ser1544 data from the triplicate Detached-Phosphoenriched data set plotted for each cell line, normalized to total SIPA1L3 content in the Detached-Input runs. Bar graphs plot mean ±SD.

(Bottom) Phospho-Ser1544 data from the one of the Attached-Phosphoenriched run plotted for each cell line, normalized to total SIPA1L3 content from the same Input runs. Bar graphs plot mean ±SD.

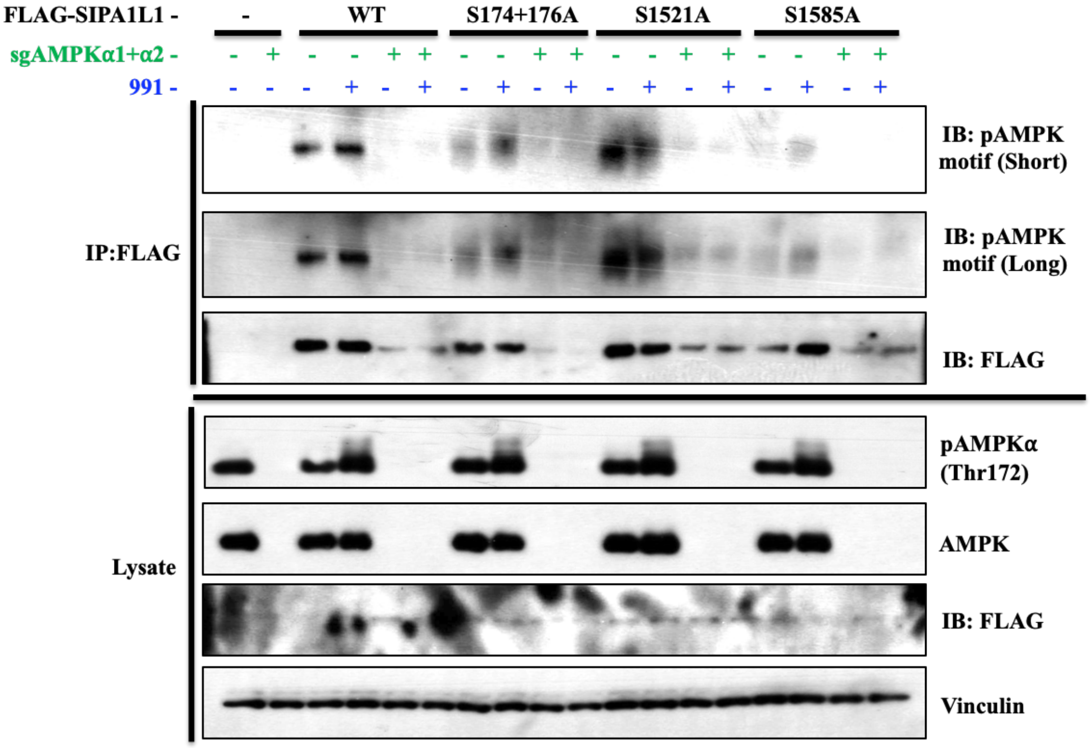

Figure 2.33. AMPK can phosphorylate SIPA1L1 on Ser1585.

Wild-Type and AMPK-null HEK293T cells transiently transfected with empty vector, FLAG tagged SIPA1L1 WT, S174+176A, S1521A and S1585A were treated with 991 or DMSO for 1 hour. Cells were lysed and lysates were subjected to FLAG immunoprecipitation (IP). The IP and lysates were immunoblotted with the indicated antibodies.

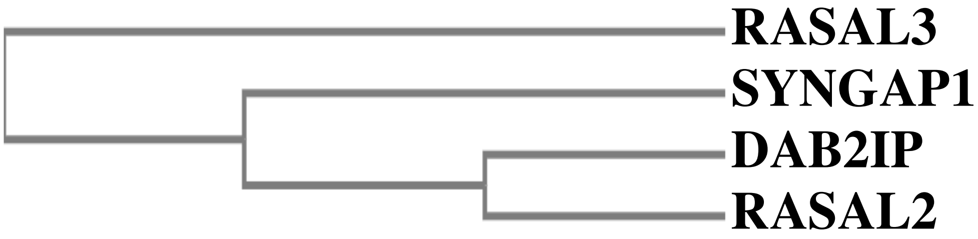

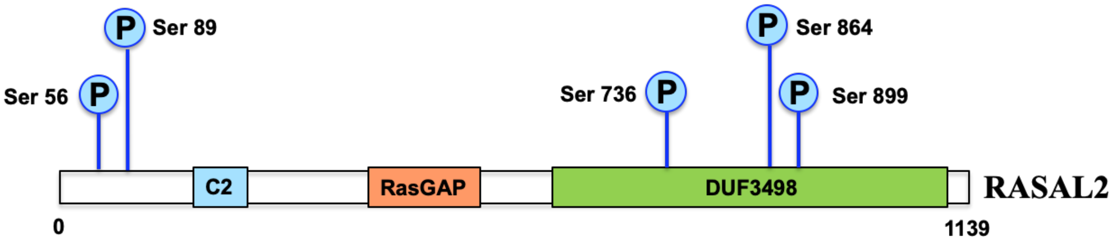

Figure 2.34. RASAL2 is a member of the RAS GTPase-activating protein family.

(Top) Simplified representation of the phylogenetic tree of subfamily of RasGAP domain containing proteins closely related to RASAL2. Human sequences of the proteins were downloaded from Uniprot. The sequences were aligned and the phylogenetic tree was generated using ClustalW.

(Bottom) Schematic of domain architecture of human RASAL2 highlighting location of the phosphorylation sites. Adapted from Phosphosite.org. Apart from the RasGAP domain, RASAL2 contains a C2 domain and a Domain of unknown function (DUF3498)

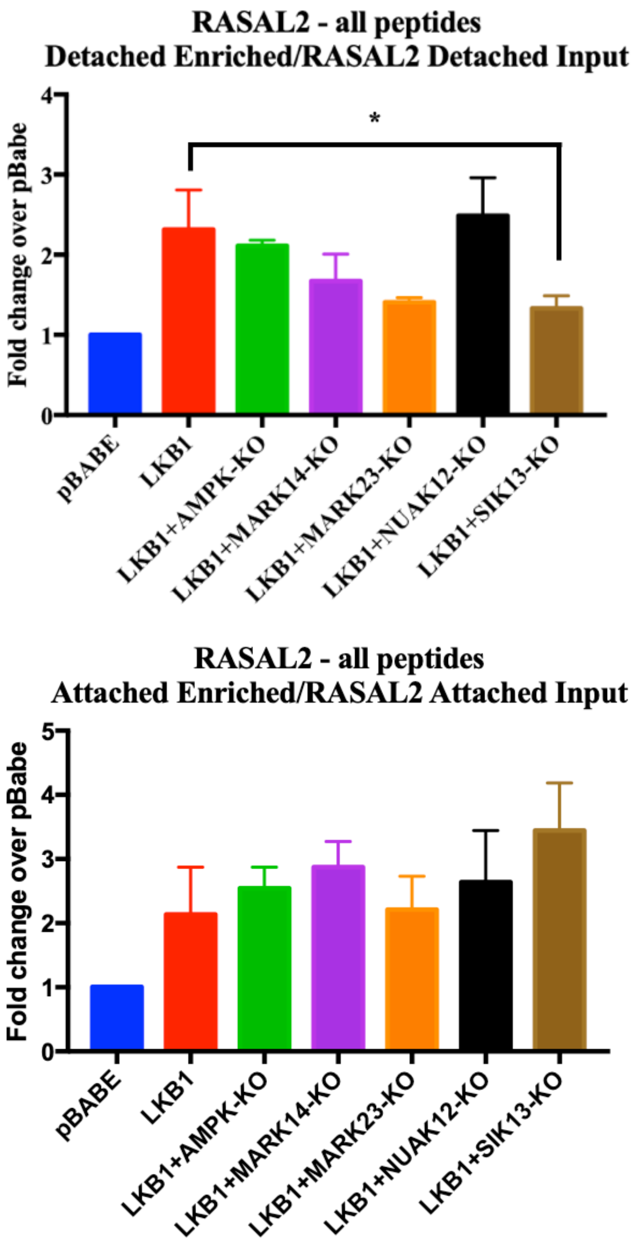

Figure 2.35. RASAL2 undergoes a strong LKB1-dependent enrichment when immunoprecipitated with the pAMPK motif antibody.

Average RASAL2 data from the triplicate Enriched data sets plotted for each cell line, normalized to total RASAL2 content in the corresponding Input runs. *, $p < .05$ compared to LKB1. Bar graphs plot mean ±SD. Statistical significance was determined by Two-way ANOVA.

(Top) Triplicate Detached-Enriched data sets
(Bottom) Triplicate Attached-Enriched data

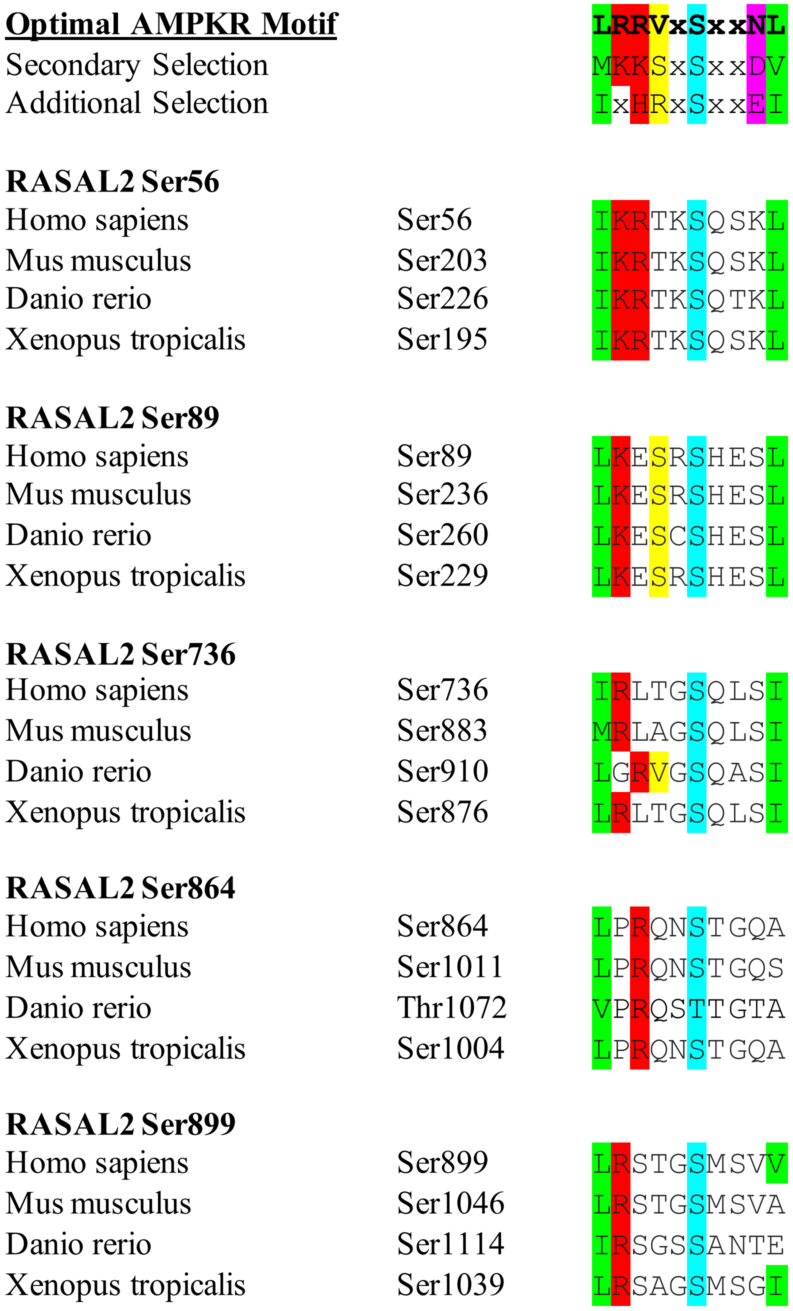

Optimal AMPKR Motif		**LRRVxSxxNL**
Secondary Selection		MKKSxSxxDV
Additional Selection		IxHRxSxxEI
RASAL2 Ser56		
Homo sapiens	Ser56	IKRTKSQSKL
Mus musculus	Ser203	IKRTKSQSKL
Danio rerio	Ser226	IKRTKSQTKL
Xenopus tropicalis	Ser195	IKRTKSQSKL
RASAL2 Ser89		
Homo sapiens	Ser89	LKESRSHESL
Mus musculus	Ser236	LKESRSHESL
Danio rerio	Ser260	LKESCSHESL
Xenopus tropicalis	Ser229	LKESRSHESL
RASAL2 Ser736		
Homo sapiens	Ser736	IRLTGSQLSI
Mus musculus	Ser883	MRLAGSQLSI
Danio rerio	Ser910	LGRVGSQASI
Xenopus tropicalis	Ser876	LRLTGSQLSI
RASAL2 Ser864		
Homo sapiens	Ser864	LPRQNSTGQA
Mus musculus	Ser1011	LPRQNSTGQS
Danio rerio	Thr1072	VPRQSTTGTA
Xenopus tropicalis	Ser1004	LPRQNSTGQA
RASAL2 Ser899		
Homo sapiens	Ser899	LRSTGSMSVV
Mus musculus	Ser1046	LRSTGSMSVA
Danio rerio	Ser1114	IRSGSSANTE
Xenopus tropicalis	Ser1039	LRSAGSMSGI

Figure 2.36. RASAL2's Ser56, Ser89, Ser736, Ser864 and Ser899 are well conserved across vertebrates.

ClustalW alignment of RASAL2's Ser56, Ser89, Ser736, Ser864 and Ser899 showing its adherence to the optimal AMPKR consensus phosphorylation motif and conservation across species

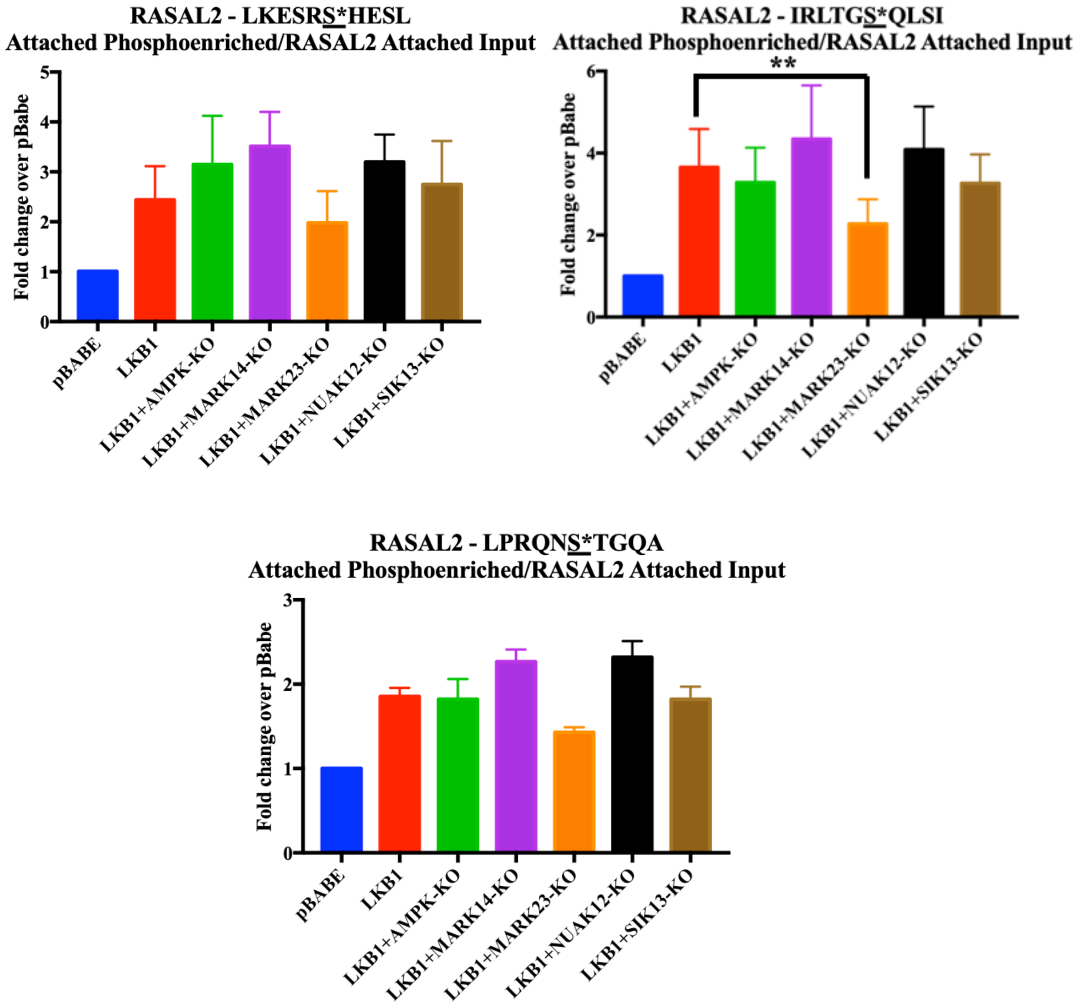

Figure 2.37. RASAL2 Phosphospecific data shows a strong LKB1-dependent enrichment when immunoprecipitated with the pAMPK motif antibody.

Average RASAL2's phospho-specific data from the triplicate Attached-Phosphoenriched data set plotted for each cell line, normalized to total RASAL2 content in the corresponding Attached-Input runs. **, $p < .005$ compared to LKB1. Bar graphs plot mean ±SD. Statistical significance was determined by Two-way ANOVA.

(Top left) RASAL2's phospho-Ser89 data
(Top right) RASAL2's phospho-Ser736 data
(Bottom) RASAL2's phospho-Ser864 data

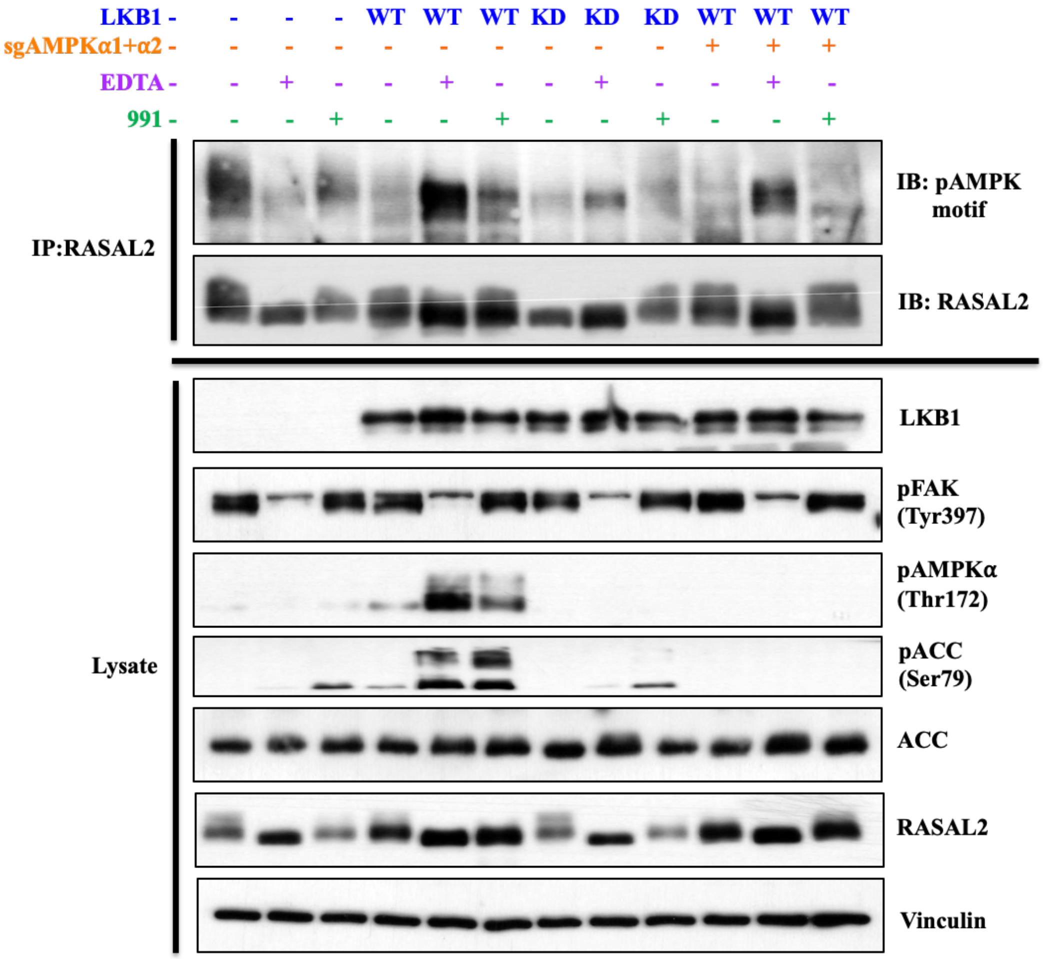

Figure 2.38. AMPK and other no additional AMPKRs can phosphorylate endogenous RASAL2.

A549 (empty vector, WT-LKB1, KD-LKB1 and WT-LKB1 further expressing sgRNA guides targeting both AMPKα's) were subjected to the detached assay or 991 treatment for an hour. Cell were lysed and lysates were subjected to endogenous RASAL2 immunoprecipitation. The IP and lysates were immunoblotted with the indicated antibodies.

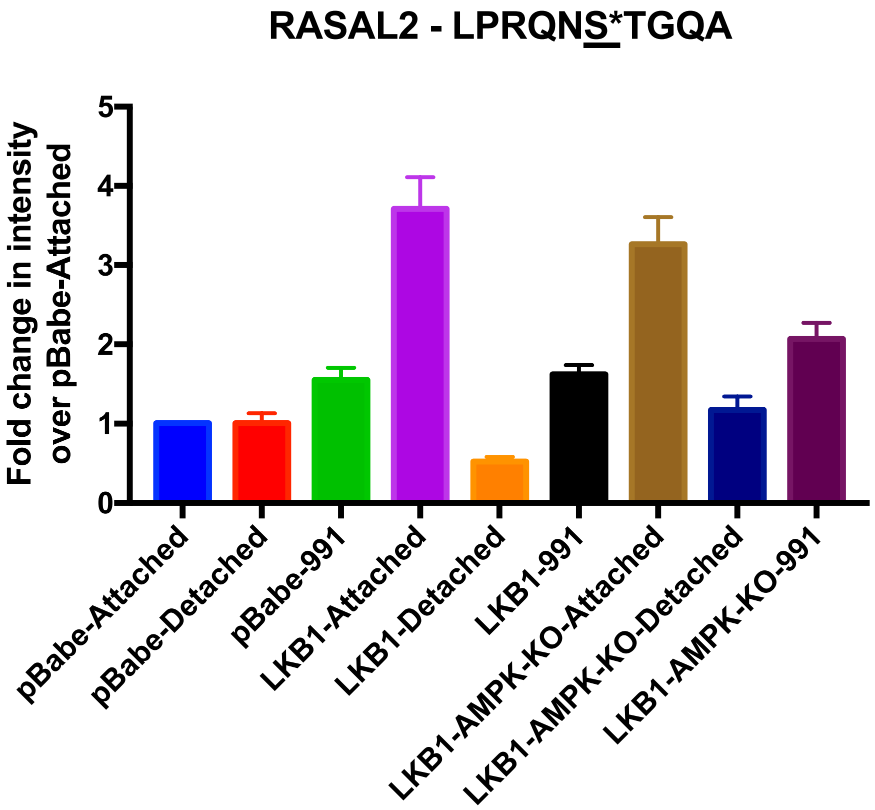

Figure 2.39. LKB1-dependent phosphorylation of RASAL2's Ser864 occurs in attached cells, which is AMPK-independent.

RASAL2's phosphorylated Ser864 specific data from the endogenous RASAL2 IP from the indicated A549 cells and treatment conditions, normalized to Input in each condition. Empty vector, wild-type (WT) and kinase dead (KD) LKB1 expressing A549 cells, along with AMPK-null A549 cells that expressed WT-LKB1 were subjected to the detached assay or 991 treatment for an hour. Cell were lysed and lysates were subjected to endogenous RASAL2 IP. Each IP was trypsin digested, TMT-labeled, combined into a single tube and run on the LC/MS.

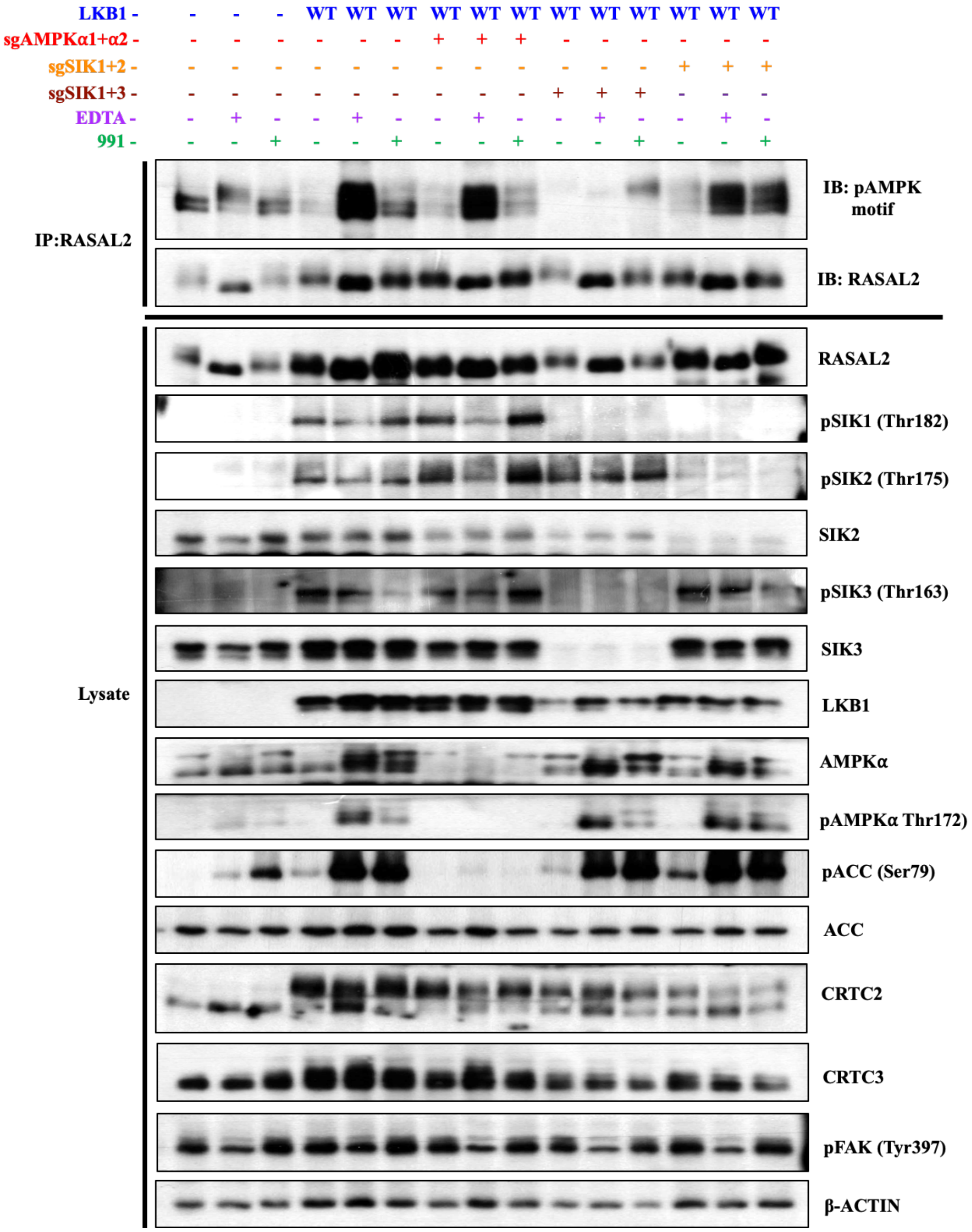

Figure 2.40. RASAL2 is an AMPK and a SIK substrate.

A549 (empty vector, WT-LKB1, and WT-LKB1 further expressing sgRNA guides targeting both AMPKα's, SIK1, SIK2 and SIK3) were subjected to the detached assay or 991 treatment for an hour. Cell were lysed and lysates were subjected to endogenous RASAL2 immunoprecipitation. The IP and lysates were immunoblotted with the indicated antibodies.

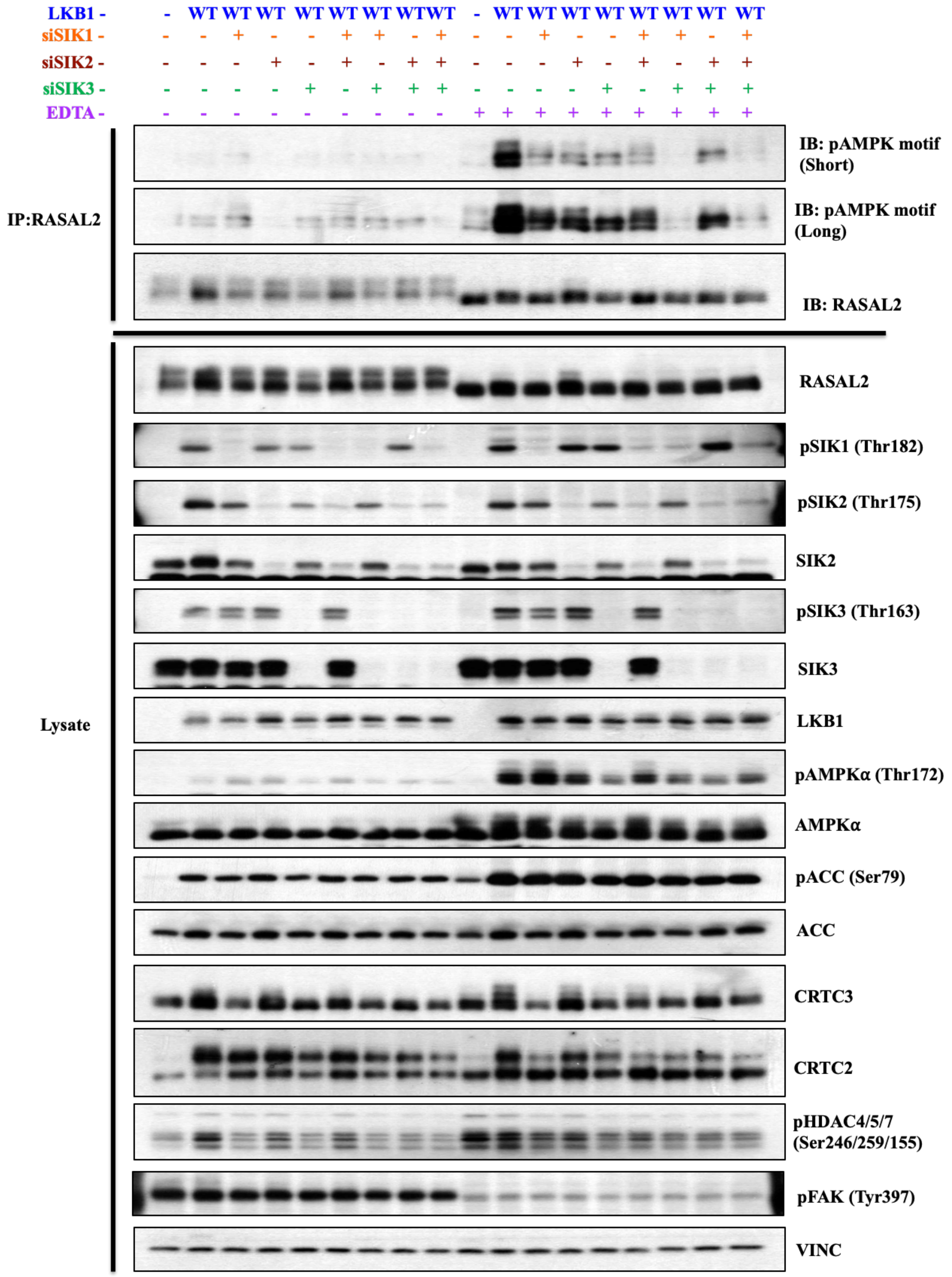

Figure 2.41. RASAL2 is a novel SIK1+SIK3 substrate.

A549 cells expressing WT-LKB1 cells were transfected with siRNA oligos (20 μM) targeting SIK1, SIK2 and SIK3 for 72 hours. Along with control siRNA treated A549 cells (empty vector and WT-LKB1), these SIK siRNA targeted cells were subjected to the detached assay for an hour. Cell were lysed and lysates were subjected to endogenous RASAL2 immunoprecipitation. The IP and lysates were immunoblotted with the indicated antibodies.

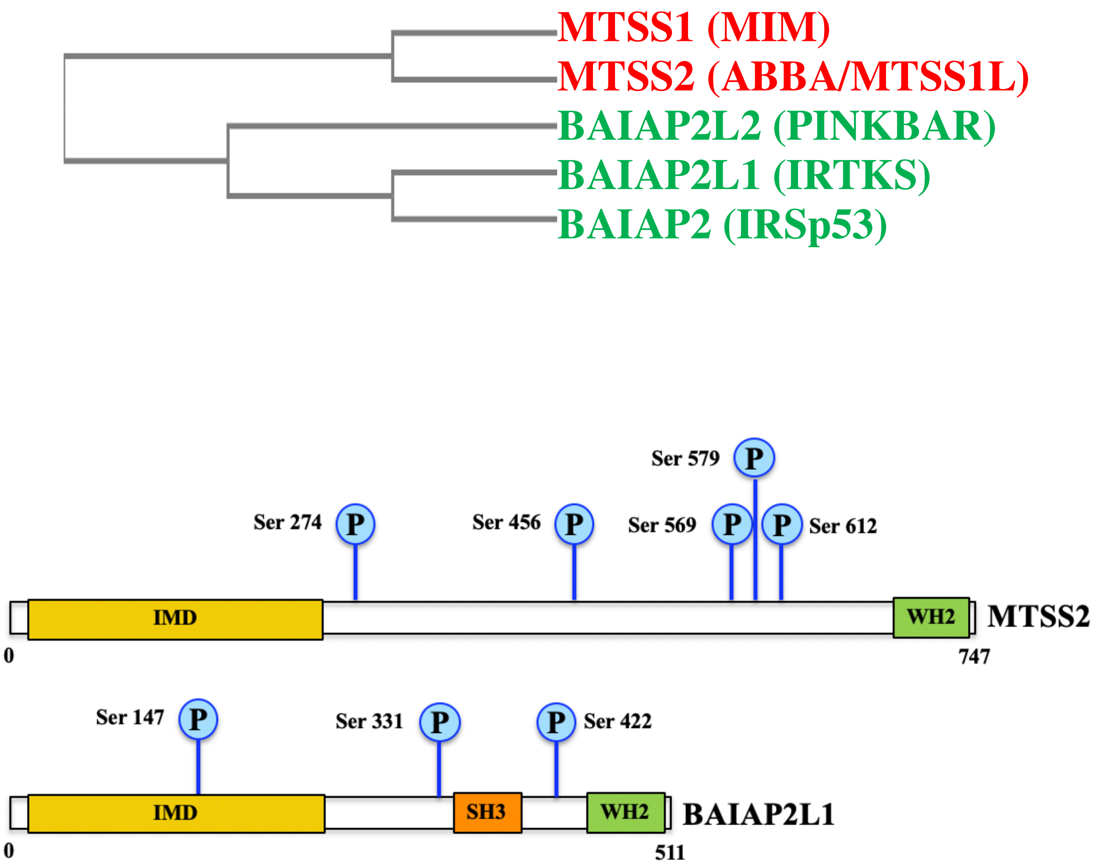

Figure 2.42. MTSS2 and BAIAP2L1 are member of the I-bar domain containing proteins.

(Top) Simplified representation of the phylogenetic tree of subfamily of I-BAR (IMD) domain containing proteins. Human sequences of the proteins were downloaded from Uniprot. The sequences were aligned and the phylogenetic tree was generated using ClustalW.

(Bottom) Schematic of domain architecture of human MTSS2 and BAIAP2L1 highlighting location of the phosphorylation sites. Adapted from Phosphosite.org. Apart from the IMD domain (IRSp53 and MIM (missing in metastases) homology Domain), these proteins also contain a WH2 (Wiskott-Aldrich syndrome homology region 2) domain. BAIAP2L1 contains an extra SH3 (SRC Homology 3) Domain.

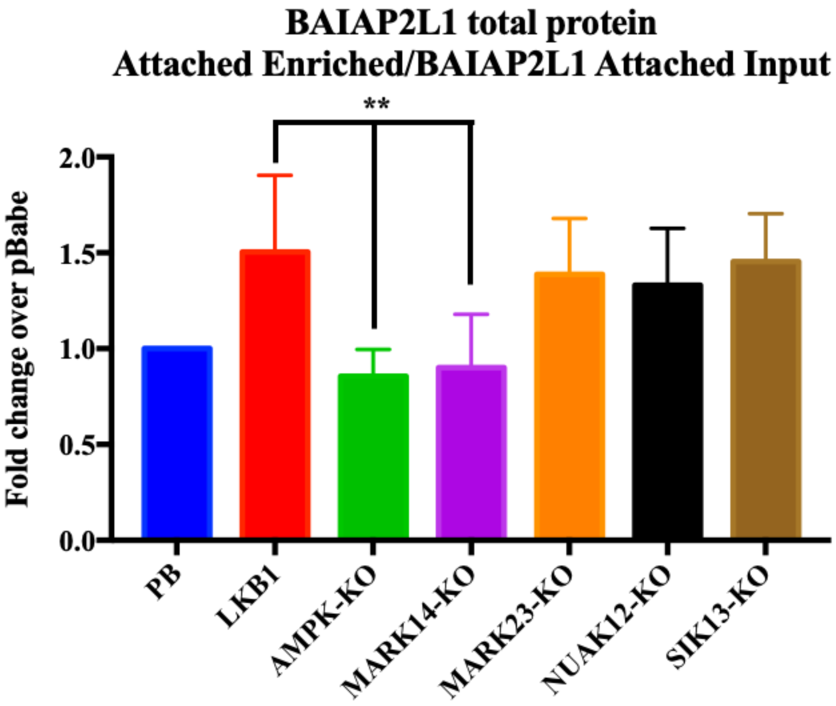

Figure 2.43. BAIAP2L1 undergoes a LKB1-dependent increase in binding to the pAMPK motif antibody, which is completely inhibited in both AMPK-null and MARK1+MARK4-null cells.

Average BAIAP2L1 data from the triplicate Attached-Enriched data set plotted for each cell line, normalized to BAIAP2L1's protein content in the Attached-Input data set. **, $p < .005$ compared to LKB1. Bar graphs plot mean ±SD. Statistical significance was determined by Two-way ANOVA.

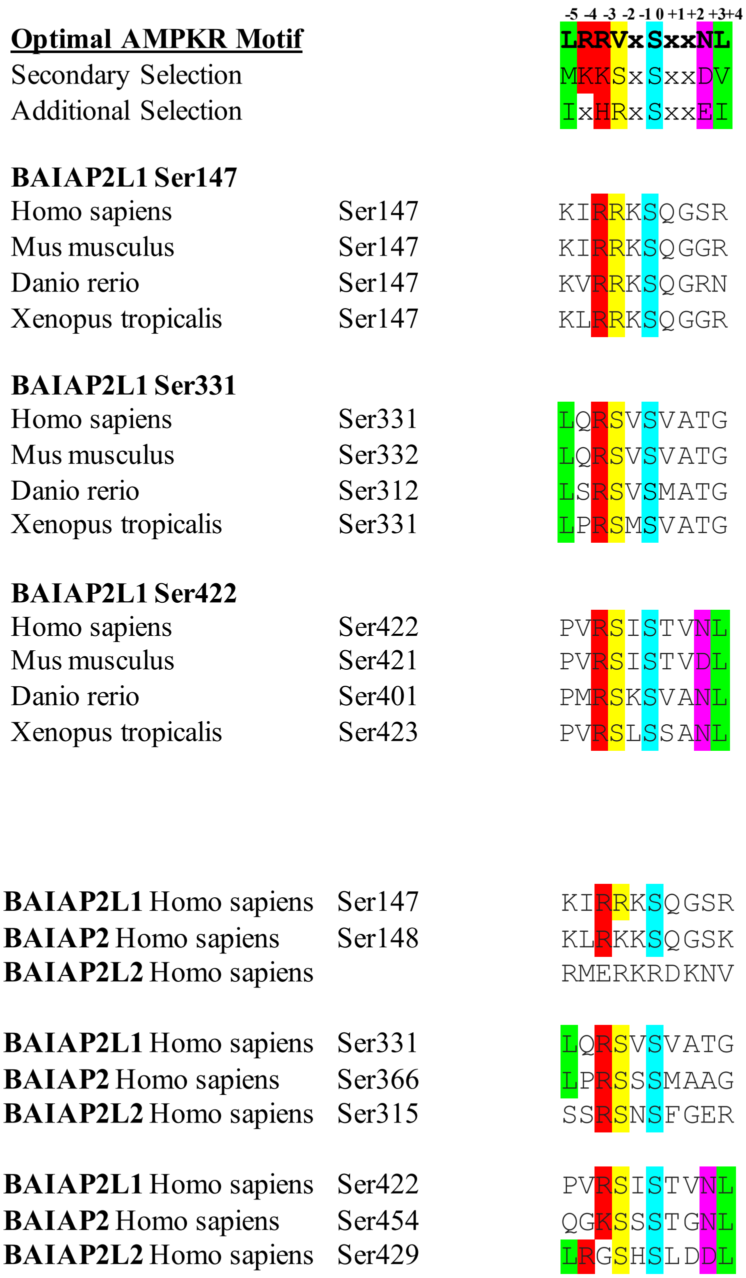

		-5 -4 -3 -2 -1 0 +1 +2 +3 +4
Optimal AMPKR Motif		**LRRVxSxxNL**
Secondary Selection		MKKSxSxxDV
Additional Selection		IxHRxSxxEI
BAIAP2L1 Ser147		
Homo sapiens	Ser147	KIRRKSQGSR
Mus musculus	Ser147	KIRRKSQGGR
Danio rerio	Ser147	KVRRKSQGRN
Xenopus tropicalis	Ser147	KLRRKSQGGR
BAIAP2L1 Ser331		
Homo sapiens	Ser331	LQRSVSVATG
Mus musculus	Ser332	LQRSVSVATG
Danio rerio	Ser312	LSRSVSMATG
Xenopus tropicalis	Ser331	LPRSMSVATG
BAIAP2L1 Ser422		
Homo sapiens	Ser422	PVRSISTVNL
Mus musculus	Ser421	PVRSISTVDL
Danio rerio	Ser401	PMRSKSVANL
Xenopus tropicalis	Ser423	PVRSLSSANL

BAIAP2L1 Homo sapiens	Ser147	KIRRKSQGSR
BAIAP2 Homo sapiens	Ser148	KLRKKSQGSK
BAIAP2L2 Homo sapiens		RMERKRDKNV
BAIAP2L1 Homo sapiens	Ser331	LQRSVSVATG
BAIAP2 Homo sapiens	Ser366	LPRSSSMAAG
BAIAP2L2 Homo sapiens	Ser315	SSRSNSFGER
BAIAP2L1 Homo sapiens	Ser422	PVRSISTVNL
BAIAP2 Homo sapiens	Ser454	QGKSSSTGNL
BAIAP2L2 Homo sapiens	Ser429	LRGSHSLDDL

Figure 2.44. BAIAP2L1's Ser147, Ser331 and Ser422 are well conserved across vertebrates and its subfamily members.

(Top) ClustalW alignment of human BAIAP2L1's Ser147, Ser331 and Ser422 across species showing conservation of the AMPKR consensus phosphorylation motif.
(Bottom) ClustalW alignment of human BAIAP2L1's Ser147, Ser33 and Ser422 and the corresponding sites on BAIAP2 and BAIAP2L2.

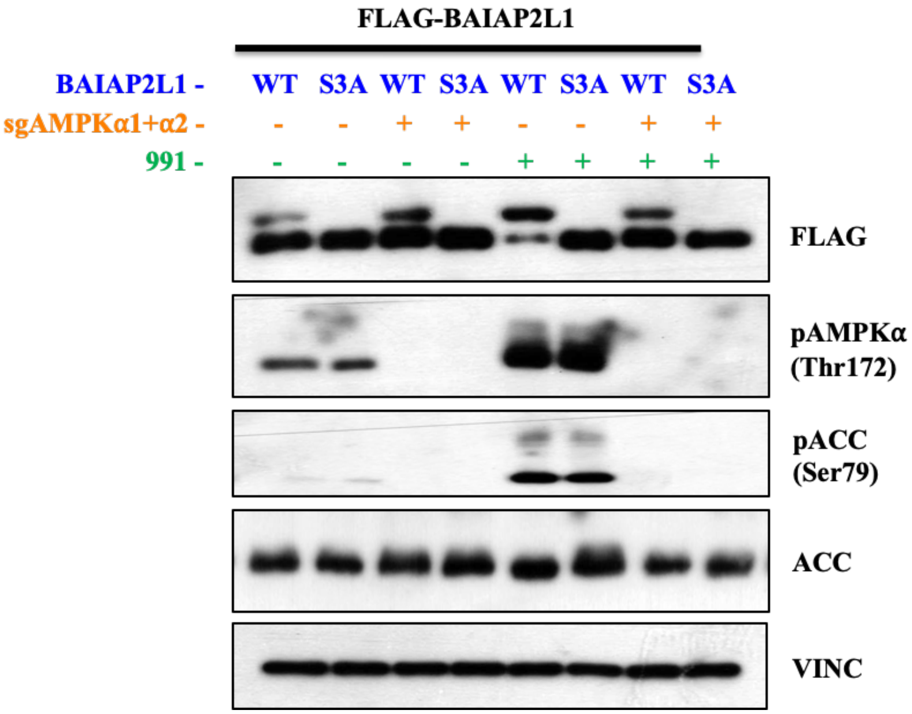

Figure 2.45. AMPK can directly phosphorylate BAIAP2L1 resulting in its band-shift.

Wild-type and AMPK-knock out U2OS cells were stably transfected with FLAG-tagged Wild-type and triple point mutant (3SA - Ser147A+Ser331A+Ser422A) msBAIAP2L1. Cells were subjected 991 treatment for an hour. Cell lysates were immunoblotted with the indicated antibodies.

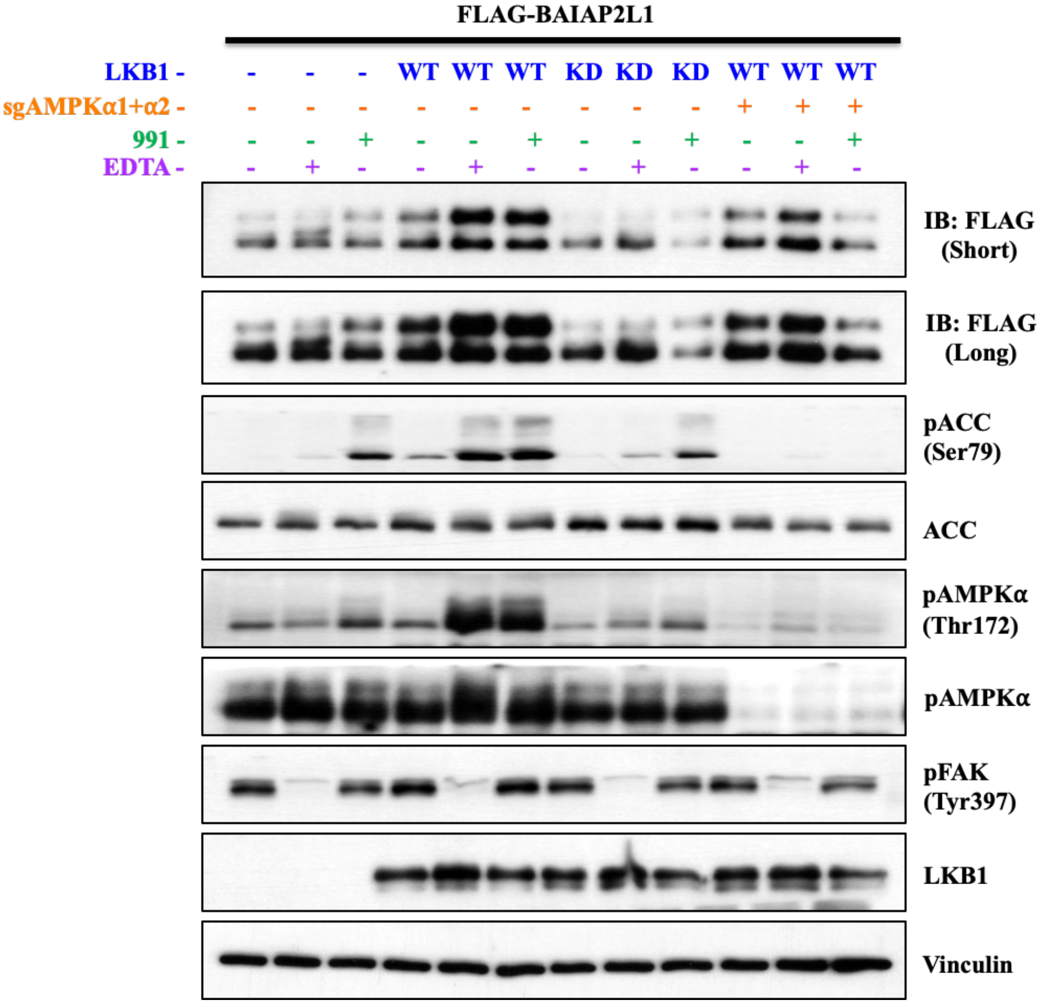

Figure 2.46. AMPK-dependent and independent phosphorylation of BAIAP2L1 occurs during cell detachment in A549 cells expressing wild-type LKB1.

A549 cells (empty vector, WT-LKB1, KD-LKB1 and WT-LKB1 further expressing sgRNA guides targeting both AMPKα's) were stably transfected with FLAG-tagged msBAIAP2L1 were subjected to the detached assay or 991 treatment for an hour. Cell lysates were immunoblotted with the indicated antibodies.

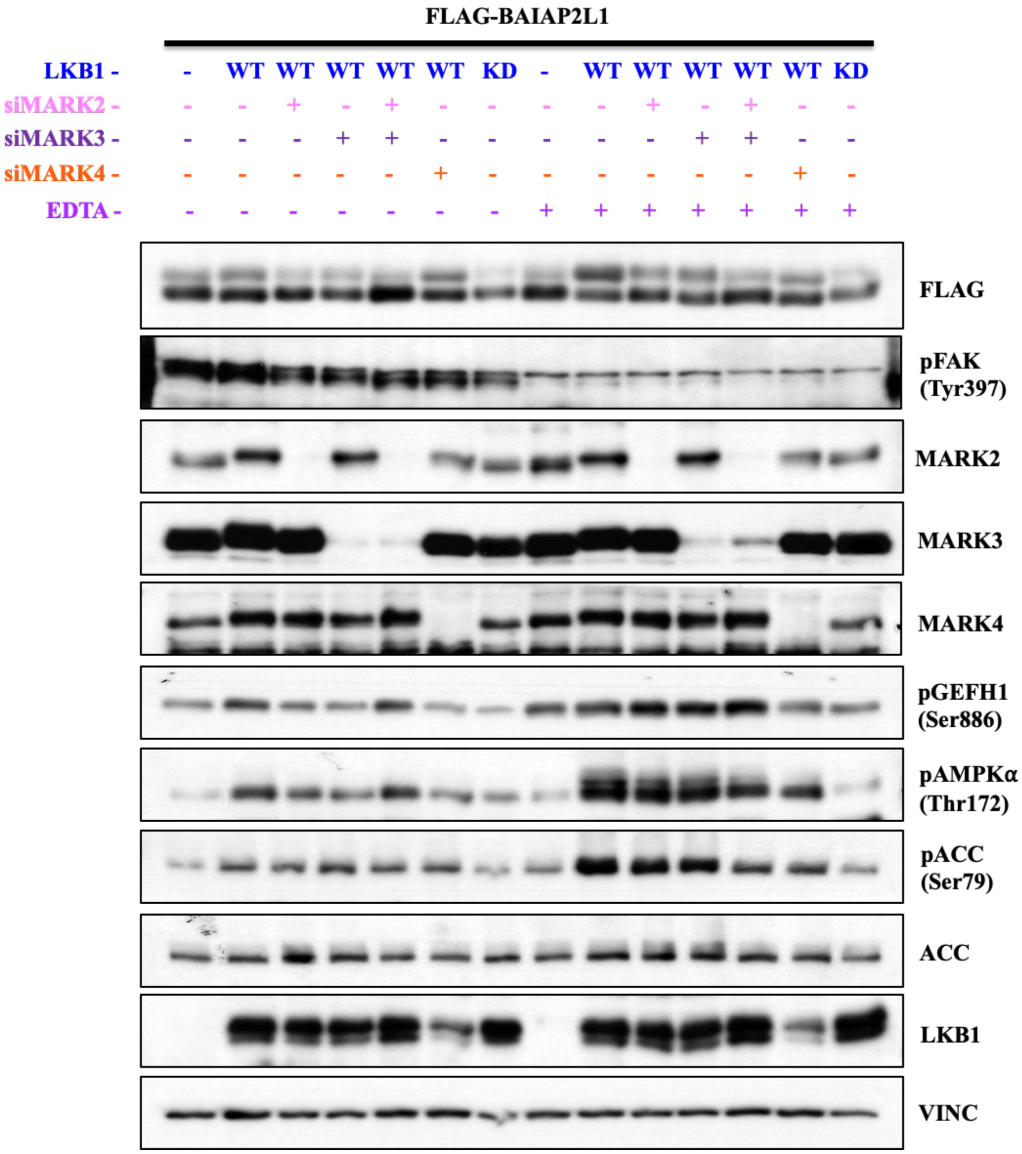

Figure 2.47. MARK2, 3 and 4 can phosphorylation BAIAP2L1.

A549 cells (empty vector, WT-LKB1 and KD-LKB1) were stably transfected with FLAG-tagged msBAIAP2L1. A549 cells expressing wild-type LKB1 were transfected with siRNA oligos (20 μM) targeting MARK2, 3 and 4for 72 hours. Cells were then subjected to the detached assay or 991 treatment for an hour. Cell lysates were immunoblotted with the indicated antibodies.

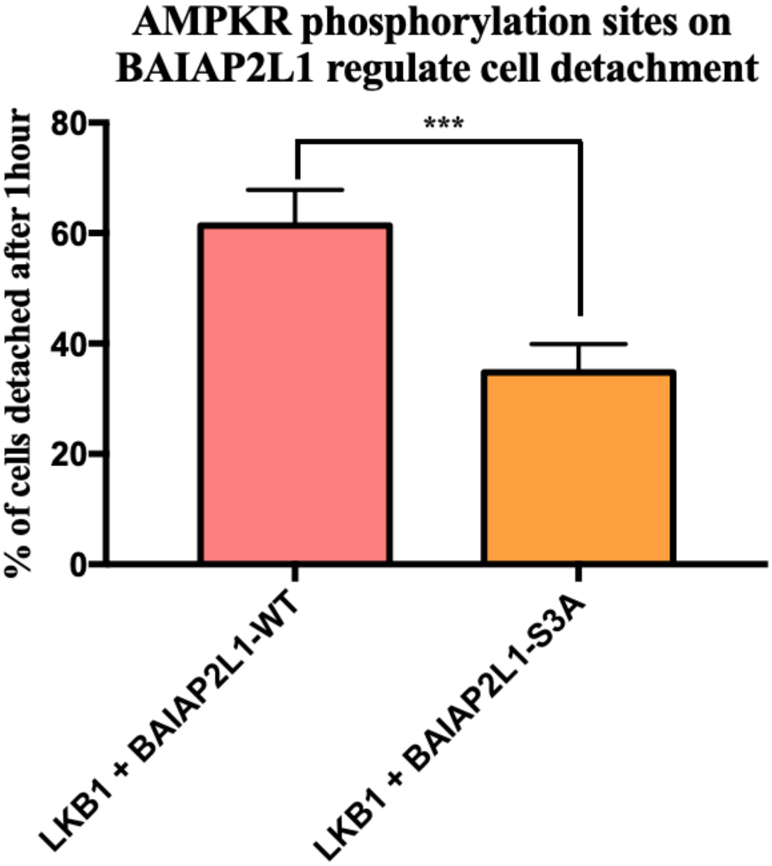

Figure 2.48. BAIAP2L1's 3SA triple point mutant regulates cell detachment by EDTA.

A549 cells expressing wild-type LKB1 and stably expressing WT and S3A (Ser147, Ser332 and Ser421) msBAIAP2L1 were subjected to the detachment assay. At one hour, the number of detached and attached cells were counted by trypan blue staining. ***, $p< .0005$ compared to LKB1 + BAIAP2L1-WT. Bar graphs plot mean ±SD. Statistical significance was determined by Student's t-test.

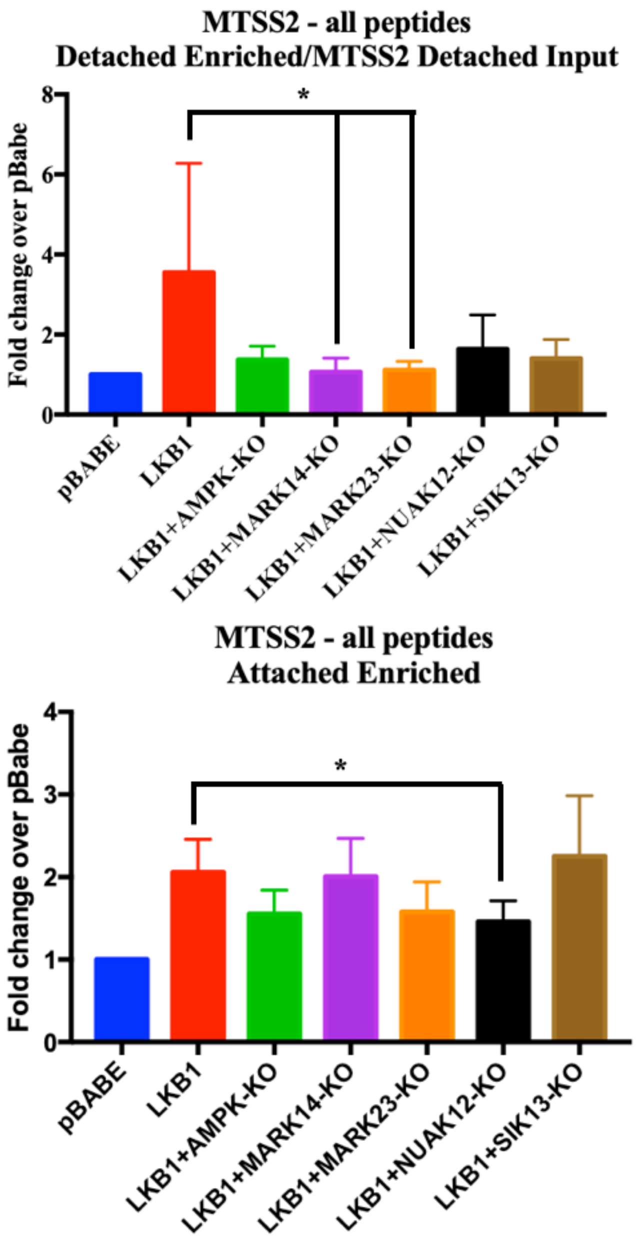

Figure 2.49. MTSS2 undergoes a strong LKB1-dependent enrichment when immunoprecipitated with the pAMPK motif antibody.

Average MTSS2 data from the triplicate Enriched data sets plotted for each cell line. *, p < .05 compared to LKB1. Bar graphs plot mean ±SD. Statistical significance was determined by Two-way ANOVA.

(Top) Triplicate Detached-Enriched data sets, normalized to total MTSS2 content in the corresponding Input runs
(Bottom) Triplicate Attached-Enriched data

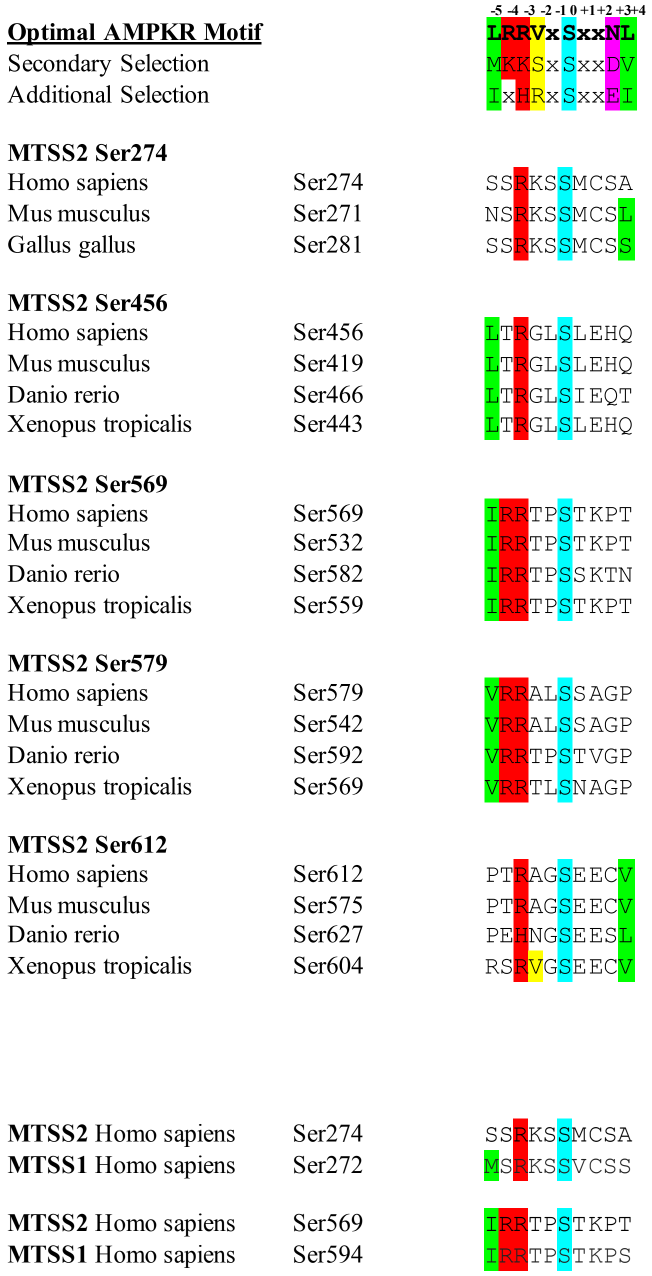

		-5 -4 -3 -2 -1 0 +1+2 +3+4
Optimal AMPKR Motif		**LRRVxSxxNL**
Secondary Selection		MKKSxSxxDV
Additional Selection		IxHRxSxxEI
MTSS2 Ser274		
Homo sapiens	Ser274	SSRKSSMCSA
Mus musculus	Ser271	NSRKSSMCSL
Gallus gallus	Ser281	SSRKSSMCSS
MTSS2 Ser456		
Homo sapiens	Ser456	LTRGLSLEHQ
Mus musculus	Ser419	LTRGLSLEHQ
Danio rerio	Ser466	LTRGLSIEQT
Xenopus tropicalis	Ser443	LTRGLSLEHQ
MTSS2 Ser569		
Homo sapiens	Ser569	IRRTPSTKPT
Mus musculus	Ser532	IRRTPSTKPT
Danio rerio	Ser582	IRRTPSSKTN
Xenopus tropicalis	Ser559	IRRTPSTKPT
MTSS2 Ser579		
Homo sapiens	Ser579	VRRALSSAGP
Mus musculus	Ser542	VRRALSSAGP
Danio rerio	Ser592	VRRTPSTVGP
Xenopus tropicalis	Ser569	VRRTLSNAGP
MTSS2 Ser612		
Homo sapiens	Ser612	PTRAGSEECV
Mus musculus	Ser575	PTRAGSEECV
Danio rerio	Ser627	PEHNGSEESL
Xenopus tropicalis	Ser604	RSRVGSEECV
MTSS2 Homo sapiens	Ser274	SSRKSSMCSA
MTSS1 Homo sapiens	Ser272	MSRKSSVCSS
MTSS2 Homo sapiens	Ser569	IRRTPSTKPT
MTSS1 Homo sapiens	Ser594	IRRTPSTKPS

Figure 2.50. MTSS2's Ser274, Ser456, Ser569, Ser579 and Ser612 are well conserved across vertebrates and its subfamily members.

(Top) ClustalW alignment of human MTSS2's Ser274, Ser456, Ser569, Ser579 and Ser612 across species showing conservation of the AMPKR consensus phosphorylation motif. (Bottom) ClustalW alignment of human MTSS2's Ser274, Ser456, Ser569, Ser579 and Ser612 and the corresponding sites on MTSS1

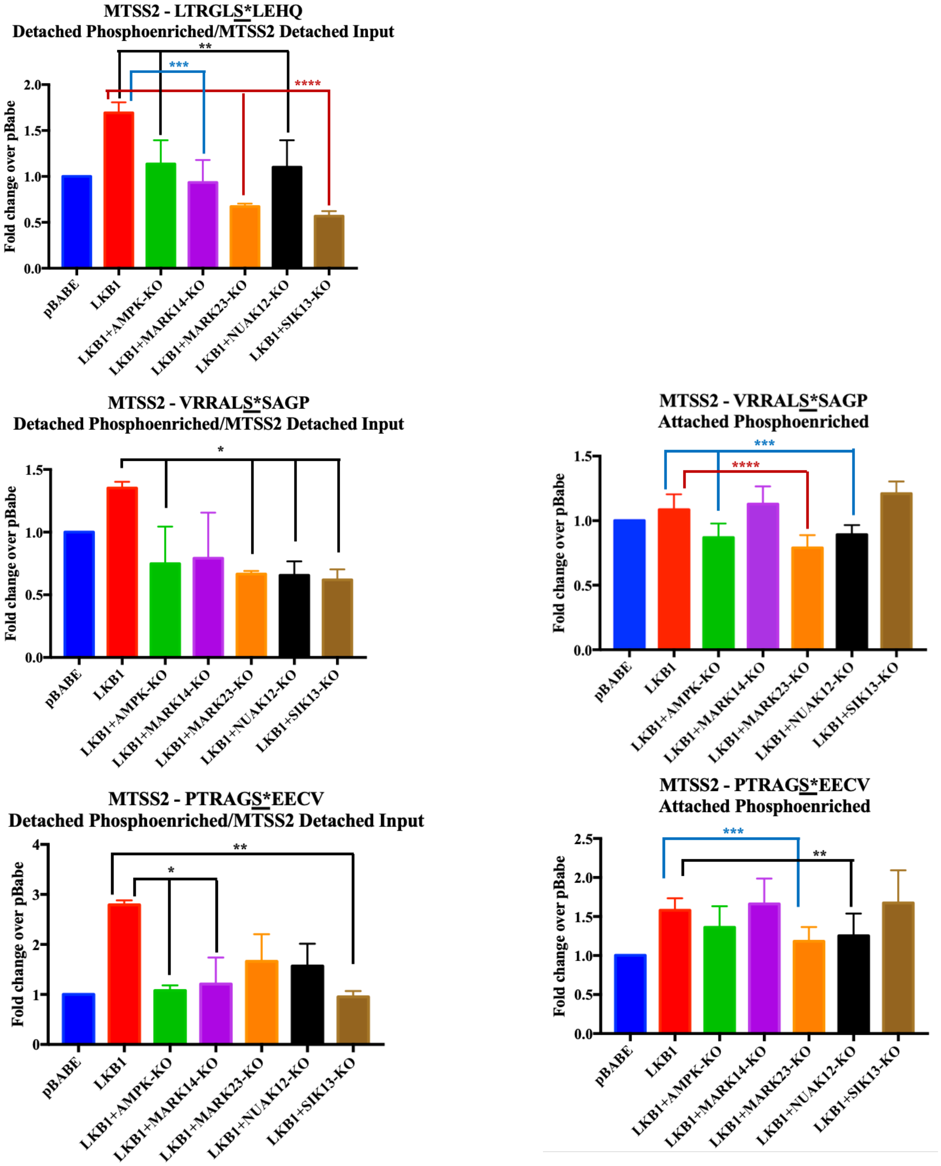

Figure 2.51. Several serines in MTSS2 undergo a significant LKB1-dependent detachment induced increase in phosphorylation.

*, p < .05; **, p < .005; ***, p< .0005; ****, p< .0001 compared to LKB1. Bar graphs plot mean ±SD. Statistical significance was determined by Two-way ANOVA.
(Left) Average MTSS2's phospho-specific data from the triplicate Detached-Phosphoenriched plotted for each cell line, normalized to MTSS2's s protein content in the Detached-Input data set.
(Right) Average MTSS2's phospho-specific data from the triplicate Attached-Phosphoenriched plotted for each cell line.

(Top left) MTSS2's phospho-Ser456 data
(Top right) MTSS2's phospho-Ser579 data
(Bottom) MTSS2's phospho-Ser612 data

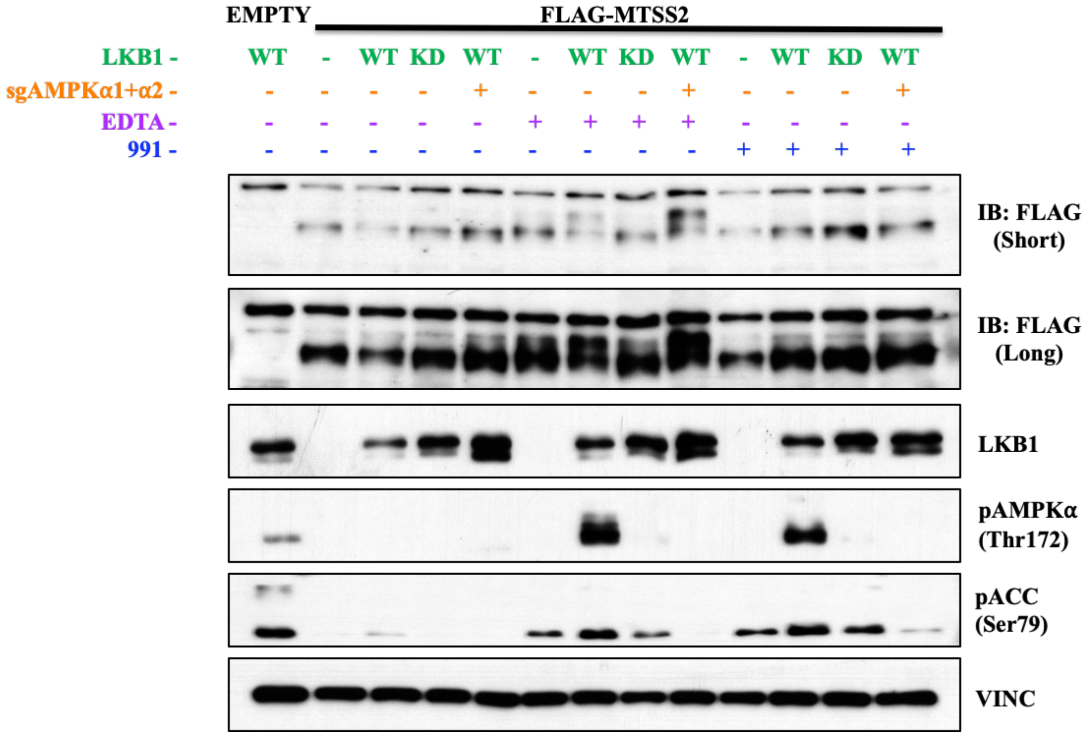

Figure 2.52. MTSS2 undergoes a LKB1-dependent band-shift upon cell detachment, which is AMPK-independent.

A549 cells (empty vector, WT-LKB1, KD-LKB1 and WT-LKB1 further expressing sgRNA guides targeting both AMPKα's) were stably transfected with FLAG-tagged msMTSS2 and empty vector control were subjected to the detached assay or 991 treatment for an hour. Cells were lysed and lysates were subjected to FLAG immunoprecipitation (IP). The IP and lysates were immunoblotted with the indicated antibodies.

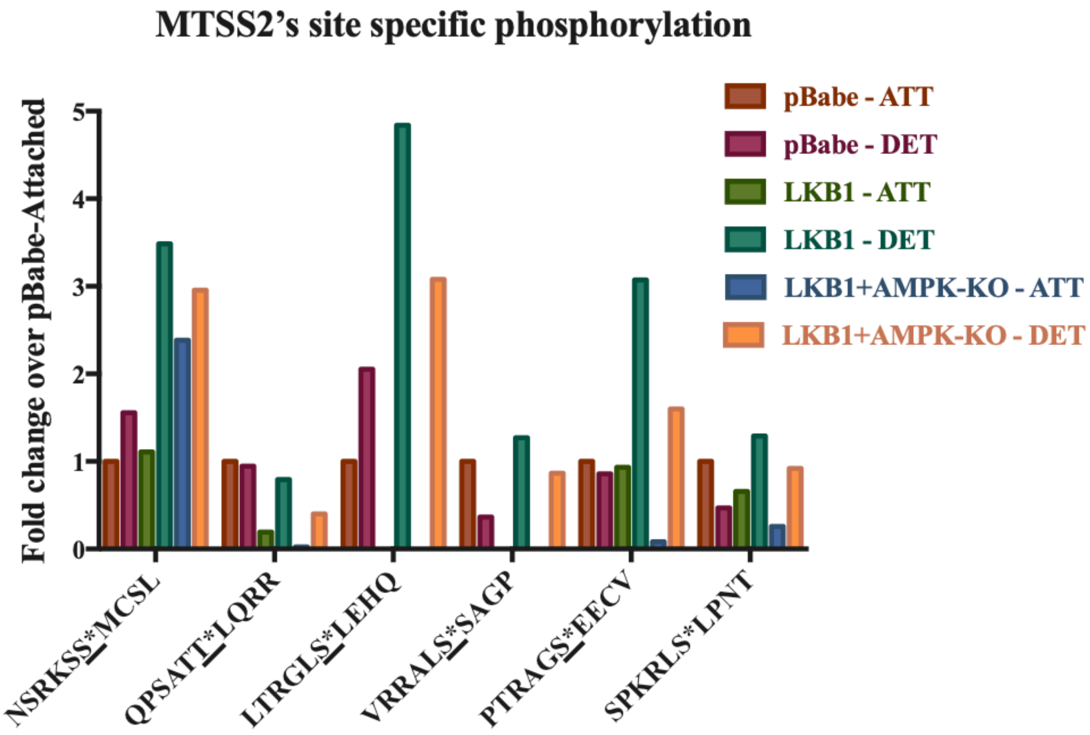

Figure 2.53. msMTSS2's Ser271, Ser419, Ser542, Ser575 undergo a LKB1-dependent detachment induced increase in phosphorylation which is not AMPK-dependent.

Site specific phosphorylation on msMTSS2's Ser271, Thr354, Ser419, Ser542, Ser575 and Ser602. A549 cells (empty vector, WT-LKB1 and WT-LKB1 further expressing sgRNA guides targeting both AMPKα's) were stably transfected with FLAG-tagged msMTSS2 were subjected to the detached assay. Cell were lysed and lysates were subjected to FLAG-MTSS2 IP. Each IP was trypsin digested, TMT-labeled, combined into a single tube and run on the LC/MS. The sequences underlined in red undergo a LKB1-dependent detachment induced increase in phosphorylation.

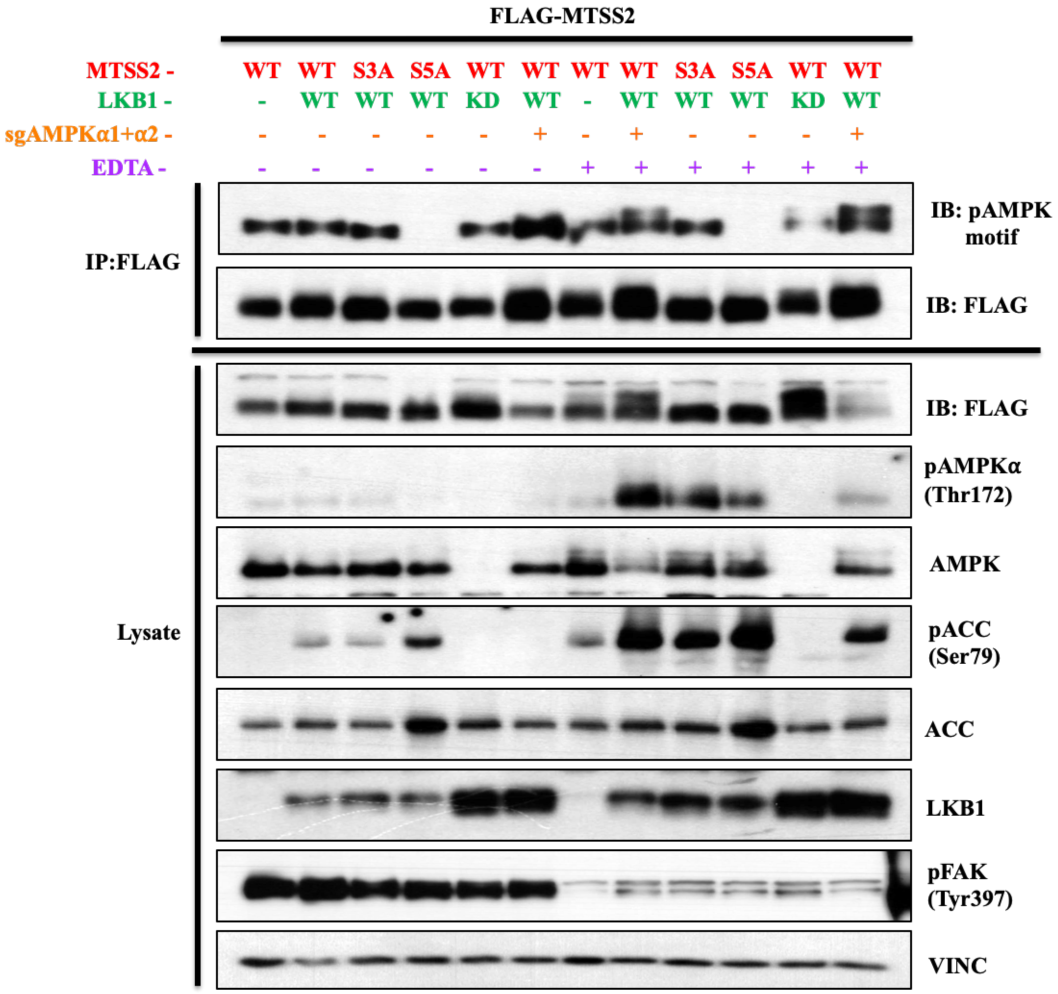

Figure 2.54. msMTSS2 undergoes LKB1-dependent, detachment induced band shift due to phosphorylation on its Ser271A, Ser419A and Ser575A.

A549 cells (empty vector, WT-LKB1, KD-LKB1 and WT-LKB1 further expressing sgRNA guides targeting both AMPKα's) were stably transfected with FLAG-tagged WT, S3A (Ser271A, Ser419A and Ser575A) and S5A (Ser271A, Ser419A, Ser532A, Ser542A and Ser575A) msMTSS2 were subjected to the detached assay or 991 treatment for an hour. Cells were lysed and lysates were subjected to FLAG immunoprecipitation (IP). The IP and lysates were immunoblotted with the indicated antibodies.

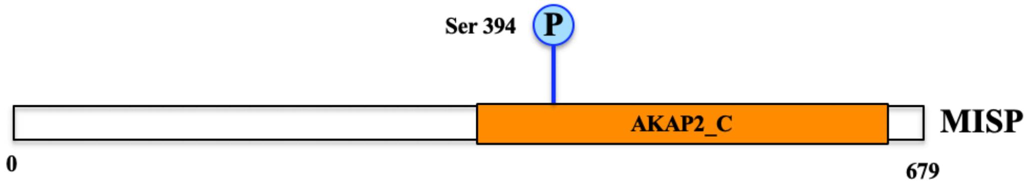

Figure 2.55. MISP is protein that controls mitotic spindle positioning.

Schematic of domain architecture of human MISP highlighting location of the phosphorylation sites. Adapted from Phosphosite.org. The only domain on the protein is the A-kinase anchor protein 2 C-terminus (AKAP2_C) domain.

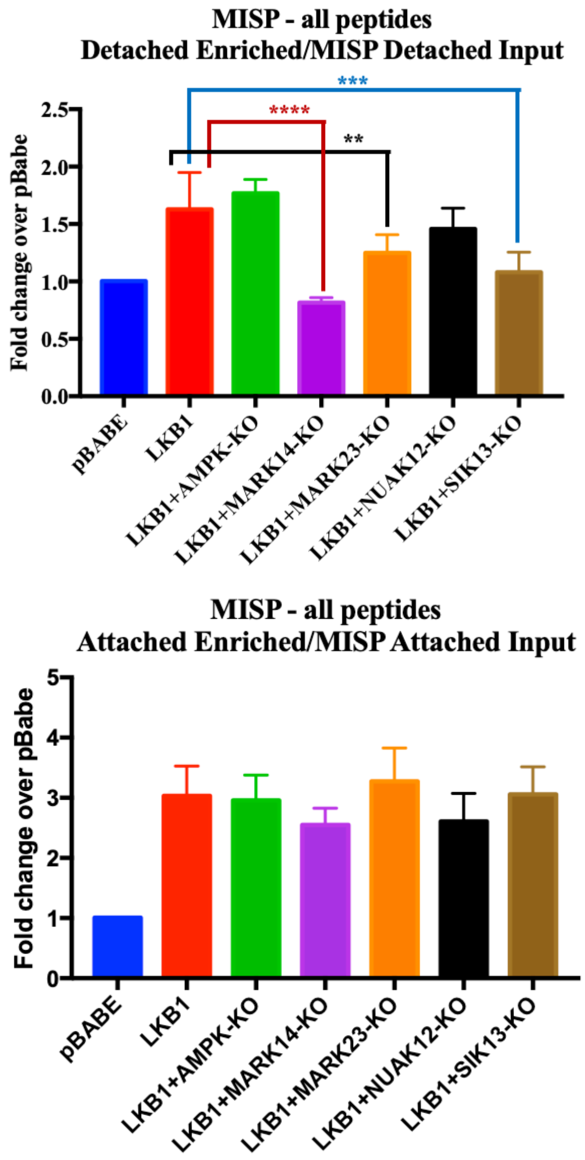

MISP - all peptides
Detached Enriched/MISP Detached Input

MISP - all peptides
Attached Enriched/MISP Attached Input

Figure 2.56. MISP undergoes a strong LKB1-dependent enrichment when immunoprecipitated with the pAMPK motif antibody.

Average MISP data from the triplicate Enriched data sets plotted for each cell line, normalized to total MTSS2 content in the corresponding Input runs. **, p < .005; ***, p< .0005; ****, p< .0001 compared to LKB1. Bar graphs plot mean ±SD. Statistical significance was determined by Two-way ANOVA.

(Top) Triplicate Detached-Enriched data sets,
(Bottom) Triplicate Attached-Enriched data

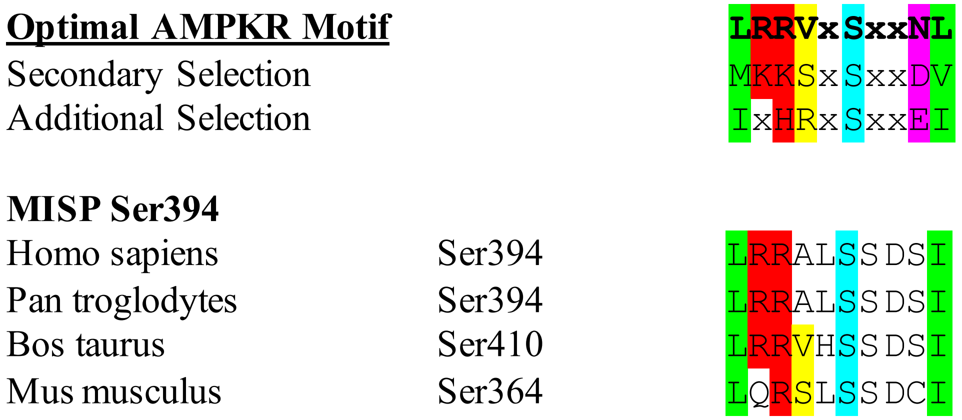

Optimal AMPKR Motif		**LRRVxSxxNL**
Secondary Selection		MKKSxSxxDV
Additional Selection		IxHRxSxxEI
MISP Ser394		
Homo sapiens	Ser394	LRRALSSDSI
Pan troglodytes	Ser394	LRRALSSDSI
Bos taurus	Ser410	LRRVHSSDSI
Mus musculus	Ser364	LQRSLSSDCI

Figure 2.57. MISP's Ser394 is conserved across mammals.

ClustalW alignment of human MISP's Ser394 across species showing conservation of the AMPKR consensus phosphorylation motif.

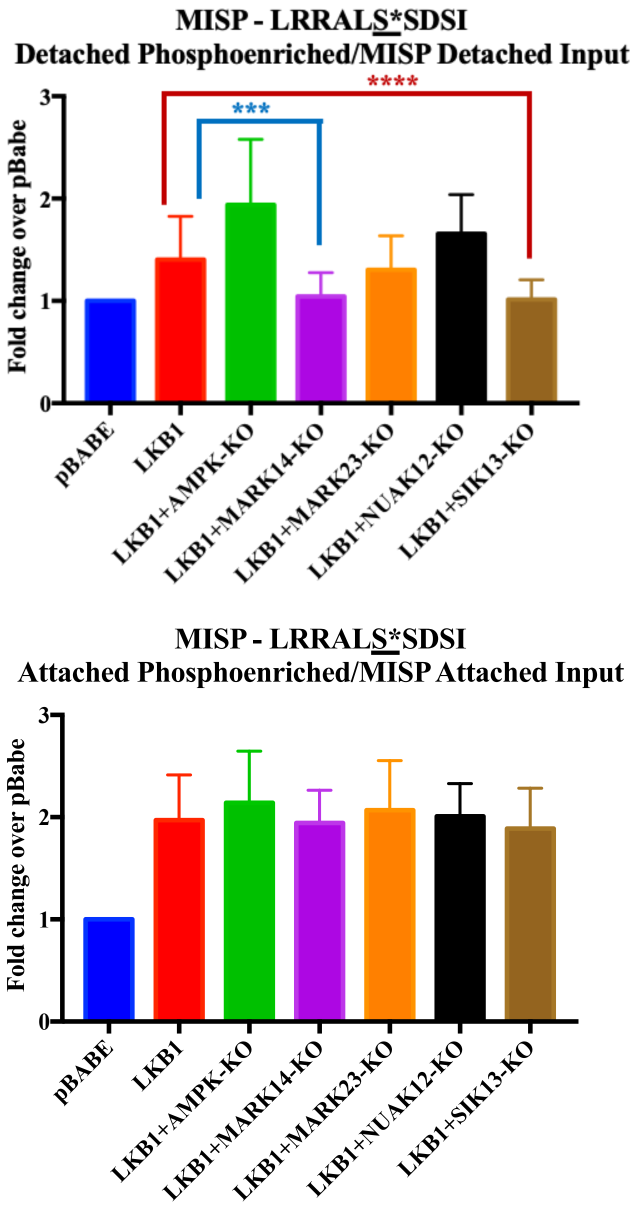

Figure 2.58. Ser394 in MISP undergoes a LKB1-dependent detachment induced increase in phosphorylation, which in inhibited in MARK1+MARK4-null and SIK1+SIK3-null A549 cells expressing wild-type LKB1

Average MISP's phospho-Ser394 data from the triplicate Phosphoenriched plotted for each cell line, normalized to MISP's s protein content in the Input data set. ***, $p < .0005$; ****, $p < .0001$ compared to LKB1. Bar graphs plot mean ±SD. Statistical significance was determined by Two-way ANOVA.

(Top) Triplicate Detached-Phosphoenriched data sets,
(Bottom) Triplicate Attached-Phosphoenriched data

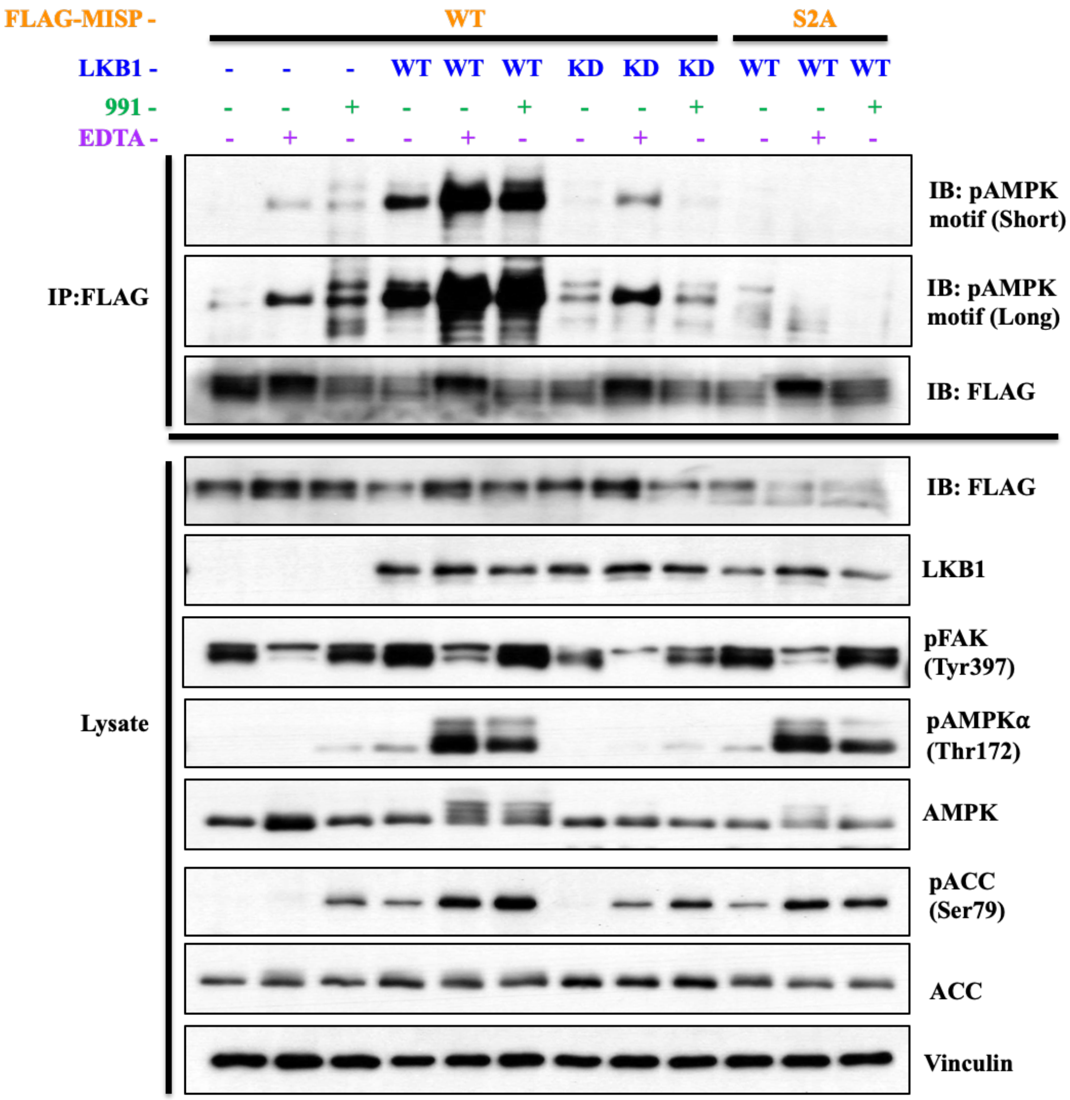

Figure 2.59. Mouse MISP undergoes LKB1-dependent detachment induced increase in phosphorylation on Ser364.

Empty vector, WT and KD A549 cells stably expressing FLAG tagged mouse MISP WT or S364-365A (S2A) were subjected to the detached assay or 991 treatment for an hour. Cell lysates were immunoblotted with the indicated antibodies.

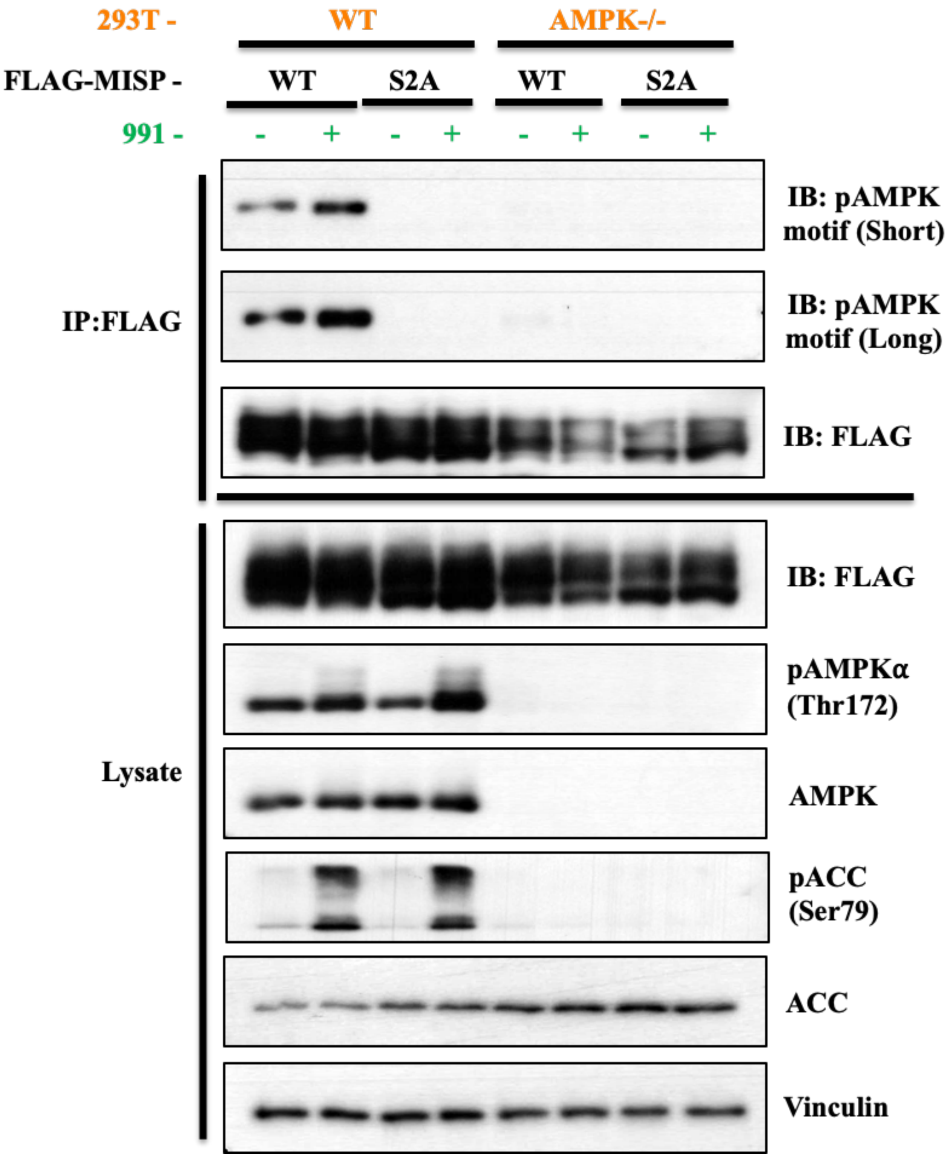

Figure 2.60. AMPK can phosphorylate mouse MISP on Ser364.

Wild-Type and AMPK-KO HEK293 cells transiently transfected with FLAG tagged mouse MISP WT or S364-365A were treated with 991 or DMSO for 1 hour. Cells were lysed and lysates were subjected to FLAG immunoprecipitation (IP). The IP and lysates were immunoblotted with the indicated antibodies.

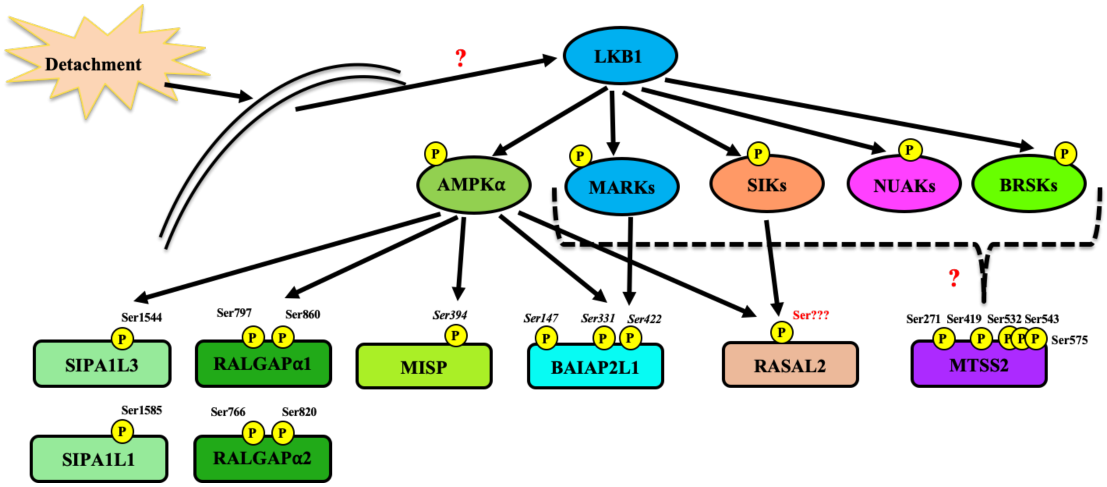

Figure 2.61. Several novel substrates of the AMPKRs discovered.

CHAPTER THREE:

AMPK governs lineage specification through Tfeb-dependent regulation of lysosomes

ABSTRACT

Faithful execution of developmental programs relies on the acquisition of unique cell identities from pluripotent progenitors, a process governed by combinatorial inputs from numerous signaling cascades that ultimately dictate lineage-specific transcriptional outputs. Despite growing evidence that metabolism is integrated with many molecular networks, how pathways that control energy homeostasis may affect cell fate decisions is largely unknown. Here, we show that AMPK, a central metabolic regulator, plays critical roles in lineage specification. Although AMPK-deficient embryonic stem cells (ESCs) were normal in the pluripotent state, these cells displayed profound defects upon differentiation, failing to generate chimeric embryos and preferentially adopting an ectodermal fate at the expense of the endoderm during embryoid body (EB) formation. AMPK-/- EBs exhibited reduced levels of Tfeb, a master transcriptional regulator of lysosomes, leading to diminished endolysosomal function. Remarkably, genetic loss of Tfeb also yielded endodermal defects, while AMPK-null ESCs over-expressing this transcription factor normalized their differential potential, revealing an intimate connection between Tfeb/lysosomes and germ layer specification. The compromised endolysosomal system resulting from AMPK or Tfeb inactivation blunted Wnt signaling, while up-regulating this pathway restored expression of endodermal markers. Collectively, these results uncover the AMPK pathway as a novel regulator of cell fate determination during differentiation.

INTRODUCTION

During embryogenesis, a series of temporal and spatially-regulated cell fate decisions must be precisely executed to ensure proper progression through the developmental program. These changes largely involve pluripotent cells, comprising the bulk of nascent embryos, transitioning to a more restricted, differentiated state. The formation of epiblast and primitive endoderm cells within blastocysts represents an early divergence in cell identity, which is then followed by further specification of the epiblast into three germ layers, the ectoderm, mesoderm, and endoderm, creating the progenitors for all of the diverse lineages found in fully developed organisms[201].

Embryonic stem cells (ESCs) are derived from a very early developmental stage prior to the onset of many of these decision points and therefore possess the capability to differentiate into a multitude of cell types[202–204]. This makes them an attractive tool to study the mechanisms underlying the acquisition of distinct cell fates. One particularly useful system that recapitulates several aspects of embryonic development consists of growing ESCs in suspension, which causes them to aggregate into clusters called embryoid bodies (EBs). Cells within EBs spontaneously differentiate, eventually forming separate lineages corresponding to all three germ layers[205]. Along with this multi-lineage specification, dramatic anatomical changes occur, transforming the dense mass of cells into hollow structures surrounded by layers of distinct cell types, highly similar to the process by which the egg cylinder arises from the blastocyst *in vivo*[206].

Many studies from both animal models and ESC systems have revealed that cell fate determination, including the formation of the different germ layers from pluripotent cells, is largely orchestrated by the spatial and temporal integration of numerous signaling cascades. Distinct levels and combinations of signals through pathways such as Wnt, Nodal/TGFβ, BMP, and FGF/MAPK direct the exit from pluripotency and govern the induction of lineage-specific transcription factors, which ultimately dictate cell type. For example, high flux through the Wnt and Nodal pathways cooperatively engages master transcriptional regulators of endoderm formation, including Sox17 and GATA4[207–209]. These factors subsequently induce more terminal differentiation makers, such as Hnf4α and albumin, to generate the specialized cells associated with this germ layer[210,211].

In the past decade there has been a newfound appreciation for the intricate connections between cellular metabolism and a wide variety of biological processes[212]. In addition to providing nutrients and raw materials, pathways regulating energy homeostasis also impinge on an array of signaling and transcription factor modules, either through direct interactions or the control of metabolite/cofactor levels[213]. As a result, energy perturbations, either naturally occurring or from environmental insults, can dramatically alter molecular networks and regulate cell proliferation, growth, and survival. Interestingly, early embryonic stages are marked by significant alterations in nutrient status and cellular metabolism, though the importance of these changes is unclear[214,215]. Furthermore, while several studies have documented large-scale metabolic reprogramming as cells transition between pluripotent and differentiated states *in vitro*, a direct role for the pathways mediating these shifts was largely unexplored[216–218].

AMP-activated protein kinase (AMPK) is a heterotrimeric complex consisting of α, β, and γ subunits that detects diminished ATP levels through direct interaction with AMP and ADP, allowing it to acutely sense energy stress[115]. Upon nucleotide binding, AMPK is directly phosphorylated by the tumor suppressor LKB1, resulting in AMPK activation and phosphorylation of a number of downstream targets, including important regulators of cell growth, metabolism, and autophagy[96,98,99,103]. This multi-faceted response comprises an important metabolic checkpoint, inhibiting energy-intensive processes while simultaneously promoting those that generate ATP[114]. AMPK is a well-established regulator of metabolic homeostasis in a wide-variety of cells and tissues in response to mitochondrial insults, metabolic hormones, and physiological stressors including exercise. However, the extent to which this pathway functions in other settings marked by metabolic reprogramming, such as during embryonic development, remains unresolved. Although previous studies briefly reported embryonic lethality as a result of combined deletion of either both α or both β subunits, no mechanistic details were provided[219,220]. In addition, whether AMPK directly impacts cellular differentiation and lineage choice is completely unknown.

Here we describe a role for the AMPK pathway in regulating cell fate. Mouse ESCs lacking both AMPK α subunits appeared normal when maintained in the pluripotent state but exhibited severe defects during differentiation, most notably an inability to contribute to chimeras *in vivo* and a marked germ layer skewing away from endoderm and towards ectoderm during EB formation. AMPK-deficient EBs displayed a dramatic reduction in lysosomal function due to diminished levels of Tfeb, a master transcriptional regulator of lysosomal genes. Genetically inactivating Tfeb also led to endodermal defects, whereas over-expressing Tfeb in AMPK-null ESCs rescued their differentiation potential, highlighting the central role of Tfeb/lysosomes in endodermal specification. Both AMPK and Tfeb mutant EBs showed attenuated canonical Wnt signaling and augmenting this pathway rescued endodermal gene expression. In summary, these results demonstrate that AMPK, through its regulation of Tfeb and the lysosomal compartment, plays an important role in cell fate determination during differentiation.

RESULTS

Dynamic AMPK signaling during ESC differentiation

We began by examining the mRNA expression pattern of the subunits that comprise the mature AMPK heterotrimeric complex during an EB differentiation time-course. Notably, at least one isoform of each subunit showed significant transcriptional up-regulation as differentiation progressed, and several of these changes were validated at the protein level (Fig. 3.1A, B). To monitor AMPK pathway activation during this process, we analyzed the phosphorylation status of several direct targets of AMPK, including ACC1, raptor, and ULK1. In order to rule out the possibility that these changes in AMPK signaling were due to limitations in nutrient availability due to media exhaustion, which can dramatically affect AMPK activity in cell culture, EBs were lysed 1-2 hours after a fresh media change in each condition. Interestingly, each substrate exhibited dynamic phosphorylation, indicative of a wave of AMPK activity that rises from relatively low levels in the pluripotent state and at day 4, peaks at around day 8, and then returns to a basal state by day 12 (Fig. 3.1B). The decrease in target phosphorylation at late time points occurred despite a steady increase in kinase subunit expression, suggesting a complex interplay between the AMPK pathway and antagonistic signaling events, such as phosphatase up-regulation, as development progresses.

During EB differentiation, aggregates of cells form dense clusters that ultimately undergo cavitation to generate distinct lineages surrounding a hollow interior[206]. We wondered if the unique pattern of AMPK activity described above was localized to particular anatomical regions of EBs. For example, prior to cavitation, cells in the interior may have limited access to nutrients, resulting in increased AMPK activity. However, phospho-ACC1 immunohistochemistry (IHC) revealed strong signal throughout densely packed EBs (Supplemental Fig 3.1A i-iii). In addition, well-differentiated EBs displayed highly variable staining across diverse structures and cell types, suggesting that AMPK signaling is not necessarily limited to specific lineages (Supplemental Fig 3.1A iv-vi). Together, these results indicate that the AMPK pathway is dynamically regulated during ESC differentiation irrespective of cell culture nutrients.

Generation and characterization of AMPKα1$^{-/-}$;AMPKα2$^{-/-}$ DKO ESCs

To begin to address if AMPK plays an important role in development, we set out to generate AMPK-deficient ESCs using the CRISPR/Cas9 system. Separate guide RNAs targeting the two genes encoding the α catalytic subunits of AMPK were introduced into the v26.2 ESC line, and we were able to isolate several independent clones that lacked expression of both AMPK α1 and α2 (Fig. 3.1C, Supplemental Fig. 3.1B, C). Treating these clones (hereafter referred to as AMPK DKO or DKO cells) with the AMP-mimetic AICAR failed to induce phosphorylation of AMPK targets, confirming that they had become functionally deficient with respect to the AMPK pathway (Fig. 3.1D). Initial characterization of AMPK DKO ESCs did not reveal any overt differences with their wild-type counterparts. The cells retained normal ESC-like morphology when passaged with and without feeders, and displayed equivalent levels of pluripotency-related alkaline phosphatase staining as well as pluripotency markers Oct4 and Nanog. (Fig. 3.1E, F, data not shown). Furthermore, cell proliferation was unaffected by AMPK deletion (Fig. 3.1G). In other contexts, AMPK-dependent phenotypes are often exacerbated when cells are placed into energy stress conditions, such as glucose-deprivation[94]. However, while lowering the glucose concentration 10-fold led to a reduction in cell division, both WT and AMPK DKO cells responded similarly (Fig. 3.1G). Finally, culturing both genotypes of cells in the absence of glucose for 2 days failed to unmask AMPK-dependent effects, as both populations displayed equivalent levels of cell death (Supplemental Fig 3.1D). Collectively, these data suggest that the AMPK pathway plays a relatively minor role in the basal ESC state or their proliferative response to glucose deprivation.

Impaired differentiation of AMPK DKO ESCs

Our results showing increased AMPK signaling during EB formation suggested a potential role for this pathway during cellular differentiation. To test this, we generated EBs from both WT and AMPK DKO ESCs, and began by looking for effects on gross morphology. Cells were grown in both high and low glucose conditions to examine how energy stress would affect AMPK-deficient cells. During the first several days, WT and DKO-derived EBs were indistinguishable from each other (data not shown). However, at mid to late stages of EB differentiation starting at day 8, regardless of glucose concentration, many WT structures had formed large internal cavities surrounded by outer layers of cells, a process that corresponds to the creation of the egg cylinder in post-implantation embryos, whereas almost all DKO EBs remained as small, dense clusters (Fig. 3.2A, data not shown). Analyzing fixed sections at both day 8 and day 12 of differentiation revealed an array of structurally diverse WT EBs, many of which contained several distinct cell morphologies, suggesting robust multi-lineage differentiation. In contrast, histological sections of DKO-derived EBs predominantly showed tightly packed structures of mostly homogenous cells at both time-points and regardless of glucose concentration (Fig. 3.2B, Supplemental Fig 3.2A, Supplemental Fig. 3.3A).

We performed mRNA-seq on developing WT and DKO EBs in order to comprehensively characterize their differentiation potential within this assay. Gene Set Enrichment Analysis (GSEA) on expression profiles from both day 8 and day 12 EBs indicated a substantial depletion of general differentiation-associated gene sets in DKO samples, as well as a strong enrichment of ESC signatures, supporting the notion that AMPK deletion retards the ability of cells to exit the pluripotent state and progress through differentiation (Fig. 3.2C, Supplemental Fig 3.2B). Indeed, Oct4 mRNA levels were elevated in DKO vs. WT EBs (Fig 3.2D). Interestingly, other signatures corresponding to the development of specific germ layers appeared uniquely up-regulated in WT or DKO samples. For example, a gene set specific to the liver, an endoderm-derived tissue, clustered in WT EBs, whereas transcripts associated with ectoderm-derived neuronal cell-types dominated among DKO-specific mRNAs (Fig 3.2C and Supplemental Fig. 3.2B). Plotting the expression of a subset of well-defined endoderm and ectoderm genes further substantiated this germ layer skewing (Fig. 3.2E). Moreover, by combining data sets from both glucose conditions, we noted even more dramatic changes, especially with regards to endoderm formation, when cells were exposed to glucose deprivation (Fig. 3.2E). These distinct lineage choices among WT and DKO cells were validated at day 8 and day 12 in subsequent rounds of EB formation using qPCR of several germ layer-specific genes (Fig. 3.2F, Supplemental Fig. 3.2C, Supplemental Fig 3.3B). To examine these lineage-specific markers at the protein level, indirect immunofluorescence analysis of EBs with antibodies against endogenous GATA4 (endoderm) and Nestin (ectoderm) was performed, revealing profound differences in their expression patterns in the WT as compared to AMPK DKO EBs (Fig. 3.2G, Supplemental Fig. 3.3C).

To confirm that these developmental abnormalities resulted from AMPK deletion and were not indirect effects of random selection during clone generation, we took two approaches. First either wild-type (WT) or kinase-dead (KD) versions of AMPK α1 cDNA were reconstituted in our DKO lines. Cells expressing WT but not KD AMPKa1 cDNA restored AMPK signaling (Supplemental Fig. 3.4A) and also partially regained the ability to up-regulate endoderm makers during EB formation, whereas effects on ectoderm markers were more variable (Supplemental Fig. 3.4B). These partial effects suggest that proper differentiation may require physiological regulation of endogenous AMPK.

In addition, we generated a distinct independent line of AMPK DKO ES cells by deriving ESCs *de novo* from intercrosses between Ubc^{CreER}; $AMPK\alpha1^{fl/fl}$;$AMPK\alpha2^{fl/fl}$ and $AMPK\alpha1^{fl/fl}$;$AMPK\alpha2^{fl/fl}$ mice (hereafter, "UAA"). UAA cells were then treated with either ethanol or 4-hydroxytamoxifen (4-OHT) prior to EB differentiation. Only CreER-positive cells incubated with 4-OHT deleted AMPKα (Supplemental Fig. 3.4C), and upon EB differentiation this resulted in the same type of germ layer skewing seen with our CRISPR-derived DKOs (Supplemental Fig. 3.4D). Together, these data strongly support that AMPK is genetically required for proper germ layer development during EB differentiation.

ESCs possess the ability to contribute to the development of most embryonic tissues when implanted into early stage blastocysts, resulting in chimeric embryos. To rigorously test the potency of AMPK DKO cells, we attempted to generate chimeras using our CRISPR lines. First, both WT and DKO cells were stably transfected with the mT/mG reporter construct[221], creating tdTomato-positive ESCs that allowed us to track their fate *in vivo*. Remarkably, while WT cells widely contributed to developing embryos, we were unable to detect any DKO cells in a majority of animals at E8.5 (Fig. 3.2H, Supplemental Fig. 3.5A). Short-term *ex vivo* culture after ESC microinjection showed that DKO cells successfully implanted into blastocysts, suggesting a defect later in the developmental process (Supplemental Fig. 3.5B). This failure of AMPK-deficient ESCs to contribute to chimeras further supports the notion that this pathway is required for proper differentiation.

Lysosomes are de-regulated in differentiating AMPK DKO cells

To search for molecular mechanisms that could explain the defective developmental potential of AMPK DKO ESCs, we mined our mRNA-seq data for additional differentially enriched gene sets apart from those relating to the distinct cell types present in late-stage EBs. Surprisingly, this analysis uncovered lysosomal genes as some of the most highly de-regulated transcripts in DKO cells, being dramatically decreased, which we validated using several markers (Fig. 3.3A, B). We also performed expression profiling on ESCs and early stages of EB differentiation (day 2 and 4) in order to identify differences that precede the acquisition of unique cell fates observed at later time points, as these changes may represent initiating events which lead to germ layer skewing as opposed to being indirect markers of cell type. Strikingly, at every stage of differentiation, a lysosomal-associated signature was significantly enriched among those genes up-regulated in WT EBs, while no such pattern was observed in the ESC state (Fig. 3.3C). In a separate analysis searching for genes regulated by energy-stress, we were surprised to find that although hundreds of transcripts had altered expression in response to differing glucose conditions in WT EBs, only a small subset required an intact AMPK pathway. Among this AMPK-dependent, glucose-sensitive gene set, the lysosome scored among the most highly enriched GO and KEGG terms, further suggesting that the AMPK pathway is required for proper function of this organelle in developing EBs (Supplemental Fig. 3.6A).

To determine if these dramatic gene expression differences translated to distinct functional outcomes, we utilized a well-established lysosomal activity assay involving DQ-BSA. Under basal conditions, this fluorogenic reagent is quenched due to the high degree of dye-labeling on protein aggregates. Once digested by intracellular proteases, many of which are present in lysosomes, individual peptides are released, leading to bright fluorescence. In both high and low glucose conditions, WT EBs produced strong signals following incubation with DQ-BSA. However, EBs derived from two separate AMPK DKO clones generated much weaker fluorescence, suggesting diminished lysosome function (Fig. 3.3D, E and Supplemental Fig. 3.6B, C). Importantly, WT but not KD AMPKα1 reconstitution in DKO cells was sufficient to boost lysosome activity (Supplemental Fig. 3.6D). Together with the gene expression analysis, these results demonstrate that AMPK is a major regulator of lysosomes during EB differentiation.

The CLEAR network and Tfeb are regulated by AMPK

Lysosomes are highly dynamic organelles, with the ability to acutely respond to a variety of stresses to mediate recycling of damaged macromolecules, nutrient replenishment, and a return to homeostasis[222,223]. Recent work has uncovered that lysosome biogenesis is predominantly controlled at the level of transcription, with most relevant genes belonging to a network (Coordinated Lysosomal Expression and Regulation-CLEAR) regulated by the MiT/TFE family of transcription factors including Tfeb, Mitf, Tfe3, and Tfec[224–227]. Within our mRNA-seq time-course, the CLEAR network was significantly down regulated in AMPK DKO cells across all stages of differentiation, starting at day 2 and progressively worsening throughout the process (Fig. 3.3F, Supplemental Fig. 3.6E). Additional analysis of these expression profiles indicated that among all the MiT/TFE members, Tfeb was the most consistently diminished in DKO cells, which we confirmed at the mRNA and protein level (Fig. 3.3G, H data not shown).

Tfeb is tightly controlled by nutrient status, with energy rich conditions leading to hyperphosphorylation and cytoplasmic retention, and low energy stores promoting hypo-phosphorylation and nuclear localization[226,228]. WT EBs displayed a mixture of hyper- and hypo-phosphorylated Tfeb species in high glucose, and lowering this energy source produced only the hypophosphorylated form. In contrast, in high glucose the DKO cells exclusively expressed the hyper-phosphorylated form, while glucose deprivation failed to produce the lower species and instead reduced overall Tfeb levels (Fig. 3.3H). This decrease in protein levels most likely results from an uncoupling of the autoregulatory loop recently described for this transcription factor[59]. As expected, alterations in Tfeb phosphorylation status led to pronounced differences in its nuclear localization, as shown by the marked reduction in nuclear Tfeb in DKO cells (Supplemental Fig 3.6F). Importantly, AMPK deletion in our UAA-derived EBs also led to the same deregulation of Tfeb phosphorylation (Supplemental Figure 3.6G), whereas re-expression of WT AMPKα1 in the CRISPR-derived DKO cells restored normal Tfeb regulation (Supplemental Figure 3.6H). Collectively, these data demonstrate significant Tfeb de-regulation upon AMPK loss in developing EBs.

We next sought to elucidate the molecular mechanism underlying this AMPK-Tfeb connection. Several signaling pathways have been implicated in controlling Tfeb phosphorylation, including MAPK, mTOR, and calcineurin[226,228–230]. Because of the well-established cross-talk between AMPK and mTOR, including AMPK-mediated phosphorylation of core mTOR components[114], we focused on this relationship first. Indeed, AMPK-deficient EBs exhibited elevated mTOR signaling, as determined by higher levels of mTOR substrates P-S6K and P-4EBP1 (Fig. 3.3I). Furthermore, a gene set comprised of transcripts up-regulated by mTOR inhibition were depleted in DKO EBs, providing additional evidence of higher flux through the mTOR pathway in these samples (Fig. 3.3J). To examine if this hyperactive signaling contributed to Tfeb de-regulation, we treated developing EBs with the mTOR inhibitor INK128. Incubating DKO EBs with INK128 completely collapsed Tfeb from the hyper- to hypo-phosphorylated state, resulting in a banding pattern similar to treated WT cells (Fig. 3.3K). Interestingly, in low glucose conditions, although acute mTOR inhibition caused this band-shift, overall Tfeb levels were much lower. This suggests additional layers of complexity with respect to Tfeb regulation, most likely including the auto-regulation mentioned above, especially when nutrients are limited. Nonetheless, these results demonstrate AMPK's inhibition of mTOR as one mechanism dictating proper Tfeb levels during EB differentiation.

Tfeb and proper lysosomal function is required for endoderm differentiation

Genetic disruption of Tfeb, as well as many lysosomal components, is known to result in embryonic lethality, although precise details regarding the underlying developmental defects are unknown[231–233]. We were intrigued by the possibility that the profound Tfeb/lysosomal abnormalities present in our AMPK DKO cells could directly affect differentiation potential. To assess the role of Tfeb in lineage specification, we first used the CRISPR/Cas9 system to generate two independent mutant ESC lines (hereafter referred to as TfebMUT) that showed loss of Tfeb mRNA and protein (Supplemental Fig. 3.7A, B; Fig.3. 4A). EBs derived from both TfebMUT lines were unable to induce several

CLEAR target genes upon nutrient deprivation (Fig. 3.4B) indicating that no other MiT/TFE family members can compensate for Tfeb-deficiency to control these targets. In addition, DQ-BSA assays revealed minimal lysosomal activity in mutant EBs compared to their WT counterparts (Fig. 3.4C). Together, these results confirmed a defective lysosomal compartment in TfebMUT cells.

To examine the developmental capabilities of Tfeb-mutant ESCs, we measured the expression of specific germ layer markers in developing EBs. Strikingly, both TfebMUT lines failed to up-regulate several endoderm markers during the differentiation process, similar to what was observed in AMPK DKO cells (Fig. 3.4D, compare to Fig. 3.2F). However, in contrast to AMPK-deficient cells, this defective endoderm formation did not coincide with an induction of ectoderm markers, which remained at WT levels, suggesting that some developmental defects in AMPK DKO cells are Tfeb-independent (Fig. 3.4E). In agreement with this notion, TfebMUT cells possessed an intermediate ability to contribute to embryonic tissues during chimera formation (Supplemental Fig. 3.7C, D). Therefore, though not as severe as AMPK deletion, Tfeb disruption in ESCs does lead to differentiation defects, most notably phenocopying an inability to properly induce the endodermal gene expression program during EB formation.

While the most established function of Tfeb relates to up-regulating lysosome-associated functions through control of the CLEAR network, it is possible that within the context of EB differentiation either newly ascribed or unknown functions of Tfeb could be responsible for its ability to regulate endoderm formation[234]. To further investigate the link between endodermal differentiation and lysosomes, we sought an independent method to disrupt this organelle. To this end, developing WT EBs were treated with bafilomycin A1 (BafA), a compound that targets vacuolar H+ ATPases and inhibits lysosomal function. Strikingly, cells treated with a chronic, low dose of BafA exhibited considerable defects in endodermal gene expression, while ectoderm markers were largely unaffected (Fig. 3.4F, G). This unique relationship between endoderm and lysosomes was further substantiated when examining the localization of Lamp2, a well-established lysosomal marker, in developing EBs. As expected, differentiated WT EBs contained an outer layer of GATA4-positive endoderm cells surrounding inner layers comprised of other cell types that border the hollow interior formed by cavitation. Remarkably, robust Lamp2 staining was observed only in the $GATA4^+$ endoderm compartment and was mostly localized to the apical side of these cells. In contrast, most DKO EBs, lacked both markers (Fig. 3.4H). These results are consistent with the model that the role of Tfeb in lysosomal maturation is critical for its ability to regulate endoderm formation, and further suggests that specification of this germ layer is especially reliant on this organelle.

Rescue of lysosomal and endodermal defects in AMPK DKO cells by Tfeb over-expression

Combining our biochemical data showing that Tfeb is downstream of AMPK, together with the fact that endoderm differentiation is highly sensitive to lysosomal function, we next wondered if correcting the defects within this cellular compartment in AMPK DKO cells would rescue their aberrant differentiation potential. In several experimental systems, over-expression of Tfeb by itself is sufficient to up-regulate a majority of the CLEAR network and significantly increase lysosomal activity in target cells[226,227]. Therefore, we set out to generate AMPK DKO ESCs stably over-producing Tfeb. Our initial efforts to create cell lines containing exogenous full-length Tfeb were unsuccessful. Based on previous experience we speculated that reducing the size of the cDNA would increase our efficiency. We deleted the first 110 amino acids on the N-terminus, leaving intact the domains responsible for DNA binding and transactivation (Fig 3.5A). Importantly, this truncated version of Tfeb ("caTfeb") was expressed and able to induce CLEAR target genes to levels higher than full length constructs when transfected into 293T cells (Supplemental Fig. 3.8A-C). This increased expression and activity is most likely due to the fact that the N-terminal region of the protein targets Tfeb to lysosomes, where it is phosphorylated and inhibited by mTOR[228]. Using this construct, we were able to generate several independent clones of AMPK DKO ESCs expressing caTfeb along with GFP-targeted cells as controls (Fig. 3.5B).

Initially, we confirmed the up-regulation of several CLEAR network members in caTfeb-expressing clones upon differentiation into EBs (Fig. 3.5C). In addition to the expected gene expression restoration, we also observed significant rescue of lysosomal activity as measured by the DQ-BSA assay (Fig. 3.5D, E). Most importantly, with respect to germ layer differentiation, caTfeb over-expression reproducibly led to elevated levels of endodermal markers, while simultaneously reducing several ectodermal genes in developing EBs, a reversal of the skewing initially documented in AMPK DKO cells (Fig. 3.5F, G). Another hallmark of differentiation, EB cavitation, was only partially restored in caTfeb clones, suggesting that either Tfeb-independent processes or proper physiological regulation of Tfeb prevented by our constitutively activated allele is required for some aspects of EB development (Supplemental Fig 3.8D). To further corroborate our results linking Tfeb over-expression and endoderm induction, additional cell lines were created expressing a full-length Tfeb cDNA referred to as TfebAA, which contained serine-to-alanine mutations at two residues whose phosphorylation was previously shown to be responsible for the mobility shifts described earlier (Supplemental Fig. 3.8A-C). Similarly to caTfeb clones, TfebAA-expressing DKO ESCs also exhibited strong induction of endodermal gene expression relative to GFP controls (Supplemental Fig. 3.8E, F). Collectively, these rescue experiments demonstrate that endodermal differentiation defects of AMPK DKO EBs result from diminished Tfeb levels and associated reductions in lysosomal activity.

Impaired canonical Wnt signaling in AMPK and Tfeb mutant cells contributes to endodermal defects

Specification of the different germ layers from multi-potent progenitors is dictated by the integration of distinct signaling pathways that in turn drive induction of lineage-restricted transcription factors. For acquisition of an endodermal fate, Wnt, Nodal (Tgfβ), and Fgf pathways are known to be particularly important[208]. To more fully characterize the molecular mechanisms underlying the altered developmental potential of AMPK-deficient ESCs, we examined if any of these signaling cascades were aberrantly regulated during EB differentiation. Initial analysis of the Fgf pathway indicated no significant changes in our mutant lines, whereas Nodal signaling dynamics were highly variable (Supplemental Fig 3.9A and data not shown). Intriguingly, GSEA of early time-point expression profiles revealed substantial enrichment of a β-catenin-associated gene set in WT samples, suggesting defects in canonical Wnt signaling in AMPK DKO cells (Fig. 3.6A). To validate these findings, we monitored the status of the Wnt pathway throughout EB differentiation by assessing levels of the inhibitory marker, phospho-β-catenin Ser33/37/41, in whole cell lysates. Developing WT EBs exhibited a progressive reduction in phospho-β-catenin, indicative of increasing Wnt activation, whereas in AMPK DKO cells this pattern was greatly attenuated (Fig. 3.6B). Importantly, we observed similar results in differentiating TfebMUT cells (Fig. 3.6B). Therefore, diminished canonical Wnt signaling is a hallmark of both AMPK and Tfeb mutant EBs.

The endolysosomal system, through its ability to recycle and/or degrade pathway components, critically controls flux through numerous signaling cascades[235]. Interestingly, recent evidence has highlighted MiT/TFE-dependent regulation of late endosomes and lysosomes as particularly important for optimal canonical Wnt signaling[224]. Indeed, treating WT EBs with BafA, the lysosomal inhibitor, significantly blunted β-catenin activation, demonstrating a connection between lysosomes and Wnt in this context (Fig. 3.6C). Furthermore, caTfeb expression partially corrected the abnormal pattern of Wnt activation present in AMPK DKO cells, suggesting that Tfeb plays a direct role in regulating this signaling pathway during EB differentiation (Supplemental Fig 3.9B).

Previous studies indicate that binding of Wnt ligands to their receptors mediates the targeting of the destruction complex (DC), a multi-protein unit containing GSK3β, the kinase responsible for phosphorylating and inhibiting β-catenin, into endolysosomal compartments known as multivesicular bodies (MVBs), allowing for newly synthesized β-catenin to enter the nucleus[46,236]. To determine if this process occurred during EB differentiation, we examined GSK3β and Lamp2 localization by indirect immunofluorescence. Notably, many cells in the outer layer of WT EBs displayed areas of punctate GSK3β, and these regions almost completely over-lapped with robust Lamp2 staining. In contrast, DKO EBs lacked this pattern of GSK3β, while Lamp2 was also much weaker and failed to show co-localization (Fig 3.6D). These results are consistent with the idea that GSK3β sequestration into Lamp2-positive structures is a part of normal EB development, and that this process is compromised in the absence of AMPK.

We speculated that the inability of AMPK DKO cells to target GSK3β into endolysosomes would lead to the inappropriate activity of the DC even in the presence of Wnt ligands, resulting in the aberrant Wnt signaling observed in mutant EBs (Fig 3.6B). Furthermore, given that key endoderm-specific transcription factors, such as Sox17, are β-catenin target genes[237], these signaling defects may be directly responsible for improper germ layer differentiation. To test these possibilities, we treated developing EBs with CHIR99021 (CHIR), a potent GSK3β inhibitor. First, we confirmed that incubation with CHIR normalized Wnt signaling, as seen by the decreased levels of phospho-β-catenin in both mutant lines (Fig. 3.6E). Strikingly, CHIR treatment restored some cavitation to AMPK DKO EBs, indicating a partial normalization of developmental processes in these mutants (Supplemental Fig 3.9C). Indeed, exposure to CHIR substantially rescued the ability of both AMPK DKO and TfebMUT cells to acquire an endodermal fate, as determined by increased mRNA levels of both Sox17 and GATA4 (Fig. 3.6F and Supplemental Fig 3.9D). Indirect immunofluorescence experiments confirmed that CHIR-treated mutant EBs displayed a pattern of GATA4 staining highly similar to that seen in WT samples (Fig 3.6G). Together, these results indicate that attenuated canonical Wnt signaling, most likely due to a down-regulated endosome/lysosomal compartment, contributes to defective endodermal lineage specification in AMPK DKO and TfebMUT ESCs.

DISCUSSION

Here we report an important role for AMPK, a central metabolic regulator, in lineage specification of pluripotent cells. Although AMPK-deficient ESCs were largely normal in the pluripotent state, profound defects were noted during EB formation, a process normally marked by differentiation into all three germ layers. Through transcriptional profiling and both loss-and-gain-of-function approaches, we identified the endolysosomal compartment as the critical component linking AMPK to these cell fate decisions. Collectively, our data lead to the following model, as depicted in Figure 3.7. Through its well-established inhibition of the mTORC1 pathway[114] AMPK counters the negative regulation of Tfeb, a master transcriptional regulator of most lysosomal genes. Optimal Tfeb activation yields a robust endolysosomal system, which in turn is required for proper signaling flux through key developmental pathways that govern germ layer differentiation. Specifically, canonical Wnt signaling, a key orchestrator of endoderm formation, depends on endolysosomal sequestration of the GSK3β-containing Destruction Complex for maximal activation of β-catenin and downstream engagement of lineage-specific transcription factors.

EB differentiation is thought to recapitulate developmental processes that occur early during embryogenesis *in vivo*. The initial determination of ectodermal and endodermal cells in EBs mirrors one of the first cell fate transitions within the inner cell mass resulting in embryonic ectoderm surrounded by primitive endoderm, whereas the cavitation of EBs is highly similar to the formation of the hollow egg cylinder shortly after implantation[238]. AMPK DKO EBs displayed dramatic defects in both of these processes, skewing towards ectoderm and away from endoderm, and also failing to reproducibly cavitate, suggesting that AMPK is required early during development. Indeed, in chimera experiments AMPK-deficient cells were undetectable in E8.5 embryos, though the extent to which this dramatic loss of development potential relates to EB phenotypes awaits further investigation. Subjecting ESCs to the complex metabolic demands during embryogenesis *in vivo* may unmask unique liabilities in cells lacking the stress-responsive AMPK pathway.

Previous studies have noted embryonic lethality following deletion of both α or β AMPK subunits, but a comprehensive phenotypic analysis is lacking. Compound mutant $AMPK\alpha1^{-/-}$; $AMPK\alpha2^{-/-}$ animals have been reported to survive until E9.5-E10.5, which is consistent with, albeit slightly later than, what we would hypothesize given our *in vivo* results with ESCs[220]. Given that our CRISPR-derived AMPK DKO cells were generated from C57Bl/6 ESCs, whereas most *in vivo* studies utilize mixed background animals, in future studies it will be important to generate pure C57Bl/6 $AMPK\alpha1^{-/-}$; $AMPK\alpha2^{-/-}$ embryos to carefully analyze all embryonic stages and compare it to the phenotypes described here.

Our model highlights the nutrient-responsive AMPK-mTOR-Tfeb axis as a critical determinant of germ layer specification, as disruptions in this pathway result in an improper balance of ectodermal vs. endodermal cells. Work from human ESCs has revealed that manipulating mTOR either positively by Rheb over-expression or negatively with rapamycin treatment leads to patterns of germ layer skewing similar to what we observe in our system, though it remains to be determined to what extent these effects may be mediated through Tfeb[239]. Notably, several members of the MiT/TFE family of transcription factors have previously been implicated in various aspects of pluripotency and differentiation. MITF is a master regulator of the melanocyte lineage, required for the specification, proliferation, and survival of these cells[240]. In contrast, TFE3 was recently identified as an important member of the core pluripotency network in mESCs, with its phosphorylation and cytoplasmic retention representing a critical event gating the exit from a stem cell state[241]. In the present study, we ascribe a dominant role for Tfeb in controlling the endodermal differentiation program. Whether these new functions relate to the embryonic lethality of *Tfeb*$^{-/-}$ animals previously reported remains to be determined[233]. Nonetheless, our results further substantiate the claim that MiT/TFE family members are critical determinants of cell fate. Given that nutrient-sensing pathways such as AMPK and mTOR have the capacity to strongly regulate these transcription factors, examining how specific family members may be uniquely controlled under distinct physiological contexts will be an important question to address in the future. This may be a mechanism through which cells couple their metabolic state to particular developmental decisions.

The coordinate regulation of endolysosomes is the most well-established role of Tfeb, but does this explain its function in germ layer differentiation? Our results showing defective endoderm formation in BafA-treated EBs, as well as the robust endoderm-specific staining of the lysosomal marker Lamp2, strongly support this notion. Within the endoderm we noted a strong polarization of Lamp2 towards the apical side of cells, a pattern highly similar to that previously observed in the visceral endoderm (VE) of developing mouse embryos[220]. Furthermore, deletion of several genes involved in endosome-lysosome traffic has been shown to dramatically impair VE formation and function early during embryogenesis[242,243]. Clearly, our data are consistent with these results from *in vivo* systems and support a model in which endoderm development critically depends on the endolysosomal compartment.

Maintaining energy homeostasis under conditions of metabolic distress is a hallmark of the AMPK pathway. Similarly, Tfeb, through its ability to up-regulate lysosomes following nutrient starvation provides important breakdown products that can fuel ATP generation and correct energy imbalances. In addition, these organelles are also integral parts of signaling cascades, effectively recycling or turning over pathway components[46]. Indeed, here we show that under basal conditions, AMPK DKO and TfebMUT EBs failed to properly activate Wnt, a master regulator of endoderm, and that simply boosting this pathway rescued germ layer specification in mutant cells. Thus, for cellular differentiation, AMPK and Tfeb appear to be most critical for the generation of a signal transduction node, the endolysosomal system, that fine-tunes signaling strength to generate appropriate transcriptional outputs.

These effects were observed in the absence of exogenous energy stress, suggesting that either normal nutrient fluctuations or unrelated inputs direct these developmental functions.

The AMPK pathway has been implicated in several disease states, including diabetes and cancer, and inducing its activity, either through compounds or lifestyle changes, represents a potential therapeutic option for a number of ailments. However, within many contexts, the relative importance of the multitude of responses controlled by this pathway remains to be determined. Our data directly linking AMPK to lysosomal biogenesis unveils a previously unknown aspect of AMPK biology that may represent a critical mediator of the ability of AMPK to promote cell survival and adapt cellular metabolism under low nutrient conditions. Furthermore, a deeper understanding of the relationship between AMPK and lysosomes may inform new treatment modalities for the variety of lysosomal inhibitors already in clinical trials[244]. How critical the fine-tuned control of Tfeb-dependent gene expression is to AMPK function in various cell fate and developmental decisions, as well as the metabolic adaptations needed to maintain homeostasis of adult stem cells will be notable areas for future investigation.

MATERIAL AND METHODS

Cell culture

All mESC lines, including the parental C57Bl/6 mESC line v26.2 (a gift from T. Jacks, MIT) and all derivatives, in addition to those derived from Ubc^{CreER}; $AMPK\alpha 1^{fl/fl}$

;AMPKα2$^{fl/fl}$ mice (UAA cells, see Supplemental Material) were passaged on gelatinized plates containing irradiated DR4 feeders in standard ES media (DMEM (Mediatech) supplemented with 15% FBS (Hyclone ES-grade), 1X MEM non-essential amino acids (Mediatech), 100 uM β-mercaptoethanol (Sigma), 100 U/mL penicillin; 100μg/mL streptomycin (Life Technologies) and 1000 U/mL ESGRO-LIF (EMD Millipore) in 5% CO_2 at 37°C. Fresh media was added daily. Prior to mRNA/protein extractions, proliferation measurements, transfection, and EB formation, mESCs were depleted of feeders for two passages and additionally supplemented with 3μM CHIR99021 (Stemgent), in order to maintain cells in a pluripotent state, as previously reported[245]. For high glucose vs. low glucose experiments, ES media was made with no glucose-DMEM (Life Technologies), adding D-(+)-glucose (Sigma) to final concentrations of 25mM (high) or 2.5mM (low). EBs were generated by typsinizing feeder-free mESC cultures and plating single cell suspensions at 5-6 x 10^4/cm^2 on low attachment tissue culture plates (Corning) in ES-media lacking ESGRO-LIF. Media was changed every other day. BafilomycinA (Sigma), CHIR99021 and INK128 (Active Biochem) were dissolved in DMSO, 4-hydroxytamoxifen (Sigma) was resuspended in ethanol, and 5-Aminoimidazole-4-carboxamide ribonucleotide (AICAR-Toronto Research Chemicals) was reconstituted in DMEM. To measure cell proliferation, 3 x 10^4 feeder-free ESCs were seeded in 6 well dishes and trypsinized, single-cell suspensions were counted using a Biorad automated cell counter. Alkaline phosphatase staining was performed using the ImmPACT Vector Red Alkaline Phosphatase Substrate Kit (Vector Libraries) according to the manufacturer's instructions.

Generation of AMPKα1$^{-/-}$;AMPKα2$^{-/-}$ DKO and TfebMUT ESCs using CRISPR

Sequences for Cas9/CRISPR-mediated gene disruption were obtained using the optimized CRISPR design tool (http://crispr.mit.edu/). Corresponding oligonucleotides from IDT were phosphorylated, annealed, and ligated into a BbsI-digested pSpCas9(BB)-2A-EGFP vector (Addgene, 48138). Sequence-verified clones were transfected into feeder-free ESC cultures using Lipofectamine 2000 (Life Technologies) using standard procedures. 24 to 48 hours later, GFP positive cells were collected by FACS and low density single cell suspensions were plated onto feeder-containing plates. Individual clones were picked and screened for disruption of the relevant genes by restriction fragment length polypmorphism of PCR fragments, followed by TOPO cloning (Life Technologies) and sequencing of PCR products. Oligonucleotide sequences are provided in Table S1.

Tfeb cell line generation

pCIP, an ESC-optimized expression vector containing a CAGGS promoter upstream of a NheI/MfeI cDNA cloning site, followed by a IRES-Puro-bpA cassette, was created using standard cloning techniques. Additional details can be provided upon request. caTfeb was generated by amplifying a fragment of human Tfeb cDNA (Addgene 44446) corresponding to the C-terminal 341 amino acids, adding a 5’ Kozak sequence and start codon. cDNA-pCIP constructs were linearized by ScaI digestion, re-purified, and introduced into feeder-free ESCs using Lipofectamine 2000. One day post-transfection, ESCs were plated onto feeders and cultured in ES media supplemented with puromycin (1-2 μg/mL). After 6-8 days individual colonies were picked and screened for expression of the relevant cDNAs by western blot. Primer sequences are listed in Table S1.

Western blotting

Cell pellets were resuspended in RIPA buffer (20 mM Tris pH 7.5, 150 mM NaCl, 1% NP-40, .5% Na deoxycholate , .1% SDS, 1 mM EDTA, 50 mM NaF, 1mM Na orthovanadate, 2.5 mM Na pyrophosphate, 2mM β-glycerophosphate) supplemented with protease inhibitor tables (Roche), followed by two 30-second rounds of sonication (65% amplitude) using a cup horn (Misonex 3000). After clarification of the lysates by centrifugation, protein concentrations were determined using the BCA assay kit (Pierce). Protein lysates were separated by SDS-PAGE and transferred to PVDF membranes, which were then incubated with the appropriate primary and secondary antibodies. Signal detection was performed with ECL (Genesee Scientific). Antibodies are listed in Table S2.

mRNA extraction and qPCR

Snap frozen ESC and EB pellets were homogenized in Qiazol (Qiagen), and the resulting aqueous phase was further purified by the RNA clean and concentrator kit (Zymo Reasearch). cDNA was synthesized from 1 µg of RNA using Superscript III (Life Technologies), and qPCR was carried out with diluted cDNA , appropriate primers, and SYBR Green PCR Master Mix (ThermoFisher Scientific). Relative mRNA levels were calculated using the $2^{-\Delta\Delta Ct}$ method, with TBP serving as the internal control. All primers are listed in Table S1.

High-throughput whole transcriptome sequencing (mRNA-Seq)

RNA was isolated by Qiazol (Qiagen) and RNA clean and concentrator kit (Zymo Research) and digested with DNAse (Qiagen). RNA integrity (RIN) numbers were determined using the Agilent TapeStation prior to library preparation. mRNA-Seq libraries were prepared using the TruSeq RNA Library Preparation Kit (v2) according to the manufacturer's instructions (Illumina). Libraries were then quantified, pooled and sequenced single-end 50 base-pair using the Illumina HiSeq 2500 platform at the Salk NGS Core. Raw sequencing data was demultiplexed and converted into FASTQ files using CASAVA (v1.8.2). Libraries were sequenced at an average depth of 15 million reads per sample.

mRNA-seq Analysis

Sequenced reads were quality tested using FASTQC and aligned to the mouse mm10 genome using the STAR aligner version 2.4.0k. Raw gene expression was quantified across all annotated exons and differential gene expression was carried out using the edgeR package v3.6.8. using duplicates to compute within-group dispersion. Differentially expressed genes were defined as having an FDR < 0.05 and a log2 fold change greater than 0.5. GO term and KEGG pathway enrichment analysis was carried out on differentially expressed genes using the HOMER analysis package[200] and the Benjamini and Yekutieli general correction for multiple testing. Alternatively, Gene Set Enrichment Analysis[246] was carried out using pre-ranked lists generated from either FDR or $\log_2$ fold-change values, setting gene set permutations to 1000 and using the c2 and c6 collections in MSigDB v5.0. Differences in natural log expression of CLEAR network genes were calculated using the R 3.1.1 language and statistical significance for differences between conditions were evaluated using a one sample t-test for non-zero mean. Clustering was performed with Gene Cluster 3.0[190] and visualized by heat maps using Java TreeView (Version 1.1.6r4)[191]. DAVID enrichment analysis was performed using the online DAVID tool. (https://david.ncifcrf.gov/)[247].

DQ-BSA lysosomal activity assay

EBs were labeled with 20 µg/ml DQ™ Green BSA (Thermo Fisher) for 1 hour in spent media at 37°C, washed twice, and then cultured for an additional 2 hours in spent media. Next, EBs were fixed for 2 hours in 4% PFA at room temperature and stored in vectashield with DAPI on chambered coverglass. Images were acquired using a Zeiss LSM 710 confocal microscope and processed with Zen 2011 SP3 software. Matlab was used to calculate the lysosomal activity as the average intensity of DQ green BSA above threshold per area of DAPI.

Histology and Immunofluorescence (IF) and Immunohistochemistry (IHC)

EB's were washed once in PBS, fixed in 4% PFA at 4 °C overnight, then embedded in pre-warmed HistoGel (Thermo Scientific, specimen processing gel). After cooling, the samples were processed and embedded in paraffin in an Excelsior ES tissue processor (Thermo Scientific). The blocks were sectioned at 5 µm on a rotary microtome (Thermo Scientific) and stained with Hematoxylin and Eosin if necessary. For IF and IHC, unstained slides underwent standard deparraffinization and rehydration, antigen retrieval in citrate buffer, followed by permeabilization in .1% Tx100 and blocking in 5% normal donkey serum (IF) or horse serum (IHC). For IF, after primary antibody incubation overnight at 4 °C, sections were stained with appropriate fluorophore-conjugated secondary antibodies (Life Technologies), washed again, DAPI stained, and mounted in ProLong Gold antifade reagent (Life Technologies). For IHC, endogenous peroxidases were quenched with H_2O_2, followed by overnight primary antibody staining and further processing with ImmPRESS and ImmPact DAB kits from Vector Labs. IF images were acquired with a Zeiss LSM700 confocal microscope and processed with Zen 2011 SP2 software while IHC images were acquired and processed with the Pannoramic MIDI slide scanner from 3DHISTECH. Primary antibody information is provided in Table S2.

Chimera generation and analysis

The Rosa26 mT-mG reporter plasmid (Addgene #17787) was linearized by KpnI digestion, purified, and introduced into feeder-free WT, AMPK DKO, and TfebMUT cells by transfection with Lipofectamine 2000. 24 hours later, ESCs were plated onto feeders and selected in neomycin (250µg/mL-Life Technologies) containing ES media for one week. TdTomato-expressing clones per line were identified by fluorescence microscopy and processed as described below.

Targeted ESCs were cultured for one passage on feeders. On the day of microinjections the cells were trypsinized and resuspended in M2 medium (Millipore). 3 weeks old C57BL/6J females were superovulated with 5 IU of PMS (Millipore), followed by injection of 5 IU of HCG (Sigma) 46h later, and mated with B6D2F1 males from Jackson Lab. Blastocyst stage embryos were collected by flashing the uterine horns of 3.5 dpc donor females with M2 medium and cultured in the pre-equilibrated drops of KSOM-AA medium (Millipore) covered with mineral oil in a 5% CO2 incubator before and after microinjections. Small and round ESCs were collected with the injection pipette and 12-15 cells were injected into each blastocyst. Injections were performed at 10°C using cooling stage. 10-12 injected embryos were surgically transferred into the uterine horns of 2.5 dpc pseudopregnant CD1 females (Charles River). Embryos were collected at E8.5 under a dissecting microscope, fixed in 4% PFA for 30 minutes at room temperature, and counterstained for 15 minutes with DAPI. Whole-mount images were acquired with a Zeiss LSM700 confocal microscope and processed with Zen 2011 SP2 software. All animal procedures were approved by the Salk Animal Care and Use Committee.

SUPPLEMENTAL MATERIAL AND METHODS

Additional cDNA cloning

To construct TfebAA, full-length Tfeb cDNA was PCR'd from a mESC cDNA library and cloned in-frame into a pENTR-Flag vector. Two serine-to-alanine mutations (S142A and S211A) were added by PCR using mutated oligonucleotides, and the resulting Flag-mTfebAA fragment was amplified for cloning into pCIP. pCIP-Tfeb constructs were tested by transient transfection into 293T cells using Lipofectamine 2000, followed by protein and mRNA analysis 48 hours later. Human AMPK α1 WT and KD (K45R) cDNAs were amplified from pre-existing plasmids. All cDNA products were digested at NheI and MfeI (or HpaI for human AMPK α1) sites added during PCR and ligated into Nhe/MfeI-cut pCIP. For AMPK α1 cloning, pCIP was digested with MfeI, blunt ended, then cut with NheI. cDNA-pCIP constructs were subsequently linearized by ScaI digestion, re-purified, and introduced into feeder-free ESCs using Lipofectamine 2000. One day post-transfection, ESCs were plated onto feeders and cultured in ES media supplemented with puromycin (1-2 µg/mL). After 6-8 days individual colonies were picked and screened for expression of the relevant cDNAs by western blot. Primer sequences are listed in Table S3.1.

De novo ESC line (UAA) generation

Blastocysts arising from intercrosses between $AMPK\alpha 1^{flox/flox}$ [1] $AMPK\alpha 2^{flox/flox}$ [2] females and $Ubc^{CreER\text{-}T2}$ [3](The Jackson Laboratory)*;* $AMPK\alpha 1^{flox/flox}$*;* $AMPK\alpha 2^{flox/flox}$ males were harvested from the uterine horns of 3.5 dpc superovulated donor females using DMEM with 10% FCS and 25 mM HEPES and placed individually into feeder coated 96 wells with ES media supplemented with CHIR99021 (3 uM) and PD0325901 (1 uM) in 5%CO2 at 37°C. After 1-2 days the embryos hatched from the zona pellucida and attached to the feeder layer. 5-7 days after plating, ICM outgrowths were removed from the surrounding trophoblast cells, mildly trypsinized and plated into fresh feeder coated 4 well plates. ES media was changed every day. Colonies appeared 3-5 days after primary ICM disaggregation, and definitive colonies were collected, dissociated and expanded to T25 cm^2 flasks. This was considered passage 1. CreER genotype was determined by PCR on gDNA harvested from feeder-free ESC cultures.

Subcellular localization studies

For nuclear vs. cytoplasmic localization analysis, cell pellets were initially resuspended in a cytoplasmic lysis buffer (20 mM Tris pH 7.5, 10 mM NaCl, 1.5 mM $MgCl_2$, 1 mM EDTA, .1% NP-40, 20% glycerol, 50 mM NaF, 1mM Na orthovanadate, 2.5 mM Na pyrophosphate, 2mM β-glycerophosphate) supplemented with protease inhibitor tablets, incubated on ice for 10 minutes, and centrifuged for 5 minutes at 500 x g at 4 °C. The supernatant, containing the cytoplasmic extract, was removed to another tube, while the pellet was processed with RIPA as outlined in Material and Methods to generate nuclear extracts. Protein lysates were separated by SDS-PAGE and transferred to PVDF membranes, which were then incubated with the appropriate primary and secondary antibodies. Signal detection was performed with ECL and film (Genesee Scientific). Antibodies are listed in Table S3.2.

Short-term culture of chimeric blastocysts

To generate GFP cells, a TdTomato-positive WT line was transfected with a Cre-expressing plasmid (Addgene 13776), followed by plating at low density to allow for clonal outgrowth and picking of GFP-positive clones. 8-cell stage embryos were flushed from the oviducts of 2.5 dpc superovulated C57BL/6J females mated with B6D2F1 males from JAX. 8-10 ES cells (either TdTomato-positive WT with GFP-WT; or TdTomato-positive DKO with GFP WT) per embryo were injected under the zona pellucida as described by Kim J., et al. 2014. Injected embryos were cultured overnight in drops of KSOM-AA medium covered with mineral oil in a 5% CO_2 incubator at 37°C. All animal procedures were approved by the Salk Animal Care and Use Committee. Images were acquired using a Zeiss LSM 710 confocal microscope and processed with Zen 2011 SP3 software.

Table S3.1: DNA Oligos

EXPERIMENT	NAME	SEQUENCE
CRISPR_sgRNA	mAMPKa1KO_1F	CACCGTTATTGTCACAGGCATATGG

Table S3.1: DNA Oligos, continued

EXPERIMENT	NAME	SEQUENCE
	mAMPKa1KO_1R	AAACCCATATGCCTGTGACAATAAC
	mAMPKa2KO_1F	CACCGACAGGCATATGGTTGTCCAT
	mAMPKa2KO_1R	AAACATGGACAACCATATGCCTGTC
	mTfebKO_1F	CACCGAGCACTGTTGCCGGCCGAGG
	mTfebKO_1R	AAACCCTCGGCCGGCAACAGTGCTC
CRISPR_screen	mA1 F4	GCCCATGAGCTCCAGAAGAA
	mA1 R4	CCTCTAAGACCCACGTGCTG
	mA2 F2	GCTGACTCCTCCAAAACATTGTGC
	mA2 R2	AGGCCAGTGTGAACTGCAATCAACC
	mTfebKO pF5	GAGGTGCTGAAGGTAAGGCC
	mTfebKO pR5.1	TGGGAAAGCACTTCTGTGAGTCTGC
cDNA_cloning	caTfeb_F	GCCATTGCTAGCACCATGGGCAACAGTGCTCCCAATAGC
	caTfeb_R	GCCAGCCAATTGTTACAGCACATCGCCCTCCTCCA
	mTfeb_cDNA_F	GGTGGAGTCGACGCTCAGCTCGCTCAGTGGT
	mTfeb_cDNA_R	GATTCGCGGCCGCTCACAGAACATCACCCTCCTCC

Table S3.1: DNA Oligos, continued

EXPERIMENT	NAME	SEQUENCE
	mTfeb_S142A_F	CCCAACGCTCCCATGGCCATGCTACATATCAGCTCC
	mTfeb_S142A_R	CATGGGAGCGTTGGGAGCACTGTTGCCGGCCGAGGTGGA
	mTfeb_S211A_F	AGCAGCGCCTGCCCTGCCGACCTGACTCAGAAGCGA
	mTfeb_S211A_R	AGGGCAGGCGCTGCTGGTGACACCCACCATGGAGGCTGT
	Flag_mTfebAA_F	GTGGAAGCTAGCGCCACCATGGATTACAAGGACGATGACG
	Flag_mTfebAA_R	GCCAGCCAATTGTCACAGAACATCACCCTCCTCC
	hAMPKa1_cDNA_F	GCCATTGCTAGCACCATGCGCAGACTCAGTTCCTG
	hAMPKa1_cDNA_R	GCCATAGTTAACTTATTGTGCAAGAATTTTAATTAGATTTGCACAC
qPCR_mRNA	Sox17 qF	ACTTGCTCCCCACAATCACT
	Sox17 qR	ACCCCGCTGTTTGTGTTTAG
	GATA4 qF	CTGTGCCAACTGCCAGACTA

Table S3.1: DNA Oligos, continued

EXPERIMENT	NAME	SEQUENCE
	GATA4 qR	GCATCTCTTCACTGCTGCTG
	Hnf4a qF	GGGAGGCAATGAAGAAATCA
	Hnf4a qR	TATGCGATGGTGGCTGTTTA
	Nestin qF	GCTGGAACAGAGATTGGAAGG
	Nestin qR	CCAGGATCTGAGCGATCTGAC
	Tubb3 qF	TGGACAGTGTTCGGTCTGG
	Tubb3 qR	CCTCCGTATAGTGCCCTTTGG
	Fgf5 qF	CTGTATGGACCCACAGGGAGTAAC
	Fgf5 qR	ATTAAGCTCCTGGGTCGCAAG
	Oct4 qF	CCAATCAGCTTGGGCTAGAG
	Oct4 qR	CCTGGGAAAGGTGTCCTGTA
	TBP qF	CCTTGTACCCTTCACCAATGAC
	TBP qR	ACAGCCAAGATTCACGGTAGA
	Tfeb qF	CGGACAGATTGACCTTCAGAG
	Tfeb qR	GCTGCTGCTGTTGCATATAAT
	Hexa qF	TGGCCCCAGTACATCCAAAC
	Hexa qR	GGTTACGGTAGCGTCGAAAGG
	Lamp1 qF	CAGCACTCTTTGAGGTGAAAAAC
	Lamp1 qR	ACGATCTGAGAACCATTCGCA
	Cd63 qF	GAAGCAGGCCATTACCCATGA
	Cd63 qR	TGACTTCACCTGGTCTCTAAACA

Table S3.1: DNA Oligos, continued

EXPERIMENT	NAME	SEQUENCE
	mRab7 qF	AGGCTTGGTGCTACAGGAAAA
	mRab7 qR	CTTGGCCCGGTCATTCTTGT
	mAMPK a1 qF	GTCAAAGCCGACCCAATGATA
	mAMPK a1 qR	CGTACACGCAAATAATAGGGGTT
	mAMPK a2 qF	CAGGCCATAAAGTGGCAGTTA
	mAMPK a2 qR	AAAAGTCTGTCGGAGTGCTGA
	mAMPK b1 qF	AGGCCCAAGATCCTCATGGA
	mAMPK b1 qR	GGGGGCTTTATCATTCGCTTC
	mAMPK b2 qF	ACCATCTCTATGCACTGTCCA
	mAMPK b2 qR	CAGCGTGGTGACATACTTCTT
	mAMPK g1 F	AATGAACACTTTCAAGAGACCCC
	mAMPK g1 R	CCAACTTGGAACTTGTGGGAAT
	mAMPK g2 qF	AAAGAACCCTAGCCTGAAGAGG
	mAMPK g2 qR	ACCTTCCGAGATGAATGCTTTT
	mAMPK g3 qF	ACCAGCTCAGAAAGAACCTGT
	mAMPK g3 qR	GTGGCCTTCGGGAATGTGG

Table S3.2: Antibodies

NAME	COMPANY	CAT. #
vinculin	Abcam	ab18058
GSK3β	BD Biosciences	610201

Table S3.2: Antibodies, continued

NAME	COMPANY	CAT. #
Tfeb (anti-mouse/human)	Bethyl Laboratories	A303-673A
4EBP1	Cell Signaling Technology	9452
ACC1	Cell Signaling Technology	3662
AMPKα	Cell Signaling Technology	2532
AMPKβ1/2	Cell Signaling Technology	4150
Akt	Cell Signaling Technology	9272
Erk1/2	Cell Signaling Technology	9102
GAPDH	Cell Signaling Technology	5174
GFP	Cell Signaling Technology	2956
HDAC3	Cell Signaling Technology	2632
Oct_4	Cell Signaling Technology	2788
P-4EBP1	Cell Signaling Technology	9451
P-ACC1 (WB)	Cell Signaling Technology	3661
P-ACC1 (IHC)	Cell Signaling Technology	11818
P-AMPKα	Cell Signaling Technology	2535
P-p70 S6K	Cell Signaling Technology	9234
P-raptor	Cell Signaling Technology	2083
P-ULK1	Cell Signaling Technology	5869
P-β-catenin	Cell Signaling Technology	9561
p70 S6K	Cell Signaling Technology	9202
PARP	Cell Signaling Technology	9542

Table S3.2: Antibodies, continued

NAME	COMPANY	CAT. #
Pathscan I (P-Erk; P-Akt)	Cell Signaling Technology	5301
raptor	Cell Signaling Technology	2280
Tfeb (anti-human only)	Cell Signaling Technology	4240
β-catenin	Cell Signaling Technology	9582
Nanog	Cosmo Bio Co.	RCAB0002PF
AMPKα1	EMD Millipore	07-350
AMPKα2	EMD Millipore	07-363
Nestin	EMD Millipore	MAB353
GATA4	Santa Cruz Biotechnology	sc-9053
ULK1	Sigma	A7481
α-tubulin	Sigma	T5168
β-actin	Sigma	A5441
Lamp2	Abcam	ab13524

ACKNOWLEDGEMENTS

This work was supported in part by R01 DK080425, R01 CA172229, P01 CA120964, and the Leona M. and Harry B. Helmsley Charitable Trust grant #2012-PG-MED002. N.P.Y. and L.J.E were supported by postdoctoral fellowships from the American Cancer Society (123016-PF-PF-12-191-01-TBE to N.P.Y. and PF-15-037-01-DMC to L.J.E.). N.P.Y. and

L.J.E. were each previously supported by a training grant (T32 CA009370) to the Salk Institute Center for Cancer Research (P30CA014195). J.V.N is a recipient of a Damon Runyon Postdoctoral Fellowship. We would like to thank Tsung-Chang Sung in the Salk Transgenic Core for help with ESC targeting and culturing, Mike Adams in the Watt Advanced Biophotonics Center for microscopy assistance, Chris Benner in the Integrative Genomics and Bioinformatics Core for bioinformatics help, and M.C. Ku and the entire staff at the H.A. and Mary K. Chapman Charitable Foundations Genomic Sequencing Core for assistance with mRNA-seq. These cores were supported by the Salk Institute (grant CCSG P30 CA014195). We would also like to thank Kim McIntyre at the UCSD Histology Core for histology assistance.

Chapter Three, in full, is a reprint of the material as it appears in: Young NP, Kamireddy A, Van Nostrand JL, Eichner LJ, Shokhirev MN, Dayn Y, Shaw RJ. (2016). AMPK governs lineage specification through Tfeb-dependent regulation of lysosomes. Genes Dev. 2016 Mar 1;30(5):535-52. doi: 10.1101/gad.274142.115. On this publication, I was the second author. Nathan P. Young was the primary author. Reuben Shaw directed and supervised the writing and oversaw the project which formed the basis for this chapter.

Figure 3.1. Dynamic AMPK signaling during EB differentiation and generation and characterization of AMPK double-knockout ESCs.

A. RT-qPCR analysis of AMPK subunits during EB differentiation. γ3 was not detected at any time point. Data are from two independent experiments. Bar graphs depict mean ± SEM. **B.** ESCs and differentiating EBs were lysed on the indicated days 1 h after a medium change and subjected to Western blotting with the antibodies listed. **C.** Western blot analysis of AMPKα1 and AMPKα2 in wild-type (WT) parental and two independent AMPK double-knockout (DKO) CRISPR clones. **D.** Immunoblot on lysates from wild-type and AMPK double knockout ESCs following vehicle or 1 h of 5-aminoimidazole-4-carboxamide ribonucleotide (AICAR) treatment (0.5 mM). **E.** Levels of pluripotency markers Oct4 and Nanog in wild-type and AMPK double-knockout ESCs as determined by Western blot. **F.** Bright-field images of wild-type and two AMPK double-knockout ESC lines grown on feeders indicating normal ESC-like morphology (panel i) and equivalent amounts of alkaline phosphatase activity between the different genotypes (panel ii). Bar, 100 μm. **G.** Proliferation curves of wildtype and AMPK double-knockout ESCs grown in the absence of feeders in both high glucose (HG; 25 mM) and low glucose (LG; 2.5 mM). n = 2 samples per condition.

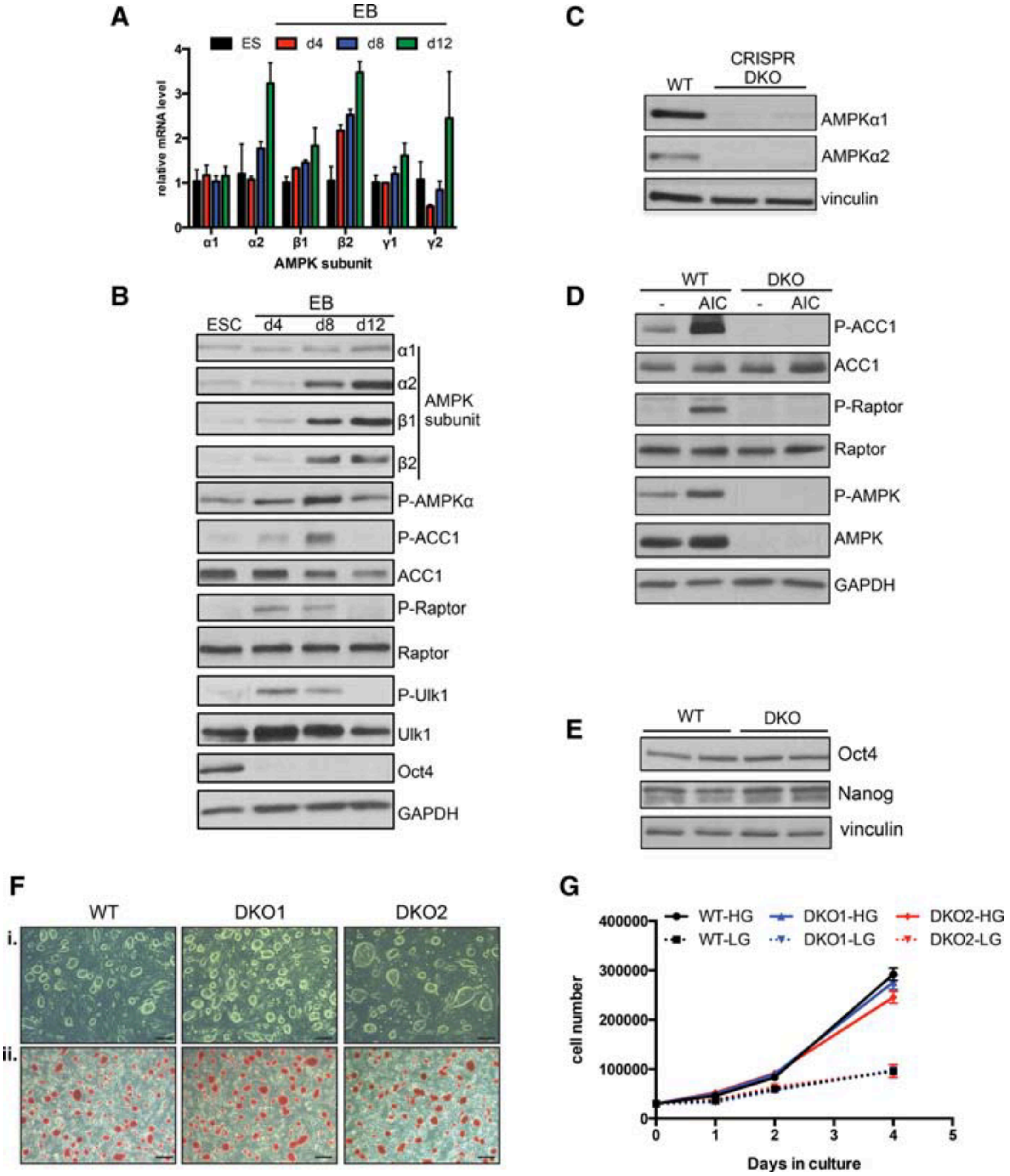
A
EB
ES
d4
d8
d12
relative mRNA level
0
1
2
3
4
α1
α2
β1
β2
γ1
γ2
AMPK subunit
B
EB
ESC
d4
d8
d12
α1
α2
β1
β2
AMPK subunit
P-AMPKα
P-ACC1
ACC1
P-Raptor
Raptor
P-Ulk1
Ulk1
Oct4
GAPDH
C
WT
CRISPR DKO
AMPKα1
AMPKα2
vinculin
D
WT
DKO
-
AIC
-
AIC
P-ACC1
ACC1
P-Raptor
Raptor
P-AMPK
AMPK
GAPDH
E
WT
DKO
Oct4
Nanog
vinculin
F
WT
DKO1
DKO2
i.
ii.
G
WT-HG
DKO1-HG
DKO2-HG
WT-LG
DKO1-LG
DKO2-LG
cell number
0
100000
200000
300000
400000
Days in culture
0
1
2
3
4
5

Supplemental Figure 3.1: Dynamic AMPK signaling during EB differentiation and AMPK DKO ESC generation and characterization.

A. Representative images of immunohistochemistry (IHC) analysis of P-ACC1 (brown staining) in day 8 (**i-iii.**) and day 12 (**iv-vi.**) EBs. **B** and **C.** Schematic showing the relevant genomic regions and nucleotide sequences around Cas9-target sites for AMPKα1 (**B**) and AMPKα2 (**C**). PAM sequences are shown in magenta, while locus-specific sgRNA sequences are depicted in green (**B**) or orange (**C**). **D.** Immunoblot analysis of WT and DKO ESCs during a time-course of complete glucose withdrawl (-Glc). P-ACC1 serves as marker of AMPK activation, and levels of cleaved PARP indicates the relative amount of cell death.

Young_274142_SFig1

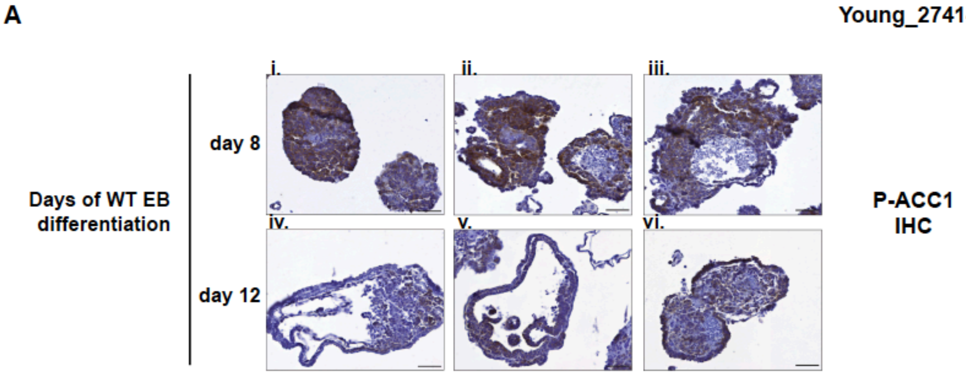

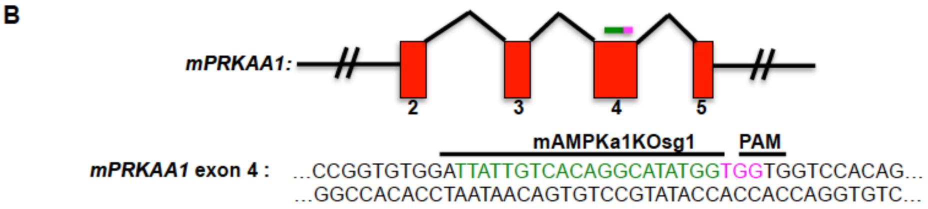

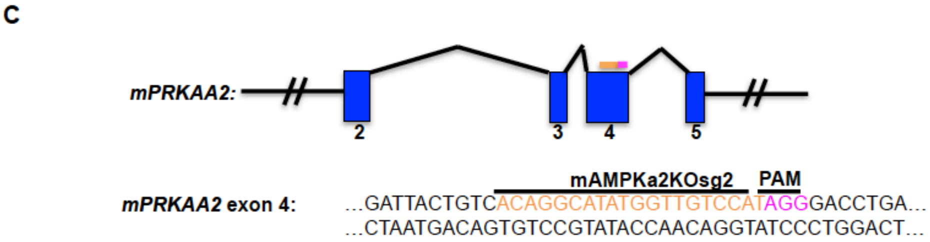

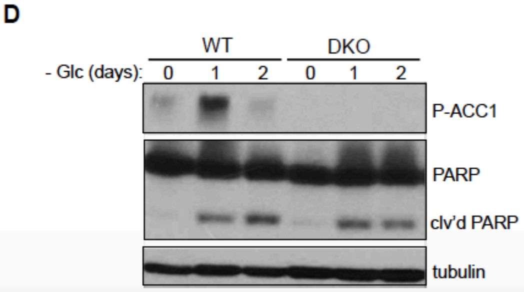

Figure 3.2: Differentiation defects of AMPK DKO ESCs.

A. Brightfield images of representative WT and AMPK DKO EBs differentiated for 12 days in high glucose conditions. Scale bar, 100 μm. **B.** Hematoxylin and Eosin (H&E)-stained sections of WT and AMPK DKO day 12 EBs in high glucose. Images on the right correspond to boxed-in sections from the left. Scale bar, 50 μm. **C.** GSEA plots from mRNA-Seq profiles of WT and AMPK DKO EBs differentiated for 12 days in high glucose. i. Top two plots correspond to general differentiation defects of AMPK DKO cells. ii. Lower plots highlight endoderm (liver) vs. ectoderm (neuronal) germ layer skewing in WT vs. DKO EBs, respectively. NES = normalized enrichment score; FDR = false discovery rate. **D.** Elevated levels of Oct4 mRNA in day 12 AMPK DKO EBs compared to WT, as determined by RT-qPCR. ***, p< .005; *, p <.05 compared to WT. Relative abundance of Oct4 was normalized to WT ESC levels. **E.** Heat map depicting relative mRNA expression of several endoderm and ectoderm markers in WT and DKO EBs at day 8 (d8) and day 12 (d12) of differentiation in high and low glucose. Values were calculated from mRNAseq data. **F.** RT-qPCR analysis of selected endoderm (top) and ectoderm (bottom) markers in high glucose day 12 EBs derived from either WT or AMPK DKO cells confirming germ layer skewing between different genotypes. Data are from 3 independent experiments. Average ± SEM is plotted. *, p< .05; #, p <.005 compared to WT. **G.** Immunofluorescence (IF) on fixed sections of WT and AMPK DKO samples after 12 days of EB differentiation in high glucose. GATA4 and Nestin serve as endoderm and ectoderm markers, respectively. Scale bar, 50 μm **H.** Representative whole-mount fluorescence images of E8.5 embryos that had been injected with tdTomato-positive WT or AMPK DKO ESCs *ex vivo* at E2.5 prior to blastocyst implantation into recipient mothers. DAPI staining was performed to outline the embryo. Scale bar, 200 μm. Statistical significance was determined by Student's t-test.

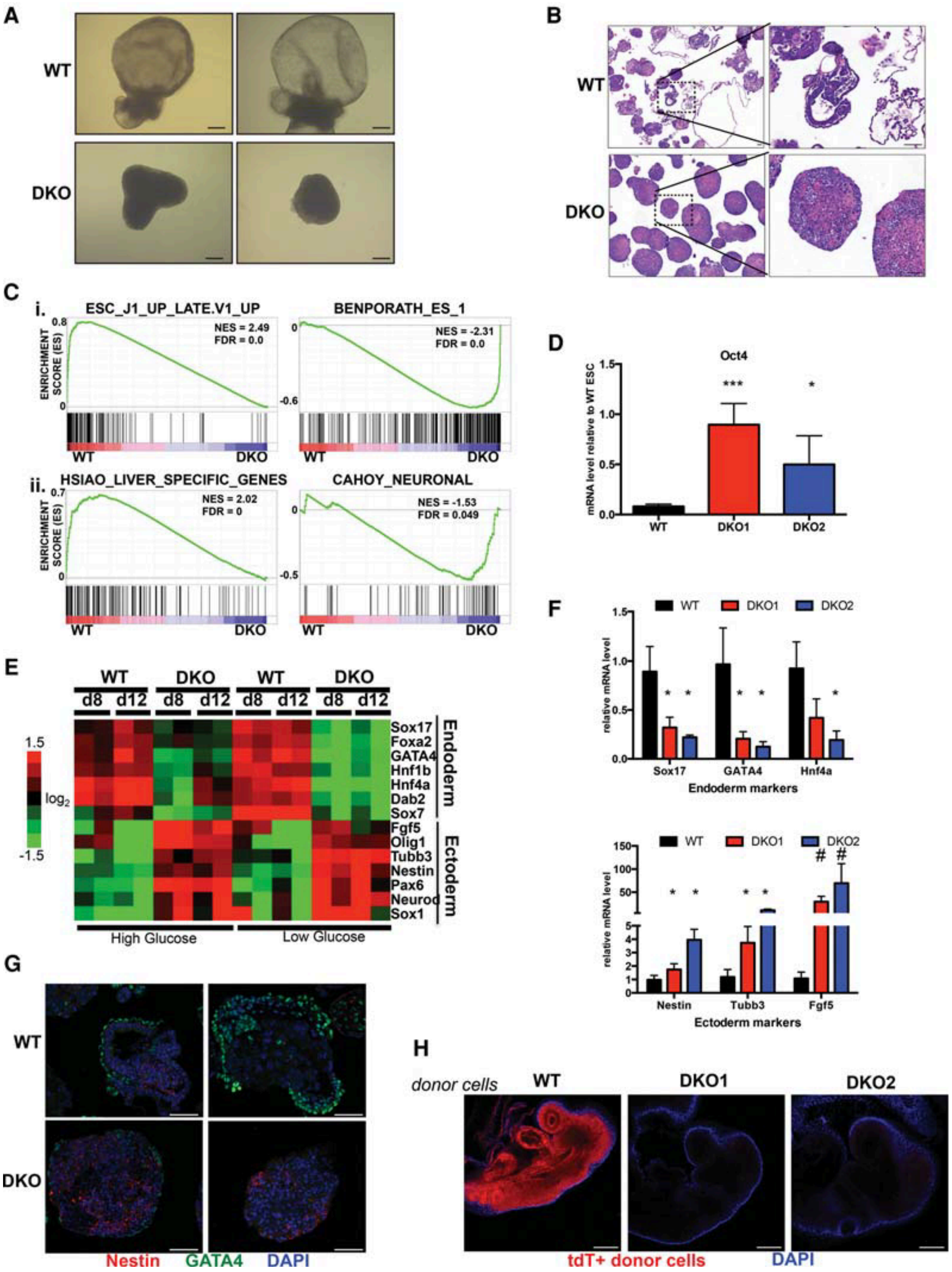
A
WT
DKO
B
WT
DKO
C
i.
ESC_J1_UP_LATE.V1_UP
NES = 2.49
FDR = 0.0
ENRICHMENT SCORE (ES)
0.8
0
WT
DKO
BENPORATH_ES_1
NES = -2.31
FDR = 0.0
0
-0.6
WT
DKO
ii.
HSIAO_LIVER_SPECIFIC_GENES
NES = 2.02
FDR = 0
ENRICHMENT SCORE (ES)
0.7
0
WT
DKO
CAHOY_NEURONAL
NES = -1.53
FDR = 0.049
0
-0.5
WT
DKO
D
Oct4
mRNA level relative to WT ESC
1.5
1.0
0.5
0.0
***
*
WT
DKO1
DKO2
E
WT
DKO
WT
DKO
d8
d12
d8
d12
d8
d12
d8
d12
1.5
log2
-1.5
Sox17
Foxa2
GATA4
Hnf1b
Hnf4a
Dab2
Sox7
Fgf5
Olig1
Tubb3
Nestin
Pax6
Neurod
Sox1
Endoderm
Ectoderm
High Glucose
Low Glucose
F
WT
DKO1
DKO2
relative mRNA level
1.5
1.0
0.5
0.0
Sox17
GATA4
Hnf4a
Endoderm markers
WT
DKO1
DKO2
relative mRNA level
150
100
50
5
4
3
2
1
0
#
#
Nestin
Tubb3
Fgf5
Ectoderm markers
G
WT
DKO
Nestin
GATA4
DAPI
H
donor cells
WT
DKO1
DKO2
tdT+ donor cells
DAPI

Supplemental Figure 3.2: Differentiation defects of AMPK DKO ESCs are apparent at day 8 of EB formation.

A. H&E-stained sections of WT and AMPK DKO day 8 EBs in high glucose. Images on the right correspond to boxed-in sections from the left. Scale bar, 50 μm. **B.** GSEA plots from mRNA-Seq profiles of WT and AMPK DKO EBs differentiated for 8 days in high glucose. **i.** Top two plots correspond to general differentiation defects of AMPK DKO cells. **ii.** Lower plots highlight endoderm vs. ectoderm germ layer skewing in WT vs. DKO EBs, respectively. **C.** RT-qPCR analysis of selected endoderm (top) and ectoderm (bottom) markers in high glucose day 8 EBs derived from either WT or AMPK DKO cells confirming germ layer skewing between different genotypes. Data are from 3 independent experiments. Average ± SEM is plotted. *, $p < .05$; #, $p < .005$ compared to WT. Statistical significance was determined by Student's t-test.

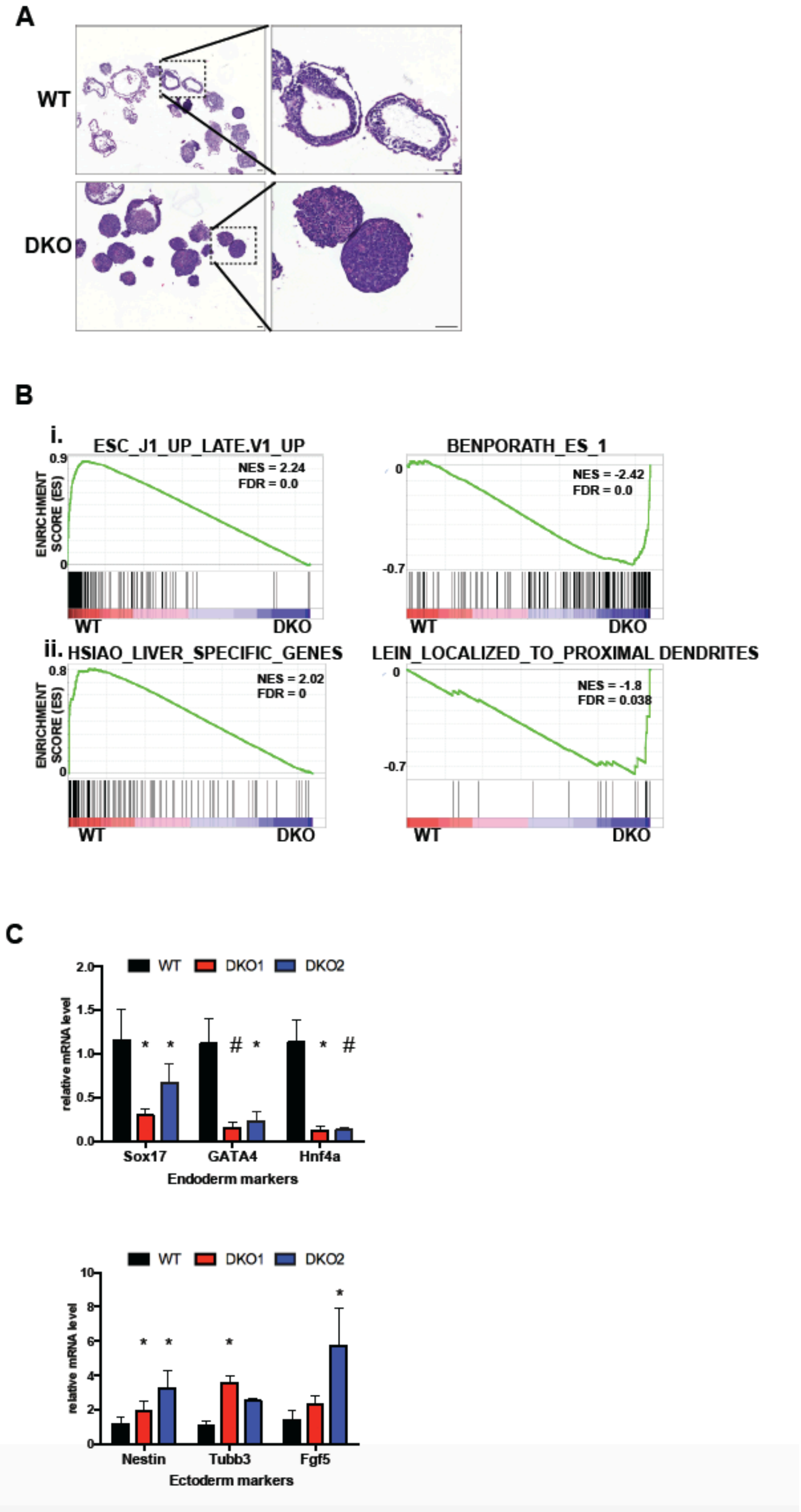
A
WT
DKO
B
i.
ESC_J1_UP_LATE.V1_UP
0.9
ENRICHMENT SCORE (ES)
0
NES = 2.24
FDR = 0.0
WT
DKO
BENPORATH_ES_1
0
-0.7
NES = -2.42
FDR = 0.0
WT
DKO
ii.
HSIAO_LIVER_SPECIFIC_GENES
0.8
ENRICHMENT SCORE (ES)
0
NES = 2.02
FDR = 0
WT
DKO
LEIN_LOCALIZED_TO_PROXIMAL DENDRITES
0
-0.7
NES = -1.8
FDR = 0.038
WT
DKO
C
WT
DKO1
DKO2
relative mRNA level
2.0
1.5
1.0
0.5
0.0
*
#
Sox17
GATA4
Hnf4a
Endoderm markers
WT
DKO1
DKO2
relative mRNA level
10
8
6
4
2
0
*
Nestin
Tubb3
Fgf5
Ectoderm markers

Supplemental Figure 3.3: AMPK DKO cells display differentiation defects in low glucose.

A. H&E-stained sections of WT and AMPK DKO day 12 EBs in low glucose. Images on the right correspond to boxed-in sections from the left. Scale bar, 50 μm. **B.** RT-qPCR analysis of selected endoderm (top) and ectoderm (bottom) markers in day 12 EBs derived from either WT or AMPK DKO cells grown in low glucose. Data are from 3 independent experiments. Average ± SEM is plotted. *, $p < .05$; #, $p < .005$ compared to WT. Bar graphs show mean ±SEM. Statistical significance was determined by Student's t-test. **C.** IF of GATA4 (endoderm marker) and Nestin (ectoderm marker) in WT and AMPK DKO EBs after differentiation for 12 days in low glucose. Scale bar, 50 μm.

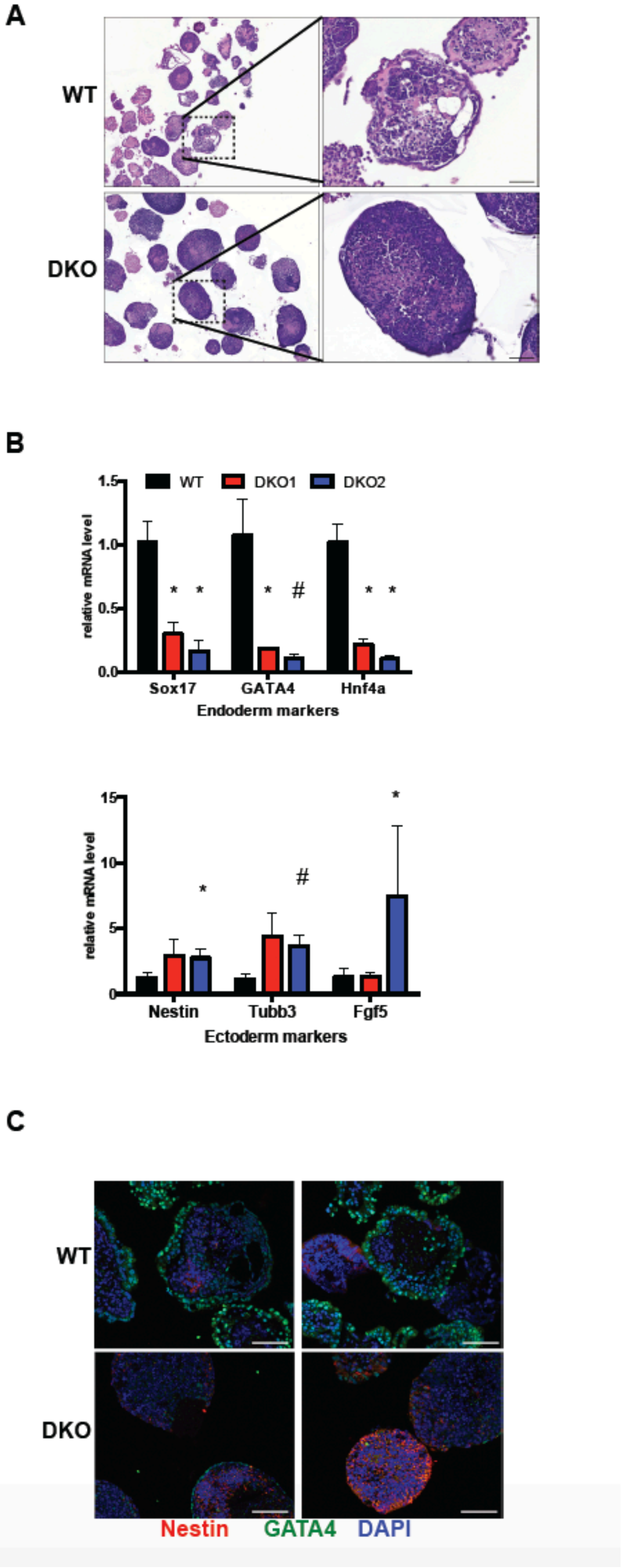
A
WT
DKO
B
WT
DKO1
DKO2
1.5
1.0
0.5
0.0
relative mRNA level
*
*
*
#
*
*
Sox17
GATA4
Hnf4a
Endoderm markers
15
10
5
0
relative mRNA level
*
#
*
Nestin
Tubb3
Fgf5
Ectoderm markers
C
WT
DKO
Nestin
GATA4
DAPI

Supplemental Figure 3.4: Confirming direct connection between AMPK status and impaired EB differentiation using gain- and loss-of-function approaches.

A. Immunoblots comparing AMPK signaling in WT ESCs, parental AMPK DKO ESCs, or a DKO line stably transfected with WT or kinase dead (KD-K45R) AMPKα1 cDNA. Re-expression of WT AMPKα1 rescues AMPK signaling, as determined by elevated levels of P-raptor (arrow). ns, non-specific signal **B.** RT-qPCR analysis of endoderm (top) and ectoderm (bottom) markers in day 7 EBs derived from either WT parental cells or AMPK DKO ESCs expressing either WT or KD AMPKα1 cDNA. Data are from two independent experiments with polyclonal pools of stable transfectants, each compared to WT parental cells. *, p < .05; ***, p < .0005. **C.** A $Ubc^{CreER\text{-}T2}$-negative and $Ubc^{CreER\text{-}T2}$-positive (both $AMPK\alpha 1^{fl/fl}$; $AMPK\alpha 2^{fl/fl}$) ESC line were either treated with vehicle (ethanol) or 4-hydroxytamoxifen (4-OHT; 500 nM) for three consecutive days before harvesting cell lysates and immunoblotting with the indicated antibodies. Only CreER-positive, 4-OHT-treated cells ablate AMPK signaling. **D.** ESCs were treated as in **C**, followed by 7 days of EB differentiation in the absence of any additional treatment. Samples were then processed for RT-qPCR of selective endoderm and ectoderm markers. Data are from 4 independent experiments. *, p < .05; **, p <.005 compared to CreER-negative, 4-OHT-treated. Bar graphs plot mean ±SEM. Statistical significance was determined by Student's t-test.

Young_274142_SFig4

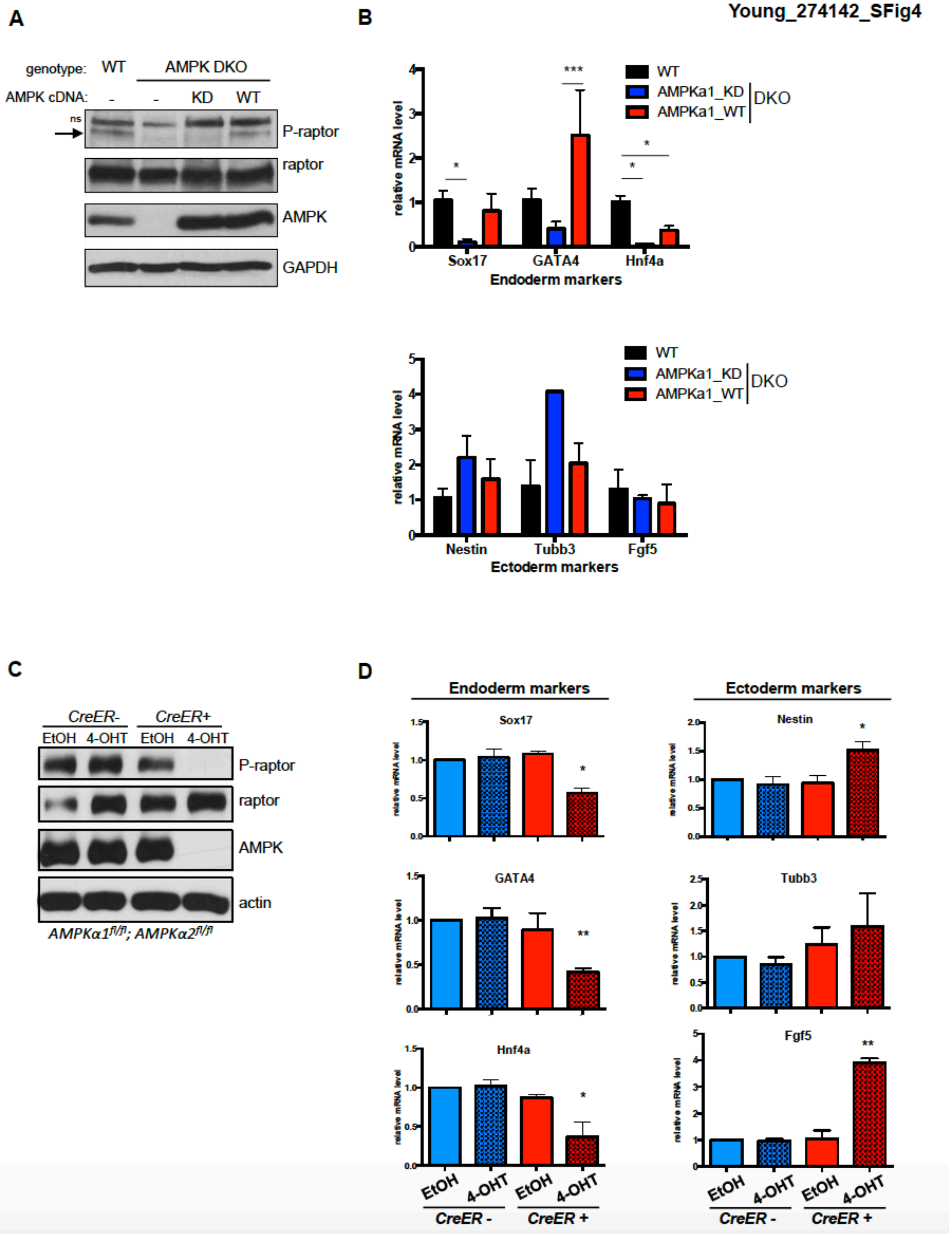

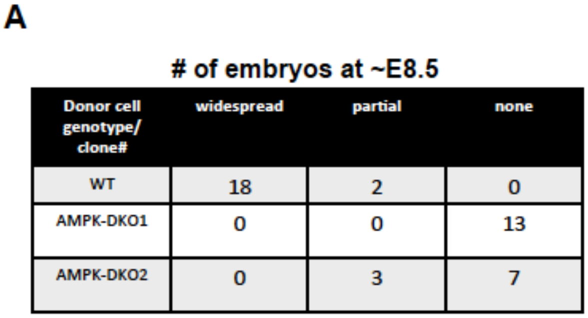

A

# of embryos at ~E8.5

Donor cell genotype/ clone#	widespread	partial	none
WT	18	2	0
AMPK-DKO1	0	0	13
AMPK-DKO2	0	3	7

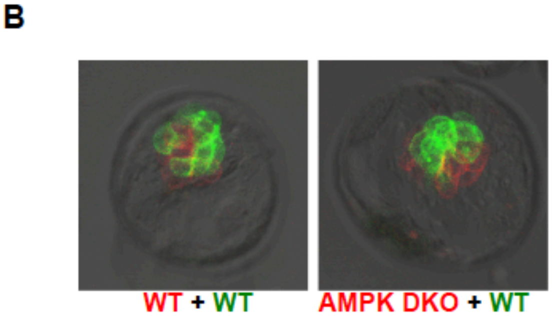

Supplemental Figure 3.5: Additional chimera analysis of AMPK DKO ESCs.
A. Table summarizing extent of chimera contribution of WT, AMPK DKO1, and AMPK DKO2 tdTomato-positive cells at E8.5. **B.** Representative whole mount images of chimeric blastocysts 24 hours after donor cell injection indicate that both WT and AMPK DKO ESCs successfully implant into the embryo. GFP-expressing WT ESCs were injected along with an equal number of tdTomato-positive WT (left) or AMPK DKO (right) ESCs. Blastocysts were maintained *ex vivo* for 24 hours before analysis.

Figure 3.3: AMPK DKO EBs exhibit defects in lysosome function and Tfeb regulation. **A.** GSEA plot showing enrichment of the gene set associated with the KEGG term "Lysosome" in WT vs. AMPK DKO day 12 EBs in high glucose. **B.** Relative mRNA levels of selected lysosomal genes in WT and AMPK DKO day 12 EBs in high glucose as assessed by qRT-PCR. n = 3 independent experiments. *, p< .05; #, p <.005 compared to WT. **C.** Plot of corrected log-transformed p-values of KEGG lysosome pathway enrichment in sets of genes identified to be up-regulated in WT vs DKO under high glucose conditions. At each time-point (x-axis), the statistical significance of enrichment of genes associated with the KEGG term "Lysosome" in WT vs. AMPK DKO samples was determined as described in Materials and Methods. The resulting p-values were log-transformed and plotted on the y-axis. Numbers in parentheses indicate number of lysosomal genes significantly up-regulated in WT samples at each time-point. **D.** Direct fluorescence images of day 12 WT and AMPK DKO EBs after 1 hr incubation with DQ-BSA-Green, followed by a 2-hour chase prior to fixation. Scale bar, 100 μm. **E.** Relative lysosomal activity, as determined by DQ-BSA assay, in day 12 WT and AMPK DKO EBs in high glucose. Results are from 2 independent experiments, with at least 10 EBs analyzed for each sample within an experiment. ****, p <.0001 compared to WT. **F.** Box and whisker plot of mRNA expression differences across 81 CLEAR network genes in AMPK DKO vs. WT samples at indicated time points. High glucose conditions only. See Materials and Methods for details. ##, $p < 10^{-8}$, one sample t-test for non-zero mean. **G.** RT-qPCR analysis of Tfeb in day 8 WT and AMPK DKO EBs in high glucose. Three independent experiments were performed. *, p < .05; ***, p< .0005 compared to WT. **H.** Immunoblot analysis of Tfeb in WT and AMPK DKO EBs differentiated in either high (HG) or low (LG) glucose for 8 days. **I.** Time-course analysis of selected mTOR signaling components during high glucose EB differentiation of WT and DKO ESCs. Lysates were immunoblotted with the indicated antibodies. **J.** GSEA plot depicting enrichment of a "mTOR inhibition" gene set (derived from everolimus-treated vs. untreated mouse tissues) in WT vs. DKO EBs at day 12. **K.** Western blot analysis of day 6 WT and AMPK DKO EBs. After overnight incubation in the indicated glucose media, EBs were treated with either vehicle (DMSO) or INK128 (500 nM) for 2 hours prior to lysate preparation and blotting with indicated antibodies. For standard bar graphs, average ± SEM is plotted. Statistical significance was determined by Student's t-test unless otherwise noted.

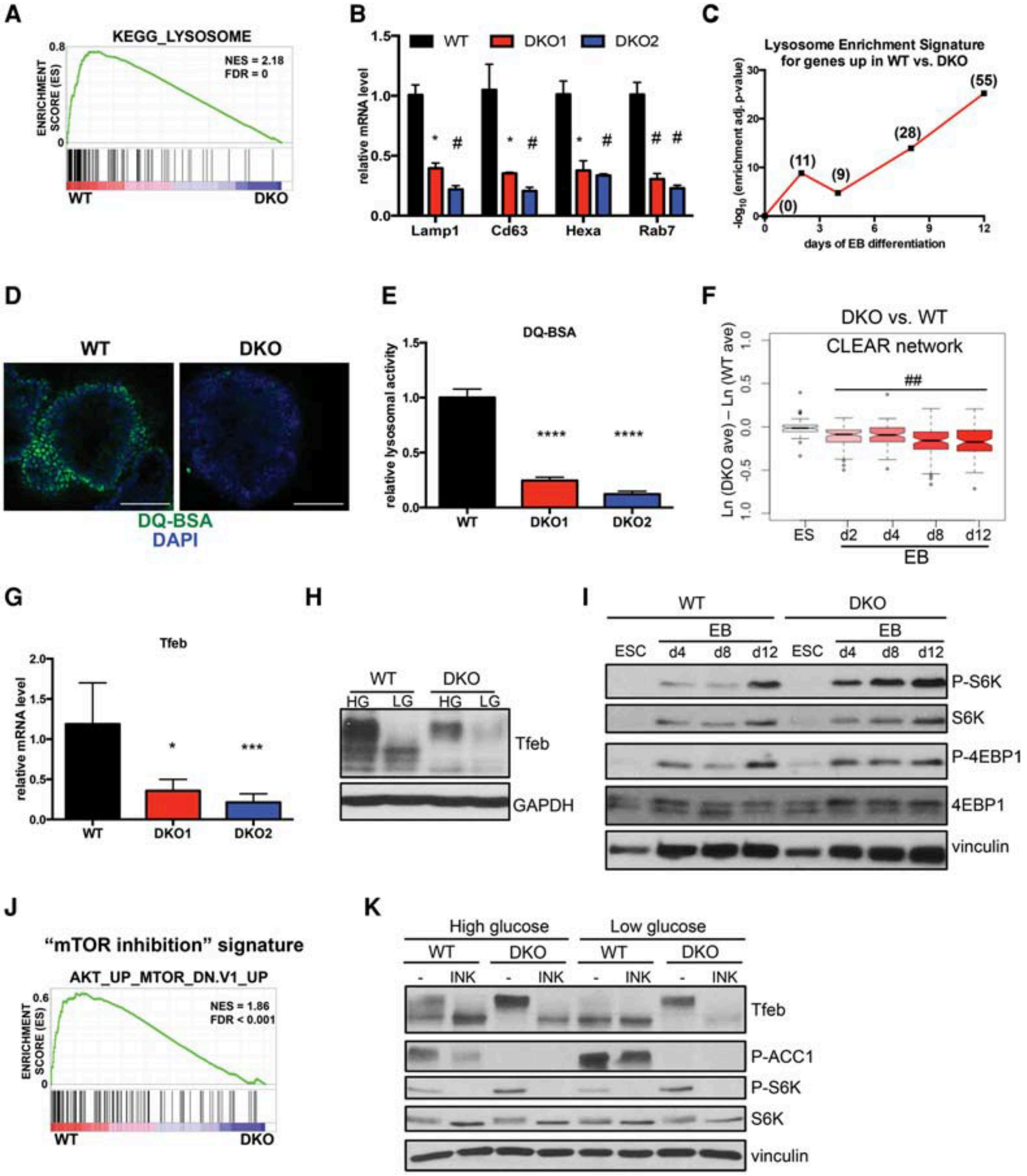
A
KEGG_LYSOSOME
ENRICHMENT SCORE (ES)
0.8
0
NES = 2.18
FDR = 0
WT
DKO
B
relative mRNA level
1.5
1.0
0.5
0.0
WT
DKO1
DKO2
*
#
Lamp1
Cd63
Hexa
Rab7
C
Lysosome Enrichment Signature for genes up in WT vs. DKO
-log10 (enrichment adj. p-value)
30
20
10
0
(0)
(11)
(9)
(28)
(55)
0
3
6
9
12
days of EB differentiation
D
WT
DKO
DQ-BSA
DAPI
E
DQ-BSA
relative lysosomal activity
1.5
1.0
0.5
0.0
****
****
WT
DKO1
DKO2
F
DKO vs. WT
CLEAR network
Ln (DKO ave) – Ln (WT ave)
1.0
0.5
0.0
-0.5
1.0
##
ES
d2
d4
d8
d12
EB
G
Tfeb
relative mRNA level
2.0
1.5
1.0
0.5
0.0
*
***
WT
DKO1
DKO2
H
WT
DKO
HG
LG
HG
LG
Tfeb
GAPDH
I
WT
DKO
EB
EB
ESC
d4
d8
d12
ESC
d4
d8
d12
P-S6K
S6K
P-4EBP1
4EBP1
vinculin
J
"mTOR inhibition" signature
AKT_UP_MTOR_DN.V1_UP
ENRICHMENT SCORE (ES)
0.6
0
NES = 1.86
FDR < 0.001
WT
DKO
K
High glucose
Low glucose
WT
DKO
WT
DKO
-
INK
-
INK
-
INK
-
INK
Tfeb
P-ACC1
P-S6K
S6K
vinculin

Supplemental Figure 3.6: Additional evidence of lysosomal and Tfeb de-regulation in differentiated AMPK DKO cells.

A. Heat map depicting expression profiles of WT and AMPK DKO EBs at day 4 of differentiation. Differentially expressed genes between WT EBs in high (HG) and low (LG) glucose were used to cluster all samples. Genes in the resulting profile were classified into three groups (A, B, C), with group B comprising those genes that are up-regulated in LG in an AMPK-dependent manner. DAVID enrichment analysis of these genes revealed a strong enrichment of lysosome-associated mRNAs in this cluster, as shown in the table at the right, which depicts the top three results from the analysis. **B.** Direct fluorescence images of day 12, low glucose WT and AMPK DKO EBs after incubation with DQ-BSA-Green, followed by a 2-hour chase prior to fixation. **C.** Relative lysosomal activity, as determined by DQ-BSA assay, in day 12 WT and AMPK DKO EBs in low glucose. See Materials and Methods for details. ****, $p < .0001$ compared to WT. **D.** Lysosomal activity was measured by DQ-BSA in AMPK DKO EBs reconstituted with KD or WT AMPKα1. ****, $p < .0001$. In **C** and **D**, results are from 2 independent experiments, with at least 10 EBs analyzed for each sample within an experiment. **E.** Box and whisker plot of mRNA expression differences across 81 CLEAR network genes in AMPK DKO vs. WT samples in low glucose. See Materials and Methods for details. ##, $p < 10^{-8}$, one sample t-test for non-zero mean. **F.** WT and DKO EBs were grown in indicated glucose conditions for 6 days prior to cytoplasmic (C) and nuclear (N) lysate preparation and immunoblotting with indicated antibodies. ACC1 and HDAC3 serve as cytoplasmic and nuclear loading controls, respectively. In bottom panel, arrow indicates band corresponding to HDAC3. ns, non-specific. **G.** Western blot analysis of Tfeb in day 7 EBs derived from UAA cells. See Supplemental Fig 3D for EB differentiation protocol. **H.** AMPK DKO ESCs were reconstituted with indicated cDNA, differentiated into EBs for 7 days in high (HG) or low (LG) glucose, and lysates were immunoblotted with the indicated antibodies. For standard bar graphs, average ± SEM is plotted. Statistical significance was determined by Student's t-test unless otherwise stated.

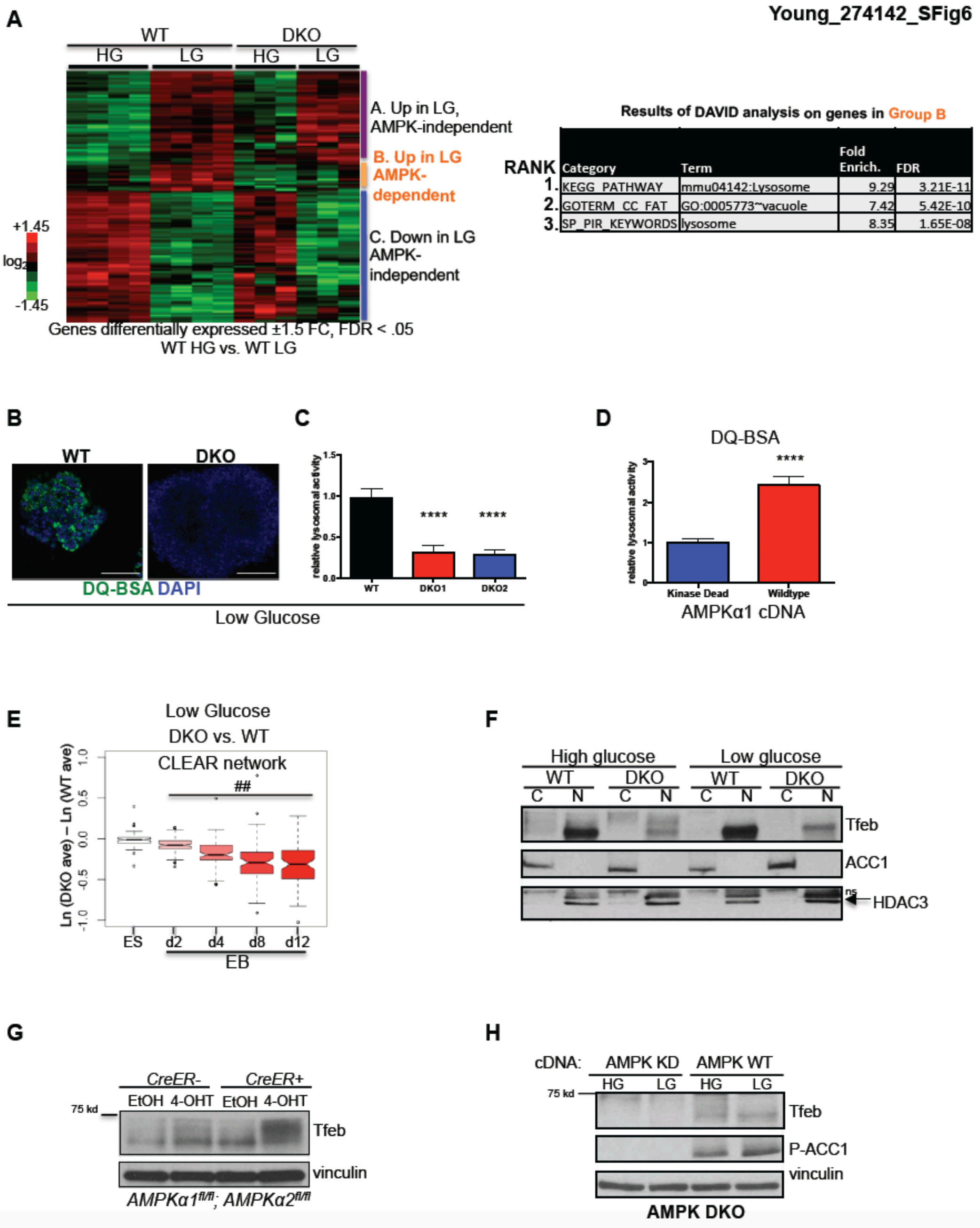

Results of DAVID analysis on genes in Group B

RANK	Category	Term	Fold Enrich.	FDR
1.	KEGG_PATHWAY	mmu04142:Lysosome	9.29	3.21E-11
2.	GOTERM_CC_FAT	GO:0005773~vacuole	7.42	5.42E-10
3.	SP_PIR_KEYWORDS	lysosome	8.35	1.65E-08

Supplemental Figure 3.7: Generation and chimera analysis of TfebMUT ESCs.
A. Schematic depicting the genomic region and nucleotide sequences around Cas9-target sites for Tfeb disruption by CRISPR. PAM sequence is shown in magenta and the locus-specific sgRNA sequence is depicted in blue. **B.** RT-qPCR analysis of Tfeb in parental WT and two independent CRISPR-derived clones of TfebMUT ESCs. Bar graph represents average ± SEM from technical triplicates. **C.** Representative whole-mount fluorescence images of E8.5 embryos that had been injected with tdTomato-positive WT or TfebMUT2 ESCs *ex vivo* at E2.5 prior to blastocyst implantation into recipient mothers. DAPI staining was performed to outline the embryo. TfebMUT2 images provide examples of partial contribution from donor cells. Scale bar, 200 µm. **D.** Table summarizing E8.5 chimeric analysis of WT and TfebMUT2 tdTomato-positive cells.

Young_274142_SFig7

A

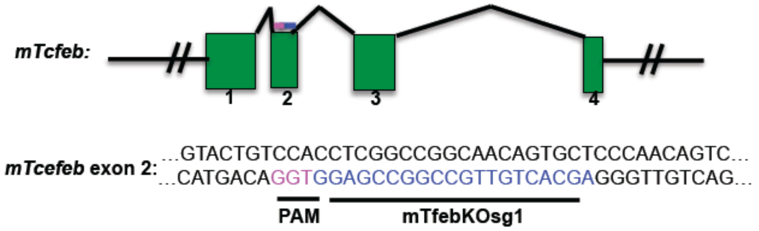

B

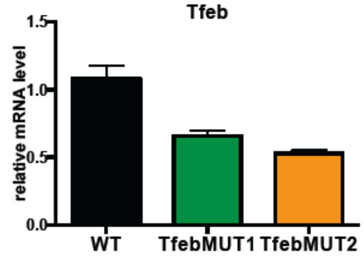

C

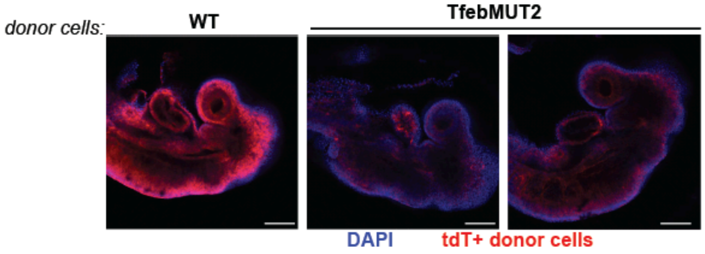

D

Donor cell genotype/ clone#	# of embryos at ~E8.5 widespread	partial	none
WT	5	0	0
TfebMUT2	11	10	4

Figure 3.4: Proper lysosomal function is required for endoderm differentiation.
A. Immunoblot analysis of Tfeb in EBs derived from WT parental and two independent TfebMUT CRISPR clones. **B.** WT and TfebMUT ESCs underwent EB differentiation for 7 days in high (HG) or low glucose (LG) followed by RT-qPCR of selected CLEAR network genes. *, $p < .05$, #, $p < .005$ compared to WT LG. **C.** Relative lysosomal activity, as determined by DQ-BSA assay, in WT and TfebMUT2- EBs. Data is from 3 independent experiments, with 10 EBs analyzed in each experiment. ****, $p < .0001$ compared to WT. **D** and **E.** RT-qPCR analysis of endoderm (**D**) and ectoderm (**E**) markers in day 7 EBs from WT and two TfebMUT clones. $p < .05$; #, $p < .005$ compared to WT. **F** and **G.** WT ESCs were differentiated into EBs for 7 days in the presence or absence of 2.5 nM Bafilomycin A (BafA). The compound was added daily. mRNA levels of selected endoderm (**F**) and ectoderm (**G**) genes were assessed by RT-qPCR. $p < .05$; #, $p < .005$ compared to DMSO. **H.** IF analysis depicting WT EB-specific co-localization of GATA4, an endoderm marker, with the highly polarized staining of lysosomal marker Lamp2 in the outer layer of cells. Most EBs derived from AMPK DKO ESCs lack appreciable staining throughout the structure, as shown on the right. Scale bar, 50 μm. For **B**, **D-G**, data are from three independent experiments. For all bar graphs, average ± SEM is plotted. Statistical significance was determined by Student's t-test.

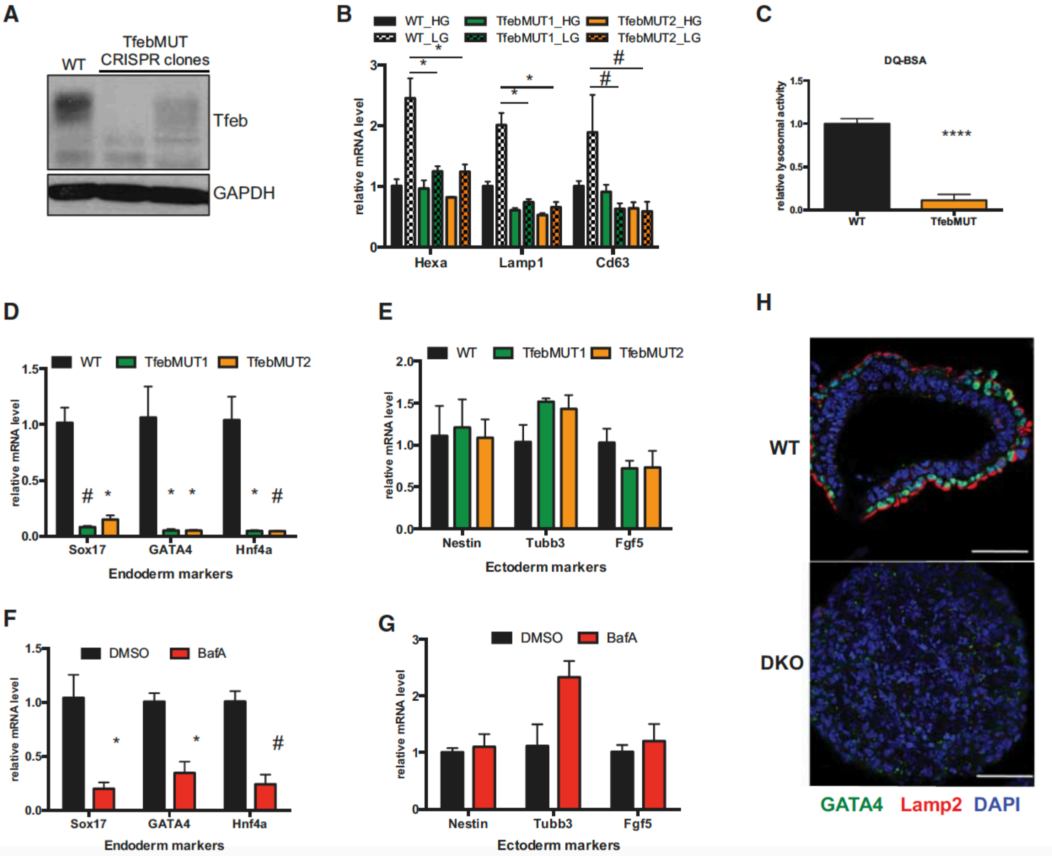
A
WT
TfebMUT
CRISPR clones
Tfeb
GAPDH
B
WT_HG
WT_LG
TfebMUT1_HG
TfebMUT1_LG
TfebMUT2_HG
TfebMUT2_LG
relative mRNA level
Hexa
Lamp1
Cd63
C
DQ-BSA
relative lysosomal activity
****
WT
TfebMUT
D
WT
TfebMUT1
TfebMUT2
relative mRNA level
Sox17
GATA4
Hnf4a
Endoderm markers
E
WT
TfebMUT1
TfebMUT2
relative mRNA level
Nestin
Tubb3
Fgf5
Ectoderm markers
F
DMSO
BafA
relative mRNA level
Sox17
GATA4
Hnf4a
Endoderm markers
G
DMSO
BafA
relative mRNA level
Nestin
Tubb3
Fgf5
Ectoderm markers
H
WT
DKO
GATA4
Lamp2
DAPI

Figure 3.5: Tfeb over-expression corrects lysosomal defects and increases endodermal gene expression in AMPK DKO cells.
A. Schematic of WT Tfeb and caTfeb cDNA constructs. TA = transactivation domain; bHLH = basic helix-loop-helix domain; LZ = leucine zipper. S142 and S211 denote phosphorylation sites that control nuclear-cytoplasmic shuttling **B.** Western blots of representative GFP and caTfeb-expressing clones following stable transfection of cDNAs into an AMPK DKO ESC CRISPR line. **C.** RT-qPCR analysis of selected CLEAR target genes in WT parental and AMPK DKO clones expressing either GFP or caTfeb following 7 days of EB differentiation. **D.** Direct fluorescence images of day 12 EBs derived from parental or caTfeb-expressing AMPK DKO ESCs after 1 hr incubation with DQ-BSA-Green, followed by a 2-hour chase prior to fixation. Scale bar, 100 µm. **E.** Relative lysosomal activity, as determined by DQ-BSA assay, in day 12 WT and AMPK DKO (parental or caTfeb-expressing) EBs in high glucose. See Materials and Methods for details. Results are from 2 independent experiments, with at least 10 EBs analyzed for each sample within an experiment. ****, $p < .0001$. **F** and **G.** WT parental and AMPK DKO ESCs expressing either GFP or caTfeb were differentiated for 7 days, followed by RT-qPCR analysis of selected endoderm (**F**) and ectoderm (**G**) markers. **C**, **F**, and **G**, show data from one representative experiment in which multiple GFP and caTfeb clones ($n = 3$ per cDNA) were analyzed and compared to WT parental controls. Similar results were observed in 4 independent experiments with additional independently derived cDNA clones. *, $p < .05$; #, $p < .005$; ^, $p < .0005$. For all bar graphs, average ± SEM is plotted. Statistical significance was determined by Student's t-test.

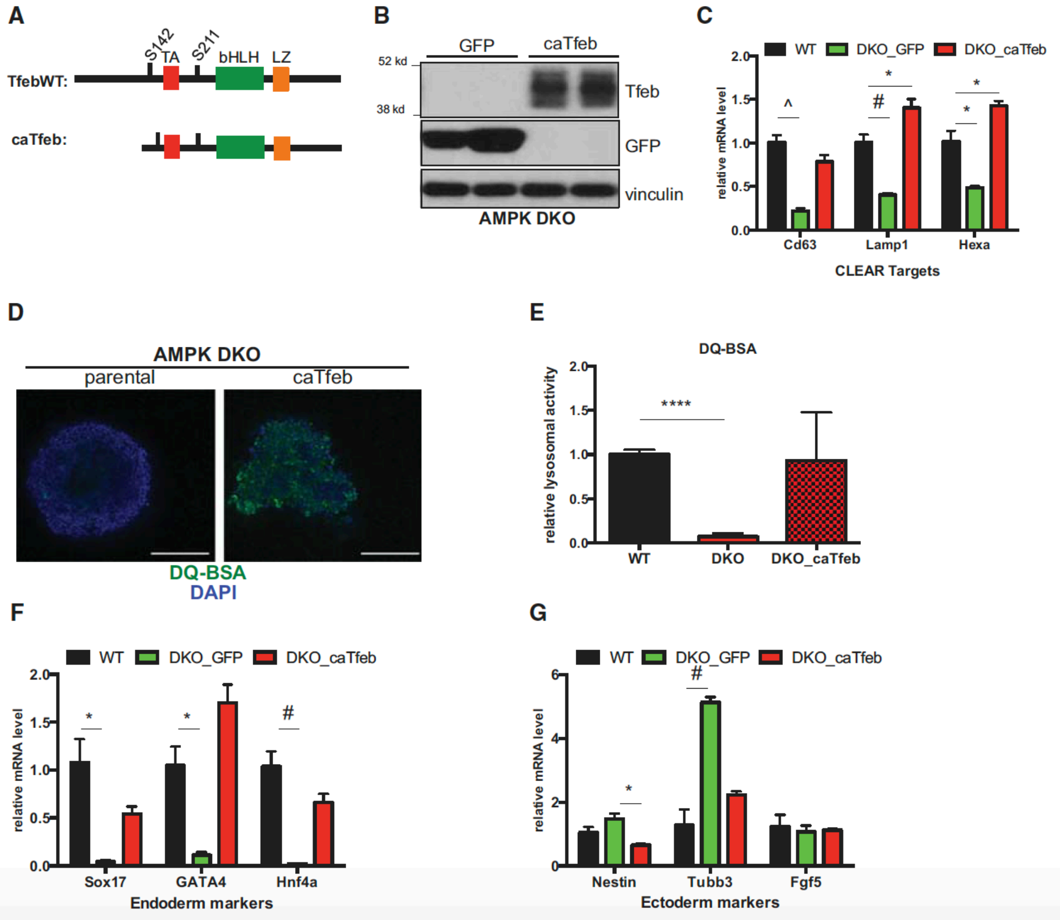
A
S142
S211
TA
bHLH
LZ
TfebWT:
caTfeb:
B
GFP
caTfeb
52 kd
38 kd
Tfeb
GFP
vinculin
AMPK DKO
C
WT
DKO_GFP
DKO_caTfeb
relative mRNA level
2.0
1.5
1.0
0.5
0.0
^
#
*
*
*
Cd63
Lamp1
Hexa
CLEAR Targets
D
AMPK DKO
parental
caTfeb
DQ-BSA
DAPI
E
DQ-BSA
relative lysosomal activity
2.0
1.5
1.0
0.5
0.0
****
WT
DKO
DKO_caTfeb
F
WT
DKO_GFP
DKO_caTfeb
relative mRNA level
2.0
1.5
1.0
0.5
0.0
*
*
#
Sox17
GATA4
Hnf4a
Endoderm markers
G
WT
DKO_GFP
DKO_caTfeb
relative mRNA level
6
4
2
0
#
*
Nestin
Tubb3
Fgf5
Ectoderm markers

Supplemental Figure 3.8: Examination of different Tfeb cDNA constructs for over-expression in AMPK DKO ESCs.

A. Schematic of various Tfeb cDNA constructs, including TfebWT and TfebAA. S142 and S211 denote phosphorylation sites that control nuclear-cytoplasmic shuttling. **B and C.** The indicated cDNAs were transiently transfected into 293T cells, and 48 hours later cells were split for western blot (**B**) and RT-qPCR (**C**) analysis. Immunoblotting indicated robust expression of a smaller version of Tfeb in caTfeb-transfected cells (**B**), which corresponded to induction of several CLEAR target genes relative to a control mRNA (**C**). Bar graph represents average ± SEM from technical triplicates. **D.** Brightfield images of representative EBs derived from parental WT or AMPK DKO cells reconstituted with GFP or caTfeb constructs. The cavitation defect in control DKO EBs (reconstituted with GFP) is partially rescued upon expression of caTfeb, as shown in the examples highlighted by red arrows. Scale bar, 100 μm **E.** Immunoblot of Tfeb in AMPK DKO clones expressing GFP or TfebAA cDNA. ESCs were differentiated into EBs for 7 days prior to analysis. ns = non-specific. **F.** RT-qPCR analysis of selected endoderm markers in day 7 EBs derived from AMPK DKO ESCs stably transfected with either GFP or TfebAA. Data represent two independent experiments with 2 (GFP) or 1 (TfebAA) clone. *, $p < .05$, ***, $p < .0005$. In **F**, average ± SEM is plotted. Statistical significance was determined by Student's t-test.

Young_274142_SFig8

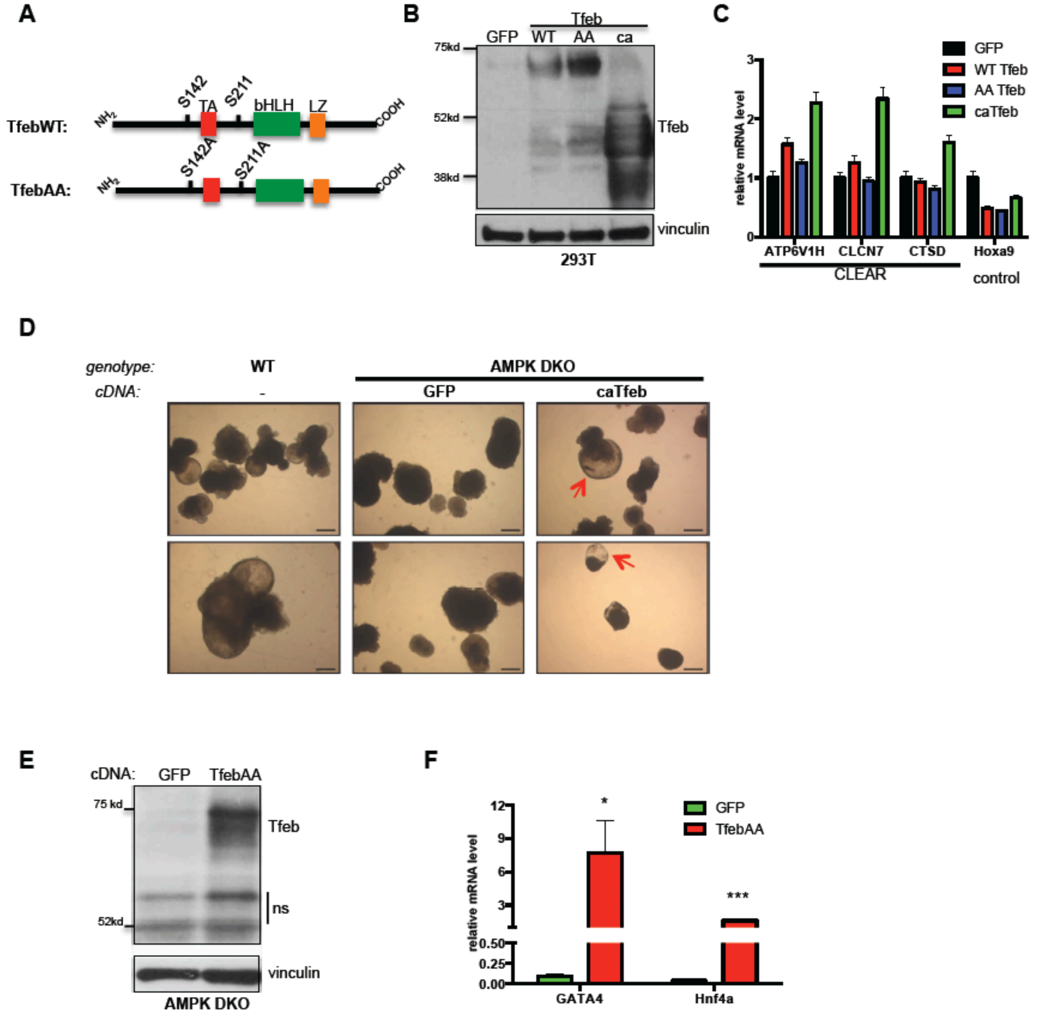

Supplemental Figure 3.9: Signaling analysis in mutant EBs and additional characterization of GSK3β inhibition on EB morphology and endodermal gene expression.

A. Immunoblot analysis of MAPK (P-Erk) and Akt (P-Akt) signaling cascades, two components of the Fgf signaling pathway, which both show similar patterns between WT, AMPK DKO, and TfebMUT cells. ESCs, day 2 (d2), day 4 (d4), and day 7 (d7) EBs were harvested and immunoblotted with the indicated antibodies. **B.** Western blot showing dynamics of phospho-βcatenin during EB differentiation time-course of AMPK DKO cells stably transfected with GFP or caTfeb. ESCs, day 4 (d4) EBs, and day 7 (d7) EBs were harvested and immunoblotted with the indicated antibodies. **C.** Representative brightfield images of EBs derived from WT and AMPK DKO cells either treated with DMSO or CHIR. Highlighted with red arrows are examples of cavitating EBs, which were seen in DKO samples only in the presence of CHIR. Scale bar, 100 µm. **D.** RT-qPCR analysis of the endoderm marker GATA4 in EBs from experiment described in Fig 6E. (DM-DMSO). *, $p < .05$, relative to WT-DM; ns, not significant. $n = 4$ independent experiments. Bar graphs represent average ± SEM. Statistical significance was determined by Student's t-test.

A

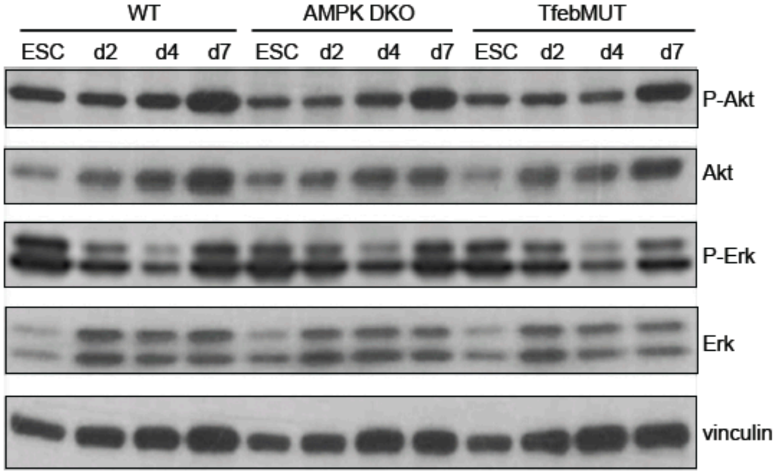
WT
AMPK DKO
TfebMUT
ESC
d2
d4
d7
ESC
d2
d4
d7
ESC
d2
d4
d7
P-Akt
Akt
P-Erk
Erk
vinculin

B

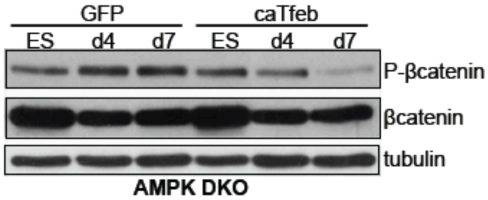
GFP
caTfeb
ES
d4
d7
ES
d4
d7
P-βcatenin
βcatenin
tubulin
AMPK DKO

C

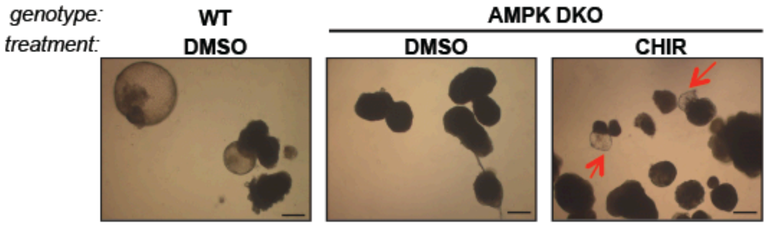
genotype:
treatment:
WT
DMSO
AMPK DKO
DMSO
CHIR

D

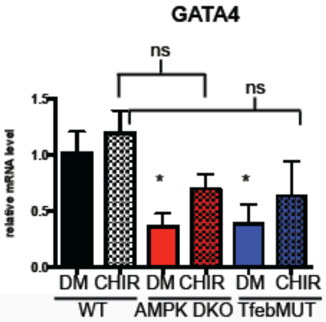
GATA4
ns
ns
1.5
1.0
0.5
0.0
relative mRNA level
*
*
DM
CHIR
DM
CHIR
DM
CHIR
WT
AMPK DKO
TfebMUT

Figure 3.6: Attenuated canonical Wnt signaling resulting from lysosomal de-regulation contributes to endodermal differentiation defects in AMPK DKO and TfebMUT cells. **A.** GSEA plot depicting a β-catenin-associated gene set up-regulated in WT vs. AMPK DKO EBs following 4 days of differentiation. **B.** Western blots showing dynamics of phospho-βcatenin during EB differentiation time-course of WT, AMPK DKO, and TfebMUT ESCs. ESCs, day 4 (d4) EBs, and day 7 (d7) EBs were harvested and immunoblotted with the indicated antibodies. **C.** WT ESCs were differentiated into EBs in the presence of vehicle (DMSO) or 2.5 nM BafA for the indicated times before being processed and analyzed as in **B**. **D.** IF of Wnt-signaling component GSK3β and lysosomal marker Lamp2 in day 8 EBs of the indicated genotypes. Note the sub-cellular co-localization of GSK3β/ Lamp2 in several cells on the outer layer of WT EBs. Insets in the bottom right of each panel depict zoomed-in images from boxed-in sections. Scale bar, 10 μm. **E.** Immunoblot analysis of day 7 WT, AMPK DKO, and TfebMUT EBs treated daily with either vehicle (DMSO) or CHIR99021 (CHIR-3 μM). One hour after the last treatment, lysates were harvested and blotted with the indicated antibodies. **F.** RT-qPCR analysis of the endoderm marker Sox17 in EBs from **E**. (DM-DMSO). *, $p < .05$ compared to WT-DM; ns, not significant. n = 4 independent experiments. **G.** IF analysis of GATA4 in day 8 WT, AMPK DKO, or TfebMUT EBs either vehicle or CHIR treated throughout the differentiation protocol. Scale bar, 50 μm. Bar graph represents average ± SEM. Statistical significance was determined by Student's t-test.

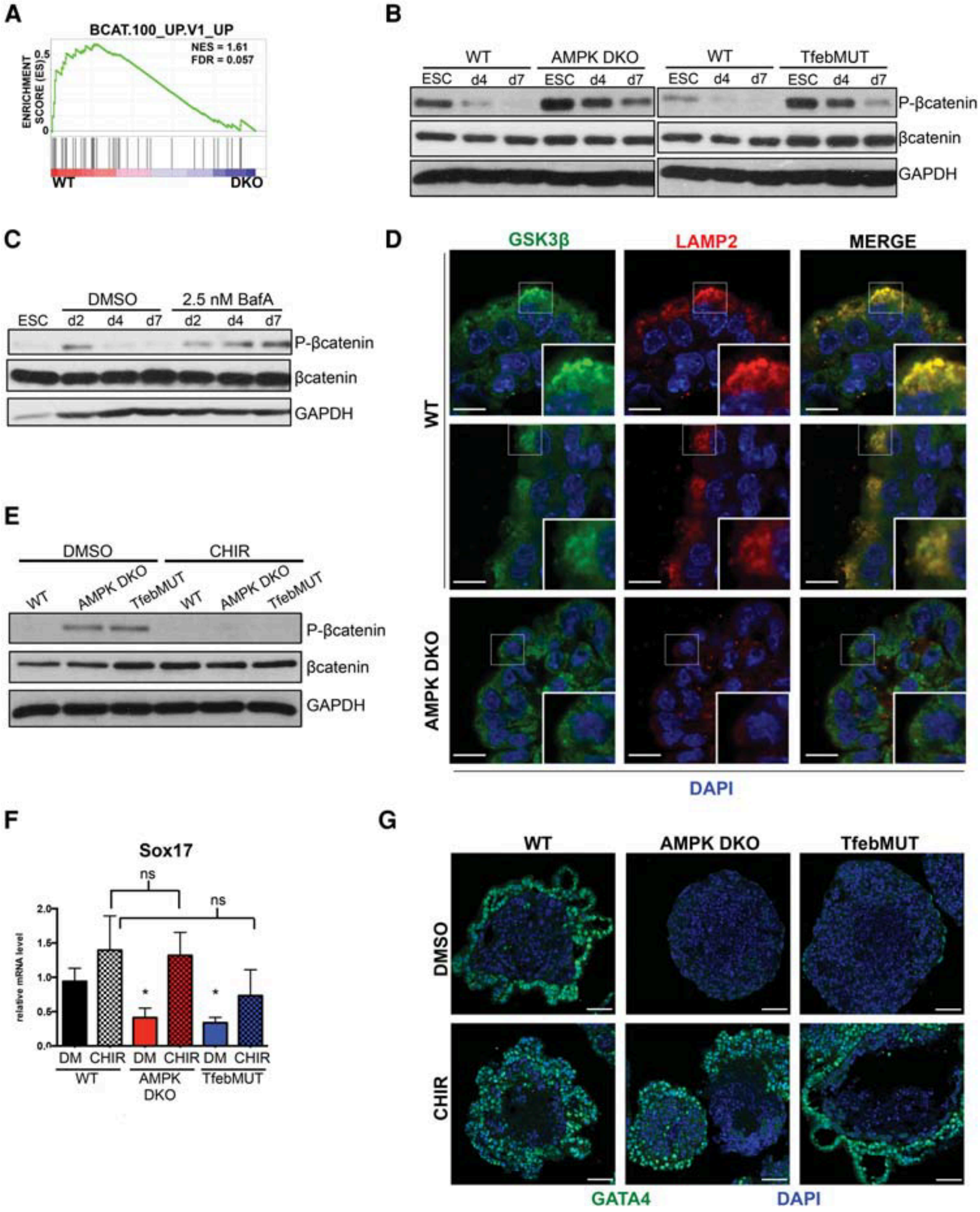
A
BCAT.100_UP.V1_UP
NES = 1.61
FDR = 0.057
ENRICHMENT SCORE (ES)
0.5
0
WT
DKO
B
WT
AMPK DKO
WT
TfebMUT
ESC
d4
d7
ESC
d4
d7
ESC
d4
d7
ESC
d4
d7
P-βcatenin
βcatenin
GAPDH
C
DMSO
2.5 nM BafA
ESC
d2
d4
d7
d2
d4
d7
P-βcatenin
βcatenin
GAPDH
D
GSK3β
LAMP2
MERGE
WT
AMPK DKO
DAPI
E
DMSO
CHIR
WT
AMPK DKO
TfebMUT
WT
AMPK DKO
TfebMUT
P-βcatenin
βcatenin
GAPDH
F
Sox17
ns
ns
relative mRNA level
2.0
1.5
1.0
0.5
0.0
*
*
DM
CHIR
DM
CHIR
DM
CHIR
WT
AMPK DKO
TfebMUT
G
WT
AMPK DKO
TfebMUT
DMSO
CHIR
GATA4
DAPI

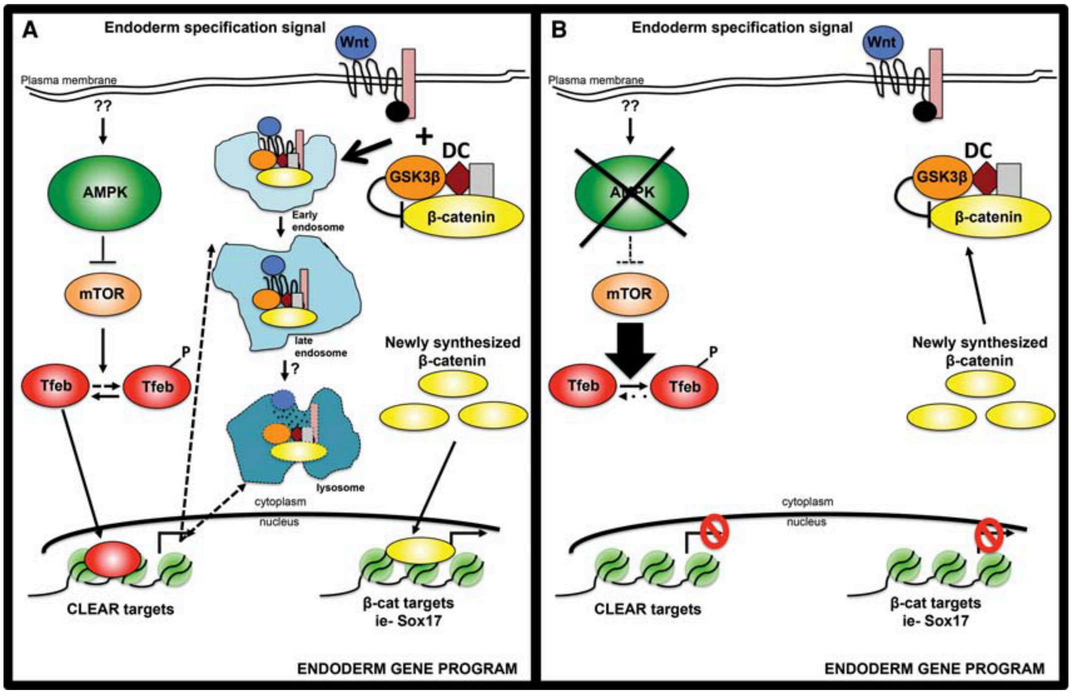

Figure 3.7: Model depicting how AMPK regulates cell fate decisions through lysosome-dependent control of Wnt signaling.

A. In WT cells, AMPK inhibition of mTOR allows sufficient levels of Tfeb to enter the nucleus and transcriptionally up-regulate endolysosomes. This organelle system is required for optimal signaling through the canonical Wnt pathway through its ability to sequester the GSK3β-containing DC, freeing β-catenin from degradation. Active β-catenin then translocates into the nucleus to induce target genes, many of which are important mediators of endodermal differentiation, including Sox17. **B.** In AMPK DKO cells, increased mTOR signaling blunts Tfeb activity, leading to a defective endolysosomal compartment. As a result, DC inhibition of β-catenin remains intact even in the presence of Wnt, preventing robust activation of endodermal genes.

BIBLIOGRAPHY

1. Lee, M. J. & Yaffe, M. B. Protein Regulation in Signal Transduction. *Csh Perspect Biol* **8,** a005918 (2016).

2. Ardito, F., Giuliani, M., Perrone, D., Troiano, G. & Muzio, L. The crucial role of protein phosphorylation in cell signaling and its use as targeted therapy (Review). *Int J Mol Med* **40,** 271–280 (2017).

3. Hunter, T. & Karin, M. The regulation of transcription by phosphorylation. *Cell* **70,** 375–387 (1992).

4. Hunter, T. Signaling—2000 and Beyond. *Cell* **100,** 113–127 (2000).

5. Hornbeck, P. V., Kornhauser, J. M., Latham, V., Murray, B., Nandhikonda, V., Nord, A., Skrzypek, E., Wheeler, T., Zhang, B. & Gnad, F. 15 years of PhosphoSitePlus®: integrating post-translationally modified sites, disease variants and isoforms. *Nucleic Acids Res* **47,** D433–D441 (2018).

6. Eid, S., Turk, S., Volkamer, A., Rippmann, F. & Fulle, S. KinMap: a web-based tool for interactive navigation through human kinome data. *Bmc Bioinformatics* **18,** 16 (2017).

7. Hunter, T. Protein kinases and phosphatases: The Yin and Yang of protein phosphorylation and signaling. *Cell* **80,** 225–236 (1995).

8. Damle, N. P. & Köhn, M. The human DEPhOsphorylation Database DEPOD: 2019 update. *Database J Biological Databases Curation* **2019,** (2019).

9. Dephoure, N., Gould, K. L., Gygi, S. P. & Kellogg, D. R. Mapping and analysis of phosphorylation sites: a quick guide for cell biologists. *Mol Biol Cell* **24,** 535–42 (2013).

10. Sugiyama, N., Imamura, H. & Ishihama, Y. Large-scale Discovery of Substrates of the Human Kinome. *Sci Rep-uk* **9,** 10503 (2019).

11. nald, M., Trost, B. & Napper, S. Conservation of kinase-phosphorylation site pairings: Evidence for an evolutionarily dynamic phosphoproteome. *Plos One* **13,** e0202036 (2018).

12. Adam, K. & Hunter, T. Histidine kinases and the missing phosphoproteome from prokaryotes to eukaryotes. *Lab Invest* **98,** 233–247 (2017).

13. Pawson, T. & Scott, J. D. Protein phosphorylation in signaling – 50 years and counting. *Trends Biochem Sci* **30,** 286–290 (2005).

14. Nishi, H., Shaytan, A. & Panchenko, A. R. Physicochemical mechanisms of protein

regulation by phosphorylation. *Frontiers Genetics* **5,** 270 (2014).

15. Nishi, H., Fong, J. H., Chang, C., Teichmann, S. A. & Panchenko, A. R. Regulation of protein-protein binding by coupling between phosphorylation and intrinsic disorder: analysis of human protein complexes. *Mol Biosyst* **9,** 1620–6 (2013).

16. Olsen, J. V., Blagoev, B., Gnad, F., Macek, B., Kumar, C., Mortensen, P. & Mann, M. Global, In Vivo, and Site-Specific Phosphorylation Dynamics in Signaling Networks. *Cell* **127,** 635–648 (2006).

17. Larance, M., Ahmad, Y., Kirkwood, K. J., Ly, T. & Lamond, A. I. Global subcellular characterization of protein degradation using quantitative proteomics. *Mol Cell Proteom Mcp* **12,** 638–50 (2012).

18. Swaney, D. L., Beltrao, P., Starita, L., Guo, A., Rush, J., Fields, S., Krogan, N. J. & Villén, J. Global analysis of phosphorylation and ubiquitylation cross-talk in protein degradation. *Nat Methods* **10,** 676–82 (2013).

19. Singh, V., Ram, M., Kumar, R., Prasad, R., Roy, B. & Singh, K. Phosphorylation: Implications in Cancer. *Protein J* **36,** 1–6 (2017).

20. Hanahan, D. & Weinberg, R. A. The Hallmarks of Cancer. *Cell* **100,** 57–70 (2000).

21. Hanahan, D. & Weinberg, R. A. Hallmarks of cancer: the next generation. *Cell* **144,** 646–74 (2011).

22. of Collaborators, G., Roth, G. A., Abate, D., Abate, K., Abay, S. M., Abbafati, C., Abbasi, N., Abbastabar, H., Abd-Allah, F., Abdela, J., Abdelalim, A., Abdollahpour, I., Abdulkader, R., Abebe, H., Abebe, M., Abebe, Z., Abejie, A., Abera, S. F., Abil, O., Abraha, H., Abrham, A., Abu-Raddad, L., Accrombessi, M., Acharya, D., Adamu, A. A., Adebayo, O. M., Adedoyin, R., Adekanmbi, V., Adetokunboh, O. O., Adhena, B., Adib, M. G., Admasie, A., Afshin, A., Agarwal, G., Agesa, K. M., Agrawal, A., Agrawal, S., Ahmadi, A., Ahmadi, M., Ahmed, M., Ahmed, S., Aichour, A., Aichour, I., Aichour, M., Akbari, M., Akinyemi, R., Akseer, N., Al-Aly, Z., Al-Eyadhy, A., Al-Raddadi, R. M., Alahdab, F., Alam, K., Alam, T., Alebel, A., Alene, K., Alijanzadeh, M., Alizadeh-Navaei, R., Aljunid, S., Alkerwi, A., Alla, F., Allebeck, P., Alonso, J., Altirkawi, K., Alvis-Guzman, N., Amare, A. T., Aminde, L. N., Amini, E., Ammar, W., Amoako, Y., Anber, N., Andrei, C., Androudi, S., Animut, M., Anjomshoa, M., Ansari, H., Ansha, M., Antonio, C. T., Anwari, P., Aremu, O., Ärnlöv, J., Arora, A., Arora, M., Artaman, A., Aryal, K. K., Asayesh, H., Asfaw, E., Ataro, Z., Atique, S., Atre, S. R., Ausloos, M., Avokpaho, E. F., Awasthi, A., Quintanilla, B., Ayele, Y., Ayer, R., Azzopardi, P. S., Babazadeh, A., Bacha, U., Badali, H., Badawi, A., Bali, A., Ballesteros, K. E., Banach, M., Banerjee, K., Bannick, M. S., Banoub, J., Barboza, M. A., Barker-Collo, S., Bärnighausen, T., Barquera, S., Barrero, L. H., Bassat, Q., Basu, S., Baune, B. T., Baynes, H., Bazargan-Hejazi, S., Bedi, N., Beghi, E., Behzadifar, M., Behzadifar, M., Béjot, Y., Bekele, B., Belachew, A., Belay, E., Belay, Y., Bell, M. L., Bello, A. K., Bennett, D. A., Bensenor, I.

M., Berman, A. E., Bernabe, E., Bernstein, R. S., Bertolacci, G. J., Beuran, M., Beyranvand, T., Bhalla, A., Bhattarai, S., Bhaumik, S., Bhutta, Z. A., Biadgo, B., Biehl, M. H., Bijani, A., Bikbov, B., Bilano, V., Bililign, N., Sayeed, M., Bisanzio, D., Biswas, T., Blacker, B. F., Basara, B., Borschmann, R., Bosetti, C., Bozorgmehr, K., Brady, O. J., Brant, L. C., Brayne, C., Brazinova, A., Breitborde, N. J., Brenner, H., Briant, P., Britton, G., Brugha, T., Busse, R., Butt, Z. A., Callender, C. S., Campos-Nonato, I. R., Rincon, J., Cano, J., Car, M., Cárdenas, R., Carreras, G., Carrero, J. J., Carter, A., Carvalho, F., Castañeda-Orjuela, C. A., Rivas, J., Castle, C. D., Castro, C., Castro, F., Catalá-López, F., Cerin, E., Chaiah, Y., Chang, J.-C., Charlson, F. J., Chaturvedi, P., Chiang, P., Chimed-Ochir, O., Chisumpa, V., Chitheer, A., Chowdhury, R., Christensen, H., Christopher, D. J., Chung, S.-C., Cicuttini, F. M., Ciobanu, L. G., Cirillo, M., Cohen, A. J., Cooper, L., Cortesi, P., Cortinovis, M., Cousin, E., Cowie, B. C., Criqui, M. H., Cromwell, E. A., Crowe, C., Crump, J. A., Cunningham, M., Daba, A., Dadi, A., Dandona, L., Dandona, R., Dang, A., Dargan, P. I., Daryani, A., Das, S. K., Gupta, R., Neves, J., Dasa, T., Dash, A., Davis, A. C., Weaver, N., Davitoiu, D., Davletov, K., Hoz, F., Neve, J.-W., Degefa, M., Degenhardt, L., Degfie, T. T., Deiparine, S., Demoz, G., Demtsu, B., Denova-Gutiérrez, E., Deribe, K., Dervenis, N., Jarlais, D. C., Dessie, G., Dey, S., Dharmaratne, S. D., Dicker, D., Dinberu, M., Ding, E. L., Dirac, A. M., Djalalinia, S., Dokova, K., Doku, D., Donnelly, C. A., Dorsey, R. E., Doshi, P. P., Douwes-Schultz, D., Doyle, K. E., Driscoll, T. R., Dubey, M., Dubljanin, E., Duken, E., Duncan, B. B., Duraes, A. R., Ebrahimi, H., Ebrahimpour, S., Edessa, D., Edvardsson, D., Eggen, A., Bcheraoui, C., Zaki, M., El-Khatib, Z., Elkout, H., Ellingsen, C., Endres, M., Endries, A., Er, B., Erskine, H. E., Eshrati, B., Eskandarieh, S., Esmaeili, R., Esteghamati, A., Fakhar, M., Fakhim, H., Faramarzi, M., Fareed, M., Farhadi, F., Farinha, C. E., Faro, A., Farvid, M. S., Farzadfar, F., Farzaei, M., Feigin, V. L., Feigl, A. B., Fentahun, N., Fereshtehnejad, S.-M., Fernandes, E., Fernandes, J. C., Ferrari, A. J., Feyissa, G., Filip, I., Finegold, S., Fischer, F., Fitzmaurice, C., Foigt, N. A., Foreman, K. J., Fornari, C., Frank, T. D., Fukumoto, T., Fuller, J. E., Fullman, N., Fürst, T., Furtado, J. M., Futran, N. D., Gallus, S., Garcia-Basteiro, A. L., Garcia-Gordillo, M. A., Gardner, W. M., Gebre, A., Gebrehiwot, T., Gebremedhin, A., Gebremichael, B., Gebremichael, T., Gelano, T., Geleijnse, J. M., Genova-Maleras, R., Geramo, Y., Gething, P. W., Gezae, K., Ghadami, M., Ghadimi, R., Falavarjani, K., Ghasemi-Kasman, M., Ghimire, M., Gibney, K. B., Gill, P., Gill, T. K., Gillum, R. F., Ginawi, I., Giroud, M., Giussani, G., Goenka, S., Goldberg, E. M., nivas Goli, Gómez-Dantés, H., Gona, P. N., Gopalani, S., Gorman, T. M., Goto, A., Goulart, A. C., Gnedovskaya, E. V., Grada, A., Grosso, G., Gugnani, H., Guimaraes, A., Guo, Y., Gupta, P. C., Gupta, R., Gupta, R., Gupta, T., Gutiérrez, R., Gyawali, B., Haagsma, J. A., Hafezi-Nejad, N., Hagos, T. B., Hailegiyorgis, T., Hailu, G., Haj-Mirzaian, A., Haj-Mirzaian, A., Hamadeh, R. R., Hamidi, S., Handal, A. J., Hankey, G. J., Harb, H. L., Harikrishnan, S., Haro, J., Hasan, M., Hassankhani, H., Hassen, H., Havmoeller, R., Hay, R. J., Hay, S. I., He, Y., Hedayatizadeh-Omran, A., Hegazy, M. I., Heibati, B., Heidari, M., Hendrie, D., Henok, A., Henry, N. J., Herteliu, C., Heydarpour, F., Heydarpour, P., Heydarpour, S., Hibstu, D., Hoek, H. W., Hole, M. K., Rad, E., Hoogar, P., Hosgood, D. H., Hosseini, S., Hosseinzadeh, M., Hostiuc, M., Hostiuc, S., Hotez, P. J., Hoy, D. G., Hsiao, T., Hu, G., Huang, J. J., Husseini, A., Hussen, M., Hutfless, S., Idrisov, B., Ilesanmi, O., Iqbal, U., Irvani, S., Irvine, C., Islam, N., Islam, S., Islami, F., Jacobsen, K. H., Jahangiry, L., Jahanmehr, N., Jain, S., Jakovljevic, M., Jalu, M., James, S. L., Javanbakht, M., Jayatilleke, A., Jeemon, P., Jenkins, K. J., Jha, R., Jha, V., Johnson, C. O., Johnson, S. C., Jonas, J. B., Joshi, A., Jozwiak, J., Jungari, S., Jürisson, M., Kabir, Z., Kadel, R., Kahsay, A., Kalani, R., Karami, M., Matin, B., Karch, A., Karema, C., Karimi-Sari, H., Kasaeian, A., Kassa, D. H., Kassa, G., Kassa, T., Kassebaum, N. J., nivasa Katikireddi, V., Kaul, A., Kazemi, Z., Karyani, A., Kazi, D., Kefale, A., Keiyoro, P., Kemp, G., Kengne, A., Keren, A., Kesavachandran, C., Khader, Y., Khafaei, B., Khafaie, M., Khajavi, A., Khalid, N., Khalil, I. A., Khan, E., Khan, M., Khan, M., Khang, Y.-H., Khater, M. M., Khoja, A. T., Khosravi, A., Khosravi, M., Khubchandani, J., Kiadaliri, A. A., Kibret, G. D., Kidanemariam, Z., Kiirithio, D. N., Kim, D., Kim, Y.-E., Kim, Y., Kimokoti, R. W., Kinfu, Y., Kisa, A., Kissimova-Skarbek, K., Kivimäki, M., Knudsen, A., Kocarnik, J. M., Kochhar, S., Kokubo, Y., Kolola, T., Kopec, J. A., Koul, P. A., Koyanagi, A., Kravchenko, M. A., Krishan, K., Defo, B., Bicer, B., Kumar, A. G., Kumar, M., Kumar, P., Kutz, M. J., Kuzin, I., Kyu, H., Lad, D. P., Lad, S. D., Lafranconi, A., Lal, D., Lalloo, R., Lallukka, T., Lam, J. O., Lami, F., Lansingh, V. C., Lansky, S., Larson, H. J., Latifi, A., Lau, K., Lazarus, J. V., Lebedev, G., Lee, P. H., Leigh, J., Leili, M., Leshargie, C., Li, S., Li, Y., Liang, J., Lim, L.-L., Lim, S. S., Limenih, M., Linn, S., Liu, S., Liu, Y., Lodha, R., Lonsdale, C., Lopez, A. D., Lorkowski, S., Lotufo, P. A., Lozano, R., Lunevicius, R., Ma, S., Macarayan, E., Mackay, M. T., MacLachlan, J. H., Maddison, E. R., Madotto, F., Razek, H., Razek, M., Maghavani, D. P., Majdan, M., Majdzadeh, R., Majeed, A., Malekzadeh, R., Malta, D., Manda, A.-L., Mandarano-Filho, L., Manguerra, H., Mansournia, M., Mapoma, C., Marami, D., Maravilla, J. C., Marcenes, W., Marczak, L., Marks, A., Marks, G. B., Martinez, G., Martins-Melo, F., Martopullo, I., März, W., Marzan, M. B., Masci, J. R., Massenburg, B., Mathur, M., Mathur, P., Matzopoulos, R., Maulik, P. K., Mazidi, M., McAlinden, C., McGrath, J. J., McKee, M., McMahon, B. J., Mehata, S., Mehndiratta, M., Mehrotra, R., Mehta, K. M., Mehta, V., Mekonnen, T. C., Melese, A., Melku, M., Memiah, P. T., Memish, Z. A., Mendoza, W., Mengistu, D., Mengistu, G., Mensah, G. A., Mereta, S., Meretoja, A., Meretoja, T. J., Mestrovic, T., Mezgebe, H., Miazgowski, B., Miazgowski, T., Millear, A. I., Miller, T. R., Miller-Petrie, M., Mini, G., Mirabi, P., Mirarefin, M., Mirica, A., Mirrakhimov, E. M., Misganaw, A., Mitiku, H., Moazen, B., Mohammad, K., Mohammadi, M., Mohammadifard, N., Mohammed, M. A., Mohammed, S., Mohan, V., Mokdad, A. H., Molokhia, M., Monasta, L., Moradi, G., Moradi-Lakeh, M., Moradinazar, M., Moraga, P., Morawska, L., Velásquez, I., Morgado-Da-Costa, J., Morrison, S., Moschos, M. M., Mouodi, S., Mousavi, S., Muchie, K., Mueller, U., Mukhopadhyay, S., Muller, K., Mumford, J., Musa, J., Musa, K., Mustafa, G., Muthupandian, S., Nachega, J. B., Nagel, G., Naheed, A., Nahvijou, A., Naik, G., Nair, S., Najafi, F., Naldi, L., Nam, H., Nangia, V., Nansseu, J., Nascimento, B., Natarajan, G., Neamati, N., Negoi, I., Negoi, R., Neupane, S., Newton, C. R., Ngalesoni, F. N., Ngunjiri, J. W., Nguyen, A., Nguyen, G., Nguyen, H., Nguyen, H., Nguyen, L., Nguyen, M., Nguyen, T., Nichols, E., Ningrum, D., Nirayo, Y., Nixon, M. R., Nolutshungu, N., Nomura, S., Norheim, O. F., Noroozi, M., Norrving, B., Noubiap, J., Nouri, H., Shiadeh, M., Nowroozi, M., Nyasulu, P. S., Odell, C. M., Ofori-Asenso, R., Ogbo, F., Oh, I.-H., Oladimeji, O., Olagunju, A. T., Olivares, P. R., Olsen, H., Olusanya, B., Olusanya, J., Ong, K. L., Ong, S., Oren, E., Orpana, H. M., Ortiz, A., Ortiz, J. R., Otstavnov, S. S., Øverland, S., Owolabi, M., Özdemir, R., Mahesh, P., Pacella, R., Pakhale, S., Pakhare, A. P., Pakpour, A. H., Pana, A., Panda-Jonas, S., Pandian, J., Parisi, A., Park, E.-K., Parry, C. D., Parsian, H., Patel, S., Pati, S., Patton, G. C., Paturi, V., Paulson, K. R., Pereira, A., Pereira, D. M., Perico, N., Pesudovs, K., Petzold, M., Phillips, M. R., Piel, F. B., Pigott, D. M., Pillay, J., Pirsaheb, M., Pishgar, F., Polinder, S., Postma, M. J., Pourshams, A., Poustchi, H., Pujar, A., Prakash, S., Prasad, N., Purcell, C. A., Qorbani, M., Quintana, H., Quistberg, A. D., Rade, K., Radfar, A., Rafay, A., Rafiei, A., Rahim, F., Rahimi, K., Rahimi-Movaghar, A., Rahman, M., Rahman, M., Rahman, M., Rai, R., Rajsic, S., Ram, U., Ranabhat, C., Ranjan, P., Rao, P. C., Rawaf, D., Rawaf, S., Razo-García, C., nath Reddy, K., Reiner, R. C., Reitsma, M. B., Remuzzi, G., Renzaho, A. M., Resnikoff, S., Rezaei, S., Rezaeian, S., Rezai, M., Riahi, S., Ribeiro, A. P., Rios-Blancas, M., Roba, K., Roberts, N. L., Robinson, S. R., Roever, L., Ronfani, L., Roshandel, G., Rostami, A., Rothenbacher, D., Roy, A., Rubagotti, E., Sachdev, P. S., Saddik, B., Sadeghi, E., Safari, H., Safdarian, M., Safi, S., Safiri, S., Sagar, R., Sahebkar, A., Sahraian, M., Salam, N., Salama, J. S., Salamati, P., Saldanha, R., Saleem, Z., Salimi, Y., Salvi, S., Salz, I., Sambala, E., my, A., Sanabria, J., Sanchez-Niño, M., Santomauro, D., Santos, I. S., Santos, J., ntric Milicevic, M., Jose, B., Sarker, A., Sarmiento-Suárez, R., Sarrafzadegan, N., Sartorius, B., Sarvi, S., Sathian, B., Satpathy, M., Sawant, A. R., Sawhney, M., Saxena, S., Sayyah, M., Schaeffner, E., Schmidt, M., Schneider, I. J., Schöttker, B., Schutte, A., Schwebel, D. C., Schwendicke, F., Scott, J. G., Sekerija, M., Sepanlou, S. G., Serván-Mori, E., Seyedmousavi, S., Shabaninejad, H., Shackelford, K., Shafieesabet, A., Shahbazi, M., Shaheen, A. A., Shaikh, M., Shams-Beyranvand, M., Shamsi, M., Shamsizadeh, M., Sharafi, K., Sharif, M., Sharif-Alhoseini, M., Sharma, R., She, J., Sheikh, A., Shi, P., Shiferaw, M., Shigematsu, M., Shiri, R., Shirkoohi, R., Shiue, I., Shokraneh, F., Shrime, M. G., Si, S., Siabani, S., Siddiqi, T. J., Sigfusdottir, I., Sigurvinsdottir, R., Silberberg, D. H., Silva, D., Silva, J., Silva, N., Silveira, D., Singh, J. A., Singh, N., Singh, P., Singh, V., Sinha, D., Sliwa, K., Smith, M., Sobaih, B., Sobhani, S., Sobngwi, E., Soneji, S. S., Soofi, M., Sorensen, R. J., Soriano, J. B., Soyiri, I. N., Sposato, L. A., eramareddy, C. T., nivasan, V., Stanaway, J. D., Starodubov, V. I., Stathopoulou, V., Stein, D. J., Steiner, C., Stewart, L. G., Stokes, M. A., Subart, M. L., Sudaryanto, A., Sufiyan, M., Sur, P., Sutradhar, I., Sykes, B. L., Sylaja, P., Sylte, D. O., Szoeke, C. E., Tabarés-Seisdedos, R., Tabuchi, T., Tadakamadla, S., Takahashi, K., Tandon, N., Tassew, S., Taveira, N., Tehrani-Banihashemi, A., Tekalign, T., Tekle, M., Temsah, M.-H., Temsah, O., Terkawi, A., Teshale, M., Tessema, B., Tessema, G., Thankappan, K., Thirunavukkarasu, S., Thomas, N., Thrift, A. G., Thurston, G. D., Tilahun, B., To, Q. G., Tobe-Gai, R., Tonelli, M., Topor-Madry, R., Torre, A. E., Tortajada-Girbés, M., Touvier, M., Tovani-Palone, M., Tran, B., Tran, K., Tripathi, S., Troeger, C. E., Truelsen, T., Truong, N., Tsadik, A., Tsoi, D., Car, L., Tuzcu, M. E., Tyrovolas, S., Ukwaja, K. N., Ullah, I., Undurraga, E. A., Updike, R. L., Usman, M., Uthman, O. A., Uzun, S., Vaduganathan, M., Vaezi, A., Vaidya, G., Valdez, P. R., Varavikova, E., Vasankari, T., Venketasubramanian, N., Villafaina, S., Violante, F. S., Vladimirov, S., Vlassov, V., Vollset, S., Vos, T., Wagner, G. R., Wagnew, F., Waheed, Y., Wallin, M., Walson, J. L., Wang, Y., Wang, Y.-P., Wassie, M., Weiderpass, E., Weintraub, R. G., Weldegebreal, F., Weldegwergs, K., Werdecker, A., Werkneh, A., West, E. T., Westerman, R., Whiteford, H. A., Widecka, J., Wilner, L. B., Wilson, S., Winkler, A., Wiysonge, C., Wolfe, C. D., Wu, S., Wu, Y.-C., Wyper, G. M., Xavier, D., Xu, G., Yadgir, S., Yadollahpour, A., Jabbari, S., Yakob, B., Yan, L. L., Yano, Y., Yaseri, M., Yasin, Y., Yentür, G., Yeshaneh, A., Yimer, E. M., Yip, P., Yirsaw, B., Yisma, E., Yonemoto, N., Yonga, G., Yoon, S.-J., Yotebieng, M., Younis, M. Z., Yousefifard, M., Yu, C., Zadnik, V., Zaidi, Z., Zaman, S., Zamani, M., Zare, Z., Zeleke, A., Zenebe, Z., Zhang, A., Zhang, K., Zhou, M., Zodpey, S., Zuhlke, L., Naghavi, M. & Murray, C. J. Global, regional, and national age-sex-specific mortality for 282 causes of death in 195 countries and territories, 1980–2017: a systematic analysis for the Global Burden of Disease Study 2017. *Lancet* **392,** 1736–1788 (2018).

23. Radivojac, P., Baenziger, P. H., Kann, M. G., Mort, M. E., Hahn, M. W. & Mooney, S. D. Gain and loss of phosphorylation sites in human cancer. *Bioinform Oxf Engl* **24,** i241-7 (2008).

24. Lim, Y. Mining the Tumor Phosphoproteome for Cancer Markers. *Clin Cancer Res* **11,** 3163–3169 (2005).

25. Kannaiyan, R. & Mahadevan, D. A comprehensive review of protein kinase inhibitors for cancer therapy. *Expert Rev Anticanc* **18,** 1249–1270 (2018).

26. Bhullar, K. S., Lagarón, N., McGowan, E. M., Parmar, I., Jha, A., Hubbard, B. P. & Rupasinghe, V. H. Kinase-targeted cancer therapies: progress, challenges and future directions. *Mol Cancer* **17,** 48 (2018).

27. Frankson, R., Yu, Z.-H., Bai, Y., Li, Q., Zhang, R.-Y. & Zhang, Z.-Y. Therapeutic Targeting of Oncogenic Tyrosine Phosphatases. *Cancer Res* **77,** 5701–5705 (2017).

28. Bollu, L., Mazumdar, A., Savage, M. I. & Brown, P. H. Molecular Pathways: Targeting Protein Tyrosine Phosphatases in Cancer. *Clin Cancer Res* **23,** 2136–2142 (2017).

29. Fontanillo, M. & Köhn, M. Advances in Experimental Medicine and Biology. *Adv Exp Med Biol* **917,** 209–240 (2016).

30. Ji, H., Ramsey, M. R., Hayes, N. D., Fan, C., McNamara, K., Kozlowski, P., Torrice, C., Wu, M. C., Shimamura, T., Perera, S. A., Liang, M.-C., Cai, D., Naumov, G. N., Bao, L., Contreras, C. M., Li, D., Chen, L., Krishnamurthy, J., Koivunen, J., Chirieac, L. R., Padera, R. F., Bronson, R. T., Lindeman, N. I., Christiani, D. C., Lin, X., Shapiro, G. I., Jänne, P. A., Johnson, B. E., Meyerson, M., Kwiatkowski, D. J., Castrillon, D. H., Bardeesy, N., Sharpless, N. E. & Wong, K.-K. LKB1 modulates lung cancer differentiation and metastasis. *Nature* **448,** 807 (2007).

31. Hemminki, A., Markie, D., Tomlinson, I., Avizienyte, E., Roth, S., Loukola, A., Bignell, G., Warren, W., Aminoff, M., Höglund, P., Järvinen, H., Kristo, P., Pelin, K., Ridanpää, M., Salovaara, R., Toro, T., Bodmer, W., Olschwang, S., Olsen, A. S., Stratton, M. R., de la Chapelle, A. & Aaltonen, L. A. A serine/threonine kinase gene defective in Peutz–Jeghers syndrome. *Nature* **391,** 184 (1998).

32. Boudeau, J., Sapkota, G. & Alessi, D. R. LKB1, a protein kinase regulating cell proliferation and polarity. *Febs Lett* **546,** 159–165 (2003).

33. Alessi, D. R., Sakamoto, K. & Bayascas, J. R. LKB1-Dependent Signaling Pathways. *Annu Rev Biochem* **75,** 137–163 (2006).

34. Sanchez-Cespedes, M. The role of LKB1 in lung cancer. *Fam Cancer* **10,** 447–453 (2011).

35. Imielinski, M., Berger, A. H., Hammerman, P. S., Hernandez, B., Pugh, T. J., Hodis, E., Cho, J., Suh, J., Capelletti, M., Sivachenko, A., Sougnez, C., Auclair, D., Lawrence, M. S., Stojanov, P., Cibulskis, K., Choi, K., de Waal, L., Sharifnia, T., Brooks, A., Greulich, H., Banerji, S., Zander, T., Seidel, D., Leenders, F., Ansén, S., Ludwig, C., Engel-Riedel, W., Stoelben, E., Wolf, J., Goparju, C., Thompson, K., Winckler, W., Kwiatkowski, D., Johnson, B. E., Jänne, P. A., Miller, V. A., Pao, W., Travis, W. D., Pass, H. I., Gabriel, S. B., Lander, E. S., Thomas, R. K., Garraway, L. A., Getz, G. & Meyerson, M. Mapping the hallmarks of lung adenocarcinoma with massively parallel sequencing. *Cell* **150,** 1107–20 (2012).

36. Makowski, L. & Hayes, D. Role of LKB1 in lung cancer development. *Brit J Cancer* **99,** 683–8 (2008).

37. Matsumoto, S., Iwakawa, R., Takahashi, K., Kohno, T., Nakanishi, Y., Matsuno, Y., Suzuki, K., Nakamoto, M., Shimizu, E., Minna, J. & Yokota, J. Prevalence and specificity of LKB1 genetic alterations in lung cancers. *Oncogene* **26,** 5911–5918 (2007).

38. Yang, J.-Y., Jiang, S.-H., Liu, D.-J., Yang, X.-M., Huo, Y.-M., Li, J., Hua, R., Zhang, Z.-G. & Sun, Y.-W. Decreased LKB1 predicts poor prognosis in Pancreatic Ductal Adenocarcinoma. *Sci Rep-uk* **5,** srep10575 (2015).

39. Witkiewicz, A. K., McMillan, E. A., Balaji, U., Baek, G., Lin, W.-C., Mansour, J., Mollaee, M., Wagner, K.-U., Koduru, P., Yopp, A., Choti, M. A., Yeo, C. J., McCue, P., White, M. A. & Knudsen, E. S. Whole-exome sequencing of pancreatic cancer defines genetic diversity and therapeutic targets. *Nat Commun* **6,** 6744 (2015).

40. Wingo, S. N., Gallardo, T. D., Akbay, E. A., Liang, M.-C., Contreras, C. M., Boren, T., Shimamura, T., Miller, D. S., Sharpless, N. E., Bardeesy, N., Kwiatkowski, D. J., Schorge, J. O., Wong, K.-K. & Castrillon, D. H. Somatic LKB1 Mutations Promote Cervical Cancer Progression. *Plos One* **4,** e5137 (2009).

41. Zhuang, Z.-G., Di, G.-H., Shen, Z.-Z., Ding, J. & Shao, Z.-M. Enhanced Expression of LKB1 in Breast Cancer Cells Attenuates Angiogenesis, Invasion, and Metastatic Potential. *Mol Cancer Res* **4,** 843–849 (2006).

42. Li, J., Liu, J., Li, P., Mao, X., Li, W., Yang, J. & Liu, P. Loss of LKB1 disrupts breast epithelial cell polarity and promotes breast cancer metastasis and invasion. *J Exp Clin Canc Res* **33,** 70 (2014).

43. Rhodes, L., Tate, C., Hoang, V., Burks, H., Gilliam, D., Martin, E., Elliott, S., Miller, D., Buechlein, A., Rusch, D., Tang, H., Nephew, K., Burow, M. & Collins-Burow, B. Regulation of triple-negative breast cancer cell metastasis by the tumor-suppressor liver kinase B1. *Oncogenesis* **4,** e168 (2015).

44. Chan, K. T., eja Asokan, B., King, S. J., Bo, T., Dubose, E. S., Liu, W., Berginski, M. E., Simon, J. M., Davis, I. J., Gomez, S. M., Sharpless, N. E. & Bear, J. E. LKB1 loss in melanoma disrupts directional migration toward extracellular matrix cues. *J Cell Biology* **207,** 299–315 (2014).

45. Liu, W., Monahan, K. B., Pfefferle, A. D., Shimamura, T., Sorrentino, J., Chan, K. T., Roadcap, D. W., Ollila, D. W., Thomas, N. E., Castrillon, D. H., Miller, R. C., Perou, C. M., Wong, K.-K., Bear, J. E. & Sharpless, N. E. LKB1/STK11 Inactivation Leads to Expansion of a Prometastatic Tumor Subpopulation in Melanoma. *Cancer Cell* **21,** 751–764 (2012).

46. Dobrowolski, R. & Robertis, E. Endocytic control of growth factor signalling: multivesicular bodies as signalling organelles. *Nat Rev Mol Cell Biology* **13,** 53–60 (2011).

47. Kline, E. R., Muller, S., Pan, L., Tighiouart, M., Chen, Z. & Marcus, A. I. Localization-specific LKB1 loss in head and neck squamous cell carcinoma metastasis. *Head Neck* **33,** 1501–1512 (2011).

48. Guervós, M., Marcos, C., Hermsen, M., Nuño, A., Suárez, C. & Llorente, J. Deletions of N33, STK11 and TP53 Are Involved in the Development of Lymph Node Metastasis in Larynx and Pharynx Carcinomas. *Anal Cell Pathol* **29,** 327–334

49. Peart, T., Valdes, Y., Correa, R. J., Fazio, E., Bertrand, M., McGee, J., Préfontaine, M., Sugimoto, A., DiMattia, G. E. & Shepherd, T. G. Intact LKB1 activity is required for survival of dormant ovarian cancer spheroids. *Oncotarget* **6,** 22424–22438 (2015).

50. Boudeau, J., Baas, A. F., Deak, M., Morrice, N. A., Kieloch, A., Schutkowski, M., Prescott, A. R., Clevers, H. C. & Alessi, D. R. MO25 / interact with STRAD / enhancing their ability to bind, activate and localize LKB1 in the cytoplasm. *Embo J* **22,** 5102–5114 (2003).

51. Hawley, S. A., Boudeau, J., Reid, J. L., Mustard, K. J., Udd, L., Mäkelä, T. P., Alessi, D. R. & Hardie, G. D. Complexes between the LKB1 tumor suppressor, STRADα/β and MO25α/β are upstream kinases in the AMP-activated protein kinase cascade. *J Biology* **2,** 28 (2003).

52. Boudeau, J., Scott, J. W., Resta, N., Deak, M., Kieloch, A., Komander, D., Hardie, G. D., Prescott, A. R., van Aalten, D. M. & Alessi, D. R. Analysis of the LKB1-STRAD-MO25 complex. *J Cell Sci* **117,** 6365–6375 (2004).

53. Zeqiraj, E., Filippi, B., Deak, M., Alessi, D. R. & van Aalten, D. M. Structure of the LKB1-STRAD-MO25 Complex Reveals an Allosteric Mechanism of Kinase Activation. *Science* **326,** 1707–1711 (2009).

54. Lizcano, J. M., Göransson, O., Toth, R., Deak, M., Morrice, N. A., Boudeau, J., Hawley, S. A., Udd, L., Mäkelä, T. P., Hardie, G. D. & Alessi, D. R. LKB1 is a master kinase that activates 13 kinases of the AMPK subfamily, including MARK/PAR-1. *Embo J* **23,** 833–843 (2004).

55. Sapkota, G. P., Kieloch, A., Lizcano, J. M., Lain, S., Arthur, S. J., Williams, M. R., Morrice, N., Deak, M. & Alessi, D. R. Phosphorylation of the Protein Kinase Mutated in Peutz-Jeghers Cancer Syndrome, LKB1/STK11, at Ser 431 by p90 RSK and cAMP-dependent Protein Kinase, but Not Its Farnesylation at Cys 433 , Is Essential for LKB1 to Suppress Cell Growth. *J Biol Chem* **276,** 19469–19482 (2001).

56. Hezel, A. & Bardeesy, N. LKB1; linking cell structure and tumor suppression. *Oncogene* **27,** onc2008342 (2008).

57. Kullmann, L. & Krahn, M. P. Controlling the master—upstream regulation of the tumor suppressor LKB1. *Oncogene* **37,** 3045–3057 (2018).

58. SAPKOTA, G. P., DEAK, M., KIELOCH, A., MORRICE, N., GOODARZI, A. A., YTHE, C., SHILOH, Y., LEES-MILLER, S. P. & ALESSI, D. R. Ionizing radiation induces ataxia telangiectasia mutated kinase (ATM)-mediated phosphorylation of LKB1/STK11 at Thr-366. *Biochem J* **368,** 507–516 (2002).

59. Liu, L., Siu, F.-M., Che, C.-M., Xu, A. & Wang, Y. Akt blocks the tumor suppressor activity of LKB1 by promoting phosphorylation-dependent nuclear retention through 14-3-3 proteins. *Am J Transl Res* **4,** 175–86 (2012).

60. Xie, Z., Dong, Y., Zhang, J., Scholz, R., Neumann, D. & Zou, M.-H. Identification of the serine 307 of LKB1 as a novel phosphorylation site essential for its nucleocytoplasmic transport and endothelial cell angiogenesis. *Mol Cell Biol* **29,** 3582–96 (2009).

61. Zhu, H., Moriasi, C. M., Zhang, M., Zhao, Y. & Zou, M.-H. Phosphorylation of Serine 399 in LKB1 Protein Short Form by Protein Kinase Cζ Is Required for Its Nucleocytoplasmic Transport and Consequent AMP-activated Protein Kinase (AMPK) Activation. *J Biol Chem* **288,** 16495–16505 (2013).

62. Xie, Z., Dong, Y., Zhang, M., Cui, M.-Z., Cohen, R. A., Riek, U., Neumann, D., Schlattner, U. & Zou, M.-H. Activation of Protein Kinase Cζ by Peroxynitrite Regulates LKB1-dependent AMP-activated Protein Kinase in Cultured Endothelial Cells. *J Biol Chem* **281,** 6366–6375 (2006).

63. Zheng, B., Jeong, J. H., Asara, J. M., Yuan, Y.-Y., Granter, S. R., Chin, L. & Cantley, L. C. Oncogenic B-RAF Negatively Regulates the Tumor Suppressor LKB1 to Promote

Melanoma Cell Proliferation. *Mol Cell* **33,** 237–247 (2009).

64. Casimiro, M. C., Sante, G., Rocco, A., Loro, E., Pupo, C., Pestell, T. G., Bisetto, S., Velasco-Velázquez, M. A., Jiao, X., Li, Z., Kusminski, C. M., Seifert, E. L., Wang, C., Ly, D., Zheng, B., Shen, C.-H., Scherer, P. E. & Pestell, R. G. Cyclin D1 Restrains Oncogene-Induced Autophagy by Regulating the AMPK–LKB1 Signaling Axis. *Cancer Res* **77,** 3391–3405 (2017).

65. Alexander, A., Cai, S.-L., Kim, J., Nanez, A., Sahin, M., MacLean, K. H., Inoki, K., Guan, K.-L., Shen, J., Person, M. D., Kusewitt, D., Mills, G. B., Kastan, M. B. & Walker, C. ATM signals to TSC2 in the cytoplasm to regulate mTORC1 in response to ROS. *P Natl Acad Sci Usa* **107,** 4153–8 (2010).

66. Lee, S.-W., Li, C.-F., Jin, G., Cai, Z., Han, F., Chan, C.-H., Yang, W.-L., Li, B.-K., Rezaeian, A., Li, H.-Y., Huang, H.-Y. & Lin, H.-K. Skp2-Dependent Ubiquitination and Activation of LKB1 Is Essential for Cancer Cell Survival under Energy Stress. *Mol Cell* **57,** 1022–1033 (2015).

67. Ritho, J., Arold, S. T. & Yeh, E. A Critical SUMO1 Modification of LKB1 Regulates AMPK Activity during Energy Stress. *Cell Reports* **12,** 734–742 (2015).

68. Zubiete-Franco, I., García-Rodríguez, J. L., Lopitz-Otsoa, F., Serrano-Macia, M., Simon, J., Fernández-Tussy, P., Barbier-Torres, L., Fernández-Ramos, D., Gutiérrez-de-Juan, V., de Davalillo, S., Carlevaris, O., Gómez, A., Villa, E., Calvisi, D., Martín, C., Berra, E., Aspichueta, P., Beraza, N., Varela-Rey, M., Ávila, M., Rodríguez, M. S., Mato, J. M., Díaz-Moreno, I., Díaz-Quintana, A., Delgado, T. C. & Martínez-Chantar, M. L. SUMOylation regulates LKB1 localization and its oncogenic activity in liver cancer. *Ebiomedicine* **40,** 406–421 (2019).

69. Barbier-Torres, L., Delgado, T. C., García-Rodríguez, J. L., Zubiete-Franco, I., Fernández-Ramos, D., Buqué, X., Cano, A., Juan, V., Fernández-Domínguez, I., Lopitz-Otsoa, F., Fernández-Tussy, P., Boix, L., Bruix, J., Villa, E., Castro, A., Lu, S. C., Aspichueta, P., Xirodimas, D., Varela-Rey, M., Mato, J. M., Beraza, N. & Martínez-Chantar, M. L. Stabilization of LKB1 and Akt by neddylation regulates energy metabolism in liver cancer. *Oncotarget* **6,** 2509–2523 (2015).

70. Liu, Z., Dai, X., Zhu, H., Zhang, M. & Zou, M.-H. Lipopolysaccharides Promote S-Nitrosylation and Proteasomal Degradation of Liver Kinase B1 (LKB1) in Macrophages in Vivo. *J Biological Chem* **290,** 19011–7 (2015).

71. Calamaras, T. D., Lee, C., Lan, F., Ido, Y., Siwik, D. A. & Colucci, W. S. Post-translational Modification of Serine/Threonine Kinase LKB1 via Adduction of the Reactive Lipid Species 4-Hydroxy- trans -2-nonenal (HNE) at Lysine Residue 97 Directly Inhibits Kinase Activity. *J Biol Chem* **287,** 42400–42406 (2012).

72. Lan, F., Cacicedo, J. M., Ruderman, N. & Ido, Y. SIRT1 modulation of the acetylation

status, cytosolic localization, and activity of LKB1. Possible role in AMP-activated protein kinase activation. *J Biological Chem* **283,** 27628–35 (2008).

73. Shackelford, D. B. & Shaw, R. J. The LKB1-AMPK pathway: metabolism and growth control in tumour suppression. *Nat Rev Cancer* **9,** 563–75 (2009).

74. Manning, G., Whyte, D., Martinez, R., Hunter, T. & Sudarsanam, S. The Protein Kinase Complement of the Human Genome. *Science* **298,** 1912–1934 (2002).

75. Woods, A., Munday, M., Scott, J., Yang, X., Carlson, M. & Carling, D. Yeast SNF1 is functionally related to mammalian AMP-activated protein kinase and regulates acetyl-CoA carboxylase in vivo. *J Biological Chem* **269,** 19509–15 (1994).

76. Yuan, S.-M., Nie, W.-C., He, F., Jia, Z.-W. & Gao, X.-D. Kin2, the Budding Yeast Ortholog of Animal MARK/PAR-1 Kinases, Localizes to the Sites of Polarized Growth and May Regulate Septin Organization and the Cell Wall. *Plos One* **11,** e0153992 (2016).

77. Tassan, J.-P. & Goff, X. An overview of the KIN1/PAR-1/MARK kinase family. *Biol Cell* **96,** 193–199 (2004).

78. Fogarty, S., Ross, F., Ciruelos, V. D., Gray, A., Gowans, G. & Hardie, D. AMPK Causes Cell Cycle Arrest in LKB1-Deficient Cells via Activation of CAMKK2. *Mol Cancer Res* **14,** 683–695 (2016).

79. Zhong, D., Sun, L. & Dong, L. Molecular mechanisms of LKB1 induced cell cycle arrest. *Thorac Cancer* **4,** 229–233 (2013).

80. Nakada, D., Saunders, T. L. & Morrison, S. J. Lkb1 regulates cell cycle and energy metabolism in haematopoietic stem cells. *Nature* **468,** 653–658 (2010).

81. Tiainen, M., Ylikorkala, A. & Makela, T. Growth suppression by Lkb1 is mediated by a G1 cell cycle arrest. *Proc National Acad Sci* **96,** 9248–9251 (1999).

82. Ui, A., Ogiwara, H., Nakajima, S., Kanno, S., Watanabe, R., Harata, M., Okayama, H., Harris, C., Yokota, J., Yasui, A. & Kohno, T. Possible involvement of LKB1-AMPK signaling in non-homologous end joining. *Oncogene* **33,** 1640–1648 (2013).

83. Gupta, R., Liu, A. Y., Glazer, P. M. & Wajapeyee, N. LKB1 preserves genome integrity by stimulating BRCA1 expression. *Nucleic Acids Res* **43,** 259–71 (2014).

84. Wang, Y.-S., Chen, J., Cui, F., Wang, H., Wang, S., Hang, W., Zeng, Q., Quan, C.-S., Zhai, Y.-X., Wang, J.-W., Shen, X.-F., Jian, Y.-P., Zhao, R.-X., Werle, K. D., Cui, R., Liang, J., Li, Y.-L. & Xu, Z.-X. LKB1 is a DNA damage response protein that regulates cellular sensitivity to PARP inhibitors. *Oncotarget* **7,** (2016).

85. Young, N. P., Kamireddy, A., Nostrand, J. L., Eichner, L. J., Shokhirev, M., Dayn, Y.

& Shaw, R. J. AMPK governs lineage specification through Tfeb-dependent regulation of lysosomes. *Gene Dev* **30,** 535–552 (2016).

86. Jishage, K., Nezu, J., Kawase, Y., Iwata, T., Watanabe, M., Miyoshi, A., Ose, A., Habu, K., Kake, T., Kamada, N., Ueda, O., Kinoshita, M., Jenne, D. E., Shimane, M. & Suzuki, H. Role of Lkb1, the causative gene of Peutz–Jegher's syndrome, in embryogenesis and polyposis. *Proc National Acad Sci* **99,** 8903–8908 (2002).

87. van der Velden, Y. U., Wang, L., Zevenhoven, J., van Rooijen, E., van Lohuizen, M., Giles, R. H., Clevers, H. & Haramis, A.-P. G. The serine-threonine kinase LKB1 is essential for survival under energetic stress in zebrafish. *P Natl Acad Sci Usa* **108,** 4358–63 (2011).

88. Sandí, M.-J., Marshall, C. B., Balan, M., Coyaud, É., Zhou, M., Monson, D. M., Ishiyama, N., Chandrakumar, A. A., Rose, J., Couzens, A. L., Gingras, A.-C., Raught, B., Xu, W., Ikura, M., Morrison, D. K. & Rottapel, R. MARK3-mediated phosphorylation of ARHGEF2 couples microtubules to the actin cytoskeleton to establish cell polarity. *Sci Signal* **10,** eaan3286 (2017).

89. Goodwin, J. M., Svensson, R. U., Lou, H., Winslow, M. M., Turk, B. E. & Shaw, R. J. An AMPK-Independent Signaling Pathway Downstream of the LKB1 Tumor Suppressor Controls Snail1 and Metastatic Potential. *Mol Cell* **55,** 436–450 (2014).

90. Kline, E. R., Shupe, J., Gilbert-Ross, M., Zhou, W. & Marcus, A. I. LKB1 Represses Focal Adhesion Kinase (FAK) Signaling via a FAK-LKB1 Complex to Regulate FAK Site Maturation and Directional Persistence. *J Biol Chem* **288,** 17663–17674 (2013).

91. Zagórska, A., Deak, M., Campbell, D. G., Banerjee, S., Hirano, M., Aizawa, S., Prescott, A. R. & Alessi, D. R. New Roles for the LKB1-NUAK Pathway in Controlling Myosin Phosphatase Complexes and Cell Adhesion. *Sci Signal* **3,** ra25–ra25 (2010).

92. Marcus, A. I. & Zhou, W. LKB1 Regulated Pathways in Lung Cancer Invasion and Metastasis. *J Thorac Oncol* **5,** 1883–1886 (2010).

93. Garcia, D. & Shaw, R. J. AMPK: Mechanisms of Cellular Energy Sensing and Restoration of Metabolic Balance. *Mol Cell* **66,** 789–800 (2017).

94. Shaw, R. J., Kosmatka, M., Bardeesy, N., Hurley, R. L., Witters, L. A., DePinho, R. A. & Cantley, L. C. The tumor suppressor LKB1 kinase directly activates AMP-activated kinase and regulates apoptosis in response to energy stress. *P Natl Acad Sci Usa* **101,** 3329–3335 (2004).

95. Woods, A., Johnstone, S. R., Dickerson, K., Leiper, F. C., Fryer, L., Neumann, D., Schlattner, U., Wallimann, T., Carlson, M. & Carling, D. LKB1 Is the Upstream Kinase in the AMP-Activated Protein Kinase Cascade. *Curr Biol* **13,** 2004–2008 (2003).

96. Gwinn, D. M., Shackelford, D. B., Egan, D. F., Mihaylova, M. M., Mery, A., Vasquez, D. S., Turk, B. E. & Shaw, R. J. AMPK Phosphorylation of Raptor Mediates a Metabolic Checkpoint. *Mol Cell* **30,** 214–226 (2008).

97. Ng, T., Leprivier, G., Robertson, Chow, C., Martin, M., Laderoute, K., Davicioni, E., Triche, T. & Sorensen, P. The AMPK stress response pathway mediates anoikis resistance through inhibition of mTOR and suppression of protein synthesis. *Cell Death Differ* **19,** cdd2011119 (2011).

98. Inoki, K., Zhu, T. & Guan, K.-L. TSC2 Mediates Cellular Energy Response to Control Cell Growth and Survival. *Cell* **115,** 577–590 (2003).

99. Li, Y., Xu, S., Mihaylova, M. M., Zheng, B., Hou, X., Jiang, B., Park, O., Luo, Z., Lefai, E., Shyy, J., Gao, B., Wierzbicki, M., Verbeuren, T. J., Shaw, R. J., Cohen, R. A. & Zang, M. AMPK phosphorylates and inhibits SREBP activity to attenuate hepatic steatosis and atherosclerosis in diet-induced insulin-resistant mice. *Cell Metab* **13,** 376–88 (2011).

100. Mihaylova, M. M., Vasquez, D. S., Ravnskjaer, K., Denechaud, P.-D., Yu, R. T., Alvarez, J. G., Downes, M., Evans, R. M., Montminy, M. & Shaw, R. J. Class IIa Histone Deacetylases Are Hormone-Activated Regulators of FOXO and Mammalian Glucose Homeostasis. *Cell* **145,** 607–621 (2011).

101. Hardie, D. AMPK: A Target for Drugs and Natural Products With Effects on Both Diabetes and Cancer. *Diabetes* **62,** 2164–2172 (2013).

102. Wu, N., Zheng, B., Shaywitz, A., Dagon, Y., Tower, C., Bellinger, G., Shen, C.-H., Wen, J., Asara, J., McGraw, T. E., Kahn, B. B. & Cantley, L. C. AMPK-dependent degradation of TXNIP upon energy stress leads to enhanced glucose uptake via GLUT1. *Mol Cell* **49,** 1167–75 (2013).

103. Egan, D. F., Shackelford, D. B., Mihaylova, M. M., Gelino, S., Kohnz, R. A., Mair, W., Vasquez, D. S., Joshi, A., Gwinn, D. M., Taylor, R., Asara, J. M., Fitzpatrick, J., Dillin, A., Viollet, B., Kundu, M., Hansen, M. & Shaw, R. J. Phosphorylation of ULK1 (hATG1) by AMP-Activated Protein Kinase Connects Energy Sensing to Mitophagy. *Science* **331,** 456–461 (2011).

104. Mack, H. I., Zheng, B., Asara, J. M. & Thomas, S. M. AMPK-dependent phosphorylation of ULK1 regulates ATG9 localization. *Autophagy* **8,** 1197–1214 (2012).

105. Kim, J., Kundu, M., Viollet, B. & Guan, K.-L. AMPK and mTOR regulate autophagy through direct phosphorylation of Ulk1. *Nat Cell Biol* **13,** 132–141 (2011).

106. Toyama, E., Herzig, S., Courchet, J., Lewis, T. L., Losón, O. C., Hellberg, K., Young, N. P., Chen, H., Polleux, F., Chan, D. C. & Shaw, R. J. AMP-activated protein kinase mediates mitochondrial fission in response to energy stress. *Science* **351,** 275–281 (2016).

107. Ducommun, S., Deak, M., Sumpton, D., Ford, R. J., Galindo, A., Kussmann, M., Viollet, B., Steinberg, G. R., Foretz, M., Dayon, L., Morrice, N. A. & Sakamoto, K. Motif affinity and mass spectrometry proteomic approach for the discovery of cellular AMPK targets: Identification of mitochondrial fission factor as a new AMPK substrate. *Cell Signal* **27,** 978–988 (2015).

108. Ahmadian, M., Abbott, M. J., Tang, T., Hudak, C. S., Kim, Y., Bruss, M., Hellerstein, M. K., Lee, H.-Y., Samuel, V. T., Shulman, G. I., Wang, Y., Duncan, R. E., Kang, C. & Sul, H. Desnutrin/ATGL is regulated by AMPK and is required for a brown adipose phenotype. *Cell Metab* **13,** 739–48 (2011).

109. Kim, S.-J., Tang, T., Abbott, M., Viscarra, J. A., Wang, Y. & Sul, H. AMPK Phosphorylates Desnutrin/ATGL and Hormone-Sensitive Lipase To Regulate Lipolysis and Fatty Acid Oxidation within Adipose Tissue. *Mol Cell Biol* **36,** 1961–76 (2016).

110. Sundararaman, A., Amirtham, U. & Rangarajan, A. Calcium-Oxidant Signaling Network Regulates AMP-activated Protein Kinase (AMPK) Activation upon Matrix Deprivation. *J Biol Chem* **291,** 14410–14429 (2016).

111. vanth Hindupur, K., Balaji, S. A., Saxena, M., Pandey, S., enivasmurthy Sravan, G., Heda, N., Kumar, V. M., Mukherjee, G., Dey, D. & Rangarajan, A. Identification of a novel AMPK-PEA15 axis in the anoikis-resistant growth of mammary cells. *Breast Cancer Res* **16,** 420 (2014).

112. Jeon, S.-M., Chandel, N. S. & Hay, N. AMPK regulates NADPH homeostasis to promote tumour cell survival during energy stress. *Nature* **485,** 661 (2012).

113. Herzig, S. & Shaw, R. J. AMPK: guardian of metabolism and mitochondrial homeostasis. *Nat Rev Mol Cell Bio* **19,** 121–135 (2017).

114. Mihaylova, M. M. & Shaw, R. J. The AMPK signalling pathway coordinates cell growth, autophagy and metabolism. *Nat Cell Biol* **13,** 1016 (2011).

115. Hardie, G. D. AMPK: positive and negative regulation, and its role in whole-body energy homeostasis. *Curr Opin Cell Biol* **33,** 1–7 (2015).

116. Shaw, R. J. AMPK Keeps Tumor Cells from Starving to Death. *Cell Stem Cell* **17,** 503–504 (2015).

117. Hardie, G. D., Schaffer, B. E. & Brunet, A. AMPK: An Energy-Sensing Pathway with Multiple Inputs and Outputs. *Trends Cell Biol* **26,** 190–201 (2016).

118. Hollstein, P. E., Eichner, L. J., Brun, S. N., Kamireddy, A., Svensson, R. U., Vera, L. I., Ross, D. S., Rymoff, T., Hutchins, A., Galvez, H. M., Williams, A. E., Shokhirev, M. N., Screaton, R. A., Berdeaux, R. & Shaw, R. J. The AMPK-related kinases SIK1 and SIK3 mediate key tumor suppressive effects of LKB1 in NSCLC. *Cancer Discov* CD-18-

1261 (2019). doi:10.1158/2159-8290.cd-18-1261

119. Cheng, H., Liu, P., Wang, Z. C., Zou, L., Santiago, S., Garbitt, V., Gjoerup, O. V., Iglehart, D. J., Miron, A., Richardson, A. L., Hahn, W. C. & Zhao, J. J. SIK1 Couples LKB1 to p53-Dependent Anoikis and Suppresses Metastasis. *Sci Signal* **2,** ra35–ra35 (2009).

120. Buchheit, C. L., Weigel, K. J. & Schafer, Z. T. Cancer cell survival during detachment from the ECM: multiple barriers to tumour progression. *Nat Rev Cancer* **14,** 632–641 (2014).

121. Paoli, P., Giannoni, E. & Chiarugi, P. Anoikis molecular pathways and its role in cancer progression. *Biochimica Et Biophysica Acta Bba - Mol Cell Res* **1833,** 3481–3498 (2013).

122. Avivar-Valderas, A., Bobrovnikova-Marjon, E., Diehl, A. J., Bardeesy, N., Debnath, J. & Aguirre-Ghiso, J. Regulation of autophagy during ECM detachment is linked to a selective inhibition of mTORC1 by PERK. *Oncogene* **32,** 4932 (2013).

123. Taddei, M., Giannoni, E., Fiaschi, T. & Chiarugi, P. Anoikis: an emerging hallmark in health and diseases. *J Pathology* **226,** 380–393 (2012).

124. Frisch & Francis, H. Disruption of epithelial cell-matrix interactions induces apoptosis. *J Cell Biology* **124,** 619–626 (1994).

125. Hoffman, N. J., Parker, B. L., Chaudhuri, R., Fisher-Wellman, K. H., Kleinert, M., Humphrey, S. J., Yang, P., Holliday, M., Trefely, S., Fazakerley, D. J., Stöckli, J., Burchfield, J. G., Jensen, T. E., Jothi, R., Kiens, B., Wojtaszewski, J. F., Richter, E. A. & James, D. E. Global Phosphoproteomic Analysis of Human Skeletal Muscle Reveals a Network of Exercise-Regulated Kinases and AMPK Substrates. *Cell Metab* **22,** 922–35 (2015).

126. Nelson, M. E., Parker, B. L., Burchfield, J. G., Hoffman, N. J., Needham, E. J., Cooke, K. C., Naim, T., Sylow, L., Ling, N. X., Francis, D., Norris, D. M., Chaudhuri, R., Oakhill, J. S., Richter, E. A., Lynch, G. S., Stöckli, J. & James, D. E. Phosphoproteomics reveals conserved exercise-stimulated signaling and AMPK regulation of store-operated calcium entry. *Embo J* (2019). doi:10.15252/embj.2019102578

127. Banko, M. R., Allen, J. J., Schaffer, B. E., Wilker, E. W., Tsou, P., White, J. L., Villén, J., Wang, B., Kim, S. R., Sakamoto, K., Gygi, S. P., Cantley, L. C., Yaffe, M. B., okat, K. & Brunet, A. Chemical genetic screen for AMPKα2 substrates uncovers a network of proteins involved in mitosis. *Mol Cell* **44,** 878–92 (2011).

128. Schaffer, B. E., Levin, R. S., Hertz, N. T., Maures, T. J., Schoof, M. L., Hollstein, P. E., Benayoun, B. A., Banko, M. R., Shaw, R. J., okat, K. & Brunet, A. Identification of AMPK Phosphorylation Sites Reveals a Network of Proteins Involved in Cell Invasion and

Facilitates Large-Scale Substrate Prediction. *Cell Metab* **22,** 907–21 (2015).

129. Stein, B. D., Calzolari, D., Hellberg, K., Hu, Y. S., He, L., Hung, C.-M., Toyama, E. Q., Ross, D. S., Lillemeier, B. F., Cantley, L. C., Yates, J. R. & Shaw, R. J. Quantitative In Vivo Proteomics of Metformin Response in Liver Reveals AMPK-Dependent and -Independent Signaling Networks. *Cell Reports* **29,** 3331-3348.e7 (2019).

130. Ducommun, S., Deak, M., Zeigerer, A., Göransson, O., Seitz, S., Collodet, C., Madsen, A. B., Jensen, T. E., Viollet, B., Foretz, M., Gut, P., Sumpton, D. & Sakamoto, K. Chemical genetic screen identifies Gapex-5/GAPVD1 and STBD1 as novel AMPK substrates. *Cell Signal* **57,** 45–57 (2019).

131. Chen, Y., Liu, Y., Zhou, Y. & You, H. Molecular mechanism of LKB1 in the invasion and metastasis of colorectal cancer. *Oncol Rep* **41,** 1035–1044 (2018).

132. He, T.-Y., Tsai, L.-H., Huang, C.-C., Chou, M.-C. & Lee, H. LKB1 Loss at Transcriptional Level Promotes Tumor Malignancy and Poor Patient Outcomes in Colorectal Cancer. *Ann Surg Oncol* **21,** 703–710 (2014).

133. Murray, C. W., Brady, J. J., Tsai, M. K., Li, C., Winters, I. P., Tang, R., Andrejka, L., Ma, R. K., Kunder, C. A., Chu, P. & Winslow, M. M. An Lkb1-Sik axis suppresses lung tumor growth and controls differentiation. *Cancer Discov* **9,** 1590–1605 (2019).

134. Rodón, L., Svensson, R. U., Wiater, E., Chun, M. G., Tsai, W.-W., Eichner, L. J., Shaw, R. J. & Montminy, M. The CREB coactivator CRTC2 promotes oncogenesis in LKB1-mutant non-small cell lung cancer. *Sci Adv* **5,** eaaw6455 (2019).

135. Eichner, L. J., Brun, S. N., Herzig, S., Young, N. P., Curtis, S. D., Shackelford, D. B., Shokhirev, M. N., Leblanc, M., Vera, L. I., Hutchins, A., Ross, D. S., Shaw, R. J. & Svensson, R. U. Genetic Analysis Reveals AMPK Is Required to Support Tumor Growth in Murine Kras-Dependent Lung Cancer Models. *Cell Metab* **29,** 285-302.e7 (2018).

136. Rizvi, H., Sanchez-Vega, F., La, K., Chatila, W., Jonsson, P., Halpenny, D., Plodkowski, A., Long, N., Sauter, J. L., Rekhtman, N., Hollmann, T., Schalper, K. A., Gainor, J. F., Shen, R., Ni, A., Arbour, K. C., Merghoub, T., Wolchok, J., Snyder, A., Chaft, J. E., Kris, M. G., Rudin, C. M., Socci, N. D., Berger, M. F., Taylor, B. S., Zehir, A., Solit, D. B., Arcila, M. E., Ladanyi, M., Riely, G. J., Schultz, N. & Hellmann, M. D. Molecular Determinants of Response to Anti–Programmed Cell Death (PD)-1 and Anti–Programmed Death-Ligand (PD-L)-Ligand 1 Blockade in Patients With Non–Small-Cell Lung Cancer Profiled With Targeted Next-Generation Sequencing. *J Clin Oncol* **36,** JCO.2017.75.338 (2018).

137. Skoulidis, F., Goldberg, M. E., Greenawalt, D. M., Hellmann, M. D., Awad, M. M., Gainor, J. F., Schrock, A. B., Hartmaier, R. J., Trabucco, S. E., Gay, L., Ali, S. M., Elvin, J. A., Singal, G., Ross, J. S., Fabrizio, D., abo, P., Chang, H., Sasson, A., nivasan, S., Kirov, S., Szustakowski, J., Vitazka, P., Edwards, R., Bufill, J. A., Sharma, N., Ou, S.-H.

I., Peled, N., Spigel, D. R., Rizvi, H., Aguilar, E., Carter, B. W., Erasmus, J., Halpenny, D. F., Plodkowski, A. J., Long, N. M., Nishino, M., Denning, W. L., Galan-Cobo, A., Hamdi, H., Hirz, T., Tong, P., Wang, J., Rodriguez-Canales, J., Villalobos, P. A., Parra, E. R., Kalhor, N., oll, L., Sauter, J. L., Jungbluth, A. A., Mino-Kenudson, M., Azimi, R., Elamin, Y. Y., Zhang, J., Leonardi, G. C., Jiang, F., Wong, K.-K., Lee, J. J., Papadimitrakopoulou, V. A., Wistuba, I. I., Miller, V. A., Frampton, G. M., Wolchok, J. D., Shaw, A. T., Jänne, P. A., Stephens, P. J., Rudin, C. M., Geese, W. J., Albacker, L. A. & Heymach, J. V. STK11/LKB1 Mutations and PD-1 Inhibitor Resistance in KRAS-Mutant Lung Adenocarcinoma. *Cancer Discov* **8,** 822–835 (2018).

138. Bonanno, L., Zulato, E., Pavan, A., Attili, I., Pasello, G., Conte, P. & Indraccolo, S. LKB1 and Tumor Metabolism: The Interplay of Immune and Angiogenic Microenvironment in Lung Cancer. *Int J Mol Sci* **20,** 1874 (2019).

139. Fang, X., Liu, X., Yao, L., Chen, C., Lin, J., Ni, P., Zheng, X. & Fan, Q. New insights into FAK phosphorylation based on a FAT domain-defective mutation. *Plos One* **9,** e107134 (2014).

140. Frisch, S., Vuori, K., Ruoslahti, E. & Chan-Hui, P. Control of adhesion-dependent cell survival by focal adhesion kinase. *J Cell Biology* **134,** 793–799 (1996).

141. Xu, Z., Mei, J. & Tan, Y. Baicalin attenuates DDP (cisplatin) resistance in lung cancer by downregulating MARK2 and p-Akt. *Int J Oncol* **50,** 93–100 (2016).

142. Shackelford, D. B., Abt, E., Gerken, L., Vasquez, D. S., Seki, A., Leblanc, M., Wei, L., Fishbein, M. C., Czernin, J., Mischel, P. S. & Shaw, R. J. LKB1 inactivation dictates therapeutic response of non-small cell lung cancer to the metabolism drug phenformin. *Cancer Cell* **23,** 143–58 (2013).

143. Yang, H., Gao, Y., Fan, X., Liu, X., Peng, L. & Ci, X. Oridonin Sensitizes Cisplatin-Induced Apoptosis via AMPK/Akt/mTOR-Dependent Autophagosome Accumulation in A549 Cells. *Frontiers Oncol* **9,** 769 (2019).

144. Shao, J., Zhang, A., Qin, W., Zheng, L., Zhu, Y. & Chen, X. AMP-activated protein kinase (AMPK) activation is involved in chrysin-induced growth inhibition and apoptosis in cultured A549 lung cancer cells. *Biochem Bioph Res Co* **423,** 448–53 (2012).

145. Hou, X., Liu, J.-E., Liu, W., Liu, C.-Y., Liu, Z.-Y. & Sun, Z.-Y. A new role of NUAK1: directly phosphorylating p53 and regulating cell proliferation. *Oncogene* **30,** 2933–42 (2011).

146. Sanjana, N. E., Shalem, O. & Zhang, F. Improved vectors and genome-wide libraries for CRISPR screening. *Nat Methods* **11,** 783–784 (2014).

147. Peng, J., Elias, J. E., Thoreen, C. C., Licklider, L. J. & Gygi, S. P. Evaluation of Multidimensional Chromatography Coupled with Tandem Mass Spectrometry

(LC/LC−MS/MS) for Large-Scale Protein Analysis: The Yeast Proteome. *J Proteome Res* **2,** 43–50 (2003).

148. Mostovenko, E., Hassan, C., Rattke, J., elder, A., van Veelen, P. A. & Palmblad, M. Comparison of peptide and protein fractionation methods in proteomics. *Eupa Open Proteom* **1,** 30–37 (2013).

149. Xu, T., Park, S., Venable, J., Wohlschlegel, J., Diedrich, J., Cociorva, D., Lu, B., Liao, L., Hewel, J., Han, X., Wong, C., Fonslow, B., Delahunty, C., Gao, Y., Shah, H. & Yates, J. ProLuCID: An improved SEQUEST-like algorithm with enhanced sensitivity and specificity. *J Proteomics* **129,** 16–24 (2015).

150. Tabb, D. L., nald, H. W. & Yates, J. R. DTASelect and Contrast: Tools for Assembling and Comparing Protein Identifications from Shotgun Proteomics. *J Proteome Res* **1,** 21–26 (2002).

151. Team, Rs. RStudio: Integrated Development for R.

152. for Computing, F. R., Vienna & Austria. R: A language and environment for statistical computing. .

153. Shaw, R. J., Bardeesy, N., Manning, B. D., Lopez, L., Kosmatka, M., DePinho, R. A. & Cantley, L. C. The LKB1 tumor suppressor negatively regulates mTOR signaling. *Cancer Cell* **6,** 91–99 (2004).

154. Spilker, C. & Kreutz, M. R. RapGAPs in brain: multipurpose players in neuronal Rap signalling. *Eur J Neurosci* **32,** 1–9 (2010).

155. Gridley, S., Chavez, J. A., Lane, W. S. & Lienhard, G. E. Adipocytes contain a novel complex similar to the tuberous sclerosis complex. *Cell Signal* **18,** 1626–1632 (2006).

156. Jia, Z., Liu, W., Gong, L. & Xiao, Z. Downregulation of RASAL2 promotes the proliferation, epithelial-mesenchymal transition and metastasis of colorectal cancer cells. *Oncol Lett* **13,** 1379–1385 (2017).

157. Sears, R. & Gray, J. W. Epigenomic Inactivation of RasGAPs Activates RAS Signaling in a Subset of Luminal B Breast Cancers. *Cancer Discov* **7,** 131–133 (2017).

158. Li, N. & Li, S. RASAL2 promotes lung cancer metastasis through epithelial-mesenchymal transition. *Biochem Bioph Res Co* **455,** 358–62 (2014).

159. McLaughlin, S., Olsen, S., Dake, B., Raedt, T., Lim, E., Bronson, R., Beroukhim, R., Polyak, K., Brown, M., Kuperwasser, C. & Cichowski, K. The RasGAP gene, RASAL2, is a tumor and metastasis suppressor. *Cancer Cell* **24,** 365–78 (2013).

160. Pan, Y., Tong, J., Lung, R., Kang, W., Kwan, J., Chak, W., Tin, K., Chung, L., Wu,

F., Ng, S., Mak, T., Yu, J., Lo, K., Chan, A. & To, K. RASAL2 promotes tumor progression through LATS2/YAP1 axis of hippo signaling pathway in colorectal cancer. *Mol Cancer* **17,** 102 (2018).

161. Fang, J.-F., Zhao, H.-P., Wang, Z.-F. & Zheng, S.-S. Upregulation of RASAL2 promotes proliferation and metastasis, and is targeted by miR-203 in hepatocellular carcinoma. *Mol Med Rep* **15,** 2720–2726 (2017).

162. Yan, M., Li, X., Tong, D., Han, C., Zhao, R., He, Y. & Jin, X. miR-136 suppresses tumor invasion and metastasis by targeting RASAL2 in triple-negative breast cancer. *Oncol Rep* **36,** 65–71 (2016).

163. Feng, M., Bao, Y., Li, Z., Li, J., Gong, M., Lam, S., Wang, J., Marzese, D. M., Donovan, N., Tan, E., Hoon, D. S. & Yu, Q. RASAL2 activates RAC1 to promote triple-negative breast cancer progression. *J Clin Investigation* **124,** 5291–304 (2014).

164. Zhou, B., Zhu, W., Jiang, X. & Ren, C. RASAL2 Plays Inconsistent Roles in Different Cancers. *Frontiers Oncol* **9,** 1235 (2019).

165. Zhao, H., Pykäläinen, A. & Lappalainen, P. I-BAR domain proteins: linking actin and plasma membrane dynamics. *Curr Opin Cell Biol* **23,** 14–21 (2011).

166. Kast, D. J. & Dominguez, R. Mechanism of IRSp53 inhibition by 14-3-3. *Nat Commun* **10,** 483 (2019).

167. Kast, D. J. & Dominguez, R. IRSp53 coordinates AMPK and 14-3-3 signaling to regulate filopodia dynamics and directed cell migration. *Mol Biol Cell* **30,** 1285–1297 (2019).

168. Robens, J., Yeow-Fong, L., Ng, E., Hall, C. & Manser, E. Regulation of IRSp53-Dependent Filopodial Dynamics by Antagonism between 14-3-3 Binding and SH3-Mediated Localization. *Mol Cell Biol* **30,** 829–844 (2009).

169. Behrends, C., Sowa, M. E., Gygi, S. P. & Harper, W. J. Network organization of the human autophagy system. *Nature* **466,** 68–76 (2010).

170. Postema, M. M., Grega-Larson, N. E., Neininger, A. C. & Tyska, M. J. IRTKS (BAIAP2L1) Elongates Epithelial Microvilli Using EPS8-Dependent and Independent Mechanisms. *Curr Biology Cb* **28,** 2876-2888.e4 (2018).

171. Millard, T., Dawson, J. & Machesky, L. Characterisation of IRTKS, a novel IRSp53/MIM family actin regulator with distinct filament bundling properties. *J Cell Sci* **120,** 1663–1672 (2007).

172. Zhu, M., Settele, F., Kotak, S., Sanchez-Pulido, L., Ehret, L., Ponting, C. P., Gönczy, P. & Hoffmann, I. MISP is a novel Plk1 substrate required for proper spindle orientation

and mitotic progression. *J Cell Biology* **200,** 773–787 (2013).

173. Maier, B., Kirsch, M., Anderhub, S., Zentgraf, H. & Krämer, A. The novel actin/focal adhesion-associated protein MISP is involved in mitotic spindle positioning in human cells. *Cell Cycle Georget Tex* **12,** 1457–71 (2013).

174. Shirakawa, R., Fukai, S., Kawato, M., Higashi, T., Kondo, H., Ikeda, T., Nakayama, E., Okawa, K., Nureki, O., Kimura, T., Kita, T. & Horiuchi, H. Tuberous Sclerosis Tumor Suppressor Complex-like Complexes Act as GTPase-activating Proteins for Ral GTPases. *J Biol Chem* **284,** 21580–21588 (2009).

175. Shirakawa, R. & Horiuchi, H. Ral GTPases: crucial mediators of exocytosis and tumourigenesis. *J Biochem* **157,** 285–299 (2015).

176. Uegaki, M., Kita, Y., Shirakawa, R., Teramoto, Y., Kamiyama, Y., Saito, R., Yoshikawa, T., Sakamoto, H., Goto, T., Akamatsu, S., Yamasaki, T., Inoue, T., Suzuki, A., Horiuchi, H., Ogawa, O. & Kobayashi, T. Downregulation of RalGTPase-activating protein promotes invasion of prostatic epithelial cells and progression from intraepithelial neoplasia to cancer during prostate carcinogenesis. *Carcinogenesis* (2019). doi:10.1093/carcin/bgz082

177. Saito, R., Shirakawa, R., Nishiyama, H., Kobayashi, T., Kawato, M., Kanno, T., Nishizawa, K., Matsui, Y., Ohbayashi, T., Horiguchi, M., Nakamura, T., Ikeda, T., Yamane, K., Nakayama, E., Nakamura, E., Toda, Y., Kimura, T., Kita, T., Ogawa, O. & Horiuchi, H. Downregulation of Ral GTPase-activating protein promotes tumor invasion and metastasis of bladder cancer. *Oncogene* **32,** 894–902 (2012).

178. Chen, Q., Quan, C., Xie, B., Chen, L., Zhou, S., Toth, R., Campbell, D. G., Lu, S., Shirakawa, R., Horiuchi, H., Li, C., Yang, Z., MacKintosh, C., Wang, H. & Chen, S. GARNL1, a major RalGAP α subunit in skeletal muscle, regulates insulin-stimulated RalA activation and GLUT4 trafficking via interaction with 14-3-3 proteins. *Cell Signal* **26,** 1636–48 (2014).

179. Dolnik, A., Kanwal, N., Mackert, S., Halbedl, S., Proepper, C., Bockmann, J., Schoen, M., Boeckers, T. M., Kühl, S. J. & Schmeisser, M. J. Sipa1l3/SPAR3 is targeted to postsynaptic specializations and interacts with the Fezzin ProSAPiP1/Lzts3. *J Neurochem* **136,** 28–35 (2015).

180. Pak, D. T., Yang, S., Rudolph-Correia, S., Kim, E. & Sheng, M. Regulation of Dendritic Spine Morphology by SPAR, a PSD-95-Associated RapGAP. *Neuron* **31,** 289–303 (2001).

181. Spilker, C., Sanhueza, G. A., Böckers, T. M., Kreutz, M. R. & Gundelfinger, E. D. SPAR2, a novel SPAR-related protein with GAP activity for Rap1 and Rap2. *J Neurochem* **0,** 071027034046003-??? (2007).

182. Zheng, D., Niu, S., Yu, D., Zhan, X. H., Zeng, X., Cui, B., Chen, Y., Yoon, J., Martin, S. S., Lu, X. & Zhan, X. Abba promotes PDGF-mediated membrane ruffling through activation of the small GTPase Rac1. *Biochem Bioph Res Co* **401,** 527–32 (2010).

183. Chao, A., Tsai, C.-L., Jung, S.-M., Chuang, W.-C., Kao, C., Hsu, A., Chen, S.-H., Lin, C.-Y., Lee, Y.-C., Lee, Y.-S., Wang, T.-H., Wang, H.-S. & Lai, C.-H. BAI1-Associated Protein 2-Like 1 (BAIAP2L1) Is a Potential Biomarker in Ovarian Cancer. *Plos One* **10,** e0133081 (2015).

184. Vodicska, B., Cerikan, B., Schiebel, E. & Hoffmann, I. MISP regulates the IQGAP1/Cdc42 complex to collectively orchestrate spindle orientation and mitotic progression. *Sci Rep-uk* **8,** 6330 (2018).

185. Kumeta, M., Gilmore, J. L., Umeshima, H., Ishikawa, M., Kitajiri, S., Horigome, T., Kengaku, M. & Takeyasu, K. Caprice/MISP is a novel F-actin bundling protein critical for actin-based cytoskeletal reorganizations. *Genes Cells Devoted Mol Cell Mech* **19,** 338–49 (2014).

186. Rovina, D., Fontana, L., Monti, L., Novielli, C., Panini, N., Sirchia, S., Erba, E., Magnani, I. & Larizza, L. Microtubule-associated protein/microtubule affinity-regulating kinase 4 (MARK4) plays a role in cell cycle progression and cytoskeletal dynamics. *Eur J Cell Biol* **93,** 355–65 (2014).

187. McAlister, G. C., Nusinow, D. P., Jedrychowski, M. P., Wühr, M., Huttlin, E. L., Erickson, B. K., Rad, R., Haas, W. & Gygi, S. P. MultiNotch MS3 enables accurate, sensitive, and multiplexed detection of differential expression across cancer cell line proteomes. *Anal Chem* **86,** 7150–8 (2014).

188. He, L., Diedrich, J., Chu, Y.-Y. & Yates, J. R. Extracting Accurate Precursor Information for Tandem Mass Spectra by RawConverter. *Anal Chem* **87,** 11361–11367 (2015).

189. Park, S., Aslanian, A., McClatchy, D. B., Han, X., Shah, H., Singh, M., Rauniyar, N., Moresco, J. J., Pinto, A. F., Diedrich, J. K., Delahunty, C. & Yates, J. R. Census 2: isobaric labeling data analysis. *Bioinformatics* **30,** 2208–2209 (2014).

190. de Hoon, M., Imoto, S., Nolan, J. & Miyano, S. Open source clustering software. *Bioinformatics* **20,** 1453–1454 (2004).

191. Saldanha, A. Java Treeview--extensible visualization of microarray data. *Bioinformatics* **20,** 3246–3248 (2004).

192. Wickham, H., François, R. & and Müller, L. dplyr: A Grammar of Data Manipulation. (2019).

193. Hunt, S. E., McLaren, W., Gil, L., Thormann, A., Schuilenburg, H., Sheppard, D.,

Parton, A., Armean, I. M., Trevanion, S. J., Flicek, P. & Cunningham, F. Ensembl variation resources. *Database* **2018,** (2018).

194. Zerbino, D. R., Achuthan, P., Akanni, W., Amode, R. M., Barrell, D., Bhai, J., Billis, K., Cummins, C., Gall, A., Girón, C., Gil, L., Gordon, L., Haggerty, L., Haskell, E., Hourlier, T., Izuogu, O. G., Janacek, S. H., Juettemann, T., To, J., Laird, M. R., Lavidas, I., Liu, Z., Loveland, J. E., Maurel, T., McLaren, W., Moore, B., Mudge, J., Murphy, D. N., Newman, V., Nuhn, M., Ogeh, D., Ong, C., Parker, A., Patricio, M., Riat, H., Schuilenburg, H., Sheppard, D., Sparrow, H., Taylor, K., Thormann, A., Vullo, A., Walts, B., Zadissa, A., Frankish, A., Hunt, S. E., Kostadima, M., Langridge, N., Martin, F. J., Muffato, M., Perry, E., Ruffier, M., aines, D., Trevanion, S. J., Aken, B. L., Cunningham, F., Yates, A. & Flicek, P. Ensembl 2018. *Nucleic Acids Res* **46,** D754–D761 (2017).

195. Durinck, S., Spellman, P. T., Birney, E. & Huber, W. Mapping identifiers for the integration of genomic datasets with the R/Bioconductor package biomaRt. *Nat Protoc* **4,** 1184–91 (2009).

196. Durinck, S., Moreau, Y., Kasprzyk, A., Davis, S., Moor, D. B., Brazma, A. & Huber, W. BioMart and Bioconductor: a powerful link between biological databases and microarray data analysis. *Bioinformatics* **21,** 3439–3440 (2005).

197. Pagès, H., Carlson, M., Falcon, S. & Li, N. AnnotationDbi: Manipulation of SQLite-based annotations in Bioconductor.

198. Swinton, J. Vennerable.

199. Chen, H. VennDiagram: Generate High-Resolution Venn and Euler Plots. (2018).

200. Heinz, S., Benner, C., Spann, N., Bertolino, E., Lin, Y. C., Laslo, P., Cheng, J. X., Murre, C., Singh, H. & Glass, C. K. Simple Combinations of Lineage-Determining Transcription Factors Prime cis-Regulatory Elements Required for Macrophage and B Cell Identities. *Mol Cell* **38,** 576–589 (2010).

201. Lanner, F. Lineage specification in the early mouse embryo. *Exp Cell Res* **321,** 32–39 (2014).

202. Evans, M. & Kaufman, M. Establishment in culture of pluripotential cells from mouse embryos. *Nature* **292,** 154–156 (1981).

203. Martin, G. Isolation of a pluripotent cell line from early mouse embryos cultured in medium conditioned by teratocarcinoma stem cells. *Proc National Acad Sci* **78,** 7634–7638 (1981).

204. Murry, C. E. & Keller, G. Differentiation of embryonic stem cells to clinically relevant populations: lessons from embryonic development. *Cell* **132,** 661–80 (2008).

205. Leahy, A., Xiong, J., Kuhnert, F. & Stuhlmann, H. Use of developmental marker genes to define temporal and spatial patterns of differentiation during embryoid body formation. *J Exp Zoology* **284,** 67–81 (1999).

206. Coucouvanis, E. & Martin, G. R. Signals for death and survival: A two-step mechanism for cavitation in the vertebrate embryo. *Cell* **83,** 279–287 (1995).

207. Gadue, P., Huber, T. L., Paddison, P. J. & Keller, G. M. Wnt and TGF-β signaling are required for the induction of an in vitro model of primitive streak formation using embryonic stem cells. *Proc National Acad Sci* **103,** 16806–16811 (2006).

208. Grapin-Botton, A. & Constam, D. Evolution of the mechanisms and molecular control of endoderm formation. *Mech Develop* **124,** 253–278 (2007).

209. Li, F., He, Z., Li, Y., Liu, P., Chen, F., Wang, M., Zhu, H., Ding, X., Wangensteen, K. J., Hu, Y. & Wang, X. Combined activin A/LiCl/Noggin treatment improves production of mouse embryonic stem cell-derived definitive endoderm cells. *J Cell Biochem* **112,** 1022–1034 (2011).

210. Bossard, P. & Zaret, K. GATA transcription factors as potentiators of gut endoderm differentiation. *Dev Camb Engl* **125,** 4909–17 (1998).

211. Kanai-Azuma, M., Kanai, Y., Gad, J. M., Tajima, Y., Taya, C., Kurohmaru, M., Sanai, Y., Yonekawa, H., Yazaki, K., Tam, P. P. & Hayashi, Y. Depletion of definitive gut endoderm in Sox17-null mutant mice. *Dev Camb Engl* **129,** 2367–79 (2002).

212. Metallo, C. M. & Heiden, M. G. Understanding metabolic regulation and its influence on cell physiology. *Mol Cell* **49,** 388–98 (2013).

213. Wellen, K. E. & Thompson, C. B. A two-way street: reciprocal regulation of metabolism and signalling. *Nat Rev Mol Cell Biology* **13,** 270–6 (2012).

214. Chason, R. J., Csokmay, J., Segars, J. H., DeCherney, A. H. & Armant, R. D. Environmental and epigenetic effects upon preimplantation embryo metabolism and development. *Trends Endocrinol Metabolism* **22,** 412–420 (2011).

215. Shyh-Chang, N., Daley, G. & Cantley, L. Stem cell metabolism in tissue development and aging. *Development* **140,** 2535–2547 (2013).

216. Cho, Y., Kwon, S., Pak, Y., Seol, H., Choi, Y., Park, D., Park, K. & Lee, H. Dynamic changes in mitochondrial biogenesis and antioxidant enzymes during the spontaneous differentiation of human embryonic stem cells. *Biochem Bioph Res Co* **348,** 1472–1478 (2006).

217. Folmes, C. D., Nelson, T. J., Martinez-Fernandez, A., Arrell, K. D., Lindor, J., Dzeja, P. P., Ikeda, Y., Perez-Terzic, C. & Terzic, A. Somatic Oxidative Bioenergetics

Transitions into Pluripotency-Dependent Glycolysis to Facilitate Nuclear Reprogramming. *Cell Metab* **14,** 264–271 (2011).

218. Moussaieff, A., Rouleau, M., Kitsberg, D., Cohen, M., Levy, G., Barasch, D., Nemirovski, A., Shen-Orr, S., Laevsky, I., Amit, M., Bomze, D., Elena-Herrmann, B., Scherf, T., Nissim-Rafinia, M., Kempa, S., Itskovitz-Eldor, J., Meshorer, E., Aberdam, D. & Nahmias, Y. Glycolysis-mediated changes in acetyl-CoA and histone acetylation control the early differentiation of embryonic stem cells. *Cell Metab* **21,** 392–402 (2015).

219. O'Neill, H. M., Maarbjerg, S. J., Crane, J. D., Jeppesen, J., Jørgensen, S. B., Schertzer, J. D., Shyroka, O., Kiens, B., van Denderen, B. J., Tarnopolsky, M. A., Kemp, B. E., Richter, E. A. & Steinberg, G. R. AMP-activated protein kinase (AMPK) beta1beta2 muscle null mice reveal an essential role for AMPK in maintaining mitochondrial content and glucose uptake during exercise. *P Natl Acad Sci Usa* **108,** 16092–7 (2011).

220. Viollet, B., Athea, Y., Mounier, R., Guigas, B., Zarrinpashneh, E., Horman, S., Lantier, L., Hebrard, S., Devin-Leclerc, J., Beauloye, C., Foretz, M., Andreelli, F., Ventura-Clapier, R. & Bertrand, L. AMPK: Lessons from transgenic and knockout animals. *Front Biosci* **Volume,** 19 (2009).

221. Muzumdar, M., Tasic, B., Miyamichi, K., Li, L. & Luo, L. A global double-fluorescent Cre reporter mouse. *Genesis* **45,** 593–605 (2007).

222. Platt, F. M., Boland, B. & van der Spoel, A. C. Lysosomal storage disorders: The cellular impact of lysosomal dysfunction. *J Cell Biology* **199,** 723–734 (2012).

223. Saftig, P. & Klumperman, J. Lysosome biogenesis and lysosomal membrane proteins: trafficking meets function. *Nat Rev Mol Cell Bio* **10,** 623–635 (2009).

224. Ploper, D., Taelman, V. F., Robert, L., Perez, B. S., Titz, B., Chen, H.-W., Graeber, T. G., von Euw, E., Ribas, A. & Robertis, E. MITF drives endolysosomal biogenesis and potentiates Wnt signaling in melanoma cells. *P Natl Acad Sci Usa* **112,** E420-9 (2015).

225. Martina, J., Diab, H., Lishu, L., Jeong-A, L., Patange, S., Raben, N. & Puertollano, R. The Nutrient-Responsive Transcription Factor TFE3 Promotes Autophagy, Lysosomal Biogenesis, and Clearance of Cellular Debris. *Sci Signal* **7,** ra9–ra9 (2014).

226. Settembre, C., Malta, D. C., Polito, V., Arencibia, M., Vetrini, F., Erdin, S., Erdin, S., Huynh, T., Medina, D., Colella, P., rdiello, Rubinsztein, D. & Ballabio, A. TFEB Links Autophagy to Lysosomal Biogenesis. *Science* **332,** 1429–1433 (2011).

227. Sardiello, M., Palmieri, M., di Ronza, A., Medina, D., Valenza, M., Gennarino, V., Malta, C., Donaudy, F., Embrione, V., Polishchuk, R. S., Banfi, S., Parenti, G., Cattaneo, E. & Ballabio, A. A gene network regulating lysosomal biogenesis and function. *Sci New York N Y* **325,** 473–7 (2009).

228. Roczniak-Ferguson, A., Petit, C., Froehlich, F., Qian, S., Ky, J., garola, Walther, T. & Ferguson, S. The Transcription Factor TFEB Links mTORC1 Signaling to Transcriptional Control of Lysosome Homeostasis. *Sci Signal* **5,** ra42–ra42 (2012).

229. Medina, D. L., Paola, S., Peluso, I., Armani, A., Stefani, D., Venditti, R., Montefusco, S., Scotto-Rosato, A., Prezioso, C., Forrester, A., Settembre, C., Wang, W., Gao, Q., Xu, H., Sandri, M., Rizzuto, R., Matteis, M. & Ballabio, A. Lysosomal calcium signalling regulates autophagy through calcineurin and TFEB. *Nat Cell Biol* **17,** 288–299 (2015).

230. Settembre, C., Zoncu, R., Medina, D. L., Vetrini, F., Erdin, S., Erdin, S., Huynh, T., Ferron, M., Karsenty, G., Vellard, M. C., Facchinetti, V., batini, D. & Ballabio, A. A lysosome-to-nucleus signalling mechanism senses and regulates the lysosome via mTOR and TFEB. *Embo J* **31,** 1095–108 (2012).

231. Sun-Wada, G.-H., Murata, Y., Yamamoto, A., Kanazawa, H., Wada, Y. & Futai, M. Acidic Endomembrane Organelles Are Required for Mouse Postimplantation Development. *Dev Biol* **228,** 315–325 (2000).

232. Eskelinen, E.-L., Schmidt, C., Neu, S., Willenborg, M., Fuertes, G., Salvador, N., Tanaka, Y., Lüllmann-Rauch, R., Hartmann, D., Heeren, J., von Figura, K., Knecht, E. & Saftig, P. Disturbed Cholesterol Traffic but Normal Proteolytic Function in LAMP-1/LAMP-2 Double-deficient Fibroblasts. *Mol Biol Cell* **15,** 3132–3145 (2004).

233. Steingrímsson, E., Tessarollo, L., Reid, S., Jenkins, N. & Copeland, N. The bHLH-Zip transcription factor Tfeb is essential for placental vascularization. *Dev Camb Engl* **125,** 4607–16 (1998).

234. Settembre, C., Cegli, R., Mansueto, G., Saha, P. K., Vetrini, F., Visvikis, O., Huynh, T., Carissimo, A., Palmer, D., Klisch, T., Wollenberg, A. C., Bernardo, D., Chan, L., Irazoqui, J. E. & Ballabio, A. TFEB controls cellular lipid metabolism through a starvation-induced autoregulatory loop. *Nat Cell Biol* **15,** 647–658 (2013).

235. Wada, Y. & Sun-Wada, G.-H. Positive and negative regulation of developmental signaling by the endocytic pathway. *Curr Opin Genet Dev* **23,** 391–398 (2013).

236. Taelman, V. F., Dobrowolski, R., Plouhinec, J.-L., Fuentealba, L. C., Vorwald, P. P., Gumper, I., Sabatini, D. D. & Robertis, E. Wnt Signaling Requires Sequestration of Glycogen Synthase Kinase 3 inside Multivesicular Endosomes. *Cell* **143,** 1136–1148 (2010).

237. Engert, S., Burtscher, I., Liao, W., Dulev, S., Schotta, G. & Lickert, H. Wnt/ -catenin signalling regulates Sox17 expression and is essential for organizer and endoderm formation in the mouse. *Development* **140,** 3128–3138 (2013).

238. Coucouvanis, E. & Martin, G. BMP signaling plays a role in visceral endoderm differentiation and cavitation in the early mouse embryo. *Dev Camb Engl* **126,** 535–46

(1999).

239. Zhou, J., Su, P., Wang, L., Chen, J., Zimmermann, M., Genbacev, O., Afonja, O., Horne, M. C., Tanaka, T., Duan, E., Fisher, S. J., Liao, J., Chen, J. & Wang, F. mTOR supports long-term self-renewal and suppresses mesoderm and endoderm activities of human embryonic stem cells. *P Natl Acad Sci Usa* **106,** 7840–5 (2009).

240. Steingrímsson, E., Copeland, N. G. & Jenkins, N. A. Melanocytes and the Microphthalmia Transcription Factor Network. *Annu Rev Genet* **38,** 365–411 (2004).

241. Betschinger, J., Nichols, J., Dietmann, S., Corrin, P. D., Paddison, P. J. & Smith, A. Exit from pluripotency is gated by intracellular redistribution of the bHLH transcription factor Tfe3. *Cell* **153,** 335–47 (2013).

242. Kawamura, N., Sun-Wada, G.-H., Aoyama, M., Harada, A., Takasuga, S., Sasaki, T. & Wada, Y. Delivery of endosomes to lysosomes via microautophagy in the visceral endoderm of mouse embryos. *Nat Commun* **3,** 1071 (2012).

243. Aoyama, M., Sun-Wada, G.-H., Yamamoto, A., Yamamoto, M., Hamada, H. & Wada, Y. Spatial restriction of bone morphogenetic protein signaling in mouse gastrula through the mVam2-dependent endocytic pathway. *Dev Cell* **22,** 1163–75 (2012).

244. Amaravadi, R. K., Lippincott-Schwartz, J., Yin, X.-M., Weiss, W. A., Takebe, N., Timmer, W., DiPaola, R. S., Lotze, M. T. & White, E. Principles and current strategies for targeting autophagy for cancer treatment. *Clin Cancer Res Official J Am Assoc Cancer Res* **17,** 654–66 (2011).

245. Ye, S., Tan, L., Yang, R., Fang, B., Qu, S., Schulze, E. N., Song, H., Ying, Q. & Li, P. Pleiotropy of Glycogen Synthase Kinase-3 Inhibition by CHIR99021 Promotes Self-Renewal of Embryonic Stem Cells from Refractory Mouse Strains. *Plos One* **7,** e35892 (2012).

246. Mootha, V. K., Lindgren, C. M., Eriksson, K.-F., Subramanian, A., Sihag, S., Lehar, J., Puigserver, P., Carlsson, E., Ridderstråle, M., Laurila, E., Houstis, N., Daly, M. J., Patterson, N., Mesirov, J. P., Golub, T. R., Tamayo, P., Spiegelman, B., Lander, E. S., Hirschhorn, J. N., Altshuler, D. & Groop, L. C. PGC-1α-responsive genes involved in oxidative phosphorylation are coordinately downregulated in human diabetes. *Nat Genet* **34,** 267–273 (2003).

247. Huang, D., Sherman, B. T. & Lempicki, R. A. Systematic and integrative analysis of large gene lists using DAVID bioinformatics resources. *Nat Protoc* **4,** 44–57 (2009).